AN ABSTRACT OF THE DISSERTATION OF

DANIEL A. HOWELL for the degree of Doctor of Philosophy in Civil Engineering presented on April 17, 2009.

Title: Shear Repair Methods for Conventionally Reinforced Concrete Girders and Deep Beams.

Abstract approved:

_____

Christopher C. Higgins

Many conventionally reinforced concrete deck girder bridges (RCDG) and their intermediate supporting bent caps were designed during the Eisenhower interstate era of the 1950's with the AASHO design equations at the time, which subsequently place higher demand on the concrete. The referenced components may exhibit diagonal cracking due to the initial design assumptions, increased traffic volume and truck weights, as well as temperature and shrinkage affects. Action is needed as these structures approach the end of their useful design life. Wholesale replacement is not economically feasible; therefore, repair may provide a more attractive alternative to maintain operational safety and freight mobility.

The current research program builds on previous work at OSU, which focused on estimating unrepaired specimen capacity, to include various repair methods. The experimental program included full scale testing of specimens with vintage 1950s details, reinforcing steel, concrete strength/composition, and flexural cutoffs details. Repairs included externally applied steel stirrups, supplemental internal stirrups, externally applied carbon fiber reinforced plastic (CFRP), carbon fiber tape utilized in a near surface mount application, and longitudinal post tensioning (bent cap specimen only). All specimens were initially loaded under quasi-static force control to produce diagonal cracks in the specimen then repaired and tested to failure.

Ultimate specimen capacity was compared against that predicted from those available in the literature (where applicable), international codes, sectional Modified Compression Field Theory (MCFT) analysis, Modified Zararis Mechanical Model (bent caps only), Strut-and-Tie methods (bent cap only), and nonlinear finite element analysis (NLFEM).

Results indicate the repair methods increased the member strength and the predicted member strenths compare well to certain international codes, sectional MCFT analysis, and nonlinear FEM element analysis. Some repair techniques such as surface mounted CFRP produced disparate outcomes for different specimen types. The NSM repair technique requires additional research to draw general conclusions. Longitudinal post tensioning compared well with the Modified Zararis method. STM methods form a very conservative lower bound for design and are thus not suggested for base specimen capacity prediction in a retrofit analysis. Design recommendations for the deep beams are not provided, as there is not sufficient data to support general conclusions.

Shear Repair Methods for Conventionally Reinforced Concrete Girders and Deep Beams

by

Daniel A. Howell

A DISERTATION

submitted to

Oregon State University

in partial fulfillment of

the requirements for the

degree of

Doctor of Philosophy

Presented April 17, 2009

Commencement June 2009

Doctor of Philosophy dissertation of Daniel A. Howell presented on April 17, 2009.

APPROVED:

_____

Major Professor, representing Civil Engineering

_____

Head of the School of Civil and Construction Engineering

_____

Dean of the Graduate School

I understand that my dissertation will become part of the permanent collection of Oregon State University libraries. My signature below authorizes release of my dissertation to any reader upon request.

_____

Daniel A. Howell, Author

ACKNOWLEDGEMENTS

The author wishes to acknowledge several individuals who have positively affected the outcome of this project. First, I would like to thank Dr. Chris Higgins, for the opportunity to work on a large project with real world objectives. I value his patience for seeing the project through. Also, his advice and guidance will continue to guide me throughout my career.

With a project of this magnitude, I could not have completed it without the help and diligence of several graduate students, including: Carl Koester, Matt Smith, Dr. Ekin Senturk, Osman Hamutcuoglu, Tugrul Turan, Jordan Pelphrey, Ae-Young Lee, Thomas Schumacher, Matt Dawson, Mikal Mitchel, and Gautum Sopal. In addition, the following undergraduates have contributed in one form or another: Kate Bradbury, Laurel Senger, Jake Goebel, and Stephanie Pershing. I could not accomplish this work without the constant support and love from my wife, Miya. Lastly, I would like to thank the Oregon Department of Transportation for funding this project.

TABLE OF CONTENTS

TABLE OF CONTENTS (Continued)

TABLE OF CONTENTS (Continued)

TABLE OF CONTENTS (Continued)

TABLE OF CONTENTS (Continued)

TABLE OF CONTENTS (Continued)

TABLE OF CONTENTS (Continued)

LIST OF FIGURES

LIST OF FIGURES (Continued)

Figure Page

LIST OF FIGURES (Continued)

Figure Page

LIST OF FIGURES (Continued)

Figure Page

LIST OF FIGURES (Continued)

Figure Page

LIST OF FIGURES (Continued)

Figure Page

LIST OF FIGURES (Continued)

Figure Page

LIST OF FIGURES (Continued)

Figure Page

LIST OF FIGURES (Continued)

LIST OF FIGURES (Continued)

LIST OF FIGURES (Continued)

LIST OF FIGURES (Continued)

LIST OF FIGURES (Continued)

Figure Page

LIST OF FIGURES (Continued)

LIST OF TABLES

LIST OF TABLES (Continued)

1. INTRODUCTION

1.1 Background

Large numbers of conventionally reinforced concrete deck girder (RCDG) bridges were built during the Eisenhower interstate era of the late 1940s to the mid 1960s. These bridges were designed following AASHO national standards of the time. The shear design requirements of this period were less stringent than those in the modern AASHTO Specifications. Higher demands have been placed on the bridge members during their service lives with increasing load magnitudes, millions of load cycles, and environmental exposure such as temperature gradients, freeze-thaw, and/or wet-dry cycles. These conditions may result in diagonal-tension cracks in the main girders and interior supports. As an example, in Oregon, a large number of RCDG bridges in the inventory are from the 1950's and state inspectors have identified diagonal cracks in the girders and supporting bent caps on over 500 of these bridges, including 200 such bridges on the state's dominant truck routes [Zaintz and Long 2007].

Wholesale replacement of the large inventory of aging RCDG bridges is not practicable due to economic constraints; therefore, a management approach that can apply effective repair methods in conjunction with replacement for bridges with insufficient live load ratings would be able to maintain system operation.. Several possible repair alternatives

are available for diagonally cracked RCDG members, including: epoxy injection, internal supplemental stirrups; external supplemental stirrups-threaded steel rod, carbon fiber reinforced plastic (CFRP) sheets, near surface mounted (NSM) fiber reinforced plastic strips; and post tensioning. However, systematic comparisons between alternatives that can quantify available capacity increases, installation sensitivity, and cost are not available for large lightly reinforced concrete members and research is needed to provide this information.

1.2 Research Objectives

Currently, structural performance of large lightly reinforced RCDG girders with diagonal cracks repaired with different materials and techniques are uncertain. No general comparisons are available among the various alternatives and there is no guidance for assessing the costs and benefits of the various methods. Further, design and analysis methods have not been validated and inspection protocols of post-repaired specimens have not been established.

The objectives of this research were to quantify the structural performance of repair techniques, at service level (before and after repair) and at ultimate load for reinforced concrete bridge girders and bent caps lightly reinforced for shear. Several available and emerging repair methods were investigated including epoxy injection, internal

supplemental steel stirrups, external supplemental steel stirrups, externally bonded carbon fiber composites (CFRP), near surface mounted composite tape (NSM), and external post-tensioning. The laboratory results were used to compare current national code and/or applicable archival literature design approaches and where appropriate, modifications are made for design. Based on laboratory tests, recommendations are made for field inspection of post-repaired girders.

1.3 Research Significance

The research provides a unique contribution to the engineering community in the broad systematic treatment of many available repair schemes for conventionally reinforced concrete girders and deep beams exhibiting diagonal tension cracks. The work fulfills a need within the engineering community as wholesale bridge replacements are not feasible due to economic constraints. However, repair of RCDG bridges may provide a viable alternative that can extend the life of the highway transportation system and maintain operational capacity. Experimental data on structural behavior of shear strengthened large size RC members is not currently available to validate design approaches for several repair alternatives, even as some of these methods are being implemented in the field, and this research fulfills this need. The research program across a broad spectrum of viable repair approaches further enables effective comparisons between the different repair schemes and will aid in the selection of the most appropriate alternative for different field conditions.

A test program with large numbers of realistically proportioned full-size laboratory specimens is at the highest level of experimental research achievement and will help identify possible performance issues that may not be apparent with small-scale specimens. The proposed bent cap tests are the largest and most realistic of their kind attempted. Incorporation of field inspection and testing data on in-service repaired bridges will enable realistic performance comparisons at service level conditions which are not commonly found in previous research. The experimental results on full-size specimens will be used to validate current design methods or lead to development of modifications or alternative approaches that are not currently available.

2. LITERATURE REVIEW

2.1. Code Provisions

The current code provisions from the United States, Canada, and Europe are included for comparison. The North American codes include American Building Code Requirements for Structural Concrete referred to as ACI318-05 (2005), American Association of State Highway and Transportation Officials LRFD Bridge Design Specifications referred to as AASHTO LRFD (2005), and Canadian Highway Bridge Design Code (2000). The European codes include Eurocode 2: Design of Concrete Structures (2004), Euro-International Committee for Concrete & International Federation for Prestressing Model Code (1990), and International Federation for Prestressing Recommendations on Practical Design of Structural Concrete (1999). Each code was reviewed with respect to shear strength of unrepaired specimens as well as any additional strength gain provided by supplemental strengthening schemes for traditional and deep beam specimens.

2.1.1 American Concrete Institute 318-05 American Building Code Requirements for Structural Concrete

ACI 318-05 provides the minimum requirements for design and construction of both traditionally reinforced and prestressed concrete structures. The occurrence of failure is minimized utilizing strength reduction factors such that the reduced nominal strength of a section is greater than the required strength or load, as denoted in Equation [2.1] below.

$$\phi(Nom\_Strength) \geq U \qquad [2.1]$$

Where ϕ is a resistance factor less than 1.0 intended to reduce the nominal strength of a section based on the applied forces and U is the required strength, as outlined in Article 9.2, based on several possible load combinations and associated factors. The requirements for shear and torsion of a concrete section are covered under Chapter 11. For shear, Equation [2.1] is modified as shown below in Equation [2.2].

$$\phi V_n \geq V_u \qquad \text{ACI 318-05 (11-1)} \qquad [2.2]$$

Where V_u (kips) is the factored shear force and the nominal shear strength V_n (kips) is computed from contributions from both concrete and steel as shown in Equation [2.3].

$$V_n = V_c + V_s \qquad \text{ACI 318-05 (11-2)} \qquad [2.3]$$

Where V_c (kips) is the nominal shear strength carried by the concrete and V_s (kips) is the nominal shear strength provided by the shear reinforcement.

2.1.1.1 ACI 318-05 Traditional Beam Capacity

Prior to calculation of the shear capacity of a section, the code requires a check to ensure minimum transverse steel area and spacing such that the behavior of the specimens is similar to laboratory tests on which the code is based. Also, Article 11.1.2 limits the value of $\sqrt{f_c'}$ to 100 psi, unless the section of interest contains the minimum web reinforcement. Minimum shear reinforcement is required, as outlined in Article 11.5.6.1 where the factored shear force V_u exceeds one half the factored nominal concrete shear strength. Once met, the minimum area of steel is denoted in Article 11.5.6.3 and as shown below in Equation [2.4].

$$A_{v,\min} = 0.75\sqrt{f_c'}\frac{b_w s}{f_{yt}} > \frac{(50 b_w s)}{f_{yt}} \qquad \text{ACI 318-05 11-13} \qquad [2.4]$$

Where $A_{v,min}$ (in.^{2}) is the minimum area of shear reinforcement within spacing s (in.), f_c' (psi) is the specified compressive strength of concrete, b_w (in.) is the web width, s (in) is the center to center spacing of the shear reinforcement, and f_{yt} (psi) is the specified yield strength of the transverse reinforcement. In addition to minimum area requirements, Article 11.5.5 limits spacing of the transverse reinforcement to the lesser of d/2 or 24 in. for nonprestressed members, except where V_s exceeds $4\sqrt{f_c'}b_w d$. In which case, the spacing must be reduced by one half (where d (in.) is defined as the distance from the extreme compression fiber to the centroid of the tension reinforcement).

Once minimum area and spacing requirements are satisfied, the nominal shear resistance resulting from the contributions of steel and concrete can be determined. The concrete contribution to shear strength is outlined in Article 11.3 utilizing two design equations. The first, denoted in Equation [2.5] below, is intended for members subjected to shear and flexure only; it is recommended unless a more detailed calculation is required.

$$V_c = 2\sqrt{f_c'}\,b_w d \qquad \text{ACI 318-05 (11-3)} \qquad [2.5]$$

A more detailed equation is shown below in Equation [2.6].

$$V_c = \left(1.9\sqrt{f_c'} + 2500\rho_w \frac{V_u d}{M_u}\right) b_w d < 3.5\sqrt{f_c'}\,b_w d \qquad \text{ACI 318-05 (11-5)} \qquad [2.6]$$

Where $\rho_w = \frac{A_s}{b_w d}$ is the reinforcement ratio, V_u (kips), and M_u (kip*ft) are the factored shear and moment at the section of interest—with the stipulation that the value $\frac{V_u}{M_u}$ not to exceed 1.0.

The shear strength provided by the steel is documented in Article 11.5.7 and shown below in Equation [2.7].

$$V_s = \frac{A_v f_{yt} d}{s} \qquad \text{ACI 318-05 (11-15)} \qquad [2.7]$$

2.1.1.2 ACI 318-05 Deep Beam Capacity

Deep beam specimens are described in detail under Section 2.1.3.2 under the AASHTO specifications utilizing the STM method, with comparisons to other remaining codes.

2.1.2 American Concrete Institute Committee 440

The 2005 American Concrete Institute Manual for Concrete Practice include the recommendations of Committee 440 regarding the design and construction of externally bonded fiber reinforced plastic systems for strengthening concrete structures. As the guideline is enveloped by ACI, the governing principles regarding load and resistance factors are the same as outlined under ACI 318-05. The scope of the document encompasses the latest technical information based on a twenty year period of experimental research, field studies, and analytical work. Within this context, the committee recommendations form a lower bound as to provide a conservative repair methodology. The application of the repair scheme on the surface of the beams requires significant surface preparation and quality control of materials, environmental factors such as temperature, humidity, and moisture concerns; the installation procedures, including curing time, temperature and humidity are included in Chapter 3.

The design requirements for ACI 440 are included in Chapter 8 of ACI 440.2R-02. Two limit states are described for design. The service limit state limits excessive deflections, cracking, vibrations, etc. while the strength limit state limits failure of the member, stress rupture, and fatigue. Consideration to the virgin specimen strength without FRP is a concern, as indicated by the strengthening limits proposed in Equation [2.8] below:

$$\left(\varphi R_n\right)_{existing} \geq \left(1.25S_{DL} + 0.85S_{LL}\right)_{new} \qquad \text{ACI 440.2R (8-1)} \qquad [2.8]$$

Equation [2.8] indicates that the existing structure must be capable of sustaining its own dead load plus a portion of the live load. The requirement is intended to safeguard the structure in the even the repaired FRP is removed or rendered ineffective by a fire event.

Environmental factors may affect the long term strength of FRP systems. As such, the committee recommends the use of an environmental reduction factor C_E as shown below in Equation [2.9].

$$f_{fu} = C_E f_{fu}^{*} \qquad \text{ACI 440.2R (8-3)} \qquad [2.9]$$

The design rupture strain is also reduced as indicated in Equation [2.10] below.

$$\varepsilon_{fu} = C_E \varepsilon_{fu}^{*} \qquad \text{ACI 440.2R (8-4)} \qquad [2.10]$$

Strengthening for shear is covered in Chapter 10 of the guide. The first consideration for strengthening pertains to the wrapping scheme used—either a full wrap, 3-sided U-wrap, or 2-sided wrap are covered. For beam strengthening, the use of a full wrap is prohibited

due to geometric constraints of the deck superstructure between adjacent beams. Of the two remaining repair schemes, the 3 sided U-wrap is preferred.

The additional strength gain from the FRP repair is analogous to the shear strength contribution from steel and concrete respectively. In this respect, the FRP repair is simply added to the previous two shear contributions, resulting in a nominal resistance as shown below in Equation [2.11].

$$\phi V_n = \phi(V_c + V_s + \Psi_f V_f) \qquad \text{ACI 440.2R (10-2)} \qquad [2.11]$$

Where ϕ is 0.90 for shear design, V_c (kips) and V_s (kips) are as determined in ACI 318-05 in Equations [2.5] or [2.6] and [2.7] respectively. The ψ_f term is an additional reduction factor for the shear contribution from FRP which varies from 0.85 for the three-sided U wrap or bonded face plies to 0.95 for completely wrapped members. The V_f (kips) term is the strength gain from the FRP.

The FRP contribution to shear strength is described in Section 10.4. Once a repair scheme has been selected, the fiber orientation to the estimated failure crack is determined. The shear strength provided by the FRP is then calculated from the force resulting from the stress in the FRP across the failure crack, as shown below in Equation [2.12].

$$V_f = \frac{A_{fv} f_{fe} (\sin\alpha + \cos\alpha) d_f}{s_f} \qquad \text{ACI 440.2R (10-3)} \qquad [2.12]$$

Where A_{fv} (in.^{2}) is defined below in Equation [2.13], f_{fe} (psi) is the effective stress in the FRP at failure, α is the inclination of the reinforcement to the longitudinal axis of the member, d_f (in.) is the depth of the FRP, and s_f (in.) is the spacing of the FRP strips.

$$A_{fv} = 2nt_f w_f \qquad \text{ACI 440.2R (10-4)} \qquad [2.13]$$

Where n is the number of plies of reinforcement, t_f (in.) is the nominal thickness of one ply of reinforcement, w_f (in.) is the width of the FRP plies. FRP remains linear until fracture, thus the effective stress f_{fe} in Equation [2.12] is proportional to the modulus and the failure strain, as denoted in Equation [2.14] below.

$$f_{fe} = \varepsilon_{fe} E_f \qquad \text{ACI 440.2R (10-5)} \qquad [2.14]$$

Where ε_{fe} (in./in.) is the effective strain in the FRP at failure and E_f (psi) is the modulus of elasticity of the FRP. The guide provides further information for calculating the effective strain at failure depending on the repair scheme. For the current investigation, utilizing a 3-sided wrap, the code directs the user to Section 10.4.1.2. The failure mode of this repair scheme is governed by the bond strength between the FRP and the concrete. Thus, the effective strain is calculated using a reduction coefficient as denoted in Equation [2.15] below.

$$\varepsilon_{fe} = \kappa_v \varepsilon_{fu} \le 0.004 \qquad \text{ACI 440.2R (10-6(b))} \qquad [2.15]$$

The reduction factor is calculated based on the concrete strength, the wrapping scheme, and the stiffness of the laminate, as denoted in English units in Equation [2.16] below.

$$\kappa_v = \frac{k_1 k_2 L_e}{468\varepsilon_{fu}} \le 0.75 \qquad \text{ACI 440.2R (10-7) U.S.} \qquad [2.16]$$

The corresponding SI factor is shown in Equation [2.17].

$$\kappa_v = \frac{k_1 k_2 L_e}{11900\varepsilon_{fu}} \le 0.75 \qquad \text{ACI 440.2R (10-7) SI} \qquad [2.17]$$

Where k_1 is a factor relating to the concrete strength denoted in Equations [2.18] (U.S. Units) and [2.19] (SI Units).

$$k_1 = \left(\frac{f_c'}{4000}\right)^{\frac{2}{3}} \qquad \text{ACI 440.2R (10-9) U.S.} \qquad [2.18]$$

$$k_1 = \left(\frac{f_c'}{27}\right)^{\frac{2}{3}} \qquad \text{ACI 440.2R (10-9) SI} \qquad [2.19]$$

Where f_c' is the concrete strength in psi (Equation [2.18]) and MPa (Equation [2.19]). The term k_2 relates to the wrapping type as shown in Equation [2.20].

$$k_2 = \begin{cases} \dfrac{d_f - L_e}{d_f} \text{ for U-wraps} \\ \dfrac{d_f - 2L_e}{d_f} \text{ for two sides bonded} \end{cases} \qquad \text{ACI 440.2R (10-10)} \qquad [2.20]$$

Where d_f has previously been defined, and L_e is the active bond length as shown below in Equations [2.21] (U.S. Units) and [2.22](SI Units).

$$L_e = \frac{2500}{\left(nt_f E_f\right)^{0.58}} \qquad \text{ACI 440.2R (10-8) U.S.} \qquad [2.21]$$

$$L_e = \frac{23300}{\left(nt_f E_f\right)^{0.58}} \qquad \text{ACI 440.2R (10-8) SI} \qquad [2.22]$$

The values used in the above equations have been previously defined.

2.1.3 American Association of State Highway and Transportation Officials LRFD Bridge Design Specifications (2005)

The 2005 AASHTO LRFD provisions "apply to design, evaluation, and rehabilitation of both fixed and moveable highway bridges." The specifications provide load and resistance factors based on the theory of reliability with appropriate load and resistance modifiers based on the current state of knowledge concerning their individual distributions as denoted below in Equation [2.23].

$$\sum \eta_i \gamma_i Q_i \leq \phi R_n \qquad \text{AASHTO LRFD } (1.3.2.1-1) \qquad [2.23]$$

Where η_i is a load modifier which is based on ductility, redundancy, and operational importance, γ_i is a load factor, Q_i is the nominal force effect, φ is a resistance factor, and R_n is the nominal resistance.

Both load and resistance are assumed to follow a normal distribution with a higher degree of uncertainty associated with the applied loads. The provisions define four limit states which encompass design loads, ultimate loading, fatigue, and extreme force effects. The first, denoted as the service limit state, places restriction on stress, deformation, and crack width under designed traffic loads. The second, identified as the strength limit state, is used to ensure global structural stability with the designed load combinations, modified by accompanying load factor(s). The third, denoted as the fatigue and fracture limit state

relates to stress range limitations and material toughness requirements for fatigue and fracture respectively. The last, denoted as the extreme event limit state, provides structural survival based on a major earthquake, flood, vessel collision, scour, or ice flow. The scope of the current research project will include service and strength limit states; repair for the latter two limit states are beyond the scope of work. For the service limit state, the load modifiers, load factors, and resistance factors are set to 1.0.

2.1.3.1 AASHTO LRFD 2005 Traditional Beam Capacity

Beams having a span-to-depth ratio greater than 2.0 conform to traditional Bernoulli beam theory in which plane sections remain plane. The design of traditionally reinforced as well as prestressed concrete members is covered under Chapter 5 within AASHTO. As with the ACI code, the minimum vertical steel reinforcing and spacing is checked prior to capacity calculations. The first condition that is checked for the shear design of a member relates to the use of minimum vertical steel reinforcement as defined in Article 5.8.2.4, and shown below in Equation [2.24].

$$V_u > 0.5\phi\left(V_c + V_p\right) \qquad \text{AASHTO LRFD 5.8.2.4-1} \qquad [2.24]$$

Where V_u (kips) is the factored shear force, V_c (kips) is the nominal shear resistance of the concrete, and V_p (kips) is the component of the prestressing force in the direction of the shear force (equal to zero in the current investigation), and φ is the resistance factor specified in Section 5.5.4.2 for shear—in this case the value is 0.90. The corresponding nominal shear resistance of the concrete is shown in Equation [2.25].

$$V_c = 0.0316\beta\sqrt{f_c'}b_v d_v \qquad \text{AASHTO LRFD 5.8.3.3-3} \qquad [2.25]$$

Where V_c (kips) is the nominal shear resistance from the concrete, β is the factor indicating the ability of the diagonally cracked concrete to transmit tension as specified in Article 5.8.3.4, f_c' (ksi) is the compressive strength of the concrete, b_v (in.) is the effective web width taken as the minimum web width within the depth d_v (in.) as determined in Article 5.8.2.9, and d_v (in.) is the effective shear depth as determined in Article 5.8.2.9.

Article 5.8.2.9 defines the shear stress on a concrete section, as denoted in Equation [2.26] below:

$$V_u = \frac{V_u - \phi V_p}{\phi b_v d_v} \qquad \text{AASHTO LRFD 5.8.2.9-1} \qquad [2.26]$$

Where b_v (in.) is defined as the effective web width taken as the minimum web width, measured parallel to the neutral axis, between the resultants of the tensile and compressive forces due to flexure while d_v (in.) is defined as the effective shear depth taken as the distance, measured perpendicular to the neutral axis, between the resultants of the tensile and compressive forces due to flexure; it need not be taken to be less than the greater of $0.9d_e$ or 0.72h. From Article 5.7.3.3.1, d_e (in.) is as shown below in Equation [2.27].

$$d_e = \frac{A_{ps} f_{ps} d_p + A_s f_y d_s}{A_{ps} f_{ps} + A_s f_y} \qquad \text{AASHTO LRFD 5.7.3.3.1-2} \qquad [2.27]$$

With no prestressing present, this formula reduces down to:

$$d_e = d_s \qquad \text{AASHTO LRFD 5.7.3.3.1-2} \qquad [2.28]$$

Where d_s (in.), as denoted in Article 5.7.3.2.2, is defined as the distance from the extreme compression fiber to the centroid of nonprestressed tensile reinforcement. The procedure for determining β, as defined in Article 5.8.3.4, provides a simplified approach which defaults to a value of 2.0, as well as a general procedure in Article 5.8.3.4.2. For the purpose of the initial check as indicated in Equation [2.25], the simplified assumption is sufficient—the general procedure is investigated in detail at a later section.

The experimental specimens in the current investigation meet the requirements of Equation [2.24]; therefore, the minimum steel reinforcing required for design is determined. Article 5.8.2.5 provides the requirements for the minimum steel reinforcing as shown below in Equation [2.29].

$$A_v \geq 0.0316\sqrt{f_c'}\,\frac{b_v s}{f_y} \qquad \text{AASHTO LRFD 5.8.2.5-1} \qquad [2.29]$$

Where A_v (in.^{2}) is the area of transverse reinforcement within a distance s (in.), f_c'(ksi) is the compressive strength of the concrete, f_y (ksi) is the tensile strength of the transverse reinforcement, s (in.) is the spacing of the transverse reinforcement, and b_v (in.) is the minimum web width, previously defined under Equation [2.26]. A further requirement within AASHTO relates to the maximum spacing of transverse reinforcement as documented in Article 5.8.2.7 and in Equations [2.30] and [2.31] below.

$$\begin{aligned} &\text{If } v_u < 0.125 f_c', \text{ then:} \\ &s_{max} = 0.8 d_v \leq 24.0 in \qquad \text{AASHTO LRFD 5.8.2.7-1} \end{aligned} \qquad [2.30]$$

$$\text{If } v_u \geq 0.125 f_c^{'}\text{, then:}$$
$$s_{max} = 0.4 d_v \leq 12.0 in \qquad \text{AASHTO LRFD 5.8.2.7-2} \qquad [2.31]$$

Where v_u (ksi) is the shear stress on the section as determined previously in Equation [2.26]. If the requirements regarding minimum shear reinforcement and spacing are satisfied, the nominal shear resistance is defined in Article 5.8.3.3 as the lesser of Equations [2.32] and [2.33] as shown below.

$$V_n = V_c + V_s + V_p \qquad \text{AASHTO LRFD 5.8.3.3-1} \qquad [2.32]$$

$$V_n = 0.25 f_c^{'} b_v d_v + V_p \qquad \text{AASHTO LRFD 5.8.3.3-2} \qquad [2.33]$$

Where the V_p component applies only to prestressed sections. Also, V_c was previously defined in Equation [2.25]. The remaining V_s term is defined in Equation [2.34] below:

$$V_s = \frac{A_v f_y d_v \left(\cot\theta + \cot\alpha\right)\sin\alpha}{s} \qquad \text{AASHTO LRFD 5.8.3.3-4} \qquad [2.34]$$

Where A_v (in.^{2}) is the area of transverse reinforcement within a distance s (in.) and α is the angle of inclination of transverse reinforcement to the longitudinal axis. The remaining terms have previously been defined. The general procedure for determining β and θ—based on Modified Compression Field Theory—are outlined in Article 5.8.3.4.2. The values are found from two tables—denoted within this text as Table 2.1 and 2.2 respectively; the first table is reserved for specimens that meet the minimum transverse steel requirement, as denoted in Equation [2.29], while the second table is reserved for specimens which have transverse steel, but do not meet the minimum requirement. As a general approach, both tables are covered as indicated below.

Table 2.1 AASHTO LRFD β and θ values for sections meeting minimum transverse steel requirements

Table 5.8.3.4.2-1 Values of θ and β for Sections with Transverse Reinforcement.

$\frac{v_u}{f'_c}$	$\varepsilon_x \times 1{,}000$								
	≤−0.20	≤−0.10	≤−0.05	≤0	≤0.125	≤0.25	≤0.50	≤0.75	≤1.00
≤0.075	22.3 6.32	20.4 4.75	21.0 4.10	21.8 3.75	24.3 3.24	26.6 2.94	30.5 2.59	33.7 2.38	36.4 2.23
≤0.100	18.1 3.79	20.4 3.38	21.4 3.24	22.5 3.14	24.9 2.91	27.1 2.75	30.8 2.50	34.0 2.32	36.7 2.18
≤0.125	19.9 3.18	21.9 2.99	22.8 2.94	23.7 2.87	25.9 2.74	27.9 2.62	31.4 2.42	34.4 2.26	37.0 2.13
≤0.150	21.6 2.88	23.3 2.79	24.2 2.78	25.0 2.72	26.9 2.60	28.8 2.52	32.1 2.36	34.9 2.21	37.3 2.08
≤0.175	23.2 2.73	24.7 2.66	25.5 2.65	26.2 2.60	28.0 2.52	29.7 2.44	32.7 2.28	35.2 2.14	36.8 1.96
≤0.200	24.7 2.63	26.1 2.59	26.7 2.52	27.4 2.51	29.0 2.43	30.6 2.37	32.8 2.14	34.5 1.94	36.1 1.79
≤0.225	26.1 2.53	27.3 2.45	27.9 2.42	28.5 2.40	30.0 2.34	30.8 2.14	32.3 1.86	34.0 1.73	35.7 1.64
≤0.250	27.5 2.39	28.6 2.39	29.1 2.33	29.7 2.33	30.6 2.12	31.3 1.93	32.8 1.70	34.3 1.58	35.8 1.50

Table 2.2 AASHTO LRFD β and θ values for sections with transverse steel, not meeting minimum transverse steel requirements

Table 5.8.3.4.2-2 Values of θ and β for Sections with Less than Minimum Transverse Reinforcement.

s_{xe} (in.)	$\varepsilon_x \times 1000$										
	≤–0.20	≤–0.10	≤–0.05	≤0	≤0.125	≤0.25	≤0.50	≤0.75	≤1.00	≤1.50	≤2.00
≤5	25.4 6.36	25.5 6.06	25.9 5.56	26.4 5.15	27.7 4.41	28.9 3.91	30.9 3.26	32.4 2.86	33.7 2.58	35.6 2.21	37.2 1.96
≤10	27.6 5.78	27.6 5.78	28.3 5.38	29.3 4.89	31.6 4.05	33.5 3.52	36.3 2.88	38.4 2.50	40.1 2.23	42.7 1.88	44.7 1.65
≤15	29.5 5.34	29.5 5.34	29.7 5.27	31.1 4.73	34.1 3.82	36.5 3.28	39.9 2.64	42.4 2.26	44.4 2.01	47.4 1.68	49.7 1.46
≤20	31.2 4.99	31.2 4.99	31.2 4.99	32.3 4.61	36.0 3.65	38.8 3.09	42.7 2.46	45.5 2.09	47.6 1.85	50.9 1.52	53.4 1.31
≤30	34.1 4.46	34.1 4.46	34.1 4.46	34.2 4.43	38.9 3.39	42.3 2.82	46.9 2.19	50.1 1.84	52.6 1.60	56.3 1.30	59.0 1.10
≤40	36.6 4.06	36.6 4.06	36.6 4.06	36.6 4.06	41.2 3.20	45.0 2.62	50.2 2.00	53.7 1.66	56.3 1.43	60.2 1.14	63.0 0.95
≤60	40.8 3.50	40.8 3.50	40.8 3.50	40.8 3.50	44.5 2.92	49.2 2.32	55.1 1.72	58.9 1.40	61.8 1.18	65.8 0.92	68.6 0.75
≤80	44.3 3.10	44.3 3.10	44.3 3.10	44.3 3.10	47.1 2.71	52.3 2.11	58.7 1.52	62.8 1.21	65.7 1.01	69.7 0.76	72.4 0.62

For the first table, for specimens meeting the minimum transverse steel requirement, the table requires three values: ε_x, v_u, and f_c', where ε_x is defined as the calculated longitudinal strain at the middepth of the member, v_u (ksi) is the average factored shear stress on the concrete previously defined in Equation [2.26], and f_c' (ksi) is the specified compressive strength of the concrete. In lieu of more accurate calculations, ε_x shall be determined by Equation [2.35] below, with an initial value not be taken greater than 0.001. It is noted that Fig. 2.1 identifies the parameters used in Equations [2.35] through [2.37] and should be used in conjunction with the described text; Equations [2.35] through [2.37] have been modified to negate the effects of prestressing.

$$\varepsilon_x = \frac{\frac{M_u}{d_v} + 0.5N_u + 0.5V_u \cot\theta}{2E_s A_s} \qquad \text{AASHTO LRFD 5.8.3.4.2-1} \qquad [2.35]$$

In equation [2.35], M_u (kip-in.) is the factored moment taken as a positive value, but not less than $V_u * d_v$, d_v was previously defined in Equation [2.26] as the effective shear depth taken as the distance, measured perpendicular to the neutral axis, between the resultants of the tensile and compressive forces due to flexure which need not be taken to be less than the greater of $0.9d_e$ or $0.72h$, N_u (kip) is the factored axial force taken as positive if tensile and negative is compressive, V_u (kip) is the factored shear force taken as a positive quantity, E_s (ksi) is the modulus of elasticity of the steel reinforcing, and A_s (in.^{2}) is the area of nonprestressed steel on the flexural tension side of the member (for bars terminating less than the full development length at the section of interest, they shall be ignored).

For the second table, ε_x is defined as the largest calculated longitudinal strain which occurs in the web of the member; it is determined as shown below in Equation [2.36], with the initial value not taken greater than 0.002.

$$\varepsilon_x = \frac{\frac{M_u}{d_v} + 0.5N_u + 0.5V_u \cot\theta}{E_s A_s} \qquad \text{AASHTO LRFD 5.8.3.4.2-2} \qquad [2.36]$$

Where the variables are as defined for Equation [2.35]. If the value of ε_x is negative for either Equation [2.35] or [2.36], then ε_x should be as defined below in Equation [2.37].

$$\varepsilon_x = \frac{\frac{M_u}{d_v} + 0.5N + 0.5V\cot\theta}{2\left(E_c A_c + E_s A_s\right)} \qquad \text{AASHTO LRFD 5.8.3.4.2-3} \qquad [2.37]$$

Where the variables are as defined for Equation [2.35] with the exception of A_c (in.^{2}) which is defined as the area of concrete on the flexural tension side of the member (refer to Fig. 2.1 for additional clarity). E_c (ksi) is defined as the modulus of elasticity of the concrete as denoted under section 5.4.2.4 and Equation [2.38] below.

$$E_c = 33{,}000 w_c^{1.5}\sqrt{f_c'} \qquad \text{AASHTO LRFD 5.4.2.4-1} \qquad [2.38]$$

Where w_c (kip/cubic foot) is the unit weight of the concrete and f'_c (ksi) is the compressive strength of the concrete.

2.1.3.2 AASHTO LRFD 2005 Deep Beam Capacity

The Traditional Bernoulli Beam Theory assumption of plane sections remaining plane does not hold true for deep beam specimens. Among the active international codes covered in the current study, the method of choice for dealing with deep beam analysis is the strut-and-tie (STM) method. The procedure is outlined below, focusing on the AASHTO interpretation due to the specificity to the bridge community with comparisons to the remaining codes.

The STM method uses an idealized truss model consisting of upper and lower chords, vertical ties, and diagonal elements to transmit concentrated loads through a member; the concrete component is idealized as a diagonal strut in compression, shear reinforcement is idealized as vertical ties, and longitudinal reinforcement at the limits of the cross section is denoted as chord members, as shown in Fig. 2.2. The intersection of these elements is denoted as a Node, and the concrete adjacent to the node is referred to as a Nodal Regions; the concrete in this area is assumed to distribute the resulting nodal forces to adjacent regions or bearings. Force equilibrium of the truss model is required, subject to truss geometry and complexity. The method provides a lower bound for capacity, such that modifying the truss geometry and/or complexity is permitted to obtain the highest capacity.

AASHTO defines a deep component as one in which the distance from the point of zero shear to the face of the support is less than 2 times the member height or structural components in which a load causing more than one-third of the shear at a support is closer than 2 times the member height from the face of the support. The STM model is documented under section 5.6.3. The capacity of the strut and ties are defined under section 5.6.3.2 and in Equation [2.39] below.

$$P_r = \phi P_n \qquad \text{AASHTO LRFD 5.6.3.2-1} \qquad [2.39]$$

Where P_r (kip) is the factored resistance and P_n (kip) is the nominal resistance. The ϕ resistance factor is based on sign convention of the component. From Article 5.5.4.2, ϕ equals 0.70 for STM compression members, 0.90 for tension members, and 0.80 for compression members in anchorage zones. Once the general equation is presented, the

nominal strength of the strut and ties must be determined. For a compressive strut, the nominal strength is defined in Article 5.6.3.3.1 and in Equation [2.40] below.

$$P_n = f_{cu} A_{cs} \qquad \text{AASHTO LRFD 5.6.3.3.1-1} \qquad [2.40]$$

Where P_n (kip) is the nominal strength of the strut, f_{cu} (ksi) is the limiting compressive strength as defined in Article 5.6.3.3.3, and A_{cs} (in.^{2}) is the effective cross sectional area of the strut as defined in Article 5.6.3.3.2 based on the anchorage conditions at the end of the strut. For a strut which is anchored by reinforcement, the effective concrete area may extend a distance up to six bar diameters from the anchored bar, as shown in Fig. 2.3. For struts anchored by bearing and reinforcement or bearing and struts, the effective concrete area is as shown in Fig. 2.4 and 2.5 respectively. The limiting compressive stress in a strut is defined in Article 5.6.3.3.3 and in Equation [2.41] below.

$$f_{cu} = \frac{f_c^{'}}{0.8 + 170\varepsilon_1} \le 0.85 f_c^{'} \qquad \text{AASHTO LRFD 5.6.3.3.3-1} \qquad [2.41]$$

Where ε_1 is defined below in Equation [2.42] as:

$$\varepsilon_1 = \varepsilon_s + (\varepsilon_s + 0.002)\cot^2 \alpha_s \qquad \text{AASHTO LRFD 5.6.3.3.3-2} \qquad [2.42]$$

In Equation [2.42], α_s is the smallest angle between the compressive strut and adjoining tension ties, ε_s (in./in.) is the tensile strain in the concrete, and f'_c (ksi) is the compressive strength of the concrete. If the compressive strut includes reinforcement that is parallel to the strut and detailed to develop its yield strength in compression, the nominal resistance is defined in Article 5.6.3.3.4 and in Equation [2.43] below.

$$P_n = f_{cu} A_{cs} + f_y A_{ss} \qquad \text{AASHTO LRFD 5.6.3.3.4-1} \qquad [2.43]$$

Were f_y (ksi) is the yield strength of the reinforcement and A_{ss} (in.^{2}) is the area of the reinforcement in the strut. Turning toward the tension ties, the nominal resistance is denoted under Article 5.6.4.3.1 and in Equation [2.44] below.

$$P_n = f_y A_{st} + A_{ps}\left[f_{pe} + f_y\right] \qquad \text{AASHTO LRFD 5.6.3.4.1-1} \qquad [2.44]$$

Where f_y (ksi) is the yield strength of the mild steel, A_{st} (in.^{2}) is the area of the mild steel, A_{ps} (in.^{2}) is the area of prestressed steel, and f_{pe} (ksi) is the stress in the prestressing steel after all losses. The anchorage of the tensile reinforcement in the nodal regions is required for this method. If confinement is not provided for the compressive strut at the nodal zone, the code requires a reduction in the available strength according to the following anchorage types: for node regions bounded by compressive struts and bearing areas, the reduction shall be $0.85\phi f_c$'. For node regions anchoring a one-direction tension tie, the reduction shall be $0.75\phi f_c$'. For node regions anchoring tension ties in more than one direction, the reduction shall be $0.65\phi f_c$'. The tension tie reinforcement shall be distributed over an area equal to the tension tie force divided by the stress reductions just mentioned. In addition, crack control measures are required on the face of the section, with a maximum spacing of 12 in. The ratio of reinforcement to gross concrete area shall not be less than 0.003 in each direction.

2.1.3.3 Deep Beam Comparison: Remaining Codes

As mentioned previously, the remaining international codes rely on the STM for analysis of deep beams. Each of the codes have requirements dealing with serviceability of crack control in terms of maximum spacing of vertical and horizontal reinforcement as well as reduction factors for the compression strut—in most cases based either a rectangular stress distribution of a typical beam or a bottle shaped strut as in a diagonal compression element. Also, the compressive concrete contribution at the nodal regions is typically reduced based on the anchorage conditions and/or stress condition at the node (ie one compression strut only is treated differently than a node with two compression struts and one tension tie). The differences of the various codes are outlined in Table 2.3.

Code:	$V_{n\,max}$	Min A_{trans}	S_{max}	Min A_{vert}	Strut		Tension	Tension Tie	Nodal Region
					Compression				
					Rectangular	Other Shape			
ACI 318-05 (US)	$10\sqrt{f'_c}bd$	0.0025bs	d/5 ≥ 12"	0.0015bs	$0.6375f'_cA_c$	$0.478f'_cA_c$	$0.3825f'_cA_{ct}$	$0.75A_tf_y$	$0.75[0.85\beta_n{}^{*4}f'_c]A_{node}$
AASHTO LRFD 2005 (US)	-	$.0316\sqrt{f'_c}\frac{bs}{f_y}$	12" or $0.003A_g$	-	$0.70\left[\frac{f'_c}{0.8+170\varepsilon_1{}^{*1}}\le 0.85f'_c\right]A_c$		-	$0.90[A_sf_y+A_{ps}(f_{pe}+f_y)]$	$\beta^{*7}0.70f'_cA_{node}$
CEB-FIP 1990 (metric)	-	$0.2\%A_g$	-	$0.2\%A_g$	Uncracked Section: $A_c0.85[1-f_{cl}/250]f_{cd}{}^{*2}$	Cracked Section: $A_c0.60[1-f_{cl}/250]f_{cd}{}^{*2}$	-	$f_{yd}/\gamma_s{}^{*5}$	$f_{cd1}A_{node}{}^{*8}$ or $f_{cd2}A_{node}{}^{*9}$
CEB-FIP 1999 (metric)	-	$0.2\%A_g$	-	$0.2\%A_g$	$A_c(1-f_{cl}/250)f_{1cd}$	$A_c\nu_2{}^{*4}f_{1cd}$	-	$f_{yd}/\gamma_s{}^{*5}$	$1.20f_{cd1}A_{node}{}^{*10}$ or $3.88f_{cd1}A_{node}{}^{*11}$
Eurocode 2 (metric)	-	$0.1\%A_g \ge 150$ mm²/m	-	$0.1\%A_g \ge$ 150 mm²/m	$A_cf_{cd}/\gamma_c{}^{*3}$	$A_c0.6(1-f_{cl}/250)f_{cd}{}^{*2}$	-	$f_{yd}/\gamma_s{}^{*5}$	$1.0[1-f_{cl}/250]f_{cd}{}^{*12}$ or $0.85[1-f_{cl}/250]f_{cd}{}^{*13}$ or $0.75[1-fck/250]fcd^{*14}$
Canadian Bridge Code (US)	-	$0.3\%A_g$ or 300 mm	-	$0.3\%A_g$ or 300 mm	$0.75\left[\frac{f'_c}{0.8+170\varepsilon_1{}^{*1}}\le 0.85f'_c\right]A_c$		-	$0.90A_sf_y+0.95A_{ps}f_{py}$	$\beta^{*7}0.70f'_cA_{node}$

*1 $\varepsilon_1 = \varepsilon_s + (\varepsilon_s+0.002)\cot^2\alpha_s$

*2 $f_{cd} = f_{cl} / \gamma_c{}^{*3}$

*3 For persistent/transient loading, $\gamma_c = 1.5$; for accidental loading $\gamma_c = 1.2$

*4 $\nu_2 = 0.80$ for struts with cracks parallel to strut and transverse reinforcement, $\nu_2 = 0.60$ for struts transferring compression across cracks with normal crack widths such as in the webs of a beam, or $\nu_2 = 0.45$ for struts transferring compression across large cracks (members with axial tension or sections with flanges in tension)

*5 For persistent/transient loading, $\gamma_s = 1.15$; for accidental loading $\gamma_s = 1.0$

*6 $\beta_n = 0.80$ for a nodal region with 1 tie, $\beta_n = 0.60$ for a nodal region with 2 ties

*7 $\beta = 0.85$ for a nodal area with a compressive strut and bearing area, $\beta = 0.75$ for a nodal area anchoring a 1-D tension tie, and $\beta = 0.65$ for a nodal area with a tension ties in more than 1 dimension

*8 For compression only and other nodes where inclusive angle between struts is > 55 degrees and the reinforcement at the node is designated "with special care"

*9 Required at a node where main tensile bars are anchored

*10 For nodes subjected to biaxial compression only

*11 For nodes subjected to triaxial compression only, for nodes with tensile forces, the node is checked for anchorage length and bearing stresses

*12 For compression only nodes

*13 For nodes with anchored ties in one direction

*14 For nodes with anchored ties in two directions

Table 2.1: Parameter for the Strut-and-Tie Method from Various International Codes

2.1.4 Canadian Highway Bridge Design Code

The design philosophy which underlies the Canadian Highway Bridge Design Code is based three limit states: the Service Limit State (SLS), Ultimate Limit State (ULS), and the Fatigue Limit State (FLS). The first limit state is in place to ensure deflection requirements are met, as well as crack control and excess vibrations are minimized. The second limit state is the failure load for the structure, while the third limit state deals with material fatigue. Safety for the Ultimate Limit State is based on the structural reliability index β, which is defined as the ratio of the mean to the standard deviation of a random variable X. In this case, X is taken as the natural logarithm of Resistance over Load Effect (refer to Fig. 2.6 for the reliability index against failure). For the Service Limit State, the variable X is taken as the safety margin, or the difference between Resistance and Load. For an intended design life of 75 years, the reliability index β is equal to 3.5.

2.1.4.1 Canadian Bridge Code Traditional Beam Capacity

Traditional beam design is outlined in Chapter 8 for the Canadian Code. The Canadian code uses a sectional analysis which applies shear, moment, and torsion at the section of interest, with no regard to the flow of forces through the member; the section is simply checked for the calculated loads at the section of interest. Article 8.9.2.2 sets the requirements for sections requiring transverse reinforcement, as denoted below in Equation [2.45].

$$V_f > 0.20\phi_c f_{cr} b_v d_v + 0.5\phi_p V_p \qquad \text{Canadian Bridge Code} \qquad [2.45]$$

Where ϕ_c is a material resistance factor equal to 0.75 for concrete from Table 8.4.6, f_{cr} (MPa) is the cracking strength of the concrete, b_v (mm) is the minimum web width within a the effective depth, d_v (mm) is the effective shear depth of the section—taken as the perpendicular distance from the resultant tensile and compression forces from flexure—it shall not be less than 0.9d for non-prestressed section, where d is measured from the extreme fiber in compression to the centroid of the tension reinforcement, ϕ_p is a material resistance factor equal to 0.90 for high strength bars from Table 8.4.6, and V_p (N) is the portion of any prestressing force in the direction of the applied force, taken as positive if resisting the applied shear force. Once the section is shown to require transverse reinforcement, then the minimum required area of steel is denoted in Article 8.9.2.3 and in Equation [2.46] below.

$$A_v > 0.15 f_{cr} \left(\frac{b_v s}{f_y} \right) \qquad \text{Canadian Bridge Code} \qquad [2.46]$$

Where A_v (mm^2) is the area of transverse steel, f_y (MPa) is the yield strength of the reinforcing steel, and s (mm) is the spacing of the transverse steel; previous variables have been defined under Equation [2.45]. In addition to minimum area requirements, the code places a limit on the amount of vertical prestressing force on the section of interest under Clause 8.9.2.4 as 400 MPa plus the effective prestress force, but not more than the yield strength of the prestressing steel. The total factored shear resistance is calculated under Article 8.9.3.3. The shear resistance is taken as the individual contributions from concrete, mild steel, and prestressing tendons, as shown in Equation [2.47].

$$V_r = V_c + V_s + \phi_p V_p \qquad \text{Canadian Bridge Code} \qquad [2.47]$$

Where V_c (N) is the concrete contribution, V_s (N) is the mild steel contribution, and V_p (N) is the prestressed steel contribution. The determination of the concrete contribution to shear strength is covered under Clause 8.9.3.5 based on the Modified Compression Theory work of Collins and Mitchell (1990) Vecchio and Collins (1986). The code provides a simplified approach that assumes a 45 angle for the internal compressive stress; it is outlined under Clause 8.9.3.4.2 and is divided between sections that meet the minimum steel requirements of Clause 8.9.2.3 shown below in Equation [2.48], and the sections that have less than or no transverse steel as shown in Equation [2.49].

$$V_c = 0.46\phi_c f_{cr} b_v d_v \qquad \text{Canadian Bridge Code} \qquad [2.48]$$

$$V_c = \left(\frac{600}{1000 + d_v} \right) \phi_c f_{cr} b_v d_v \geq 0.23\phi_c f_{cr} b_v d_v \qquad \text{Canadian Bridge Code} \qquad [2.49]$$

The code also permits a general approach to the concrete contribution, which is similar to the AASHTO specifications, shown below in Equation [2.50].

$$V_c = 2.5\beta\phi_c f_{cr} b_v d_v \qquad \text{Canadian Bridge Code} \qquad [2.50]$$

The β and corresponding θ terms used in Equation [2.50] are located in two tables based on two conditions: sections meeting the minimum transverse steel requirements of Clause 8.9.2.3 (Table 8.9.3.4.1(a)) and sections with less than or no transverse steel (Table 8.9.3.4.1(b)). The commentary of Clause 8.9.3.5 provides the iterative procedure for determining β and θ. First, the shear stress ratio is calculated from Clause 8.9.3.5, as shown below in Equation [2.51].

$$\frac{\left(\frac{V_f - \phi_p V_p}{b_v d_v}\right)}{\phi_c f_c'} \qquad \text{Canadian Bridge Code} \qquad [2.51]$$

Next, an iterative process is followed to determine the appropriate angle and corresponding value of ε_x. Clause 8.9.3.6 illustrates the equation for determining ε_x as shown below in Equation [2.52].

$$\varepsilon_x = \frac{0.5N_f + 0.5\left(V_f - \phi_p V_c\right)\cot\theta + \frac{M_f}{d_v} - A_{ps} f_{po}}{E_s A_s + E_p A_{ps}} \leq 0.002 \text{ CBC} \qquad [2.52]$$

Where N_f (N) is the factored load acting perpendicular to the cross section acting simultaneously with V_f, including the effects of creep and shrinkage, M_f (N-mm) is the factored moment at the section of interest, A_{ps} (mm^2) is the area of prestressed steel, f_{po} (MPa) is the stress in the prestressing steel when the stress in the surrounding concrete is zero—which may be taken as 110% of f_{se} (MPa), the effective stress in the prestressing after all losses have occurred.

Leaving cotθ as an unknown, the possible values for θ are determined based on the shear stress ratio (Equation [2.51]) from Table 8.9.3.4.1(a). Choose a value of θ and the corresponding value of ε_x from the Table. Now, calculate the value of ε_x from Equation [2.52]. Using this value of ε_x, determine the corresponding θ value from Table 8.9.3.4.1(a). Check the assumed value of θ; if the value is less than the second θ, then ε_x is a conservative value. If the converse is true, repeat the steps until the initial θ value is less

than the second θ. Once a satisfactory result is reached, β can be found from Table 8.9.3.4.1(a).

The steel contribution to shear strength is outlined in Clause 8.9.3.8 and in Equation [2.53] below.

$$V_s = \frac{\phi_s f_y A_v d_v \cot\theta}{s} \qquad \text{Canadian Bridge Code} \qquad [2.53]$$

Where ϕ_s is a material resistance factor equal to 0.90 for mild steel from Table 8.4.6, θ is the angle of the principal diagonal compressive stresses to the longitudinal axis of the member—taken as 45 for the simplified method, or from Tables 8.9.3.4.1(a) or 8.9.3.4.1(b) for sections containing the minimum transverse steel and less than or no transverse steel respectively; all other parameters have previously been introduced.

2.1.4.2 Canadian Bridge Code: Deep Beam Capacity

As indicated previously, the deep beam analysis for all codes utilize the STM method. It was discussed in detail under the AASHTO LRFD specifications, with special attention to the differences among the active international codes.

2.1.5 Eurocode 2: Design of Concrete Structures

The European Standard EN 1992-1-1:2004 denoted as the Eurocode is the British Standard for design. The design guide encompasses many nations and is subject to variability in terms of various factors used throughout the document. However, the code provides recommended design values in lieu of country specific values. For the current investigation, the recommended design values were followed as opposed to country specific values. The rationale for the code relies on a service condition and ultimate strength condition denoted as Serviceability Limit State (SLS) and Ultimate Limit State (ULS) respectively.

2.1.5.1 Eurocode 2 Traditional Beam Capacity

Prior to application of design equations, detailing requirements for shear reinforcement must be satisfied, as outlined in Chapter 9. The first requirement, under Section 9.2.2, requires the orientation of the shear reinforcement to form an angle α between 45 and 90 degrees with the longitudinal axis of the bridge. Once orientation has been established, the requirement for the combination of closed stirrups and open stirrups—denoted in this context as links and bent up bars—are defined. The specifications require the closed stirrups (links) to encompass the longitudinal tension reinforcement and the compression zone, with half of the stirrups to be closed. The code also requires the shear reinforcement ratio—a measurement of the shear reinforcement per unit length—to be greater than

minimum value. The shear reinforcement ratio is defined in Article 9.4 and in Equation [2.54] below.

$$\rho_w = \frac{A_{sw}}{sb_w \sin\alpha} \qquad \text{Eurocode 2; 9.4} \qquad [2.54]$$

Where A_{sw} (mm^2) is the area of shear reinforcement within a distance s (mm), s (mm) is the spacing of the shear reinforcement measured along the longitudinal axis of the member, b_w (mm) is the web width, and α is the angle between the shear reinforcement and the longitudinal axis of the member. The minimum shear reinforcement ratio is given under Equation [2.55] below.

$$\rho_{w\_\min} = \frac{0.08\sqrt{f_{ck}}}{f_{yk}} \qquad \text{Eurocode 2; 9.5N} \qquad [2.55]$$

Where f_{ck} (MPa) is the 28 day compressive cylinder strength of the concrete and f_{yk} (MPa) is the yield strength of the transverse steel. The final condition relates to the spacing of the shear steel-both in terms of the links and bent up bars about the longitudinal axis of the member and the lateral spacing among the links and bent up bars. The maximum spacing of the link elements is shown below in Equation [2.56].

$$s_{l\_\max} = 0.75d(1+\cot\alpha) \qquad \text{Eurocode 2; 9.6N} \qquad [2.56]$$

Where d (mm) is the effective depth of the cross section and α has previously been defined as the angle the shear reinforcement makes with the longitudinal axis of the member. The maximum spacing of the bent up bars is as shown in Equation [2.57].

$$s_{b\_\max} = 0.6d(1+\cot\alpha) \qquad \text{Eurocode 2; 9.7N} \qquad [2.57]$$

The requirement for the lateral spacing of the link and bent up bars are as shown in Equation [2.58].

$$s_{t\_\max} = 0.75d \le 600mm \qquad \text{Eurocode 2; 9.8N} \qquad [2.58]$$

The requirements for strength at the Ultimate Limit State is covered under Section 6.2.3 based on a truss analogy, as shown in Fig. 2.7. The shear strength is the lesser of Equations [2.59] and [2.60].

$$V_{Rd,s} = \frac{A_{sw}}{s} z f_{ywd} \cot\theta \qquad \text{Eurocode 2; 6.8} \qquad [2.59]$$

$$V_{Rd,\max} = \frac{\alpha_{cw} b_w z v_1 f_{cd}}{\cot\theta + \tan\theta} \qquad \text{Eurocode 2; 6.9} \qquad [2.60]$$

Where A_{sw} (mm^2) is the cross sectional area of the shear reinforcement, s (mm) is the spacing of the shear reinforcement along the longitudinal axis of the bridge, z (mm) is the internal lever arm denoted in Fig. 2.8, f_{ywd} (MPa) is the design yield strength of the shear reinforcement, θ is the angle of the concrete compressive strut and beam axis, perpendicular to the shear force, α_{cw} is a coefficient taking into account the state of stress in the tension chord (taken as 1.0 for non-prestressed members), b_w (mm) is the width of the web, v_1 is a strength reduction factor for concrete cracking in shear, f_{cd} (MPa) is the design cylinder compressive strength. The code includes several additional notes regarding the use of these equations. The first limits the value of cotθ as shown below in Equation [2.61]

.

$$1 \le \cot\theta \le 2.5 \qquad \text{Eurocode 2; 6.7N} \qquad [2.61]$$

The recommended value of v_1 is v as described in Article 6.2.2, as shown below in Equation [2.62].

$$v = 0.6\left[1 - \frac{f_{ck}}{250}\right] \qquad \text{Eurocode 2; 6.6N} \qquad [2.62]$$

If the design stress in the shear reinforcement is less than 80% of f_{yk} (MPa), then:

$$v_1 = 0.6 \text{ for } f_{ck} \le 60MPa$$
$$v_1 = 0.9 - \frac{f_{ck}}{200} > 0.5 \text{ for } f_{ck} \ge 60MPa$$

The maximum effective cross sectional area of the shear reinforcement for $\cot\theta = 1.0$ is defined in Equation [2.63] below.

$$\frac{A_{sw,\max} f_{ywd}}{b_{ws}} < \frac{1}{2}\alpha_{cw} v_1 f_{cd} \qquad \text{Eurocode 2; 6.12} \qquad [2.63]$$

2.1.5.2 Eurocode 2: Deep Beam Capacity

As indicated previously, the deep beam analysis for all codes utilize the STM method. It was discussed in detail under the AASHTO LRFD specifications, with special attention to the differences among the active international codes.

2.1.6 Euro-International Committee for Concrete Publications

The CEB-FIP is a model code that provides general design guidelines for civil engineering structures; it is not specific to building, bridge, or other specialized civil infrastructure components. However, the code does provide interpretation developing such codes within governing entities throughout Europe. As such, several codes, such as the Eurocode, are derived from the CEB-FIP. The code includes a 1990 publication, in addition to a 1999 state-of-the-industry publication denoted as practical design of structural concrete. Together, these documents represent the latest advances from academia in terms of analysis as well as a focus on safety for the analysis and design of concrete structures. The current investigation will focus on the 1990 model code, as the 1999 addition is aimed at clarification for the STM. The code utilizes a limit state approach that seeks to control deflections and vibrations at service loads (service limit state) while ensuring local element and global structural stability under the ultimate loads (ultimate limit state). In addition, the model code utilizes reduction factors for load and resistance denoted as partial safety factors. As such, the factors for specific loading combinations are increased while material strength characteristics are reduced.

2.1.6.1 CEB-FIP Model Code 1990: Traditional Beam Design

Traditional beam design is outlined under Chapter 6: verification of the ultimate limit states. The code idealizes a beam for shear and axial loading as a truss member under

subsection 6.3.3 consisting of longitudinal steel chords, compressive concrete struts, and steel web reinforcement in one or more directions. The code precludes the effects of torsion, longitudinal shear, and transverse bending within this definition. Subsection 6.3.3 further separates the analysis based on the section type with reinforced or prestressed concrete beams are treated separately than reinforced concrete columns, subject to the conditions of subsection 6.3.3.1. The first condition of subsection 6.3.3.1 relates to the reinforcement ratio of the longitudinal steel such that the section is not over-reinforced, as indicated in Equations [2.64] and [2.65] below.

$$0.0035\frac{d-x}{d} > \frac{f_{yd}}{E_s} \qquad \text{CEB-FIP 6.3-1a} \qquad [2.64]$$

$$0.0035\frac{d-x}{d} > \frac{f_{yk}}{E_s\gamma_s} \qquad \text{CEB-FIP 6.3-1b} \qquad [2.65]$$

Where d (mm) is the effective depth of the section, x (mm) is the height of the compression block, f_{yd} (MPa) is the design yield strength of the longitudinal reinforcement, E_s (MPa) is the modulus of elasticity of the longitudinal reinforcement, f_{yk} (MPa) is the characteristic design yield strength of the longitudinal reinforcement, and γ_s is a partial material factor equal to 1.15 for persistent/transient events and 1.0 for accidental events (taken from Table 1.6.2 for reinforcing steel). The second condition under subsection 6.3.3.1 relates to the area of transverse steel, denoted in the code as the mechanical ratio in Equation [2.66] below.

$$\omega_{sw} = \frac{A_{sw}f_{yk}}{b_w s f_{ctm}\sin\alpha} \geq 0.2 \qquad \text{CEB-FIP 6.3-1b} \qquad [2.66]$$

Where A_{sw} (mm^2) is the area of transverse reinforcement, f_{yk} (MPa) is the yield strength of the transverse reinforcement, b_w (mm) is the width of the web, s (mm) is the spacing of the transverse reinforcement perpendicular to the longitudinal axis of the member, α is the angle between the transverse reinforcement and the longitudinal axis of the member, and f_{ctm} (MPa) is the mean characteristic tensile strength of the concrete. The mean tensile strength is defined under subsection 2.1.3.3.1 and in Equation [2.67] below.

$$f_{ctm} = f_{ctko,m}\left(\frac{f_{ck}}{f_{cko}}\right)^{\frac{2}{3}} \qquad \text{CEB-FIP 2.1-4} \qquad [2.67]$$

Where $f_{ctko,m}$ (MPa) is equal to 1.40 MPa, f_{cko} (MPa) is equal to 10 MPa, and f_{ck} (MPa) is the characteristic compressive strength of the concrete. In addition to minimum area requirements, the code requires the inclination of the stirrups to the longitudinal axis be at least 45 degrees and 30 degrees for bent up bars while the spacing of stirrup legs (longitudinal and transverse) shall not exceed the lesser of 0.75d or 800 mm. Finally, the code requires the shear reinforcement to be adequately anchored to the chords.

Once the requirements of subsection 6.3.2 are satisfied, the code identifies the value for the components of the idealized truss. Starting with the tension chord, the maximum force is as indicated in Equation [2.68].

$$F_{st} = \frac{|M_{Sd}|}{z} + N_{Sd}\frac{(z - z_s)}{z} + \frac{V_{Sd}}{2}(\cot\theta - \cot\alpha) \qquad \text{CEB-FIP 6.3-4} \qquad [2.68]$$

Where M_{Sd} (N-mm) is the moment at the section of interest, z (mm) is the internal lever arm between the resultant chord forces, N_{Sd} (N) is the axial load taken positive for tension

and negative for compression, z_s (mm) is the distance from the line of action of the axial force N_{Sd} to the centroid of the tension reinforcement, V_{Sd} (N) is the shear force at the section of interest, θ is the angle the compression strut makes with the longitudinal axis of the member, and α is the angle of the transverse reinforcement with the longitudinal axis of the member. If support reactions and/or direct loads are applied to the section as to induce transverse compression along the depth, then the tension force is limited by Equation [2.69].

$$F_{st} \le \frac{|M_{Sd,\max}|}{z} + N_{Sd}\frac{(z - z_s)}{z} \qquad \text{CEB-FIP 6.3-5} \qquad [2.69]$$

For cases in which the tensile reinforcement is entirely contained in the web of a section, the tension chord force may be determined from Equation [2.70] below.

$$F_{Rt} = A_s f_{yd} \qquad \text{CEB-FIP 6.3-6} \qquad [2.70]$$

Moving to the compression chord, the allowable force is shown in Equation [2.71] below.

$$F_{Sc} = \frac{|M_{Sd}|}{z} - N_{Sd}\frac{z_s}{z} - \frac{V_{Sd}}{2}(\cot\theta - \cot\alpha) \qquad \text{CEB-FIP 6.3-7} \qquad [2.71]$$

Equation [2.71] governs except in the case of direct loading at the location of maximum moment, in which case Equations [2.72] and [2.73] govern.

$$F_{Sc} = \frac{|M_{Sd,\max}|}{z} - N_{Sd}\frac{z_s}{z} \qquad \text{CEB-FIP 6.3-8} \qquad [2.72]$$

$$F_{Rc} = f_{cd1}A_c + f_{ycd}A_{sc} \qquad \text{CEB-FIP 6.3-9} \qquad [2.73]$$

Where f_{cdl} (MPa) is the design strength of the concrete in the compression chord, A_c (mm^2) is the area of the compression chord, f_{ycd} (MPa) is the yield strength of the transverse steel,

A_{sc} (mm^2) is the area of transverse steel within the compression chord. The compressive concrete strut force is limited to Equations [2.74] and [2.75] below.

$$F_{Scw} = \frac{V_{Sd}}{\sin\theta}\left(\frac{\cot\theta}{\cot\theta + \cot\alpha}\right) \qquad \text{CEB-FIP 6.3-10} \qquad [2.74]$$

$$F_{Rcw} = f_{cd2} b_w z \cos\theta \qquad \text{CEB-FIP 6.3-11} \qquad [2.75]$$

Where V_{Sd} (N) is the design value the acting design shear force and f_{cd2} (MPa) is the design yield strength of the concrete in the compressive strut; the remaining parameters have previously been defined. The final component, the tension of the web steel, is denoted in Equations [2.76] and [2.77] below.

$$F_{Stw} = \frac{V_{Sd}}{\sin\alpha} \qquad \text{CEB-FIP 6.3-12} \qquad [2.76]$$

$$F_{Rtw} = \left[\frac{A_{sw} f_{yd}}{s}\right] z\left(\cot\theta + \cot\alpha\right) \qquad \text{CEB-FIP 6.3-13} \qquad [2.77]$$

Where A_{sw} (mm^2) is the area of the transverse steel, f_{yd} (MPa) is the yield strength of the transverse steel, and the remaining parameters have previously been defined.

2.1.6.2 CEB-FIP Model Code 1990: Deep Beam Analysis

As noted previously, the deep beam analysis among the active international codes rely on the STM method for analysis. The STM is described in detail under the AASHTO LRFD section, with special attention given to the differences of the method among the active international codes.

2.2. Earlier Work

2.2.1 Epoxy Injection Repair

The use of epoxy injection, as a repair has been used for several decades, primarily as a maintenance remedy for sealing cracks. However, laboratory tests to indicate any additional strength gain with the method were limited to small scale specimens, which may not be indicative of full size specimen behavior. Therefore, an experimental program was carried out in conjunction with the current study to investigate the affect of epoxy injection to specimen capacity at OSU. Smith investigated the curing of diagonally cracked full size deck girders under superimposed dead load, dead plus cyclic live load, and axial tension to simulate temperature and shrinkage affects [Smith, 2007]. Results indicate the epoxy injected crack remained closed up to previous load levels. However, at slightly higher loads, a second crack adjacent to the original formed. Stress levels of the integrally cast stirrups also reduced prior to recracking. Overloads producing equivalent cracks are anticipated for epoxy injection as a stand alone repair.

Curing of the epoxy by simulation of a live load event resulted in similar response compared to the other specimens. However, cores of the injected cracks after the testing was complete indicate the live load specimen exhibited bubbles within the epoxy matrix which is indicative of the live loading events. The live load force was indicative of a 15.2 m (50 ft.) continuous span with traffic moving at a speed of 32 kph (20 mph). For higher

speeds and other curing temperatures, additional data is needed. Axial tension while curing, representing shrinkage and temperature affects, did not alter the specimen behavior.

2.2.2 External Steel Stirrup Repair

Mihn, *et al.* in 2001 produced the earliest publication utilizing external steel stirrups as one of five different repair methods for traditionally reinforced concrete beams [Minh, *et al.* 2001]. The experimental program included six half scale square beams, including one control specimen, with identical longitudinal reinforcement ratios, no integrally cast steel stirrups, and a shear span to depth ratio of 3.85. Dimensions of the beams were 300 mm (11.81 in.) in height/width including a shear span of 1000 mm (39.37 in.). The components of the repair included two-10 mm (0.39 in.) diameter steel rods attached to a steel angle section (L50 x 50 x 8) about the top and bottom of the beam. The experimental program did not include initial loading of the specimens prior to application of the repair media. Of the five repair specimens, only the external stirrup specimen failed in flexure. A corresponding Finite Element Model (FEM) for the external stirrup specimen was created that indicated a shear failure at a load slightly lower than the experimental results. The author attributes the difference in the failure mode to an unreported prestress force applied to the external stirrups that was not accounted for in the FEM. The article did not give guidance as to strength gain from the external stirrups with respect to governing codes or recommendations for future research needs of the repair method.

Altin, *et al.* published an article utilizing external steel stirrups on traditionally reinforced concrete T beams in 2003 [Altin, *et al.* 2003]. The experimental program included 13-half scale beams with two different shear span to effective depth (a/d) ratios (3.3 and 4.5) and identical longitudinal reinforcement. The beam dimensions were 360 mm (14.17 in.) deep, with a flange width of 360 mm (14.17 in.), a web width of 120 mm (4.72 in.), and a flange thickness of 75 mm (2.95 in.). The repair media included 60 mm (2.36 in.) square by 10 mm (0.39 in.) thick steel plate washers on the top of the flange with two-500 mm (19.68 in.) long partially threaded steel rods extending through holes in the flange terminating at a 40 mm (1.57 in.) by 40 mm (1.57 in.) by 10 mm (0.39 in.) thick steel tube section at the base of the stem secured with 40 mm (1.57 in.) square by 10 mm (0.39 in.) thick steel plate washers and high strength nuts. Details of the specimens and their repair method are shown in Fig. 2.9.

Within each group of a/d ratios, both the integrally cast and externally applied stirrup spacing was varied. Of the 13 specimens, three were designated as control and one specimen was strengthened with external stirrups but devoid of integrally cast stirrups. The remaining nine specimens consisted of two distinct repair types; the first group included seven beams with varying a/d ratios which were strengthened with external stirrups prior to application of load and consequently loaded to failure while the second group of two beams included one from each a/d ratio which were loaded up to 60% of the estimated base capacity of the section, unloaded, repaired, then loaded to failure. All repair specimens were cast under strength for shear, with an anticipated flexural failure mode after strengthening.

The research program produced several noteworthy results. The calculated capacity, based on ACI 318, was 20% to 30% higher than the experimental results for the specimens strengthened prior to application of load, but 6% to 7% lower than the experimental results for the specimens strengthened after cracking was achieved. The article includes recommendations for future work, including the load sharing among internal and external stirrups in terms of strain data. The article does not investigate the possible deformation loss due to bending of the tube section or compare the results with design codes other than ACI 318.

Kim, *et al.* published a journal in 2007 which utilized wire rope as an external strengthening method [Kim, *et al.* 2007]. While this is not a direct comparison to the method utilized in the current study, the common goal of applying a post-tensioning force about the transverse axis of the beam is achieved. The experimental study included 15 quarter scale beams with three differing shear span to effective depth (a/d) ratios-1.5, 2.5, and 3.25 to encompass deep beam specimens. Beam specimens were 400 mm (15.75 in) deep and 200 mm (7.87 in.) wide. The beams were devoid of integrally cast stirrups, relying on the rope units and concrete contribution to shear capacity. The repair apparatus included a wire rope that formed a U shape about the bottom of the beam; attached to a 20 mm (0.79 in.) thick steel plate at the top of the beam via two I-bolts with corresponding nuts and washers. An angle section at the lower corner of the web completed the repair

method in order to minimize local crushing of the concrete. Details of the repair scheme are shown in Fig. 2.10.

The experimental program looked at the effect of epoxy injection as a stand alone repair, the inclination of the wire rope units to the longitudinal axis of the beam, prestress force applied to the wire rope units, and the spacing of the wire rope units for a fixed prestressing force for each a/d ratio. Within this framework, all the beams were incrementally loaded to failure (defined in the article as formation of a single shear crack due to a lack of integrally cast stirrups), unloaded, then repaired with epoxy injection. One beam for each a/d ratio was tested to failure with epoxy injection as the only repair. The remaining beams in each group were repaired with the wire rope units at 45 and 90 degrees to the longitudinal axis of the beam, with the prestress force kept at a constant 46 kN (10.43 Kip). However, for beams with an a/d ratio of 2.5, the prestressing force was varied from 33.2 kN (7.46 Kip) to 60 kN (13.49 Kip) for both the orthogonal and inclined repair.

Results from the tests were compared to ACI 318-05 (including a STM comparison for the deep beam specimens) and Eurocode 2. Due to the lack of internal stirrups, the capacity equations simply used the area of the wire rope units for the steel contribution to shear strength. Both ACI and Eurocode permit a contribution for the total shear strength from the concrete and steel as denoted in Equation [2.78].

$$V_n = V_c + V_w \qquad \text{Kim et al.} \qquad [2.78]$$

From ACI 318-05, the concrete contribution was estimated as shown below in Equation [2.79].

$$V_c = \left(0.16\sqrt{f_c^{'}} + 17\rho \frac{V_n d}{M_n} \right) b_w d \le 0.29\sqrt{f_c^{'}} b_w d \qquad \text{Kim et al.} \qquad [2.79]$$

Where f_c' (MPa) is the compressive cylinder strength of the concrete, ρ is the longituidinal reinforcement ratio defined as $A_{st}/b_w d$, V_n (MPa) is the ultimate shear at the section of interest, M_n (kN-mm) is the moment corresponding to the shear at the section of interest, d (mm) is the effective depth, and b_w (mm) is the web width. The corresponding steel contribution was calculated as shown in Equation [2.80].

$$V_w = \frac{A_w f_{sw} d \sin\beta(1+\cot\beta)}{s_w} \le 0.66\sqrt{f_c^{'}} b_w d \qquad \text{Kim et al.} \qquad [2.80]$$

Where A_w (mm^2) is the area of external stirrup reinforcement, f_{sw} (MPa) is the yield strength of the reinforcement, s_w (mm) is the spacing of the wire ropes, and β is the angle the external stirrups make with the longitudinal axis of the member; all remaining parameters were previously defined.

For the deep beam specimens, the ACI STM method was used. The capacity of the compressive concrete strut was calculated using Equation [2.81] below.

$$V_n = v_e f_c^{'} b_w w_s \sin\alpha_1 \qquad \text{Kim et al.} \qquad [2.81]$$

Where v_e is the strut efficiency factor equal to 0.6 for specimens without both vertical and horizontal reinforcement, w_s (mm) is the width of the strut as denoted in Equation [2.82] below.

$$w_s = w_t \cos\alpha_1 + l_p \sin\alpha_1 \qquad \text{Kim et al.} \qquad [2.82]$$

In the above equation, α_1 is the angle the strut makes with the longitudinal axis of the beam ($\alpha_1=\tan^{-1}(jd/a)$), w_t (mm) is the depth of the bottom node, and l_p (mm) is the support width (refer to Fig. 2.11). The tension tie contribution from the wire rope units was calculated using equation [2.80].

The Eurocode included a similar contribution from steel and concrete; the concrete contribution for traditional and deep beam specimens are shown in Equations [2.83] and [2.84] respectively.

$$V_c = \left[C_{Rd} k_1 (100\rho f_c')^{0.333}\right] b_w d \geq 0.035 k_1^{1.5} b_w d \text{ for } \frac{a_v}{d} > 2.0 \quad \text{Kim et. al.} \quad [2.83]$$

$$V_c = \left[\beta_d C_{Rd} k_1 (100\rho f_c')^{0.333}\right] b_w d \leq 0.5 v_e f_c' b_w d \text{ for } \frac{a_v}{d} \leq 2.0 \quad \text{Kim et. al} \quad [2.84]$$

Where C_{Rd} is an empirical factor equal to 0.18, $k_1=1+ (200/d)^{0.5} \leq 2.0$ is a scale factor to allow for the size effect, ρ is the longitudinal reinforcement ratio—limited to a maximum of 0.2, $\beta_d = 2d/a_v \leq 4.0$ is a coefficient to allow for shear enhancement of deep beams having $a_v /d \leq 2.0$, where a_v (mm) is the clear shear span, and $v_e = 0.6(1-f_c'/250)$ is the effectiveness factor for concrete. The code assumes a 45 degree strut angle for the concrete, thus the wire rope contribution is presented in Equation [2.85] below.

$$V_w = \frac{A_w f_{sw} jd \sin\beta(1+\cot\beta)}{s_w} \geq 0.4 b_w d \qquad \text{Kim et al.} \qquad [2.85]$$

Where jd = 0.9d is the internal lever arm. The code also places restrictions on the shear reinforcement ratio as shown in Equation [2.86].

$$\frac{A_v f_{yh}}{b_w s_v} < \frac{0.5 v_e f_c^{'}}{\sin\beta} \qquad \text{Kim et al.} \qquad [2.86]$$

Where A_v (mm^2) is the area of shear reinforcement, f_{yh} (MPa) is the yield stress of the shear reinforcement, s_v (mm) is the spacing of the shear reinforcement, and b_w (mm) is the width of the web. It follows that the stress in the wire ropes should follow the relationship denoted in Equation [2.87].

$$f_{sw} = f_{su} - f_i \leq \frac{0.5 v_e f_c^{'}}{\sin\beta} \frac{b_w s_w}{A_w} \qquad \text{Kim et al.} \qquad [2.87]$$

Where f_{sw} (MPa) is the stress in the wire rope units after the onset of a diagonal crack, f_{su} (MPa) is the tensile strength of the wire rope units, and f_i (MPa) is the prestress in the wire rope units.

All test specimens failed in shear after repair, indicating that the increase in strength was quantifiable. Conclusions from the experimental program indicate that the use of inclined wire rope units provided higher shear capacity when compared to the orthogonal wire rope units due to a closer alignment to the principle axis stress in the concrete. Higher shear capacity was achieved within the 2.5 a/d ratio group by increasing the post tensioned force in the wire rope units. Comparisons with the two codes indicate that the ACI 318-05

analysis method is conservative for a shear-to-depth ratio below 2.5, while the Eurocode is unconservative for shear-to-depth ratio of 3.25.

Shamsai, *et al.* published an article in 2007 that dealt with remedial strengthening of traditionally reinforced concrete girders for earthquake loading [Shamsai, *et al.* 2007]. The research plan included 24-quarter scale rectangular beams, including three control specimens, with longitudinal reinforcement ratios of $\frac{1}{2}\rho_{max}$ and $\frac{2}{3}\rho_{max}$ as defined by ACI 318-95 corresponding to two different shear spans. Beam dimensions were 150 mm (4.72 in.) deep, 80 mm (3.15 in.) wide, with shear spans of 420 mm (16.53 in.) and 275 mm (10.83 in.) representing a/d ratios of 3.5 and 2.3 respectively. The beams were subjected to four point loading such that integrally cast steel stirrups were included only in the middle section of the beam. The repair apparatus consisted of undocumented size unequal leg steel angles, placed such that the longer end was in bearing with the beam, a steel plate and elastomeric pad just below the angles along the top and bottom of the beam intended to distribute the vertical force over the entire shear span, and two unidentified connecting rods and associated hardware. Specimen details and repair apparatus are shown in Fig. 2.12.

Testing protocol included seven beams which were loaded until a shear crack propagated in the shear span, unloaded, repaired, then loaded to failure as well as beams repaired prior to application of load. The experimental program also included two post-tensioning forces within the shear span equal to $0.04f_c'$ and $0.075f_c'$. Capacity of the section reflected the

traditional approach from ACI by including the contribution from the concrete and steel separately, with the addition of a third term to compensate for the external stirrups as shown below in Equation [2.88].

$$V_{sb} = \frac{A_{vb} f_{yb} h}{s_b} \qquad \text{Shamsai et al.} \qquad [2.88]$$

Where A_{vb} (mm^2) is the area of steel for the external stirrups, f_{yb} (MPa) is the yield strength of the external stirrups, h (mm) is the height of the beam, and s_b (mm) is the spacing of the external stirrups. Results from the experimental work indicate that increasing the shear capacity regardless of the presence of integrally cast stirrups or shear cracks resulted in a traditional flexural failure. Thus, due to the failure mechanism, it is unfeasible to identify the discrete shear contribution from the external stirrups. Also, due to the small scale of the specimens, large angle sections, and plate section used between the angle and concrete surface, the effective bearing area of the reaction sections produced a post tensioning force distributed evenly over the shear span. At full scale, the use of a similar setup may be cost/weight prohibitive.

2.2.3 Internal Supplemental Steel Stirrup Repair

The earliest and most complete account of utilizing internal supplemental steel stirrups to strengthen traditionally reinforced concrete specimens was provided by Kansas Department of Transportation (KDOT) from 1976-1984. Kansas' bridge inventory at that time included several hundred adjacent two girder cast-in-place deck girder bridges; a

majority of which were multi span bridges continuous over intermediate supports. The bridges were lightly reinforced for shear, having been designed with the AASHO code coincident with construction (1955-1965). Consequently, the bridges began to exhibit shear cracks primarily near the interior supports. Originally, the problem was thought to be simply a maintenance issue, with the objective to seal the cracks that formed as a preventative measure against corrosion. The initial remedy was to seal the cracks with a two part epoxy injected under low pressure. However, this method was abandoned because the epoxy matrix would fail within a short amount of time and the crack would reopen. Due to this failure, KDOT looked at a method which involved temporary shoring of the beam at the interior support, removal of the cracked concrete, placing additional mild steel in the location, and finally restoring the beam to its original shape with additional scab concrete. The method was effective, but it was expensive and resulted in temporary closure of the bridge for an extended period of time.

A third solution was suggested—as reported in the 1977 report by Stratton, *et al.*—that required the insertion of mild steel within the center of the beam, utilizing a drill rig and vacuum system capable of drilling a hole at any angle in a matter of minutes from the top of the deck was implemented [Stratton, *et al.* 1977]. After trial and error with existing machinery within the maintenance department, a rig capable of drilling a 19 mm (0.75 in.) diameter hole a distance of 2.1 m (7 ft) to 2.4 m (8 ft) in a time of 22 minutes was achieved. After drilling, half of the drilled hole was filled with a two part epoxy and a grade 420 MPa (60 ksi), 15.8 mm (0.625 in.) diameter bar was inserted in the hole.

Gravity leakage of the epoxy to the outer limits of the girders experienced during the initial test was rectified in subsequent applications.

Two additional reports by Stratton, *et al.* produced in 1978 and 1982, outlined the progress of the program and future plans [Stratton, *et al.* 1978, 1982]. The development of an industrial drilling rig was required due to the harsh conditions of drilling a small diameter hole a relatively long distance. Upon completion of the new drill rig, additional repairs were completed. Also, a method to seal the outer crack surface in a quick efficient manner was proposed. At the completion of the year, 19 girders were repaired, at an estimated savings of over $1 million dollars (1978 dollar amount) for the comparable repair noted earlier. Thus, the initial investment in equipment and training proved lucrative. The two reports also document a computer analysis program used to determine the additional shear strength gain utilizing the additional area of steel from the 1981 AASHTO shear equations.

Engineering calculations at the time estimated the use of supplemental internal stirrups used in Kansas provided a shear strength increase 10% above the 1981 AASHTO standard. However, no laboratory tests were concluded to determine the actual strength gain for the specimens. The assumption of using an additional area of steel consistent with the shear equations in AASHTO has not been confirmed. On the other hand, many of the repaired bridges still exist within Kansas' bridge inventory; the durability of the epoxy and overall repair method has stood the test of time. Recent contact with KDOT's maintenance engineers indicate that the bridges repaired with this method have shown no additional

signs of shear distress over a period of roughly 30 years. Thus, while the actual strength gain for this repair methodology has not been validated by conventional laboratory tests, serviceability and crack control over a large population of different span lengths and varying concrete strengths over an extended period of time attest to the robust nature of the repair.

The primary concern regarding supplemental internal stirrups is with regard to the shear strength of the epoxy matrix to the steel reinforcing bar and surrounding concrete. A comprehensive study by Cook, *et al.*, published in 1998, proposed a simplified model for concrete anchors which included a review of 2,929 bond tests with varying embedment depths, concrete strengths, number of anchors, cracked or uncracked concrete, different epoxy manufacturers, confined and unconfined concrete, and loading near or away from the free edge of the specimen [Cook, *et al.* 1998]. The number of tests were reduced to include only unconfined tension tests of threaded rod and reinforcing bar anchors tested at least a distance equal to the embedment length away from the free edge and where the cored/drilled hole was clean, dry, and free of dust. The reduction also excluded steel failures which reduced the number of tests to 888. The effect of hole diameter d, embedment depth h_{ef}, and concrete strength f_c were determined according to a least squares approach, with the results indicated in Equation [2.89].

$$N_u = \alpha d^{\beta} h_{ef}^{\gamma} f_c^{\delta} \qquad \text{Cook et al.} \qquad [2.89]$$

Where N_u (kN) is the ultimate predicted strength of the anchor system, and α, β, γ, and δ are parameters which form a best fit to the database. The variations of parameters are

shown below in Table 2.4. From hundreds of tests, the main variation appears to come from the concrete strength (while the comparable variation for hole diameter and embedment depth can be essentially taken as 1.00 with a 0.25 coefficient of variation), indicating that for some epoxy manufacturers, a variation in concrete strength has a great effect on the resulting capacity of the anchor system.

Table 2.4 Bond model variations based on tests compiled by Cook *et al.*

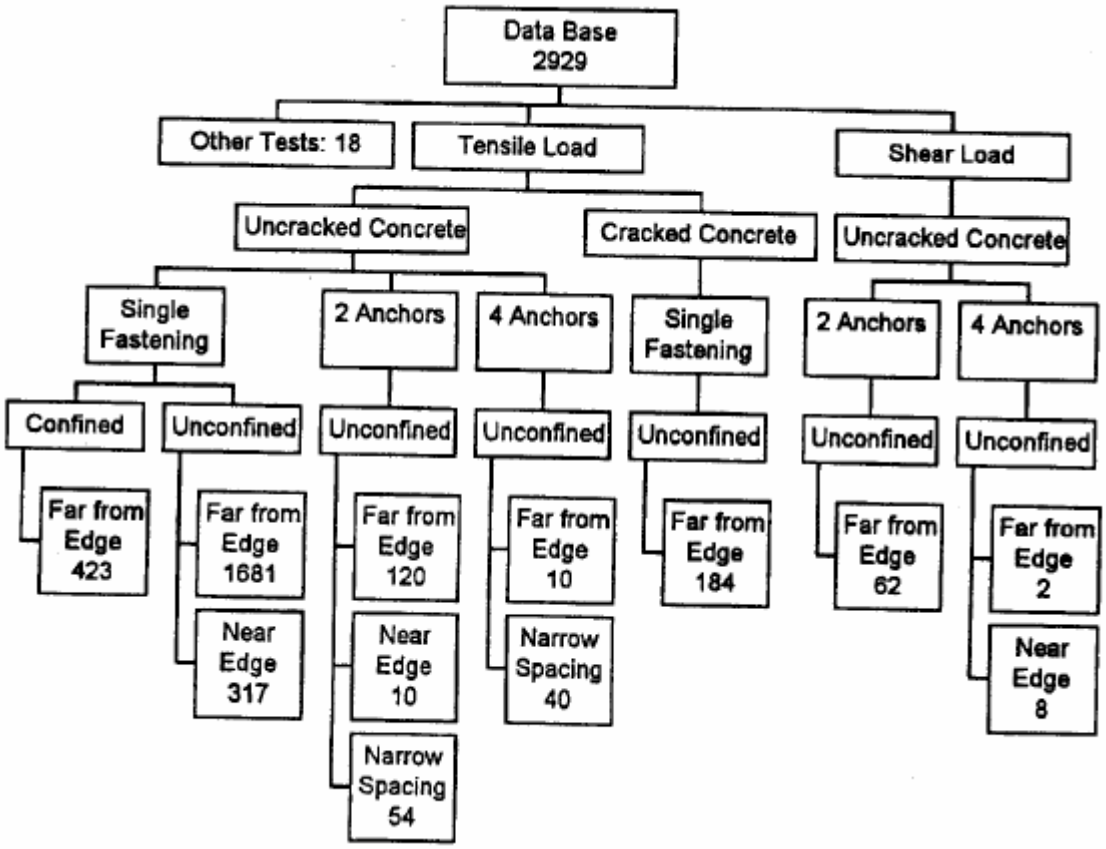

Throughout the literature review of bond models for concrete anchors, Cook, *et al.* determined six primary failure models. The first model identifies failure primarily from a cone shaped pullout, such that the capacity of the system is a function of the square root of the concrete compressive strength and the embedment depth; no dependency on the diameter of the anchor is required. The second model identifies a bond failure of the epoxy matrix at the interface of the reinforcing bar or anchor with no mention of a cone failure. In this case, failure is defined as a function of the bond strength of the surrounding epoxy, the diameter of the bar, and the embedment depth. The third model is also based on bond failure, but takes into account a shallow cone pullout by reducing the effective depth of the anchor if such a failure occurs. The fourth model assigns failure from a cone model for shallow depths and a bond failure for deeper embedment. The fifth model looks at a cone failure for shallow depths, with a combined cone/bond failure for deeper embedment depths. The sixth failure model accounts for the interface stresses between the adhesive/steel and the adhesive/concrete locations.

After introducing the six design models in the literature, the authors compare the design equations for the six methods to a uniform bond stress model, as identified in Equation [2.90].

$$N_u = \tau\pi d h_{ef} \qquad \text{Cook et al.} \qquad [2.90]$$

Where τ (MPa) is the bond stress of the anchor. Comparisons of the uniform bond model to the database of 888 tests indicate a good fit when compared to the models which differentiate between shallow cone failure and/or a mixture of shallow cone and bond

failure. However, the sixth model, which accounts for the interface stresses between the adhesive and concrete/steel, produced the best fit. In order to modify the uniform bond model shown in Equation [2.90], the concrete dependence on concrete strength was included in the equation—recall the compressive strength was the most variable term in Equation [2.89]. The revised equation uses the lesser of failure due to steel capacity of the anchor and bond strength of the adhesive/concrete system as defined in Equations [2.91] through [2.93].

$$N_u = \min(\phi_s N_{n,steel}, \phi_b N_{n,bond}) \qquad \text{Cook et al.} \qquad [2.91]$$

Where ϕ_s and ϕ_b are strength reduction factors presented as 0.90 and 0.85 for steel and bond respectively.

$$\phi_s N_{n,steel} = \phi_s A_e f_y \qquad \text{Cook et al.} \qquad [2.92]$$

$$\phi_b N_{n,bond} = \phi_b \tau' \pi d h_{ef} \Psi_c \qquad \text{Cook et al.} \qquad [2.93]$$

Where A_e (mm2) is the effective tensile stress area of the anchor or reinforcing bar, f_y (MPa) is the yield strength of the anchor or reinforcing bar, τ' is the bond stress based on the concrete strength as shown in Equation [2.94] and ψ_c is defined in Equation [2.95].

$$\tau' = \tau_{fc=20MPa}(1 - K \cdot COV) \qquad \text{Cook et al.} \qquad [2.94]$$

Where K is a coefficient based on the number of tests performed with a specific epoxy and the confidence used in the design; a value of 1.65 was used in the article. COV is the coefficient of variation of the coefficient K, which was taken as 0.2.

$$\Psi_c = \sqrt[n]{\frac{f_c'}{20}} \qquad \text{Cook et al.} \qquad [2.95]$$

Where Ψ_c equals 1.0 for f_c'=20 MPa, n is an epoxy dependent value based on the concrete strength used, and f_c' (MPa) is the compressive strength of the concrete.

An experimental program by Colak in 2001 looked at the influence of embedment length, adhesive thickness, percentage of filler material, and type of two-part epoxy used on simple direct pull-out tests of deformed mild steel reinforcing bars [Colak, 2001]. Two types of epoxy were used, denoted as EP1 and EP3, with the same resin, reactive diluents, but differing curing agents. Each epoxy also had a varying level of filler content, denoted as EP2 and EP4 relating to EP1 and EP3 respectively, in order to identify what effect the filler had on the shear modulus of the epoxy. The investigation looked at three different embedment lengths—50 mm (1.97 in.), 75 mm (2.95 in.), and 100 mm (3.94 in.)—as well as adhesive thickness varying from 1 mm (0.04 in.) to 4 mm (0.16 in.) for epoxies EP1 and EP3. The effect of increasing the embedment length indicated a linear bond stress relationship for the 50 mm (1.97 in.) embedment, turning toward a higher order curve as the embedment length crossed the 75 mm (2.95 in.) plateau for both epoxies, as indicated in Equation [2.96] below.

$$P = \frac{\pi u_{\max} d^{1.5}}{\lambda'} \tanh\left(\frac{\lambda' L}{\sqrt{d}}\right) \text{ where } \lambda' = \frac{\sqrt{4G}}{tE} \quad \text{Colak} \qquad [2.96]$$

Where u_{max} (MPa) is the maximum shear stress in the epoxy, d (mm) is the diameter of the drilled/cored hole, L (mm) is the embedment legth, G (MPa) is the shear modulus of the adhesive, t (mm) is the thickness of the adhesive layer, and E (MPa) is the modulus of elasticity of the steel. It is of interest to note that the author compared the results of their

work with that of Cook et al. and determined the values for λ' were of similar range of 0.036 to 0.046.

Recall for the 50 mm (1.97 in.) embedment, the relationship was linear, leading to a simplified result in Equation [2.97].

$$u_{\max} = \frac{P}{\pi L} \qquad \text{Colak} \qquad [2.97]$$

From Equation [2.97], the shear modulus of the EP2 and EP4 was determined for filler content ranging from 0% to 74% by volume. Results for filler up to 46% indicate a similar shear strength between the epoxies, decreasing and diverging (with EP2 having a higher modulus) as the filler neared 74%. Epoxies EP1 and EP3 (with no fillers) were used in determining the effect of epoxy thickness with shear modulus. Results indicate that the shear strength for EP1 increased as the epoxy thickness increased from 1 mm (0.04 in.) to 2 mm (0.08 in.), but decreasing at 3 mm (0.12 in.) and finally becoming static from 3 mm (0.12 in.) to 4mm (0.16 in.). On the other hand, epoxy EP3 was consistent through the range of thicknesses. It is noteworthy that the results of each thickness were based on a series of three tests, indicating it is not likely that the increase for EP1 at a thickness of 2 mm (0.08 in.) was due to experimental error.

Another investigation by Hammad, *et al.* in 2006 compared the bond capacity of integrally cast straight and 90 degree hooked bars meeting the minimum embedment depths provided by ACI 318-05 with post-inserted straight bars secured with two commercially available

epoxies [Hammad, *et al.* 2006]. The authors proposed that steel reinforcing bars meeting minimum spacing requirements and/or having confining steel to prevent a splitting failure anchored with epoxy should provide a bond greater than or equal to that of an integrally cast bar. In order to justify this hypothesis, the authors investigated the termination detail of a floor slab into a wall. Due to space limitations, bars extending from a girder or floor slab into a wall are typically bent utilizing a 90 or 180 degree hook, as recommended by Section 12 of ACI 318-05 to reach the yield strength of the bar. The scope of work included two bar sizes, three development lengths, two concrete strengths, and two epoxies; all reinforcing steel for the project met the deformation requirements of ASTM 615, Grade 420 (60 ksi).

As the purpose of the experimental program was to investigate additions or use changes resulting in structural detailing of buildings, the authors modeled the connection of a floor slab to a column as the location of a possible tie-in point, as shown in Fig. 2.13, with two cantilever vertical sections anchored to a horizontal section. As such, the specimens were modeled using the STM method which requires equilibrium at the location of the joint or node. Based on the geometry of the node, the value of the resultant inclined compressive force C_0 and the angle θ formed between the vertical tensile force from the post installed anchor and the resultant compressive force from the vertical member, as shown in Fig. 2.14, were determined. Assuming the reinforcing bars achieved yield just as they failed in bond, as would be the case utilizing the ACI bond equations, the lever arm z_0 can be determined by Equation [2.98].

$$z_0 = t_b - \frac{l_b}{2} - c_s \qquad \text{Hammad et al.} \qquad [2.98]$$

Where t_b (mm) is the depth of the drilled hole, c_s (mm) is the concrete cover to the center of the upper reinforcement of the horizontal base element, and l_b (mm) is the embedment length required to reach yield of the reinforcement as defined in Equation [2.99].

$$l_b = \frac{f_y d_b}{4 f_{db}} \qquad \text{Hammad et al.} \qquad [2.99]$$

Where f_y (MPa) is the yield strength of the reinforcing steel, d_b (mm) is the diameter of the reinforcing steel, and f_{db} (MPa) is the design bond strength of either the surrounding concrete or the epoxy used in the study. For the STM method, the resulting vertical compressive stress z_{1R} is defined as ϕ0.90d, where ϕ is equal to 0.85. Due to different thicknesses of the vertical members and embedment depths of the post repaired specimens, the resulting θ values, as denoted in Equation [2.100], varied.

$$\tan\theta = \frac{z_0}{z_{1R}} \qquad \text{Hammad et al.} \qquad [2.100]$$

The results of the experiment showed that variations in concrete strength and bar diameter had little effect on the failure modes of the post-installed bars compared to the integrally cast bars. The failure loads indicate the integrally cast hooked bars provided the greatest anchorage, followed by bars secured with epoxy No. 2, epoxy No. 1, and finally the integrally cast straight bars. All but the shallowest embedment lengths resulted in yielding of the reinforcement just prior to failure of the concrete cover and subsequent pullout of the bars. The shortest embedment depths resulted in a cone type failure which is indicative of a direct tension failure mode. Another interesting aspect of the research relates to the

failures with respect to the angle of the inclined strut C_0 and the horizontal direction, defined by θ. For angles of θ less than 30 degrees, the ACI method for embedment overestimated the capacity of the connection, but for values between 35 and 50 degrees, the method quite accurately predicts the ultimate strength of the connection.

2.2.4 Surface Mounted Carbon Fiber Reinforced Plastic (CFRP) Repair

Carbon Fiber Reinforced Plastic (CFRP) has been used with great success in the aerospace industry, but has only gained attention for use in civil infrastructure applications over the past two decades. Historically, the early use of CFRP for flexural repair is well documented within the available literature. However, a shift toward shear repair methods for CFRP began in the early 1990s. Moreover, many of the recommendations from the influx of articles by researchers since that time have been incorporated into the current ACI 440 recommendations. Thus, the bulk of the literature review in this area will account for the major articles that have contributed to the ACI 440 recommendations; in this light, the review is not intended to be an exhaustive list on the subject.

One of the first papers to investigate repair of concrete beams by way of CFRP sheets was undertaken by Chajes, *et al.* at the University of Delaware in 1995 [Chajes, *et al.* 1995]. The experimental program included 12 quarter scale T beams devoid of integrally cast stirrups which included four control specimens and three different woven fabric

configurations: aramid, E-glass, and graphite. The beam dimensions were 1219 mm (48 in.) long, 191 mm (7.5 in.) deep, with a flange width of 140 mm (5.5 in.), a web width of 64mm (2.5 in.), and a shear span of 406 mm (16 in.) (a/d ratio of 2.67). The composite materials were applied prior to loading of the specimens utilizing the three-sided U wrap and designed to fail in shear even with the anticipated increase in capacity from the composite materials.

In order to determine the bond characteristics of the two component epoxy with respect to the three composite materials, single shear pull-off tests were performed on a one in. width of each material. The anchorage lengths varied from 25 mm (1 in.) to 76 mm (3 in.) and indicate that the development length for the E-glass and graphite fabric required to reach fracture of the material was 25 mm (1 in.) while the aramid fabric required 76 mm (3 in.). Failure modes for the graphite and E-glass beams were due to rupture of the composite material at the location of the shear failure crack while the aramid woven fabric failed by bond. Failure strains indicated that the full capacity of the composite materials were not obtained. In spite of this drawback, the shear contribution of the composite materials were back-calculated by subtracting the concrete contribution (as determined from ACI 318-89) from the total shear load. A corresponding design equation for the composite material contribution was presented as shown in Equation [2.101].

$$V_{f_m} = A_f E_f \varepsilon_{v_{cu}} d \qquad \text{Chajes et al. (1995)} \qquad [2.101]$$

Where V_{fm} (ksi) is the nominal composite contribution to shear strength, A_f (in.^{2}) is the area of fabric shear reinforcement per in. of beam, ε_{vcu} is the ultimate vertical tensile strain

of the concrete, and d (in.) is the effective height of the beam. The contribution of the composite material was limited by strain equal to 0.005 in/in based on experimental work.

The results of the initial study lead to a second investigation by Chajes, *et al.* in 1996, to investigate bond and force transfer between the epoxy and composite material as they pertain to concrete surface preparation, type of adhesive, and concrete strength [Chajes, *et al.* 1996]. The test setup was previously described, with a constant development length of 76 mm (3 in.), which corresponded to the longest length for rupture of the aramid fiber in the previous study. The investigation looked at four commercially available epoxies: Sikadur 32 Hi-Mod, Sikadur 31 Hi Mod gel, and two manufactured by the Lord Corp.—Tyrite 7500 and Fusor 320/322. Results of the surface preparation indicated that mechanical abrasion resulted in the highest average bond stress when compared to grinding and the as formed surface. Failure of the bond tests for all but the Tyrite epoxy exhibited concrete shear failure, while the Tyrite sample failed within the epoxy matrix. The tests also indicated average bond stress increased with increasing concrete compressive strength. The experimental program investigated the strain distribution of the composite materials along the bonded length. General trends for lengths of 51, 102, 152, and 203 mm (2, 4, 6, and 8 in.) indicate the distribution was highest at the start of the bonded length, decreasing to zero strain at the free end.

The next paper of interest was published by Sato, *et al.* in 1996 [Sato, *et al.* 1996]. The experimental program included six quarter scale rectangular beams including one control

specimen. Beams dimensions were 200 mm (7.87 in.) in width, 300 mm (11.81 in.) in depth, with a shear span of 700 mm (27.56 in.), tested under four point loading. The shear span of all but one of the CFRP repaired beams were cast devoid of stirrups. The beams were repaired with both side and U wrap orientation schemes, with discrete and continuous strips over the length of the shear span; no load was applied prior to application of the FRP.

Failure modes for the beams without integrally cast stirrups resulted from diagonal tension failure after delamination and peeling of the FRP, while the specimen that included integrally cast stirrups in the shear span failed in a flexural mode. The authors provided general equations for calculating the FRP contribution to shear, but do not include the effect of bond stress in their simplified equations. The paper does provide the first experimental data that validates the use of a three sided U wrap compared to a side wrap that terminates at the base of the web.

The next noteworthy article was published by Norris, *et al.* in 1997 and included quarter scale testing of six rectangular beams, including one control specimen [Norris, *et al.* 1997]. Beam dimensions were 127 mm (5 in.) wide, 203 mm (8 in.) deep, with a 457 mm (18 in.) shear span (a/d ratio of 2.69). The specimens were repaired with a 3-sided U wrap both prior to application of load and after application of a precrack load. The investigation also included unidirectional and 45 degree strand orientations within the FRP. By applying the two FRP fabrics in the same U-shaped repair scheme, the principle tensile strength of the

FRP was changed based on the fiber orientation. Results indicate no significant difference in strength gain for precracked versus virgin specimens. Also, the beams with the fiber oriented at 45 degrees achieved higher load than the corresponding unidirectional fiber orientation—based on the fact that the 45 degree fibers were aligned closer to the principle tensile stresses in the concrete. The authors also provided strength contribution equations similar to Sato, *et al.*, only noting that the effect of limited bond stress may reduce the contribution from FRP and further work is needed in this area.

The next article, published by Kachlakev and McCurry in 2000, investigated the flexural and shear repair of an existing historic structure slated for rehabilitation [Kachlakev and McCurry 2000]. Due to the age of the structure, changing the physical appearance was prohibited, thus FRP was chosen as the repair medium. The in-service rectangular beams were replicated by four full scale specimens, including one control specimen, in the laboratory. Beam dimensions were 305 mm (12 in.) wide, 762 mm (30 in.) deep, with a shear span of 1829 mm (72 in.) and corresponding a/d ratio of 2.60. The replicated beams were cast without internal steel stirrups to reflect the condition of the in-service beams. The remaining specimens were repaired for shear, flexure and a combination of the two with no load applied prior to the carbon fiber application. The beam repaired for shear included unidirectional GFRP sheets attached in a 3-sided U wrap about the tension side of the beam. Failure of the beam was via yielding of the tension steel followed by crushing of the compression concrete. The beam repaired for both flexure and shear did not have a definitive failure mode, although from the strain data at the maximum load, it appeared that an over reinforced failure due to excessive deflection and strain hardening of the flexural

steel would have occurred. As this article dealt primarily with a case study of one structure, design equations were not included in the discussion.

While previous work has focused on the contribution for FRP based on the tensile capacity of the strips, the focus on limiting the strain in the FRP based on bond failure was first introduced by several articles, the first of which were published by Triantafillou and Khalifa, *et al.* in 1998. The paper by Triantafillou is especially beneficial, as it reviews the pertinent models in the literature at that time (including Berset, Dolan, Al-Sulaiman, Uji, Ohuchi et al., Chajes, *et al.*, Malvar, Vielhaber and Limberger, and Sato, *et al.*), many of which contradict each other in their recommendations for determining the shear contribution from FRP [Triantafillou 1998]. The author described two failure modes that dominate the literature in terms of a debonding failure originating at the free edge or rupture of the FRP, both of which lead to an abrupt non ductile failure mode. Triantafillou proposed limiting the effective strain in the FRP would produce a lower bound for the contribution. The shear contribution from FRP by Traintafillou (in Eurocode format) is presented below in Equation [2.102].

$$V_{frp} = \frac{0.9}{\gamma_{frp}} \rho_{frp} E_{frp} \varepsilon_{frp} b_w d \left(1 + \cot \beta\right) \sin \beta \qquad \text{Triantafillou (1998)} \qquad [2.102]$$

Where γ_{frp} is a material reduction factor proposed to equal 1.15, 1.20, or 1.25 for CFRP, AFRP, and GFRP respectively, ρ_{frp} is the FRP reinforcement ratio equal to $2t/b_w$ (where t (in.) is the thickness of the FRP), E_{frp} (ksi) is the modulus of elasticity of the FRP, ε_{frp} is the strain in the FRP, b_w (in.) is the smallest width of the web over the depth, d (in.) is the

effective height of the beam, and β is the angle the FRP makes with the longitudinal axis of the member. The only parameter that is not readily known from the previous tests is ε_{frp} or the strain in the FRP at failure.

In order to add to the existing database of shear repaired specimens, the author included a series of eleven rectangular beams without integrally cast stirrups and side wrapping utilizing CFRP at 90, 45, and 56 degrees to the longitudinal axis of the beam. Dimensions of the beams were 70 mm (2.75 in.) wide, 110 mm (4.33 in.) deep, with a shear span of 320 mm (12.60 in.) resulting in an a/d ratio of 3.2. All beams in the test matrix failed in shear, and the corresponding contribution from CFRP was back calculated by subtracting the concrete contribution from the total experimental shear stress. Then, the corresponding effective strain the CFRP was determined and compared to the test data of seven of the nine other investigators, resulting in a total of 42 shear tests for comparison. Triantafillou produced a plot of the effective strain in the FRP at failure versus the FRP reinforcement ratio times the material modulus. The plot indicated a similar trend regardless of the wrapping scheme. In addition, a best fit curve to the data indicated a decreasing second order polynomial for $\rho_{frp}E_{frp}$ less than 1, but a linear decreasing fit for values greater than 1. The resulting best fit equations for the effective strain in the FRP at failure were presented, based Equations [2.103] for $0 \le \rho_{frp}E_{frp} \le 145$ ksi and [2.104] for $\rho_{frp}E_{frp} > 145$ ksi.

$$\varepsilon_{frp} = .0119 - .0205\left(\rho_{frp}E_{frp}\right) + .0104\left(\rho_{frp}E_{frp}\right)^2 \text{ Triantafillou} \qquad [2.103]$$

$$\varepsilon_{frp} = -0.00065\left(\rho_{frp} E_{frp}\right) + 0.00245 \quad \text{Triantafillou} \qquad [2.104]$$

The relative shortcomings of Tiantafillou's 1998 paper, including the effect of concrete strength on bond and the various repair wrapping schemes were noted in the publication by Khalifa, *et al.* in 1998 [Khalifa, *et al.* 1998]. The article also presented the FRP contribution in terms of an ACI format, as denoted in Equation [2.105].

$$V_f = \frac{A_{fv} f_{fe} \left(\sin\alpha + \cos\alpha\right) d_f}{s_f} \qquad \text{Khalifa et al.} \qquad [2.105]$$

Where f_{fe} (ksi) is the effective stress in the FRP. Due to the linear elastic properties of FRP, this relates directly to the effective strain in the FRP, and indirectly to the bond model for side and U-wrapped specimens. The problem related to the bond model is based on the work of Maeda, *et al.* in 1997, which documented the effective bond length for FRP based on a series of direct tension tests, but was limited to one design concrete strength [Maeda, *et al.* 1997]. Utilizing the work of Horiguchi and Saeki in 1997, Khalifa, *et al.* modified the bond model to include the effect of varying concrete strength [Horiguchi and Saeki 1997].

Khalifa, *et al.* also modified the capacity equation to include an effective width of the FRP, based on the wrapping scheme and the distance the FRP strip was to the failure crack. Utilizing the modified effective bond length, the contribution to shear strength based on proximity to the failure crack and in effect the anchoring scheme/wrapping type was proposed. The authors also included a reduction factor for FRP equal to 0.7, in order to

produce a lower bound failure mode in design, which could be modified as more data populated the existing database. The value proposed by ACI 440 is currently equal to 0.765.

Triantafillou and Antonopoulos published an article in 2000 to address the concerns pointed out by Khalifa, *et al.* to include the effect of concrete strength on the bond model and to differentiate failure based on the wrapping scheme [Triantafillou and Antonopoulos 2000]. The governing equation for FRP contribution was modified to follow the Madea, *et al.* bond model (modified for varying concrete strengths), as shown below in Equation [2.106].

$$\varphi_f V_f = \varphi_f \varepsilon_{f,e,A} E_f \rho_f \left(\sin\beta + \cos\beta\right) bd \quad \text{Triantafillou \& Antonopoulos} \quad [2.106]$$

Where φ_f is the strength reduction factor for FRP previously defined in Equation [2.102] and $\varepsilon_{f,e,A} = 0.9\varepsilon_{f,e} \leq \varepsilon_{max,A}$. As such, $\varepsilon_{f,e}$ is defined for fully wrapped CFRP, side or U-wrapped CFRP, and fully wrapped AFRP are shown in Equations [2.107], [2.108], and [2.109], where ε_{fu} may be taken as 0.006.

$$\varepsilon_{f,e} = 0.17\left(\frac{f_c^{2/3}}{E_f \rho_f}\right)^{0.30} \varepsilon_{fu} \quad \text{Triantafillou \& Antonopoulos} \quad [2.107]$$

$$\varepsilon_{f,e} = \min\left[\begin{array}{l} 0.65\left(\dfrac{f_c^{2/3}}{E_f \rho_f}\right)^{0.56} \times 10^{-3}, \\ 0.17\left(\dfrac{f_c^{2/3}}{E_f \rho_f}\right)^{0.30} \varepsilon_{f,u} \end{array}\right] \quad \text{Triantafillou \& Antonopoulos} \quad [2.108]$$

$$\varepsilon_{f,e} = 0.048\left(\frac{f_c^{2/3}}{E_f \rho_f}\right)^{0.47} \varepsilon_{fu} \quad \text{Triantafillou \& Antonopoulos} \quad [2.109]$$

Thus, from the early series of investigators, the contribution of FRP was presented, based on the wrapping scheme. For a side or U wrapped specimen, the failure occurred from bond, and results in a limiting of the effective strain in the FRP, based on a maximum value of 0.004 or a value related to the active bond length and concrete strength.

2.2.5 CRFP Tape as a Near Surface Mount (NSM) Repair

The use of carbon fiber as a near surface mount application has gained attention as of early 2001, with a bulk of the initial work completed at the University of Missouri-Rolla by De Lorenzis and Nanni. They published several papers, the first two in 2001, which outlined a research program that included both bond and beam tests [De Lorenzis and Nanni 2001a, 2001b]. For the bond tests, a beam-type pull out specimen was used to determine the local bond-slip characteristics of the FRP-to-epoxy system in order to quantify the effect of development length and minimum cover requirements. The beam tests included eight full scale T beams, including two control specimens. The beam dimensions were 406 mm (16 in.) deep, with a flange width of 381 mm (15 in.), a web width of 152 mm (6 in.), a flange thickness of 102 mm (4 in.), and a shear span of 107mm (42 in.) resulting in an a/d ratio of 3.0. Only two of the eight beams were cast with internal steel stirrups including one control specimen. The research program included parameters such as NSM spacing, orientation (orthogonal to the tension steel or oriented at 45 degrees to the tension steel),

and anchorage (into the flange or termination of the rod at the junction of the web and flange). Failure was due to either lack of confining stirrups at the base of the stem resulting in a splitting of the concrete cover along the bottom flexural steel or insufficient epoxy cover to the FRP bar.

Results from the research program indicate higher shear strength was gained (in order of least to most important) by: decreasing the spacing of the FRP, orienting the rods closer to the principle tensile stress in the shear span, and increasing the anchorage length of the rods into the flange. A design method was presented that determined the total shear capacity based on the contributions from steel, concrete, and FRP, as shown in Equation [2.110].

$$V_n = V_s + V_c + V_{NSM} \qquad \text{De Lorenzis \& Nanni (2001a)} \qquad [2.110]$$

The contribution from the NSM was presented as the lesser of two equations; the first is related to the bond of the NSM with respect to the surrounding concrete while the second limits the strain in the NSM to 4000 $\mu\varepsilon$. The first equation related to bond failure is based on three assumptions: the formation of shear cracks occur at 45 degrees to the longitudinal axis of the member, the distribution of bond stresses along the effective lengths of the FRP is uniform, and the ultimate bond strength is reached in all rods intersecting the failure crack at the same time. The total shear force from NSM is taken as the summation of each individual rod that crosses the failure crack. The minimum length of the FRP measured from the crack to the termination of the rod is used such that V_{1F} is calculated in Equation [2.111].

$$V_{1F} = 2\sum A_i f_i = 2\pi d_b \tau_b L_{tot\_\min} \qquad \text{De Lorenzis \& Nanni (2001a)} \quad [2.111]$$

Where d_b (in) is the diameter of the FRP rod, τ_b (ksi) is a bond strength parameter specific to the type of FRP bar and epoxy/mortar used—in a previous investigation De Lorenzis and Nanni determined a value of 1.0 ksi is sufficient for the combination of bar and epoxy utilized—and L_{tot_min} (in) is the total minimum length of FRP contributing to the strength gain. The second failure mode, limited by the strain in the FRP, utilizes equilibrium to calculate the contribution based on the smaller effective length of the FRP measured from the crack to the termination of the rod as indicated in Equation [2.112].

$$L_i = 0.001\frac{d_b E_b}{\tau_b} \qquad \text{De Lorenzis \&Nanni (2001a)} \qquad [2.112]$$

The paper presents three different scenarios for calculating the contribution of the effective lengths L_i, based on the spacing of the strips, the total height of the strip, and the effective height measured from the crack to the termination of the rod. Using this method, a plot of the theoretical to experimental capacity resulted in a best fit slope of 1.052 with an R^2 value of 0.9595 indicating a well defined goodness of fit.

A second paper by De Lorenzis and Nanni, also published in 2001, investigated bond characteristics of the FRP and included two full scale repaired beams and one control specimen that were included in the previous paper and are not reviewed a second time [De Lorenzis and Nanni 2001b]. For the bond tests, a beam type pull-out test was performed in lieu of a traditional direct tension pull-out test with the objective of determining the effect of the bonded length to bar diameter with three different ratios—6, 12, and 18. For the

ratio of 12, the width and corresponding depth of the groove were varied from one-half, three-quarter, to one in. Results from the test indicated a splitting failure of the epoxy cover in all but one of the tests—the bonded length to bar diameter of 12 with the one in. groove indicated a failure due to cracking of the concrete. Due to the configuration of the test, the average bond stress was calculated as shown below in Equation [2.113].

$$\tau_b = \frac{T_u}{\pi d_b l_b} \qquad \text{De Lorenzis \&Nanni (2001b)} \qquad [2.113]$$

Where τ_b (ksi) is the average bond stress over the bonded length, T_u (kips) is the ultimate tensile load, d_b (in.) is the nominal diameter of the rod, and l_b (in.) is the bonded length. The effect of the bonded length indicate a higher ultimate tensile load with increasing bonded length; however, strain gage data along the bonded length indicate a nearly uniform distribution of strain over this length at failure.

A third paper by De Lorenzis and Nanni published in 2002 extended the objectives of the previous bond paper [De Lorenzis and Nanni 2002]. In the paper, the same beam type pull-out tests were used but the investigation included two bar diameters (9.5 mm (0.375 in) and 12.7 mm (0.5 in)), two different bar types (CFRP and GFRP rod), four bonded length to diameter ratios (6, 12, 18, and 24), and four groove sizes (12.7 mm (0.5 in.), 15.9 mm (0.625 in.), 19 mm (0.75 in.), and 25.4 mm (1 in.)). For the GFRP rods, two surface treatments were investigated—sand blasted and traditionally deformed bars. Across all test variables, the maximum load, as a percentage of the ultimate tensile capacity of the FRP

rod, turned out to be 60% for the 12.7 mm (0.5 in) diameter bar with a 25.4 mm (1 in.) groove size and a bonded length equal to 24 bar diameters.

Failure modes varied based on the specific test configurations, although general trends were evident. For a majority of the specimens, a splitting failure in the epoxy matrix led to failure; however, stress cracking in the concrete at the interface with the epoxy was also noted in several of the longer embedment lengths. For the GFRP sand blasted specimens, the lack of rib geometry resulted in a small circumferential stress field surrounding the bar. Consequently, the sand blasted GFRP bars experienced a pullout failure due to lack of mechanical anchorage that is typical of a deformed bar once the chemical adhesive bond limit is reached and bar slip initiates.

Analysis of a bar assuming a linear elastic behavior in the rod over a differential length dx is shown in Equation [2.114].

$$\tau(x) = \frac{d_b}{4} E_b \frac{d\varepsilon_b(x)}{dx} \qquad \text{De Lorenzis \& Nanni (2002)} \qquad [2.114]$$

Where d_b (in) is the diameter of the bar, E_b (ksi) is the modulus of elasticity of the bar, ε_b is the strain in the rod, and τ (ksi) is the bond stress as a function of length x. The authors also present an equation for the slip of the bar, s, as a function x, assuming the strain in the adjacent epoxy is negligible, as denoted in Equation [2.115].

$$s(x) = s(0) + \int_0^x \varepsilon_b(x)dx \qquad \text{De Lorenzis \& Nanni (2002)} \qquad [2.115]$$

In addition, the governing differential equation for bond is presented based on equilibrium and compatibility, as shown in Equation [2.116].

$$\frac{d^2 s}{dx^2} - \frac{4}{d_b E_b}\tau(s(x)) = 0 \qquad \text{De Lorenzis \& Nanni (2002)} \qquad [2.116]$$

Where the bond-slip relationship $\tau(s(x))$ must be determined experimentally. For analysis of the joint within the linear elastic range, the authors assumed a linear bond-slip relationship which was accurate up to "moderate load levels", with K defined as the slip modulus. A solution to Equation [2.116], assuming a linear slip relationship is shown below in Equation [2.117].

$$\varepsilon_b(x) = \frac{\sigma_{appl}}{E_b}\frac{\sinh \alpha x}{\sinh \alpha l_b} \qquad \text{De Lorenzis \& Nanni (2002)} \qquad [2.117]$$

Where σ_{appl} (ksi) is the tensile stress applied in the rod, l_b (in.) is the bonded length, and α is as shown in Equation [2.118].

$$\alpha = \sqrt{\frac{4K}{E_b d_b}} \qquad \text{De Lorenzis \& Nanni (2002)} \qquad [2.118]$$

Strain data collected for all specimens was used to evaluate the bond-slip coefficient K, utilizing a least squares approach. However, for higher load levels, the local bond-slip relationship must be determined following one of several available models in the literature; the authors chose to follow a modified version of the Bertero-Popov-Eligenhausen (BPE) relationship proposed by Cosenza, *et al.* used for deformed bar specimens [Cosenza, *et al.*

1997]. The relationship assumes a nonlinear ascending branch followed by a linear softening branch; individual parameters in the bond-slip relationship are determined experimentally for each material (both reinforcing bar and encasing material). Once an analytical expression for the local bond-slip of the joint has been determined, the failure load of the joint and corresponding embedment length can be calculate by solving the differential Equation [2.115], for given boundary conditions related to slip in the bar at the loaded or free end, as well as bar strain at the loaded or free end. The authors provide a solution for the embedment length of the bars assuming the stress in the bars is limited to a value on the ascending portion of the bond-slip relationship.

A final paper published by De Lorenzis in 2004 attempts to provide a governing explanation of the bond model from two additional papers (published in 2002 and 2004 respectively) which looked at the experimental bond model of ribbed CFRP rods in both epoxy and mortar, GFRP ribbed and spiral bars in epoxy and cement paste, and GFRP sandblasted rods in epoxy [De Lorenzis 2004]. Combining the latest experiments with the previous work on bond, De Lorenzis used an analytical approach to the bond modeling based on the experimental work. As such, the bond models are divided into three different curves. The first deals exclusively with deformed CFRP rods with failure at the interface of the concrete and the groove filler (for smooth grooves only), splitting failure of the epoxy, and all bars in cement paste. The second curve deals with splitting failure of GFRP deformed and spiral bars in epoxy or pull-out type failure of spiral bars in cement paste. The last curve deals with sand blasted bars in epoxy which result in a pull-out failure mode.

Once the bond stress-slip relationship is measured experimentally, an analytical model was chosen to describe the behavior. As in the previous article, the Bertero-Popov-Eligenhausen (BPE) relationship proposed by Cosenza, *et al.* for deformed bar specimens was used for the ascending branch of the curve with post peak responses modeled based on experimental data. For each bond test, the maximum bond stress at failue τ_m (ksi) and the slip corresponding to this maximum bond stress s_m (in) were recorded. These values were used to determine the shape of the ascending and post peak response utilizing α and α' parameters respectively.

General trends from the bond tests are useful to point out prior to derivation of equation. For specimens failing at the epoxy to concrete interface, τ_m decreased with increasing groove depth. For the epoxy filled specimens, failure occurred at the interface with the surrounding concrete or within the epoxy matrix; the highest bond stresses were from spirally wound bars, followed by deformed CFRP bars, and finally deformed GFRP bars. The use of sand blasted bars is not recommended due to the low bond stresses attributed to lack of deformations. The small amount of slip during the ascending branch of the curves indicate that experimental error in measuring the slip values will produce different α values for specimens which failed due to cracking of the epoxy cover. On the other hand, specimens that failed at the epoxy to concrete interface had fairly consistent α parameters, as did the sand blasted bars since they failed in a pull-out fashion.

A revised differential equation for the bond behavior is presented in Equation [2.119]; the modification from the previous paper now includes possible failure at the interface of the epoxy or mortar and the concrete.

$$\frac{d^2 s}{dx^2} \chi \tau(s(x)) = 0 \qquad \text{De Lorenzis (2004)} \qquad [2.119]$$

Where χ is defined in general terms in Equation [2.120].

$$\chi = \frac{\Sigma}{AE} \qquad \text{De Lorenzis (2004)} \qquad [2.120]$$

Where Σ is the perimeter along which the bond stress acts, A (mm^2) is the area on which the tensile strength acts, and E (MPa) is the modulus of the material on which the tensile stress acts. Equation [2.120] can be written for the case of failure of the epoxy/mortar to the concrete as in Equation [2.121], or as failure of the FRP bar within the epoxy/mortar as denoted in Equation [2.122].

$$\chi = \frac{4}{E_b d_b} \qquad \text{De Lorenzis (2004)} \qquad [2.121]$$

Where E_b (MPa) is the modulus of elasticity of the FRP and d_b (mm) is the diameter of the FRP rod.

$$\chi = \frac{3d_g}{E_e A_{om}} = \frac{3k}{d_b E_e \left[k^2 + (n-1)\frac{\pi}{4} \right]} \qquad \text{De Lorenzis (2004)} \qquad [2.122]$$

Where d_b (mm) is the size of the square groove, E_e (MPa) is the modulus of elasticity of the epoxy or mortar, A_{om} (mm^2) is the area of the groove (including the FRP), k is the ratio of the groove size to the bar diameter, and n is the ratio of the modulus of elasticity of the

FRP to the epoxy or mortar. De Lorenzis then determined the maximum stress that can be applied to the joint, irrespective of the bonded length from the previously mentioned 2002 paper as denoted in Equation [2.123].

$$\sigma_{\max} = \sqrt{2E\frac{\Sigma}{A}A_{\tau\max}} \qquad \text{De Lorenzis (2004)} \qquad [2.123]$$

Where E (MPa) is the modulus of the FRP or the epoxy/mortar, A (mm^2) is the area of the groove or the bar, and $A_{\tau max}$ (kN-M) is the fracture energy of the bonded joint, as shown in Equation [2.124].

$$A_{\tau\max} = \int_0^x \tau(s)ds \qquad \text{De Lorenzis (2004)} \qquad [2.124]$$

For the two failure modes noted previously, Equation [2.123] can be rewritten as shown in Equations [2.125] and [2.126] for failure of the FRP bar and epoxy or mortar bond and failure of the epoxy or mortar and concrete bond respectively.

$$\sigma_{\max} = \sqrt{\frac{8E_b}{d_b}A_{\tau\max}} \qquad \text{De Lorenzis (2004)} \qquad [2.125]$$

$$\sigma_{\max} = \sqrt{\frac{6d_g E_e}{A_{om}}A_{\tau\max}} \qquad \text{De Lorenzis (2004)} \qquad [2.126]$$

In the above equations, if the stress calculated is less than the tensile strength of the FRP rod, then the full capacity of the bar is not possible. This scenario is a direct result of the fracture energy calculation and in turn the post-peak response of the local bond stress-slip relationship. For case 1—the use of CFRP bars in epoxy—the post peak response results in an infinite fracture energy for $\alpha' > -1$ and a finite value for $\alpha' < -1$. For a rough groove, the

post-peak curve results in a α'<-1, indicating that a limiting stress value is possible and that any additional length beyond this critical value will not result in additional capacity. However, for a smooth groove specimen, the opposite is true—that is, α'<-1 and thus the FRP bars are able to reach their full capacity at a given length. It should be noted that for a given embedment length less than the required development length for fracture of a smooth groove, a comparable rough groove will typically result in a higher bond stress, even though the smooth grooved specimen will achieve higher loads if simply the embedment length is increased.

The author further presents the maximum stress to be applied to a boded joint (both in terms of the bond of the epoxy and FRP rod and the epoxy and the concrete) is a function of design requirements at the service level. As such, slip at the free end under service loads is assumed to be equal to zero and to anchor the FRP bar on the ascending portion of the local bond stress-slip curve. Following these recommendations, Equations [2.125] and [2.126] are then revised as shown below in Equations [2.127] and [2.128].

$$\sigma_1 = \sqrt{\frac{8E_b}{d_b}\frac{\tau_m s_m}{1+\alpha}} \qquad \text{De Lorenzis (2004)} \qquad [2.127]$$

$$\sigma_1 = \sqrt{\frac{6E_e d_g}{A_{om}}\frac{\tau_m s_m}{1+\alpha}} \qquad \text{De Lorenzis (2004)} \qquad [2.128]$$

Where τ_m (MPa) is the maximum bond stress of the joint, s_m (mm) is the slip at peak bond stress. The corresponding development length for the two cases are shown below in Equations [2.129] and [2.130].

$$l_m = \frac{\sigma_1 d_b}{4\tau_m}\frac{1+\alpha}{1-\alpha} \qquad \text{De Lorenzis (2004)} \qquad [2.129]$$

$$l_m = \frac{\sigma_1 A_{om}}{3 d_g \tau_m}\frac{1+\alpha}{1-\alpha} \qquad \text{De Lorenzis (2004)} \qquad [2.130]$$

The remainder of the paper deals with splitting of the epoxy cover, modeled as a thick cylinder; the derivation is not included in the current investigation.

An article by Cruz and Barros in 2004 looked at analytical modeling of the bond for NSM and concrete via an epoxy matrix [Cruz and Barros 2004]. The research program looked at a beam type pullout test setup similar to that of De Lorenzis, as shown in Fig. 2.15. The authors presented the equilibrium of an infinitesimal length dx of FRP subjected to strain as shown in Equation [2.131].

$$\tau(x) = \frac{E_f t_f}{2}\frac{d\varepsilon_f}{dx};\ \text{where } \varepsilon_f = \frac{ds}{dx} \qquad \text{Cruz \& Barros} \qquad [2.131]$$

Where E_f (MPa), t_f (mm), and ε_f are the modulus of elasticity, thickness, and strain of the FRP. The strain in the FRP is measured as a relative slip value compared to the surrounding epoxy and concrete, with the assumption that the strain in the epoxy and concrete are quite small in comparison. Thus, the strain in the FRP can be measured experimentally at both the free and loaded end. Combining the FRP strain into Equation [2.131], the result is shown below in Equation [2.132].

$$\frac{d^2 s}{dx^2} = \frac{2}{\tau_f E_f}\tau(x) \qquad \text{Cruz \& Barros} \qquad [2.132]$$

The form of this equation is similar to that found by De Lorenzis in Equation [2.119], shown below for clarity.

$$\frac{d^2 s}{dx^2}\chi\tau(s(x)) = 0 \qquad \text{De Lorenzis (2004)}$$

In both cases, the local bond stress-slip relationship must be determined. In Cruz & Barros' investigation, the behavior adopted for the τ-s relationship was similar to that of De Lorenzis with a non-linear ascending branch following the Eligehausen model until the bond stress reached a maximum value for the corresponding slip (identified as s_m), followed by a post peak softening response. The governing equations for the τ-s relationship are shown in Equation [2.133].

$$\tau(s) = \begin{cases} \tau_m \left(\frac{s}{s_m}\right)^{\alpha} & \text{if } s < s_m \\ \tau_m \left(\frac{s}{s_m}\right)^{-\alpha} & \text{if } s > s_m \end{cases} \qquad \text{Cruz \& Barros} \qquad [2.133]$$

In order to evaluate the parameters s_m, τ_m, α, and α', a iterative procedure was implemented such that the solution of the second order differential equation shown in Equation [2.132] could be found by the Runge-Kutta-Nyström method.

Results indicate that the analytical bond stress parameter τ_m was modeled accurately, with an average value of 19.81 MPa and corresponding coefficient of variation of 6.6%. The remaining values of slip at maximum bond stress s_m and shape parameters, α, and α' indicate a large scatter with COV values from 21.40 to 36.19 percent. Therefore, the

goodness of fit for the parameter does not agree well with the proposed analytical method. The authors also performed FEM testing to find the total pullout force and loaded end slip with results comparable to the analytical and experimental work. The authors proposed a development length equation that was generically based on the specific τ-s relationship of the joint in question. The relationship is highly susceptible to the geometry of the grooves, the concrete strength, and the epoxy used, thus the equation is excluded from the current discussion.

The suite of articles published by De Lorenzis and other colleagues present the initial thrust into determining an analytical bond model for round FRP bars used in a NSM application. However, the current study utilizes rectangular FRP tape as opposed to a circular FRP rod. This decision was based on the work of Shield and French in 2005 utilizing the same rectangular tape with various epoxy manufacturers in direct pull-out tests to determine the best pairing of epoxy to FRP tape since most repair systems for FRP do not couple the FRP with the epoxy [Shield and French 2005].

Shield and French's experimental program was twofold: initial testing on scaled specimens included seven different epoxies with six specimens per adhesive; upon results of the small scaled testing, two epoxies were used on larger scaled specimens. Material specifications were as followed: the FRP was Aslan 500 CFRP tape, manufactured by Hughes Brothers with dimensions of 2 mm (0.079 in.) by 16 mm (0.63 in.) and a cross sectional area of (32.3 mm^2 (0.05 $in.^2$). The guaranteed ultimate strength of the tape was reported as 2,068

MPa (300 ksi), although test results by Shield and French achieved an ultimate strength closer to 2,482 MPa (360 ksi) with a 4.5% Coefficient of Variation. Epoxies included SIkadur AnchorFix-3, Master Builders/Chemrex Concresive 1420, 3M DP600NS, 3M DP460NS, Sonneborn Epofil, Sikadur 35 Hi-Mod LV, and Sikadur 32 Hi-Mod.

Scaled specimens were 152 mm (6 in.) by 152 mm (6 in.) by 203 mm (8 in.) in length. A groove measuring 6.4 mm (0.25 in.) wide by 19 mm (0.75 in.) deep was cut along one of the 152 mm (6 in.) sides of the specimens. Once the groove was cut, it was cleaned out with compressed air to remove any trace amounts of cement that may interfere with the bond. Some of the epoxy manufacturers did not provide a mixing applicator, thus mixing was accomplished in a separate container prior to application. For the remaining epoxies, an applicator gun with a static mixing nozzle was provided thus ensuring the correct proportions prior to application. The NSM tape was anchored in the groove and allowed to cure for 24 hours prior to testing. The anchor block was placed in compression at the bottom of a universal testing machine via a reaction section placed on top of the concrete block. The free end of the NSM tape extended upward, with two aluminum tabs inserted into the grips of the machine. Once secured, the NSM tape was pulled out of the testing block.

Results from the small scale test indicate a mixed failure mode across the seven manufacturers. For Sikadur AnchorFix-3, Master Builder/Chemrex Concresive 1420, Sikadur 32 Hi-Mod, Sikadur 35 Hi-Mod LV, and Sonneborn Epofil, the failure occurred

between the tape and the adhesive, indicating a poor bond between the epoxy and NSM surface. 3M DP600NS failed between the adhesive and the concrete, while 3M DP460NS exhibited several failure modes including bond between the tape and adhesive, within the adhesive matrix, failure within the concrete surrounding the adhesive, and failure of the FRP—in which case the failure was progressive, as each individual strand within the tape failed, until the entire specimen failed. However, the 3M DP460NS achieved the highest average and maximum load for the small scaled tests, indicating a stress up to 98% of the experimental capacity of the FRP tape.

The authors attempted to correlate the manufacturer's adhesive properties with respect to the small scale specimens with poor results. Among the manufacturers investigated, the adhesive tensile strength and shear strength had a correlation (r^2 value) of 0.07 and 0.02 respectively. The results were better for the tension modulus and elongation at failure at 0.053 and 0.42 respectively, but still less than half of what was reported by the manufacturer. The authors conclude that choosing an FRP system and corresponding epoxy system is not based solely on manufacturers reported test values.

From the results of the small scale tests, Sikadur AnchorFix-3 and 3M DP40NS were chosen for the larger scaled test. The test consisted of two reinforced concrete blocks to simulate a crack between two pieces of concrete. A 76 mm (3 in.) groove oriented perpendicular to the "crack" was cut on both sides of each block resulting in two NSM tapes per test. In addition to the orthogonal test, grooves cut at 45 degrees to the crack

were included in the test to simulate a shear repair. The blocks were situated in a Universal testing machine with LVDT sensors at all four corners to ensure linear loading of the specimen (to eliminate any eccentric loading or rotation).

Results from the large scale tests indicate the 3M 460NS was superior both in total load and post investigation of the failure plane. The 3M product consistently anchored the NSM, with failure occurring in the surrounding concrete; no failure between the tape and epoxy or epoxy and concrete was found. The authors theorize that the 3M 460NS has a higher ductility compared with the other manufacturers, thus allowing higher strains than are permitted in the adjoining concrete.

An article published in 2006 by Barros and Dias looked at the shear strength contribution from traditional steel stirrups, CFRP fiber wrap, and NSM rectangular FRP laminates [Barros and Dias 2006]. The investigation included 20 quarter scale beams with several design parameters. The breakdown of the 20 beams were as follows: four sets of five beams included one control specimen devoid of integrally cast stirrups, one beam with integrally cast stirrups, one beam devoid of integrally cast stirrups utilizing CFRP U-wrapping as the shear reinforcement, and the last two beams were cast devoid of integral stirrups reinforced with rectangular FRP laminates at 90 and 45 degrees to the axis of the beam. Within this general architecture, the four groups varied in specimen depth, shear span, and longitudinal reinforcement ratio. The first two sets each had a rectangular cross section of 300 mm (11.8 in.) by 150 mm (5.9 in.) with differing longitudinal reinforcement

and a 600 mm (23.6 in.) shear span, while the second two sets had a 150 mm (5.9 in.) square cross section with differing longitudinal reinforcement; in both cases the shear span was equal to twice the depth, resulting in an a/d ratio of 2.2 and 2.4 respectively.

In order to test the shear contribution from each specimen, the concrete contribution was determined from the Portuguese code which is modeled after the CEB-FIP. The steel contribution was also taken from the Portuguese code, but did not take into account the dowel action which is outlined in the CEB-FIP model code. The shear contribution from CFRP wrapping was taken from ACI 440 and fib provisions. As there are no specific guidelines for implementation of NSM as a shear repair, the author chose the recommendations of Nanni, *et al.* (2004). From these provisions, all the specimens were designed to fail in shear. Also, due the lack of internal stirrups, the FRP beams were not loaded prior to application of the appropriate system.

Results from the test indicate that the prediction models for the CFRP wrapping were quite accurate with a slight underestimation of 2% and 8% respectively for the ACI 440 and *fib* methods. However, using the design method by Nanni, *et al.* (2004) with a maximum bond stress in the FRP equal to 0.59% of the tensile capacity of the section (taken from the beam type pullout tests previously performed by Cruz and Barros), resulted in a strength prediction equal to 79% of the experimental work. This may provide a useable lower bound for design, but could also be higher as more tests confirm or refine the method proposed by Nanni, *et al.*

A paper by Dias and Barros published in 2008 investigated the effect of rectangular NSM as a shear repair on 12 quarter scale T beams [Dias and Barros 2008]. The beam dimensions were 400 mm (15.7 in.) deep, with a flange width of 450 mm (17.7 in.), a web width of 180 mm (7.1 in.), a flange thickness of 100 mm (3.9 in), and shear span of 900 mm (35.4 in.) resulting in an a/d ratio of 2.5. The study looked at several parameters including NSM shear reinforcement ratio (in terms of spacing of the strips) and orientation of the NSM with respect to the longitudinal axis of the beam (90, 60, and 45 degrees were used). The paper calculated the ratio of shear reinforcement as shown below in Equation [2.134].

$$\rho_{fw} = \frac{2a_f b_f}{b_w s_f \sin\theta_f} \qquad \text{Diaz \& Barros} \qquad [2.134]$$

Where a_f (mm) and b_f (mm) correspond to the thickness and width of the CFRP laminate, b_w (mm) is the width of the beam web, and s_f (mm) is the spacing of the CFRP laminate along the shear span, and θ_f is the angle between the longitudinal axis and the CFRP. The beams were subjected to three point loading, eccentric to the centerline of the beam. In order to force a shear failure in the shorter shear span, the longer shear span was over reinforced. The authors also chose to limit the stress in the laminate equal to a strain of 0.5% as a compromise that is higher than the 0.4% recommended from ACI 440 for externally applied CFRP and pullout bending tests from Cruz and Barros (2004) of 0.59% [Cruz and Barros 2004].

The experimental setup included three control beams. One was devoid of integrally cast stirrups within the shorter shear span, while the remaining two had two and six 6 mm diameter stirrups within the 900 mm shear span. The remaining nine beams had varying NSM and internal stirrup spacing as well as varied NSM orientation to the longitudinal axis of the beam. Within the test matrix, one integrally cast stirrup and one CFRP laminate near the same location were instrumented to compare the relative strain measurements. The stirrups were instrumented at three locations whereas the CFRP were instrumented at 1/5 points, as shown in Fig. 2.16. The beams were not subjected to any previous load prior to installation of the NSM; the beams were tested to failure after the NSM was applied.

The research program produced some noteworthy results. The control specimen with no integrally cast stirrups in the shear span failed at a 45 degree crack relative to the longitudinal axis, whereas the two remaining control beams failed at an approximately 55 degree angle to the longitudinal axis of the beam. As such, the efficiency of the NSM material for the beams with integrally cast stirrups in the shear span was highest for the 60 degree specimen, then the 45 degree specimen and finally the 90 degree specimen. The spacing of the NSM also played a role in the increased capacity of the section based on the shear cracks that formed. For the widest spacing of NSM, only one or two shear cracks formed, resulting in a longer development length of the NSM from the crack to the terminating end of the strip. For the narrowest spacing, several shear cracks formed along the shear span, thus reducing the developed lengths between cracks or from one crack to the terminating end of a strip. This resulted in the lowest strain distribution of the FRP, indicating the efficiency of the repair as a whole is compromised. The authors indicate this

may result in a maximum spacing requirement to fully utilize the strength of individual NSM strips. In addition, once a shear crack formed within the shear span, the stiffness of the beam increased with the addition of the NSM reinforcement..

2.2.6 Zararis Method (Bent Cap Specimen Only)

The STM method can lead to over conservative design for deep beam analysis beyond the service level; based on previous work on full scale bent cap specimens at Oregon State University [Senturk and Higgins 2009]. However, within the review of academic research in this area, the work of Zararis stood out as a reasonable estimate of the capacity of deep beam specimens encompassing several parameters including stirrup grade and spacing, flexural cutoffs, and beam depth [Zararis 2003]. The method provides a fundamental theory on the behavior of deep beams having a shear span to depth ratio (a/d) of 1.0 to 2.5 with and without transverse steel. It assumes an ultimate shear force on a section based on a reduced compression zone and moment equilibrium with the vertical and flexural steel.

The method assumes at a crack location, strain is perpendicular to the crack—no aggregate interlock or shear transfer along the interface is assumed. In this respect, the only stresses that are formed at the crack are in the longitudinal and transverse steel. In addition to pure tensile stresses, Zararis assumes the reinforcement also undergoes shear deformations. By

orienting the stresses at the crack location from those perpendicular to the crack to a vertical and horizontal direction, the stresses can be as shown in Equation [2.135].

$$\begin{bmatrix} \sigma_{sx} & \tau_{sxy} \\ \tau_{syx} & \sigma_{sy} \end{bmatrix} = E_s \varepsilon_{cr} \begin{bmatrix} \cos^2 \varphi & 0.4 \sin \varphi \cos \varphi \\ 0.4 \sin \varphi \cos \varphi & \sin^2 \varphi \end{bmatrix} \quad \text{Zararis} \qquad [2.135]$$

Where E_s (MPa) is the modulus of elasticity of the steel, ε_{cr} is the strain perpendicular to the crack, and φ is the angle between the crack and the vertical. After the formation of the critical shear crack, Zararis uses moment equlilibirum to calculate the depth of the compression zone above the crack. The sequence of failure of a deep beam with transverse reinforcement proposed by Zararis assumes the transverse steel yields, which causes an increased shear force V_d which must be compensated by the flexural steel. Once the flexural steel is exhausted, a horizontal crack will form at the location of the flexural steel and the increased shear force V_d will begin to decrease. At which point the forces in the compression zone become too great and crushing of the concrete in this area begins. By taking a free body of the forces acting on the top and bottom half of the wedge shape, the ultimate shear strength of the section is as denoted in Equation [2.136] below.

$$V_u = \frac{bd}{a/d}\left[\frac{c_s}{d}\left(1 - 0.5\frac{c_s}{d}\right)f_c' + 0.5\rho_v f_{yv}\left(1 - \frac{c_s}{d}\right)^2\left(\frac{a}{d}\right)^2\right] \quad \text{Zararis} \qquad [2.136]$$

Where b (mm) is the width of the web, d (mm) is the effective depth of the section, a (mm) is the length of the shear span, f_c' (MPa) is the compressive strength of the concrete, ρv is the ratio of the transverse steel, f_{yv} (MPa) is the yield strength of the transverse reinforcement, and c_s (mm) is the reduced depth of the compression block, defined in Equation [2.137] below.

$$\frac{c_s}{d} = \frac{1+0.27R(a/d)^2}{1+R(a/d)^2}\frac{c}{d} \qquad \text{Zararis} \qquad [2.137]$$

Where R is denoted in Equation [2.138] and the c/d term is derived from a second degree polynomial, shown in Equation [2.139]; the remaining terms have previously been defined..

$$R = 1+(\rho_v/\rho)(a/d)^2 \qquad \text{Zararis} \qquad [2.138]$$

$$\left(\frac{c}{d}\right)^2 + 600\frac{\rho}{f_c'}\frac{c}{d} - 600\frac{\rho}{f_c'} = 0 \qquad \text{Zararis} \qquad [2.139]$$

2.2.7 Post-Tensioning (Bent Cap Specimen Only)

The use of post-tensioning for repair of concrete structures is limited in the literature mainly toward flexural repair. However, Aravinthan and Suntharavadivel published a paper in 2007 regarding the post-tensioning of bent cap specimens as a shear repair method [Aravinthan and Suntharavadivel 2007]. The paper is divided into two sections—the first focused on the testing of a quarter scale single column cantilever bent cap while the second investigated a quarter scale model for the repair of an existing two column bent cap. Both portions of the experimental work included a control specimen loaded to failure without repair and two additional specimens loaded to what the authors denote as failure, although no qualifying criteria is given for the definition. After preloading, the force was removed from the specimen, a post tensioning force was applied, and the specimens were loaded to failure. The tapered bent cap had dimensions 250 mm (9.8 in.) wide with a varying depth

of 400 mm (15.7 in.) at the heel tapering to 350 mm (13.8 in.) at the toe and a shear span of 750 mm (29.5 in.) resulting in an a/d value of 2.2. The two-column bent cap had dimensions 220 mm (8.6 in.) wide, 420 mm (16.5 in.) deep, and a 395 mm (15.5 in.) shear span resulting in an a/d value of 1.0. Details of the two specimens are shown in Fig. 2.17 and 2.18 respectively.

For the tapered rectangular cantilever bent cap, the test setup included an active load cell placed on one end of the cantilever with a passive constraint consisting of two channel sections anchoring the adjacent cantilever end. The control specimen failed at a load of 149 kN (33.5 kip). The second specimen was preloaded to 135 kN (30.3 kip), experiencing a maximum shear crack width of 2 mm (0.08 in.), unloaded, a post tensioning force of 150 kN (33.7 kip) was applied reducing the crack width to 0.5 mm (0.02 in.), and the specimen failed at a load of 180 kN (40.5 kip). For the third specimen, it was again preloaded to 135 kN (30.3 kip), experiencing the same 2 mm (0.08 in.) shear crack width, unloaded, a post tensioning force of 300 kN (67.4 kip) was applied although the maximum crack width reduced to 1mm (0.04 in), and the specimen failed at a load of 105 kN (23.6 kip), or 30 kN (6.7 kip) less than the preload force. The authors contribute the lack of strength gain to the crack inclination and width. According to their analysis, the shear capacity of a section is governed by aggregate interlock and the ability of the concrete along the interface to prevent sliding of the two rigid bodies along the crack. As the angle of the crack decreases and the crack width increases, the shear capacity is reduced. For the third specimen, the crack width was only reduced to 1 mm (0.04 in.) during post tensioning, even though the post tensioning force was doubled. In order to further test the third specimen, the failure

crack was injected with a two part epoxy, permitted to cure, then the specimen was retested to a failure load of 201 kN (45.2 kip).

The second part of the experimental study included the quarter scale testing of the Tenthill Creek Bridge, which was slated for external post-tensioning as the repair method. The bridge consists of two columns at each end of the rectangular bent with four girders resting on bearing pads on top of the cap. The first interior girder was modeled in the laboratory, thus creating two unequal shear spans with 1.2 and 2.9 shear span to depth (a/d) ratios respectively. As in the first investigation, the control specimen was loaded until a shear crack formed in the shorter span with loading continuing until failure, at a load of 366 kN (82.3 kip). The control specimen failed in the larger shear span by diagonal tension. The second specimen was preloaded to 250 kN (56.2 kip), unloaded, a post tensioning force of 239 kN (53.7 kip) was applied, and failure occurred from diagonal tension in the shorter shear span at a load of 333 kN (74.9 kip). The ultimate load was lower than the control specimen, but was contributed to a lower concrete strength. The second specimen was further tested after epoxy injection and the same post tensioned force resulting in a shear compression failure within the shorter shear span at a load of 420 kN (94.4 kip). The third specimen was preloaded to 423 kN (95 kip), unloaded, epoxy injected, a post tensioning force of 245 kN (55.1 kip) was applied, and failure occurred at a load of 546 kN (122.7 kip) due to shear compression in the shorter shear span. The authors point to the different failure modes of the control specimen and the second specimen without epoxy injection as evidence that the use of epoxy injection changes the behavior and ultimately the capacity of the section in shear.

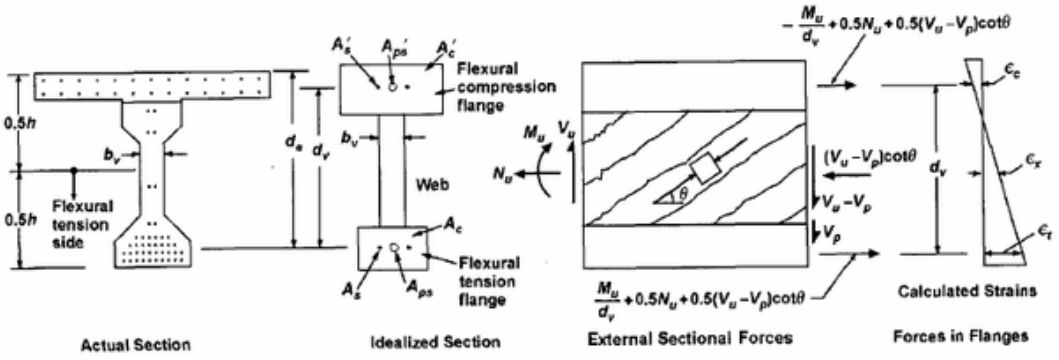

Fig. 2.1 AASHTO LRFD general approach for determining β and θ values

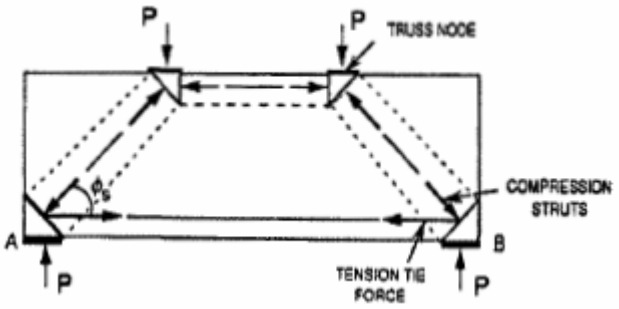

Fig. 2.2 AASHTO LRFD Strut-and-Tie component identification

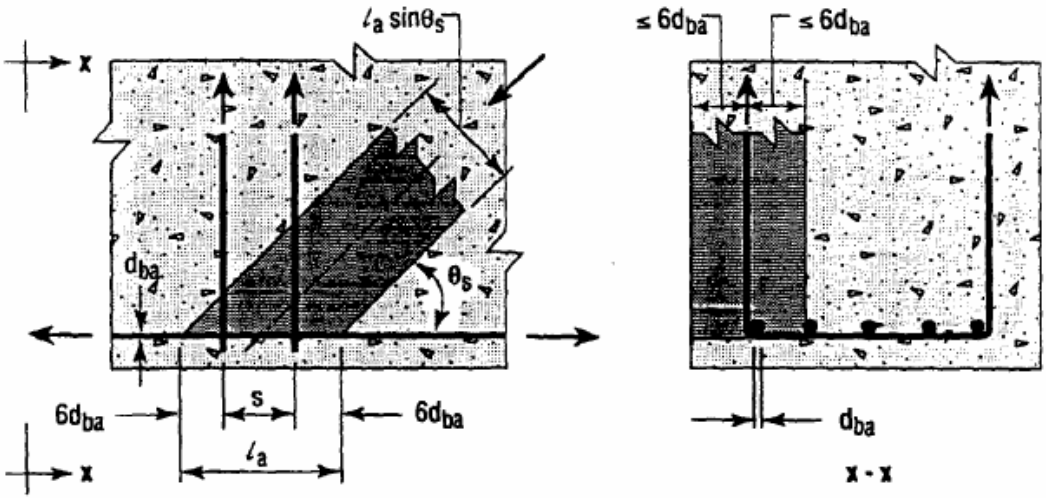

Fig. 2.3 AASHTO LRFD effective area of concrete strut anchored by reinforcement

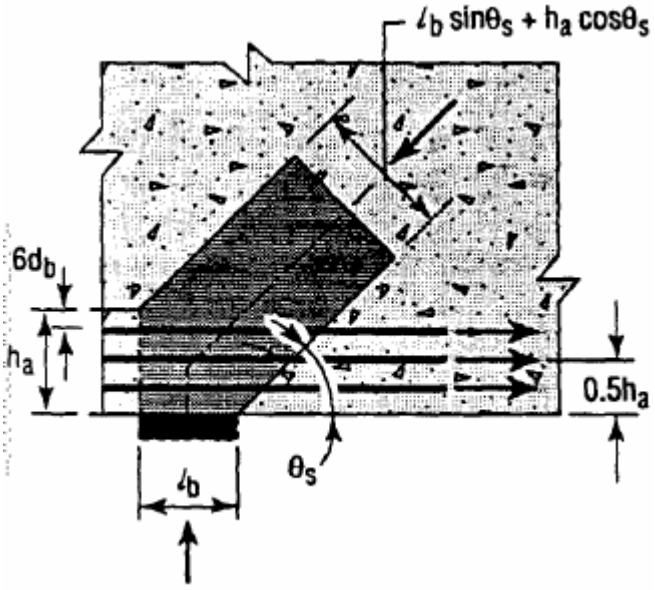

Fig. 2.4 AASHTO LRFD effective area of concrete for strut anchored by bearing and reinforcement

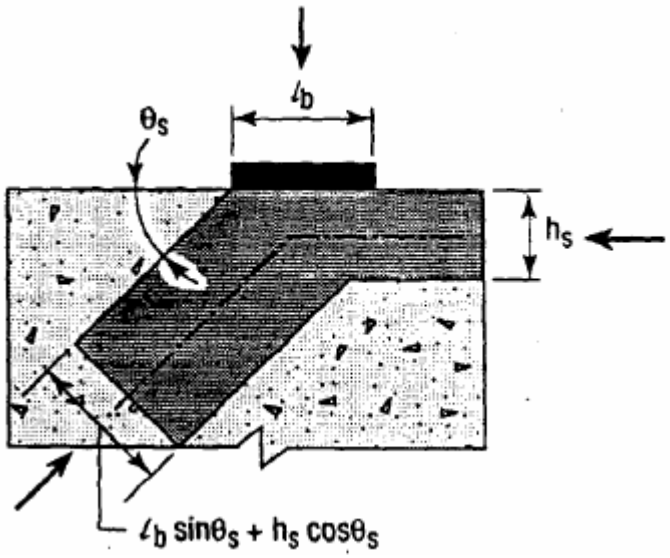

Fig. 2.5 AASHTO LRFD effective area of concrete for strut anchored by bearing and struts

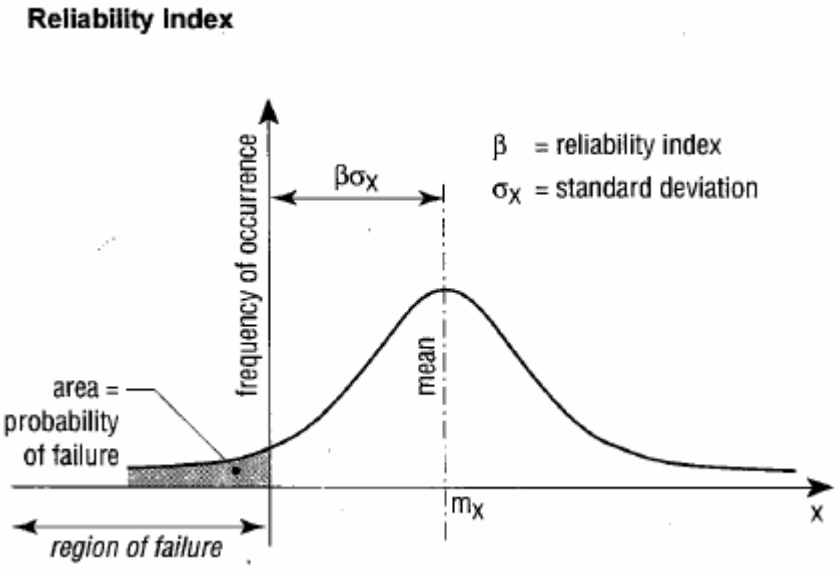

Fig. 2.6 Canadian code reliability index against failure

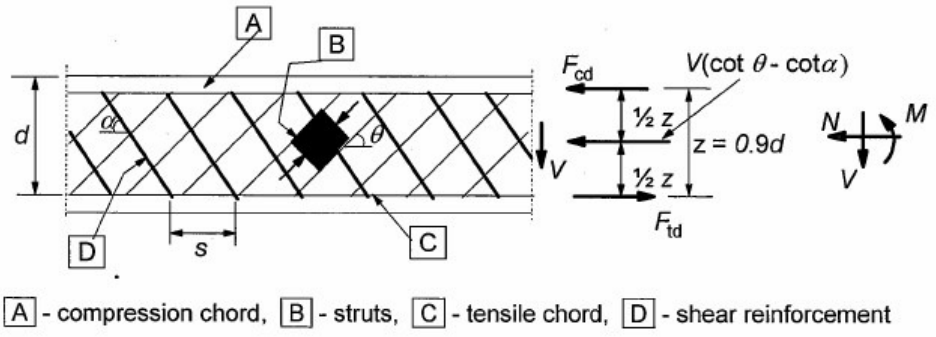

Fig. 2.7 Eurocode 2 ultimate limit state truss model analogy

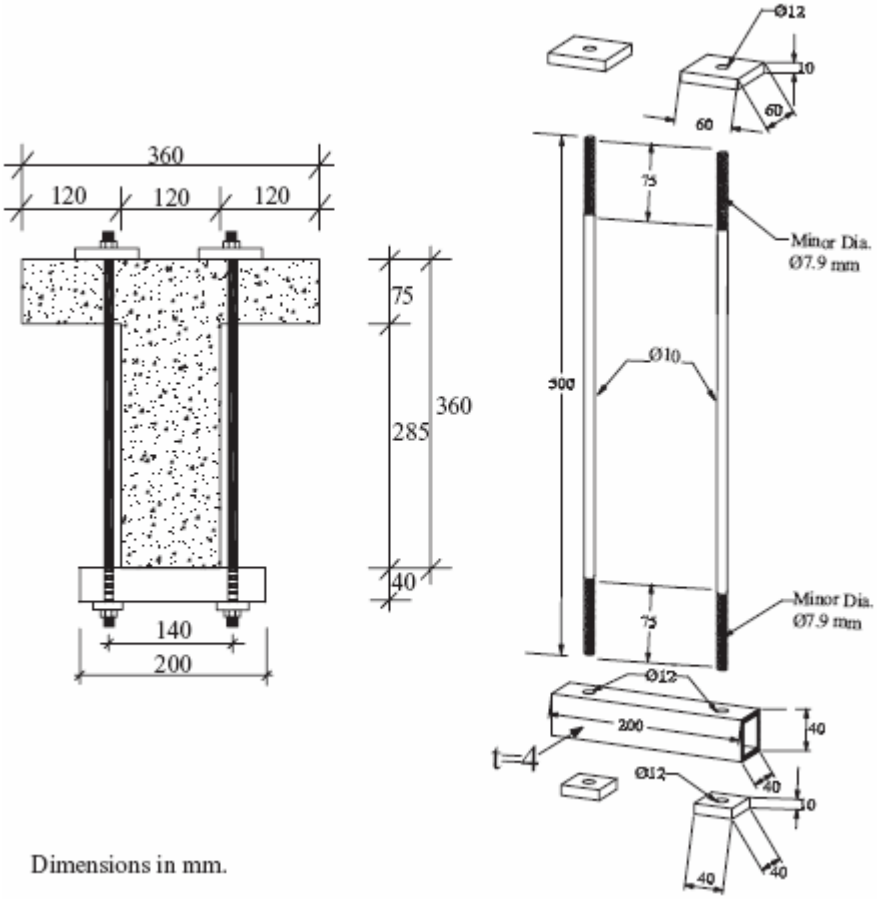

Fig. 2.8 External stirrup repair scheme from Altin, *et al.*

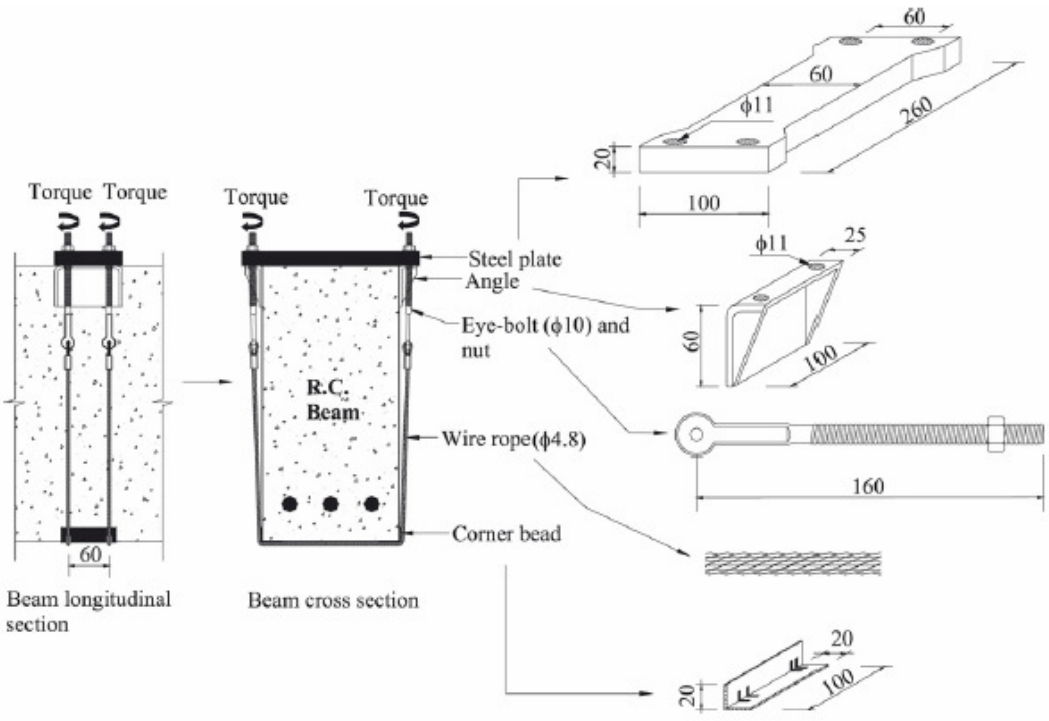

Fig. 2.9 External stirrup repair scheme from Kim, *et al.*

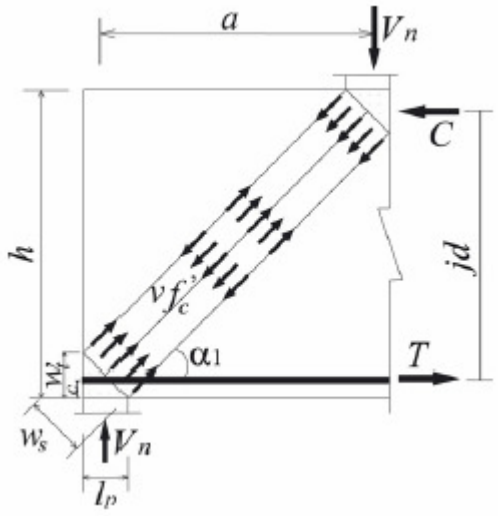

Fig. 2.10 External stirrup repair model for deep beams taken from Kim, *et al.*

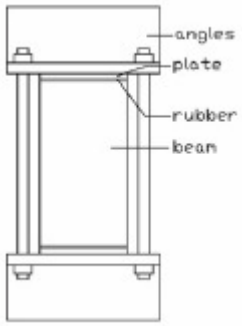

Fig. 2.11 External stirrup repair scheme from Shamsai, *et al.*

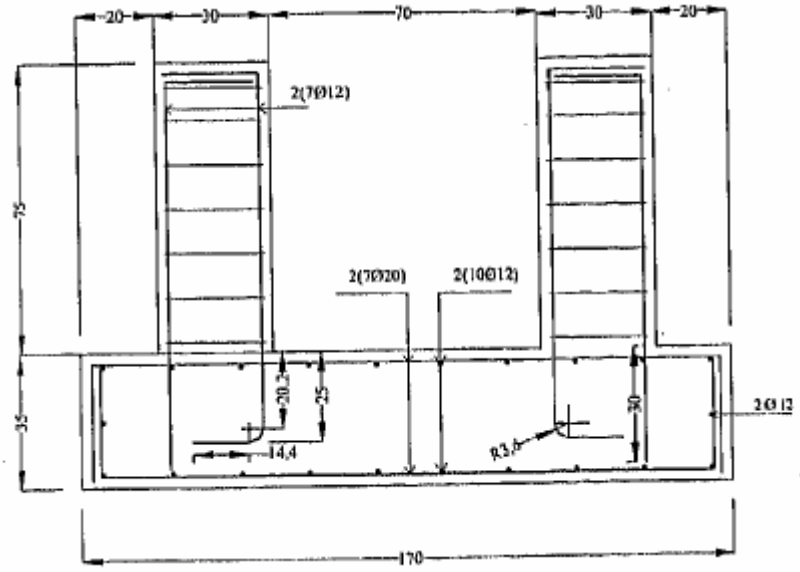

Fig. 2.12 Test setup for post installed anchors taken from Hammad *et al.*

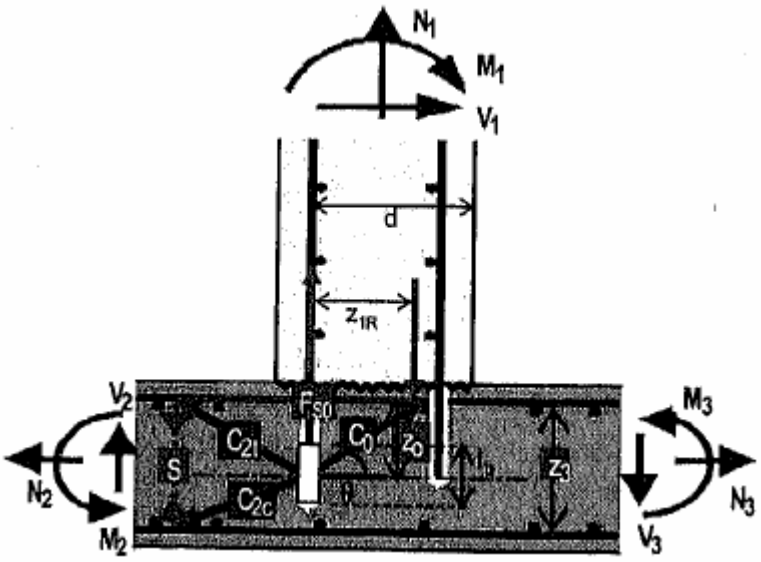

Fig. 2.13 Force diagram for post installed anchors taken from Hammad *et al.*

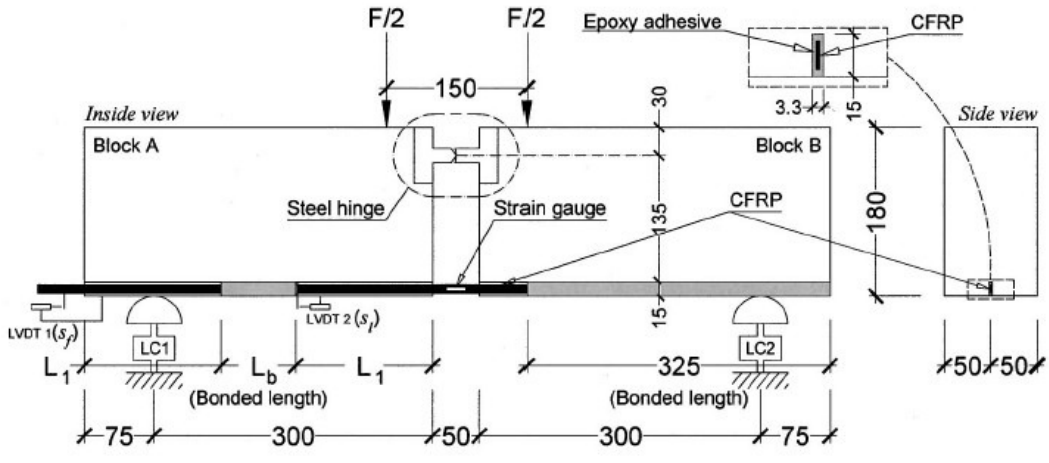

F

Fig. 2.14 Near Surface Mount beam type pullout test setup taken from Cruz and Barros

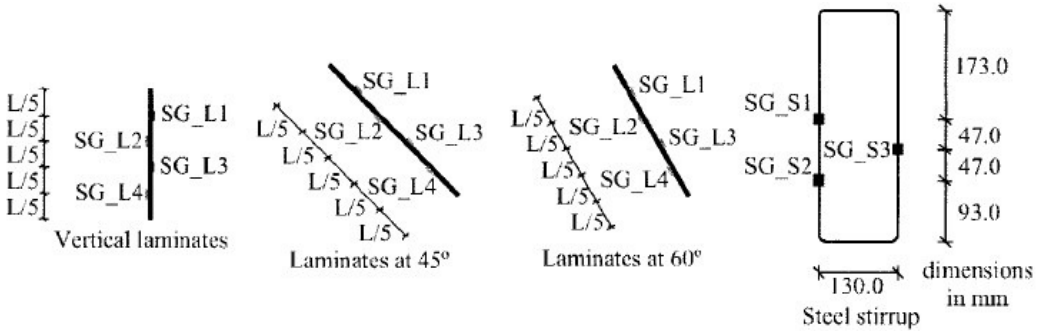

Fig. 2.15 Instrumentation of CFRP taken from Cruz and Barros

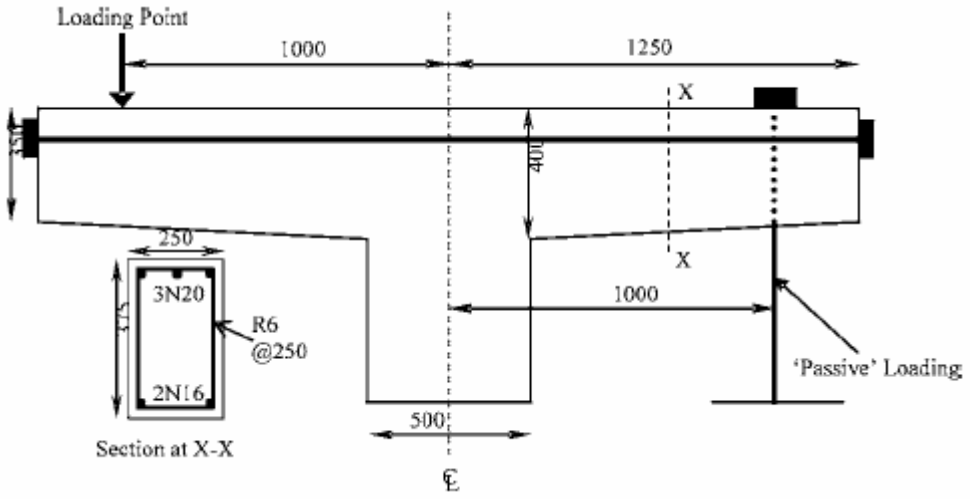

Fig. 2.16 Deep beam specimen 1 details taken from Aravinthan and Suntharavadivel

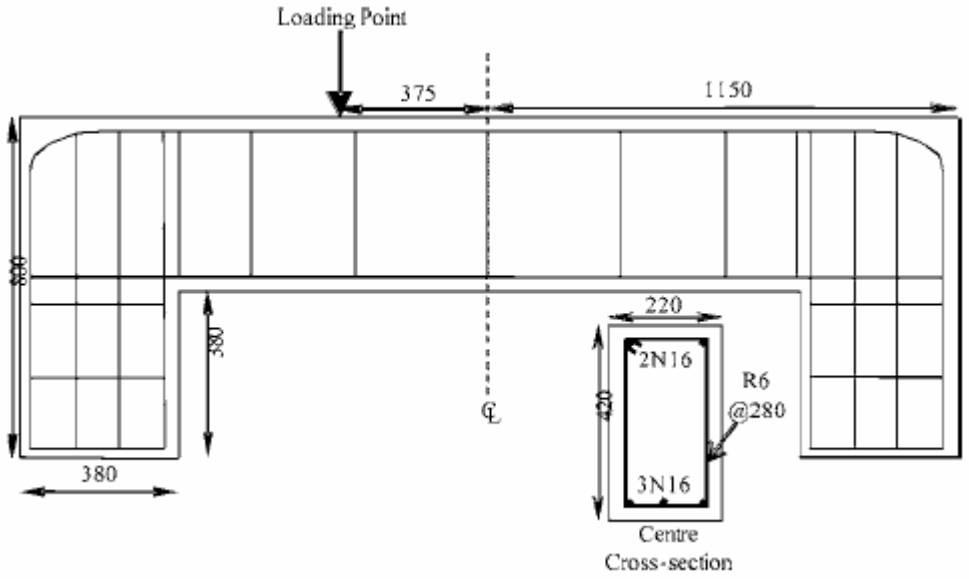

Fig. 2.17 Deep beam specimen 2 details taken from Aravinthan and Suntharavadivel

3. EXPERIMENTAL MATERIALS AND METHODS

To evaluate the various shear repair methods described in Chapter 2, an experimental research program was implemented which included design of full-scale specimens, instrumentation, construction, and application of each repair type. Repair for the beam specimens included surface bonded carbon fiber reinforced plastic (CFRP) strips, external supplemental steel stirrups, internal supplemental steel stirrups, and carbon fiber tape in a near surface mount (NSM) application while the bent cap specimens were repaired with surface bonded CFRP strips and longitudinal post tensioning. Once cast, the specimens were loaded to produce initial diagonal cracking, unloaded, repaired by the previously mentioned methods, and then tested to failure. The specimen descriptions, design, construction, and material property designations for base specimens are presented followed by specific details of each repair method—including repair installation procedures, testing protocol, and instrumentation for the test beams and bent caps.

3.1. Specimen Identification

To readily identify the specimens used in the current study, the following convention is used, with reference to Fig. 3.1. The first letter identifies the repair specimen as either a Beam (B) or a Deep Beam (D). The second term indicates if the specimen is tested such

that the deck is placed in flexural compression (T) or in flexural tension (IT). The third term differentiates beams that have flexural tension cutoff details located within the shear span (C) from specimens which have fully developed flexural bars within the shear span (NC). The final term designates the repair medium for each specimen. The abbreviations are: CF for surface bonded CFRP strips, ES for external steel stirrups, IS for internal steel stirrups, NS for Near Surface Mount CFRP tape, and PT for post tensioning (bent cap specimen only). Table 3.1 indicates the tests matrix for the specimens in the current study.

Table 3.1 Specimen Test Matrix

Specimen Identification:	Type:	Flexural Cutoffs?	Precrack Shear		Repair Type:
			kN	kip	
B.IT.NC.ES	IT Beam	No	556	125	External Stirrups
B.IT.C.ES	IT Beam	Yes	445	100	External Stirrups
B.IT.NC.IS	IT Beam	No	445	100	Internal Stirrups
B.IT.C.IS	IT Beam	Yes	445	100	Internal Stirrups
B.IT.NC.CF	IT Beam	No	445	100	CFRP Strips
B.IT.NC.NS	IT Beam	No	445	100	FRP NSM
B.T.NC.ES	T Beam	No	445	100	External Stirrups
B.T.NC.IS	T Beam	No	445	100	Internal Stirrups
D.IT.C.CF	Deep Beam	Yes	890	200	CFRP Strips
D.IT.C.PT	Deep Beam	Yes	890	200	Longitudinal PT

3.2. Specimen Design

3.2.1. Beam Specimen Design

Beam specimens were designed to reflect the anchorage details and relative specimen sizes indicative of 1950s vintage highway bridges [Higgins, *et al.* 2004a]. Beams used in the study were full scale, designed to place the deck in either flexural compression—denoted as a T beam—or in flexural tension—denoted as an inverted T (IT) beam. These conditions replicate shear in the presence of positive moment, typical of a bridge girder near an abutment, or shear in the presence of negative moment, typical of a bridge girder near an interior support. The T beams were designed with stirrups spaced at 607 mm (24 in.), or h/2, while the IT beams were designed with 457 mm (18 in.) stirrup spacing. In each case, the repaired beams were designed to fail in a shear dominated mode. Specimens with the NC designation contained fully developed flexural steel within the shear span. Specimens B.IT.C.ES and B.IT.C.IS, representing external and internal supplemental steel stirrup repairs, were cast with two flexural cutoff bars cutoff within the shear span to investigate the performance of the repair method in the presence of an abrupt decrease in flexural steel, as is typically encountered for older bridge girders. The specimens had a 1219 mm (48 in.) overall height, with a flange width of 914 mm (36 in.), a web width of 356 mm (14 in.), and a flange thickness of 152 mm (6 in.). Beam specimens were cast to a total length of 7925 mm (312 in.); the shear span of the T beams was 2896 mm (114 in.)

while the IT beams had a shear span of 2997 mm (118 in.) corresponding to a span-to-depth ratio of 2.5 and 2.6 respectively. Typical T and IT beam elevations are shown in Fig. 3.2, with typical sections shown in Fig. 3.3.

Support conditions for the beam specimens were similar for both T and IT specimens. Both specimen types were supported on reaction beams with 102 mm (4 in.) wide plates, 51 mm (2 in.) diameter high strength steel rollers supporting the beams on 25 mm (1 in.) thick by 102 mm (4 in.) wide steel plates extending across the appropriate flange/web width. The T beam specimens were supported laterally at the support locations by steel column sections attached to the reaction beams and rollers that permitted end rotations under positive moment but prevented out of plane movement. Load was applied by a single actuator at midspan, by way of a spreader beam, with loading points offset 305 mm (12 in.) from midspan of the beam. Capture plates were welded to the underside of the spreader beam, which was in turn supported on 51 mm (2 in.) diameter high-strength steel rollers and 102 mm (4 in.) wide steel plates in contact with the specimen. In order to assure a level bearing surface at the junction of the final steel plate and the concrete, Hydro-stone—a quick-setting gypsum cement with a dry compressive strength of 69 MPa (10 ksi)—was applied between the concrete surfaces and steel plates. The loading frame and support conditions are shown in Fig. 3.4

3.2.2. Bent Cap Specimen Design

Full-scale bent cap specimen design was based on previous work at Oregon State University; specimen dimensions, span lengths, flexural and transverse steel details, and utility hole opening locations were based on a review of existing bent caps within Oregon Department of Transportation's (ODOT) bridge inventory. The bent cap specimens were designed as single span beams with four girders framing into the bent. The two exterior girder loads were assumed to be transmitted directly into the columns and were not included in the experimental setup while the two interior girders provided load into the cap from the adjacent longitudinal spans. Thus, the cap beam was loaded indirectly from the two interior girders in the form of a shortened stub section, not directly loaded on the cap beam itself. The specimen dimensions are as follows, with reference to Fig. 3.5 and 3.6: columns were 610 mm (24 in.) square, the cap beam was 1829 mm (72 in.) deep by 406 mm (16 in.) wide with a span-to-overall height ratio of 1.33. The overall specimen length was 7925 mm (312 in.) with a 6706 mm (264 in.) length excluding the columns. The stub girders were 1219 mm (48 in.) deep with a 357 mm (14 in.) by 406 mm (16 in.) cross sectional area.

Support conditions for the bent cap simulated those of an externally determinant rigid frame. The square concrete columns, which extended a distance of 610 mm (24 in.) down from the bottom of the cap beam, were cast onto single 25 mm (1 in.) thick steel plates

with identical cross sectional area. One column was supported by a 51 mm (2 in.) diameter high strength steel roller placed on a slightly curved 38 mm (1.5 in.) steel plate. The steel plate for the second column was welded to a series of slightly larger perimeter steel plates such that the column bases could translate relative to one another and also rotate. The stub girders were supported laterally with vertical rollers to restrict out of plane motion. The columns were also supported laterally at the same elevation as the stub girders, as shown in Fig. 3.7. Also, the loading frame was braced laterally out of plane with steel channel sections anchored to the strong floor.

Since the bent cap was loaded through each individual stub girder, two actuators and associated reaction beams were required. A capture plate mounted to the underside of the actuator was supported by a single 51 mm (2 in.) diameter high strength steel roller and 102 mm (4 in.) wide by 25 mm (1 in.) thick plate bearing on the top midpoint of the reaction beams. This was to ensure free rotation of the reaction beam within the plane of the stub girders. A second set of capture plates, similar to those used for the beam specimens, were welded to the underside of the reaction beams at the location of the stub girders, supported on 51 mm (2 in.) diameter high strength steel rollers, and corresponding 102 mm (4 in.) wide by 25 mm (1 in.) thick steel plates in bearing with the top of the stub girders. As with the beam specimens, the plates in contact with the top of the stub girders were leveled utilizing Hydro-stone gypsum cement.

The column reinforcing cage consisted of Grade 420 MPa (60 ksi) #36 (#11) corner bars with Grade 420 MPa (60 ksi) #10 (#4) ties at 102 mm (4 in.) within the isolated column section, with 203 mm (8 in.) spacing throughout the beam height, as shown in Fig. 3.5. The longitudinal column bars were welded to the base plates.

The flexural steel configuration followed the work of previous bent cap specimens, consisting of three cutoff locations within the shear span. The flexural steel was placed in three layers, with a 4-4-2 bar configuration, from the bottom of the cap beam. Previous test results showed the specimen with two bottom bars extending into the column provided the lowest overall strength [Senturk and Higgins 2008]. Thus, the two outer bars within the bottom layer extending into the column were selected for the repair specimens. For this scenario, the remaining two bars within the bottom layer terminated at the face of the column. The second layer of reinforcing included two outer bars terminating at the face of the column, while the two inner bars were placed at 2679.5 mm (105.5 in.) from the centerline of the bent. The top layer of flexural steel included two outer bars at 2146.5 mm (84.5 in.) from the centerline of the bent.

In addition to flexural details, the repaired bent caps reflected similar stirrup details to the previous work at OSU. In the previous study, the stirrup size and grade varied from Grade 280 MPa (40 ksi) #13 (#4) to Grade 420 MPa (60 ksi) #16 (#5) with a consistent 222 mm (8.75 in.) average spacing. Thus, to replicate the weakest specimen from the previous

work, Grade 280 (40 ksi) #13 (#4) stirrups at 222 mm (8.75 in.) spacing were used in the current study.

The indirect loading of the bent cap required heavily reinforced stub girders to ensure failure occurred within the shear span. As such, the stub girders consisted of Grade 420 MPa (60 ksi) 16 (#5) horizontal and #19 (#6) vertical closed ties.

3.3. Materials and Repair Schemes

The materials selected for each repair method were based on products that were readily available, representative of similar products, and pre-approved by state transportation agencies. Application of each individual repair method followed the manufacturer's recommendations and/or the advice of suppliers and approved contractors. Material tests of the repair media as well as traditional steel and concrete materials were included for each specimen.

3.3.1. Concrete

Concrete was provided by a local ready-mix supplier for both beam and bent cap specimens. The mix design was based on 1950's AASHO "Class A" concrete used in previous research at OSU [Higgins, *et al.* 2004a] with a specified minimum compressive strength of 21 MPa (3000 psi)—similar to the design strength of the original in-service bridges. Actual concrete compressive strengths varied across the test matrix. Tensile and compressive strengths were based on ASTM C39M/C 39M-05 and ASTM C617-05 completed on 152 mm (6 in.) diameter, 305 mm (12 in.) deep cylinders. Compressive concrete strength calculations for the beam specimens were completed at 7, 14, and 28 days after casting, while bent cap concrete strength was documented at a closer interval in order to complete repaired testing at a strength close to the 21 MPa (3000 psi) compressive strength—which occurred at an average of 20-25 days after casting. Tensile and compressive concrete strengths were also determined on the day of test for both precrack and failure tests. Results of the concrete compressive and tensile strengths as previously described are shown in Table 3.2.

The aggregate composition for the mix was reported by the supplier as: 97% passing the 19 mm sieve (3/4 in.), 82% passing 16 mm (5/8 in.), 57% passing 12.5 mm (1/2 in.), 33% passing 9.5 mm (3/8 in.), 21% passing 8 mm (5/16 in.), 9.3% passing 6.3 mm (1/4 in.), 3.0% passing 4.75 mm (#4), 0.6% passing 2.36 mm (#8) and 0.3% passing the 0.075 mm

(#200) sieve. The sand composition of the mix was also reported as: 99.7% passing the 6.3 mm sieve (1/4 in.), 96.8% passing 2.36 mm (#8), 59.4% passing 1.18 mm (#16), 44.9% passing 0.600 mm (#30), 17.9% passing 0.300 mm (#50), 3.7% passing 0.150 mm (#100) and 1.7% passing the 0.075 mm (#200) sieve. The coarse aggregate was from Willamette River bed deposits consisting of smooth rounded basaltic rock.

Table 3.2 Concrete properties

Specimen:	7 Day Compressive Strength		14 Day Compressive Strength		28 Day Compressive Strength		Precrack:				Repair:			
							Days since cast	Compressive Strength:		Tensile Strength:		Days since cast	Compressive Strength:		Tensile Strength:	
	kPa	psi	kPa	psi	kPa	psi		kPa	psi	kPa	psi		kPa	psi	kPa	psi
B.IT.NC.ES	19095	2769	22559	3272	25489	3697	81	25938	3762	2707	393	98	26359	3823	2338	339
B.IT.C.ES	14350	2081	17618	2555	21687	3145	104	20440	2965	1555	226	104	20440	2965	1555	226
B.IT.NC.IS	19000	2756	19875	2883	26642	3864	103	24726	3586	2278	330	138	26783	3884	1960	284
B.IT.C.IS	16197	2349	23900	3466	23804	3452	145	24442	3545	2087	303	154	24854	3605	1795	260
B.IT.NC.CF	16659	2416	20901	3031	26303	3815	80	26350	3822	2342	340	109	27376	3970	2266	329
B.IT.NC.NS	14988	2174	19435	2819	20765	3012	175	25637	3718	2266	329	222	23019	3338	2236	324
B.T.NC.ES	19318	2802	24912	3613	28845	4184	122	32660	4737	2268	329	125	31814	4614	2678	388
B.T.NC.IS	14990	2174	20144	2922	23969	3476	131	27529	3993	2294	333	150	26394	3828	2510	364
D.T.C.PT	17444	2530	21169	3070	-	-	19	22919	3324	2396	348	19	22919	3324	2396	348
D.T.C.CF	-	-	-	-	-	-	8	8612	1249	1373	199	24	15534	2253	1693	246

3.3.2. Mild Steel

All mild reinforcing steel used in the experimental program met the spacing and deformation requirements of ASTM 615/615M-05a (2005), while selection of the steel was based on an intermediate—280 MPa (40 ksi)—grade used in the original beams. The lower grade steel posed a problem, since the steel industry has since migrated to a 420 MPa (60 ksi) standard grade bar. A solution was presented by permitting only the stirrup steel to be designated Grade 280 (40 ksi), with the remainder of the mild steel designated Grade 420 (60 ksi). A local steel producer provided a single heat of the Grade 280 (40 ksi), #13 (#4) for all of the stirrups used in the beams and bent caps. Flexural steel consisted of Grade 420 (60 ksi) #36 (#11). The actual tensile properties of the steel bars were based on testing outlined in ASTM A370-97a utilizing a 489 kN (110 kip) capacity hydraulically controlled universal testing machine under displacement control of 0.0169 mm/sec (0.000667 in./sec). The large diameter #36 (#11) bars exceeded the capacity of the testing frame, thus they were machined down to a 13 mm (0.5 in.) diameter coupons with threaded ends and tested in accordance with ASTM E8-00. Strain in the bar was measured with a class B1 extensometer with a 50 mm (2 in.) gage length. Tensile properties for beam and bent cap reinforcing steel are shown in Table 3.3.

Table 3.3 Reinforcing steel properties

Specimen:	#36 (#11) 420 Mpa (60 ksi) Bar					#13 (#4) 280 Mpa (40 ksi) Bar				
	Yield Strength		Ultimate Strength		% Strain at Failure	Yield Strength		Ultimate Strength		% Strain at Failure
	Mpa	ksi	Mpa	ksi		Mpa	ksi	Mpa	ksi	
Beam	468.1	67.9	710.8	103.1	23.9	343.4	49.8	541.9	78.6	28.4
Bent Cap	458.0	66.4	706.0	102.4	22.5	343.1	49.8	541.8	78.6	27.6

3.3.3. External Stirrup Repair

The materials used for the external stirrup steel threaded rod repair were based on a repair of a bent cap on an in-service bridge located in Salem, Oregon. The repair consisted of two C152 X 16 (C6 X 13) sections anchored by 724 MPa (105 ksi) steel threaded rod meeting the requirements of ASTM A449. The superstructure of the bridge consisted of steel girders supported on bearing assemblies atop the reinforced concrete cap beam, thus there was no interference with an integral concrete diaphragm at the pier location. The aim of the current study was to assess the performance of this repair technique within the laboratory environment. Thus, ASTM A449, 13 mm (0.5 in.) diameter threaded rod was chosen to anchor the previously described channel sections on a typical beam repair specimen. The remainder of the apparatus consisted of ASTM A36 5mm (2 in.) square by 6 mm (0.25 in.) thick plate washers, ASTM F436-1 25 mm (1 in.) outer diameter (OD) round washers, and ASTM A194-2H heavy hex nuts, as shown in Fig. 3.8. During the analysis phase of the repair method, the stiffness of the supporting steel sections was

considered important to performance. As a result, both the channel sections and a W6X20 section under weak axis bending with a moment of inertia 13 times stiffer than that of the channel section as shown in Fig. 3.9 were investigated. However, the initial test setup for the W section placed the steel web in local bending between the flanges, resulting in a similar performance compared to the channel section as will be seen in Chapter 4. A third test setup for the external stirrup repair was then used, as shown in Fig. 3.10, resulting in a significantly stiffer section. Material tests for the threaded rod were performed as outlined in Section 3.3.2, and presented in Table 3.4. Elevation views of the repair schemes for beams B.IT.NC.ES, B.IT.C.ES, and B.T.NC.ES are shown in Fig. 3.11 through 3.13 respectively.

Table 3.4 External stirrup reinforcing steel properties

External Stirrup Steel	Yield Strength		Ultimate Strength		% Strain at Failure
	Mpa	ksi	Mpa	ksi	
	581.2	84.3	621.9	90.2	8.3

3.3.4. Internal Supplemental Stirrup Repair

Materials for the supplemental internal stirrup repair were chosen with the assistance of a contractor who successfully installed the repair method on several Oregon bridges. This

approach was beneficial because it replicated the repair method both in terms of materials used and installation technique. The primary obstacle regarding the use of this method was the insertion point of the steel—either from the deck down or from the bottom of the beam up. The former method has the drawback of restricting traffic on a bridge which may be cost prohibitive on a heavily traveled truck route, but has the advantage of epoxy flowing with gravity. The latter method is more attractive in terms of lane closures, but may require temporary supports below the bridge to support the worker and equipment. In addition, the problem of injecting a crack against gravity posed a significant installation issue. The solution posed by the contractor was to use a high strength steel reinforcing bar with a void through the center such that epoxy could be injected through the center hole eventually exiting through the void space between the bar and the concrete. Thus, the steel used for the internal stirrup repair was high strength 627 MPa (91 ksi) hollow steel rod meeting the height and deformation requirements of ASTM 615/615M-05a (2005) with an outer diameter of 25 mm (1 in.) and 484 mm^2 (0.75 $in.^2$) cross sectional area. The typical section for the IT internal stirrup repair is shown in Fig. 3.14. After subsequent use in the two IT specimens, it was apparent that the large diameter, high strength bars would not be suitable for the T beam repair (i.e. possibly forcing a flexural failure). Therefore, traditional ASTM A615 deformed grade 420 (60 ksi) size #19 (#6) steel rebar was used for the T beam repair. Elevation views of the repair schemes for beams B.IT.NC.IS, B.IT.C.EI, and B.T.NC.IS are shown in Fig. 3.15 through 3.17, respectively.

The high strength and mild steel bars were subjected to uniaxial tensile tests as well as pullout tests with the same epoxy to determine ultimate strength of the bars and qualitative bond properties of the repair system. Tension tests on the 627 MPa (91 ksi) hollow rod and grade 420 (60 ksi) mild steel specimens were performed as outlined in Section 3.3.2 and are shown in Table 3.5. The pull-out tests were performed to indicate the embedment length required to reach yield. The process entailed coring a vertical hole within the beam, placing a premeasured amount of epoxy within the hole, placing the reinforcing bar in the hole, and anchoring it in the vertical direction. The epoxy was allowed to cure for one week. After curing, a center hole actuator, load cell, and reaction plates were mounted concentrically with the bar. Then, a mechanical splice was placed around the bar and individual screws along the splice were torque to the manufacturer's specifications. The test setup is shown in Fig. 3.18. Three embedment lengths were used; the largest representing the distance from a 45 degree diagonal crack to the limit of the cross section (762 mm (30 in.)). The remaining two embedment lengths—254 mm (10 in.) and 508 mm (20 in.)—were chosen to represent typical lengths available at different positions along a diagonal crack.

Table 3.5 Internal stirrup reinforcing steel properties

Specimen:	Yield Strength		Ultimate Strength		% Strain at Failure
	Mpa	ksi	Mpa	ksi	
B.IT.NC.IS	468.1	120	468.1	155.2	19.3
B.IT.C.IS					
B.T.NC.IS	488.8	70.9	812.9	117.9	19.6

The results from the pullout tests provided general trends for the steel-epoxy-concrete system. Bar stress versus relative displacement for each of the three embedment lengths are shown Fig. 3.19 and 3.20 for the ASTM high strength 627 MPa (91 ksi) bar and 413 MPa (60 ksi) bar respectively. The shallowest embedment for the high strength rods resulted in a maximum bar stress of 374 MPa (54 ksi) prior to first slip. Slip continued until a shallow cone failure occurred prior to yield strength of the bar. The 508 mm (20 in.) embedment depth resulted in a bar stress of 528 MPa (77 ksi) prior to first slip, again failing to reach the yield strength of the internal stirrup. The final 762 mm (30 in.) embedment length achieved a bar stress of 737 MPa (107 ksi) and resulted in eventual fracture of the bar after strain hardening. For the lower strength ASTM A615 grade 60 bars, the bar diameter and yield stress were reduced, thus the 508 mm (20 in.) and 762 mm (30 in.) bars both achieved yield and strain hardening, although they were very ductile and did not reach ultimate strength. The shallowest embedment did not reach yield, with a maximum bar stress of 268 MPa (39 ksi) prior to first slip. The results of the pull out tests are presented in Table 3.6, although it is noted that the state of stress produced by the pull-

out specimens do not represent the true state of stress within the actual repaired beam and does not account for any possible dowel action that may help anchor the bars across a diagonal crack.

Table 3.6 Internal stirrup pullout tests data

	Specimen embedment depth:	Max bar stress:		Yield stress:	
		MPa	ksi	MPa	ksi
High strength bar	254 mm (10 in.)	434	63	813	120
	508 mm (20 in.)	618	90		
	762 mm (30 in.)	743	108		
Mild steel bar	254 mm (10 in.)	366	53	813	70.9
	508 mm (20 in.)	765	111		
	762 mm (30 in.)	638	93		

3.3.5. Surface Mounted CFRP Repair

Material used for the CFRP repair was provided by the Watson Bowman Acme Corporation (BASF) consisting of the Wabo® MBrace CF130 unidirectional carbon fiber fabric. In addition to the fabric, the manufacturer provided several additional products as part of the application procedure including a low viscosity epoxy primer, high viscosity epoxy paste, and finally an epoxy resin (saturant). Details of the application procedure are illustrated in Section 3.5.5.

A three sided U wrap repair scheme was selected with a wet lay up installation procedure for both the beam and bent cap specimen. For the IT beam in the current study, the three sided U wrap was placed such that the CFRP terminated at the stem-flange interface, which was under flexural tensile stresses, as shown in Fig. 3.21, whereas the CFRP for the bent cap specimen terminated at the stem-flange interface of the section under compressive stresses, as shown in Fig. 3.22. CFRP strips came from the manufacturer at 508 mm (20 in.) widths. The strips were reduced to 254 mm (10 in.) widths and placed on the beams with 51 mm (2 in.) wide gaps between strips resulting in a 305 mm (12 in.) center-to-center spacing between strips, as shown in Fig. 3.23. The same strip widths and spacing were adopted for the bent cap specimen, as shown in Fig. 3.24.

Material testing of the CFRP system consisted of direct tensile tests of CFRP fabric embedded with saturant as well as pull off tests to indicate the level of bond between the resin and concrete in the repaired specimen. Preparation of the CFRP tensile coupons coincided with application of the CFRP for the beam and bent cap respectively. During CFRP application, a 610 mm (24 in.) square sheet of CFRP was cut and placed on a larger perimeter non-stick Teflon plate, previously coated with saturant. Once the sheet was placed, it was impregnated with the use of a plastic putty knife and a second coat of saturant was applied to the CFRP. A second Teflon plate was placed over the sample, and the process was repeated until several CFRP sheets were assembled. After completion of

the samples, a large weight was placed atop the Teflon sheets and the apparatus was placed adjacent to the repaired specimen thus replicating the curing conditions of the CFRP.

The CFRP was permitted to cure for seven days, after which time the sheets were removed and prepared for testing. The 610 mm (24 in.) square sheet was reduced to an individual coupon size of 25 mm (1 in.) by 305 mm (12 in.) using a wet tile saw in order to conform to the testing requirements of ASTM D 3039/D 3039M. While great care was taken to trim the specimens to the correct size, cutting along the primary fiber direction resulted in slight variations among the individual coupons. As a result, the coupons with the best alignment of the cut edge to the fiber orientation were used for testing purposes. Fiberglass electronic boards measuring 25 mm (1 in.) wide by 57 mm (2.25 in.) long were cut and attached to the ends of the coupons with a cyanoacrolyte quick setting adhesive in an effort to reduce failure at the anchorage locations. Once completed, the coupons were tested utilizing a 89 kN (20 kip) hydraulically controlled universal testing machine under displacement control of 1.25 mm/min (0.05 in./min). Strain in the CFRP was measured with a class B extensometer with a 25 mm (1 in.) gage length. Results of the CFRP coupon tests, with comparison to the manufacturer's specifications, for the beam and bent cap repair are shown in Table 3.7.

Table 3.7 CFRP tensile test data

Property:	Wabo® Design	B.IT.NC.CF		D.IT.C.CF	
		Test Mean	Test Standard Deviation	Test Mean	Test Standard Deviation
Coupon Thickness	0.6 - 1.0	1.14	0.024	1.26	0.058
mm (in.)	[0.02-0.04]	[0.045]	[0.00095]	[0.05]	[0.00227]
Tensile Strength:	625 - 1042	707.5	36.5	538.7	11.1
Mpa (ksi)	[89 - 179]	[103]	[5.3]	[78]	[1.6]
Unit Strength:	0.625	1.3	0.063	1.1	0.038
kN/mm/ply (kip/in/ply)	[3.57]	[4.62]	[0.232]	[3.89]	[0.14]
Elastic Modulus:	37.4-62.4	36.7	4.6	32.9	1.1
Gpa (ksi)	[5300-10700]	[5325]	[667]	[4775]	[155]
Rupture Strain %:	1.67	1.94	0.147	1.6	0.046
Nominal Fabric	0.165	0.165	n/a	0.165	n/a
mm (in.)	[0.0065]	[0.0065]	n/a	[0.0065]	n/a
Tensile Strength*:	3800	4897	246	4125	149
Gpa (ksi)	[550]	[710]	[35.7]	[598]	[21.5]
Elastic Modulus*:	227	254	30.3	252	13.9
Gpa (ksi)	[33000]	[36846]	[4402]	[36577]	[2015]

*Based on nominal fabric dimensions

Direct tension pull off tests were performed after failure testing of the beam and bent cap specimens in accordance with ASTM D 4541-93: Standard Test Method for Pull-off Strength of Coatings Using Portable Adhesion Tester. Three pull off locations were chosen at random, lightly sanded, then chemically treated to provide a clean dry surface to attach a 51 mm (2 in.) square steel dolly with a high strength two part epoxy. After curing of the epoxy, the CFRP around the dolly was removed with a circular disc grinder, thus providing an equal surface area of the CFRP to the attached dolly. Next, a 1.6 kN (3000 lb) capacity manually operated portable testing machine was attached to the dolly and the test conducted to failure. The portable machine recorded the maximum load at failure and

the process was repeated at the remaining two locations. The average bond stress of the CFRP to the concrete was calculated based on the area of the dolly. All direct pull off tests indicate failure occurred within the concrete substrate and not within the epoxy resin. Results of the direct pull off are shown in Table 3.8.

Table 3.8 CFRP pull off test results

Specimen:	B.IT.NC.CF	D.IT.C.CF
Mean	2137	3546
KPa (psi)	[310]	[514]
Standard Deviation	461	547
KPa (psi)	[67]	[79]

3.3.6. FRP NSM Repair

The materials used for the NSM repair method were based on two criteria: limiting the bond thickness of the epoxy between the concrete and FRP and maximizing the surface area of FRP relative to the concrete. Within these requirements, a rectangular saw cut groove placed vertically along the web of the beams precluded the use of round NSM in favor of rectangular tape. Consequently, Aslan 500 rectangular tape manufactured by Hughes Brothers was chosen as the FRP material with a 3M DP460NS epoxy based on the work of Shield and French (2005) from the literature review. Typical section of the NSM repair is shown in Fig. 3.25. Spacing of the NSM relative to the anticipated failure crack

resulted in three strips per side of the beam within the shear span, as shown in Fig. 3.26. This ensured the two outer strips would participate with a partial development while the center strip, located equidistant from the anticipated failure crack would be fully developed at failure.

Tensile tests on the FRP were performed, with specimen preparation similar to that of the CFRP coupons noted in Section 3.3.5. Failures typically occurred from splitting longitudinal to the specimen at or within the grip. Consequently, the tensile strength was a bit lower than that reported by the manufacturer. However, the modulus values and corresponding % strain at failure were within the range of values shown. If a gripping failure would have been prevented, it is possible that the ultimate strength values would be more in line with the manufacturer's reported values. Results of the tensile tests are shown in Table 3.9 with comparison to the manufacturer's design values. Direct pull-off tests of the epoxy were performed on the concrete, similar to that of the CFRP specimens with failure occurring within the concrete substrate.

Table 3.9 NSM tensile test data

Property:	Hughes Bros. Reported Data	B.IT.NC.NS	
		Test Mean	Test Standard Deviation
Coupon Thickness	2	2	0.00
mm (in.)	[0.079]	[0.079]	[0.000]
Tensile Strength:	2068	1491	139
Mpa (ksi)	[300]	[216]	[16]
Elastic Modulus:	124	138.5	3.9
Gpa (ksi)	[18000]	[20082]	[568]
Rupture Strain %:	1.7	1.08	0.1

In addition to pull-off tests of the epoxy, direct tension pull out tests were performed at depths of 51 mm (2 in.), 102 mm (4 in.), and 152 mm (6 in.) to qualitatively show the strain in the FRP at different embedment depths. Two issues made the test setup more complex than the corresponding internal stirrup pullout test. The first obstacle involved loading a single embedded NSM tape eccentrically from the center line of the beam. The second condition related to gripping of the FRP, as a mechanical splice used in the internal stirrup pull out tests was not feasible. Therefore, a test setup was created to resolve the previously mentioned obstacles, with reference to Fig. 3.27. Loading of the FRP came from the center hole actuator used previously in the internal stirrup pull out tests, with a reaction section modified from the external stirrup apparatus. The 51 mm (2 in.) and 102 mm (4 in.) embedment depths were located on the same end of the beam, such that reacting on the W beam induced equal stress in the two embedment depths. Gripping of the

specimen was resolved by bonding two angle sections to the FRP with the same 3M DP460NS epoxy and reacting against the angle sections to induce stress in the FRP. The goal was to fail the 51 mm (2 in.) embedment first, then anchor the failed end with a threaded rod anchor. Then, the 102 mm (4 in.) side would be loaded to failure. The remaining 152 mm (6 in.) embedment was placed at another location along the beam, with the NSM located on one side and the threaded rod anchor on the opposite face.

The goals of the initial test for the 51 mm (2 in.) and 102 mm (4 in.) embedment lengths lead to unintended results. During the test, failure of the 51 mm (2 in.) embedment resulted in a rapid release of energy that sent the reaction section in a clockwise motion in the direction of the 102 mm (4 in.) embedment depth, resulted in fracture of the 102 mm (4 in.) embedment FRP. Therefore, additional testing of the 102 mm (4 in.) embedment was not possible. The strain data from the first test indicate a slight eccentricity of the load resulting in a higher force in the 102 mm (4 in.) embedment length.

Testing of the single 152 mm (6 in.) side resulted in a similar failure mode to the previous embedment lengths. Recall from Fig. 3.28 that the NSM was anchored on one side of the beam and the opposite side was anchored by a threaded rod. A wedge type failure in the concrete resulted in a rapid release of energy thereby permanently deforming the threaded rod anchor. A plot of the bar stress versus displacement is shown in Fig. 3.27 for all three embedment lengths. For the 152 mm (6 in.) embedment, the sensor for recording the

displacement of the NSM reached its maximum value prior to failure of the wedge; therefore the plot in Fig. 3.27 which indicates a higher stress for a fixed displacement is not an accurate representation of the test outcome. Results of both the pull off and pull out tests are presented in Table 3.10.

Table 3.10 NSM pull off and pullout test results

Specimen:		B.IT.NC.NS	
Pulloff Tests	**Mean**	3076	
	KPa (psi)	[446]	
	Standard Deviation	264	
	KPa (psi)	[38]	
Pullout Tests	**Embedement Depth**	**Max Stress**	
	51 mm (2 in.)	462 MPa	[67 ksi]
	102 mm (4 in.)	565 MPa	[82 ksi]
	152 mm (6 in.)	1193 Mpa	[173 ksi]

3.3.7. Longitudinal Post Tensioning Repair

Longitudinal post tensioning for the bent cap specimen required few materials. For an in-service repair, two reaction beams and post tensioning rod would be needed; post tensioning of the individual bars would be accomplished by a center hole ram, typically used in the prestressed industry. For the laboratory specimen, a 3.56 MN (800 kip) hydraulic cylinder and associated 1.34 MN (300 kip) load cell were used to more readily

control the post-tensioning force. The test setup for the post tensioning of the bent cap is shown in Fig. 3.29 and 3.30. The test setup included two W12X120 reaction beams mounted on temporary supports to provide the post tensioning force at the lowest possible point on the section, but located above the sensors to measure relative bar slip of the anchored flexural steel. The reaction beams were post tensioned by four 32 mm (1.25 in.) diameter 1034 MPa (150 ksi) high strength Dywidag bars; the bars were instrumented to indicate the relative force distribution from the load cell, which indicates if uniform load distribution is present in the test specimen.

3.4. Specimen Construction and Instrumentation

3.4.1. Beam Specimen Construction and Instrumentation

All beam specimen construction and instrumentation was performed in Oregon State University's Structural Engineering Laboratory. Prior to casting, general purpose quarter bridge foil strain gages were placed at midheight of the stirrups within the shear span and along the tensile flexural steel bars at midspan, as shown in Fig. 3.31 and 3.32. In addition, strain gages were placed at the cut off locations for specimen B.IT.C.ES and B.IT.C.IS to indicate the relative increase in strain in the remaining flexural bars at the cutoff locations.

Once instrumentation of individual reinforcing bars was complete, the reinforcing cage was assembled adjacent to the formwork, as denoted in Fig. 3.33. Three free standing support sections composed of tube steel were placed at third points along the reinforcing cage in order to support the reinforcing steel as it was assembled. Standard reinforcing ties were used to secure the reinforcing bars to one another. The formwork for the beam specimens consisted two adjacent T beams such that two specimens were poured at one time. After assembly of the first reinforcing cage, it was temporarily moved into the formwork and a second reinforcing cage was assembled with the previously mentioned support sections. The first reinforcing cage was then removed from the formwork so that a form release agent could be applied to the surfaces in order to ease removal of the final cast specimens. After application of the release agent, the reinforcing cages were placed within the formwork and concrete was placed in three equal height lifts. Due to the size of the specimens, one concrete truck per beam was used for placement. A concrete vibrator was used to ensure proper consolidation of the concrete for each individual lift. Concrete for test cylinders was obtained midway through the placement process for each beam in order to ensure a representative sample of concrete. After placement, the top surface of each beam was troweled to a smooth surface. Approximately one hour after pouring, a saturated burlap mesh and a thin plastic sheet was placed over the length of the beams and the specimens cured for a minimum of 28 days prior to removal from the forms.

Once cured, the beam specimens were removed from the formwork and prepared for testing. External sensors were placed along the beam as indicated schematically in Fig. 3.34. Mid-span displacements along both sides of the beam were recorded with 127 mm (5 in.) range string potentiometers, while support settlements at four corners were recorded with 13 mm (0.5 in.) range displacement sensors. Support settlements were then averaged and subtracted from the mid-span displacement to reveal the true specimen deformation. Diagonal displacements were measured with 51 mm (2 in.) range string potentiometers. Load was measured through a 2450 kN (550 kip) load cell integrated with the hydraulically controlled actuator. Data was recorded on a 16 bit data acquisition system with multiple channel assignments to include strain, displacement, and load. Crack widths for the specimens were recorded by visual inspection with a hand held crack comparator.

3.4.2. Bent Cap Specimen Construction and Instrumentation

Construction of the bent cap specimen was similar to that of the beam specimen in terms of steel instrumentation and assembly. General use quarter bridge foil strain gages were attached to the stirrup and flexural steel. Based on prior tests, the location of the failure crack within the shear span was known a priori to testing, thus the stirrups were instrumented along the projected failure crack, not at midheight as they were for the beam specimens. Within each layer of flexural steel, one bar of each cutoff length was instrumented. For example, the first layer included two fully developed bars into the

column and two bars terminating at the face of the column. In this example, one of the fully developed bars and one of the cut off bars were instrumented at midspan. The distribution of strain for the anchorage bars into the column was of interest, thus three strain gages were attached to each anchorage bar, one at the inside face of the column, a second 152 mm (6 in.) further into the column, and a third located at the centroid of the column at a distance of 305 mm (12 in.) from the inside face.

Once the individual reinforcing bars were instrumented, assembly of the reinforcing cage and subsequent pouring began. Unlike the beam specimens, the size and relative weight of the bent cap precluded casting near the testing bay. As a result, the reinforcing cage and associated formwork were assembled within the testing bay as outlined below.

Assembly of the bent cap reinforcing steel began with the column sections, followed by compression steel, stirrups, tension steel, and stub girders. The column sections, as noted previously, were cast on 25 mm (1 in.) thick steel plates. The reinforcing steel consisting of four #36 (#11), 420 MPa (60 ksi) bars were welded to the corners of the steel plates. Closed #13 (#4), 420 MPa (60 ksi) reinforcing bars were secured with standard wire ties at 102 mm (4 in) for the isolated column section, and 203 mm (8 in.) spacing within the height of the beam. In order to support the wet concrete and reinforcing cage during curing, a 9 mm (0.375 in.) thick steel plate, supported on a combination of adjustable height inverted steel channels and tube sections, were placed at fifth points between the

columns. Next, the compression steel was supported from above the testing bay by two braided steel wires, turnbuckles, and several small clevises. The stirrups were attached to the compression steel at 222 mm (8.75 in.) spacing within the shear span with wire ties, as shown in Fig. 3.35. Once in place, the tension steel was placed within the stirrups and secured with wire ties. The stub girders were then attached to the stirrup sections, as shown in Fig. 3.36.

Formwork assembly and concrete placement followed after completion of the reinforcing cage. A custom built formwork system consisting of a combination of NDM fiberboard and common construction lumber was assembled around the reinforcing cage with assorted nuts, bolts and washers. The height of the bent prohibited pouring directly from a typical concrete truck; a pump truck was used to place concrete in three lifts. A concrete vibrator was used to ensure concrete consolidation in the forms. After pouring was complete, the top surface of the concrete was troweled smooth. Approximately one hour after pouring, a saturated burlap material and thin plastic sheet were placed over the top surface of the concrete.

After curing, the formwork for the bent cap was removed and the specimen was prepared for testing. External sensors were placed along the bent as indicated schematically in Fig. 3.37. Mid-span and stub girder displacements along both sides of the beam were recorded with 254 mm (10 in.) and 127 mm (5 in.) range string potentiometers respectively, while

support settlements at four corners were recorded with 38 mm (1.5 in.) range displacement sensors. Support settlements were then averaged and subtracted from the mid-span and stub girder displacements to reveal the specimen deformation. The two anchorage bars within the column were monitored for slip at the free end with a single 102 mm (4 in.) range string potentiometer mounted to the outside face of the columns. Elongation between the column sections was measured at midheight of the isolated columns. The absolute movement of the column supported on the roller end was measured by a 102 mm (4 in.) string potentiometer. Diagonal displacements within the two shear spans were measured with 51 mm (2 in.) range string potentiometers. Load was measured through a 2450 kN (550 kip) load cell integrated with the two hydraulically controlled actuators. Data was recorded on a 16 bit data acquisition system with multiple channel assignments including strain, displacement, and load. Crack widths for the specimens were visually inspected and measured with a hand held crack comparator.

3.5. Testing Protocol and Repair Methodology

3.5.1. Beam Specimen Testing

The testing protocol for beam specimens included incremental loading to produce initial diagonal cracking of the specimens. The maximum applied load during precracking was

determined as a percentage of the ultimate capacity of the base specimen. The base beam specimen capacity was determined using the computer program Response 2000 [Bentz 2000]. The program estimates capacity of traditionally reinforced and post tensioned concrete sections based on a sectional analysis (all steel specified in the analysis is assumed developed at the point of interest) utilizing Modified Compression Field Theory. Force was applied at 222 kN (50 kip) increments through a hydraulically controlled 2224 kN (500 kip) capacity actuator under force control at a quasi-static rate of 9 kN/sec. (2 kip/sec.). The initial IT beam was loaded up to 1112 kN (250 kip), representing approximately 70% of the base specimen capacity. Due to loss of internal foil strain gages at this level, the remainder of the IT and T beams were loaded up to 890 kN (200 kip). This represents 55% of the ultimate strength of the T and IT specimens respectively. At each load increment, the maximum force was reduced by 10% in order to take crack width measurements, map crack lengths, and reduce the effect of creep. After the maximum load was reached, the specimen was unloaded, the sensors were zeroed and a second test was conducted to obtain the new post-cracked baseline response of the beam. The crack condition maps for all beam specimens prior to repair installation are shown in Fig. 3.38.

3.5.2. Bent Cap Specimen Testing

The testing protocol for the bent cap specimens mirrored that of the beam specimens, with a slight modification for the use of two actuators. Estimation of the base specimen

capacity followed from the results of previous work at OSU for specimens with comparable concrete strength. Force was again applied at 222 kN (50 kip) increments through a hydraulically controlled 2224 kN (500 kip) capacity actuator under force control at a quasi-static rate of 9 kN/sec. (2 kip/sec.). Initially one actuator was loaded to the first load point of 1112 kN (50 kips), then reduced by 10% in order to reduce the effects of creep while taking crack width and length measurements. Then, the specimen was unloaded, and the second actuator was loaded to the first load point, measurements were taken, and load released. Next, the two actuators were loaded together, the first followed by the second, measurements were taken, and load released in the reverse order it was applied. This sequence was repeated until a combined load of 8896 kN (400 kip) was applied to the base specimen. As with the beam specimens, once the bent cap was unloaded, the sensors were zeroed and a second test was conducted to obtain the new post-cracked baseline response of the bent cap. The crack condition maps for the two bent cap specimens prior to repair installation are shown in Fig. 3.39.

3.5.3. External Stirrup Repair

The process used for repairing the specimens with external stirrups is outlined below with reference to Fig. 3.40.

- Identify external stirrup spacing along shear span

- Locate flexural and deck steel locations on specimen with a rebar locator
- Mark hole locations such that they fall outside the width of the web
- Drill holes with a rotary hammer drill with caution if steel is encountered
- Place threaded rod through holes in the flange
- Connect reaction sections to the threaded rod and tighten to predetermined force

3.5.4. Internal Supplemental Stirrup Repair

The process for internal stirrup repair is outlined below, with reference to Fig. 3.41.

- Identify internal stirrup locations along the span of the beam
- Locate flexural and deck reinforcing within the specimen using a rebar detector
- Mark the location of the internal stirrups
- Drill the holes with either a water required concrete coring machine or a dry system with vacuum attachment
- For traditional reinforcement:
    - Pour epoxy into hole such that it will fill the void space around the bar and concrete once the bar is inserted
    - Insert reinforcing bar and add additional epoxy as needed until seepage is minimized
- For center hole reinforcement:

- Place reinforcement into hole
- Pump epoxy through the center of the reinforcement until it fills the void space surrounding the top of the bar
- Add additional epoxy as needed until seepage has been minimized

3.5.5. Surface Mounted CFRP Repair

As opposed to the two previous repair methods, the CFRP strips were applied according to the manufacturer's instructions. For the beam and bent cap specimen, the manufacturer recommended a working time to complete application of CFRP system (not including epoxy injection) of approximately 12 hours; in each case, the process was completed in approximately six hours. The first step in the process was to epoxy inject cracks wider than 0.25 mm (0.010 in.). This involved the use of a wire brush to clean the cracks and adjacent surface of any loose debris. Then, injection ports were mounted to one side of the specimen using a two part 100% solids Concresive SPL epoxy paste at roughly the thickness of the specimen (355 mm (14 in.) for both the beam and bent cap repairs), as shown in Fig. 3.42. On the opposite face of the member, two or three ports are applied equally spaced along the crack, as so called "window ports" for quality control measures to ensure full penetration through the width of the stem. Once the surface paste cured for 24 hours, the epoxy injection began. The epoxy used was Chemrex SCB Concresive 1360, which is a two part, ultra low viscosity liquid epoxy with a manufacturer specified tensile

strength of 55.2 MPa (8.0 ksi). A specialized injection machine was used to mix the two part epoxy to the manufacturers specifications (2.5 Part A to 1.0 Part B). The epoxy was injected starting at the lowest port, with care given not to exceed a pressure of 690 kPa (100 psi) while injecting the cracks. As epoxy became visible at the next highest port, the lower port was sealed and the injection nozzle moved to the next highest port. The process was repeated until the last port was encountered—at which point the dissipation of pressure within the crack slowed significantly as the void space within the crack decreased. Occasionally, a leak near a port or along a crack would form. Repairs to the crack were made with paraffin wax, which tended to seal most small to moderate sized cracks. Once complete, the epoxy was left to cure for a period of seven days. Temperature data was recorded during this time, to ensure ambient air temperature above 4.5^{o} C (40^{o} F) as required by the manufacturer.

The next step in the process involved application of the CFRP itself, as denoted in Fig. 3.43 and 3.44. First, the paste on the outside of the beam was removed by heating the paste with a propane torch and scraping off the surface. The outer surface of the beam was ground using a diamond dressed masonry disc to expose the aggregate and then vacuum brushed to remove any dust that may have accumulated during the process. Once the surface was prepared, a two part MBrace Primer was mixed for three minutes according to the manufacturer specifications with a hand held drill and applied to the surface using short nap paint rollers. The pot life of the primer component was 30 minutes; the product was

applied prior to this threshold. A two-part putty, mixed for three minutes separately for Part A and Part B, then mixed for three minutes combined—as per the manufacturers specifications—was then applied to the surface using hand trowels, intended to fill small voids on the surface of the beam. The manufacturer permitted application of the putty while the primer coat was still wet; however, the primer was left to set up for a period of 30-45 minutes prior to mixing of the putty. The putty was permitted to setup for 30-45 minutes prior to the next step, although the manufacturer did not place any restrictions on placing the saturant directly on the wet putty. A two part saturant which included a three minute Part A premix followed by a three minute combined mix was then applied with common paint rollers. Precut 25 mm (10 in.) wide CF130 carbon fiber strips were then applied to the beam using a plastic putty knife to impregnate the fibers with the saturant beneath. A second coat of saturant was applied to the CF130 carbon strips to complete the process. The manufacturer recommended curing for seven days at an ambient air temperature of at least 4.5^{o} C (40^{o} F). When colder temperatures were anticipated, enclosures with space heaters were provided to raise the ambient temperature during curing above the specified minimum. Results of the ambient air temperature for specimens B.IT.NC.CF and D.IT.C.CF are included in Table 3.11 for both epoxy injection and CFRP application.

Table 3.11 Curing temperatures for B.IT.NC.CF and D.IT.C.CF

Specimen:	Temperature °C [°F]		
	Average	High	Low
B.IT.NC.CF	8.7	18.6	6.1
	[46.8]	[50.3]	[40.4]
D.IT.C.CF	8.2	10.2	4.7
	[47.6]	[65.4]	[43]

3.5.6. FRP NSM Repair

The process for installation of the FRP NSM stirrup repair is outlined below , with reference to Fig. 3.45 and 3.46.

- Determine spacing and location of FRP NSM reinforcement along the span of the specimen
- Locate the integral steel stirrups with a rebar locator such that the NSM locations do not coincide with the integral stirrups (due to variations in the concrete cover)
- Saw cut the beam along the locations for the FRP
- Remove any remaining slurry residue or debris from the grooves
- Apply the epoxy two thirds the depth of the hole
- Insert the FRP rod or tape
- If needed, apply additional epoxy to ensure complete penetration around the FRP

3.5.7. Surface Mounted CFRP Bent Cap Specimen

The process for CFRP installation on the bent cap specimen was similar to that of the beam specimens. Refer to Fig. 3.47 through 3.49 for installation of CFRP on the bent cap specimen.

3.5.8. Post Tensioning-Bent Cap Specimen

The repair method for post-tensioned bent cap specimen was based on reducing the flexural demand of the system. Final installation of the post tensioning system is shown in Fig. 3.50 and 3.51.

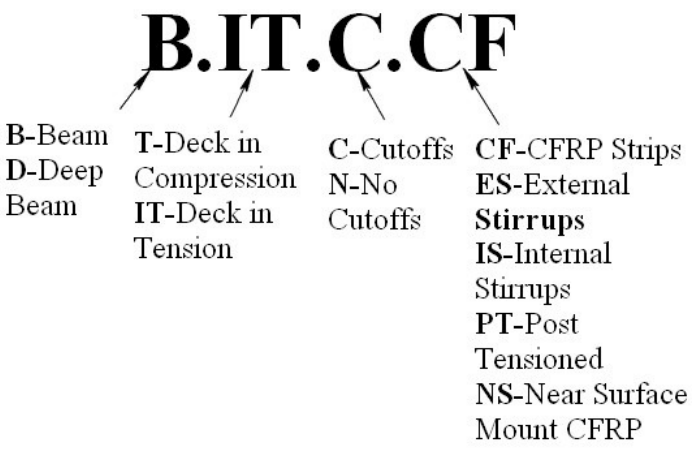

Fig. 3.1 – Specimen Identification.

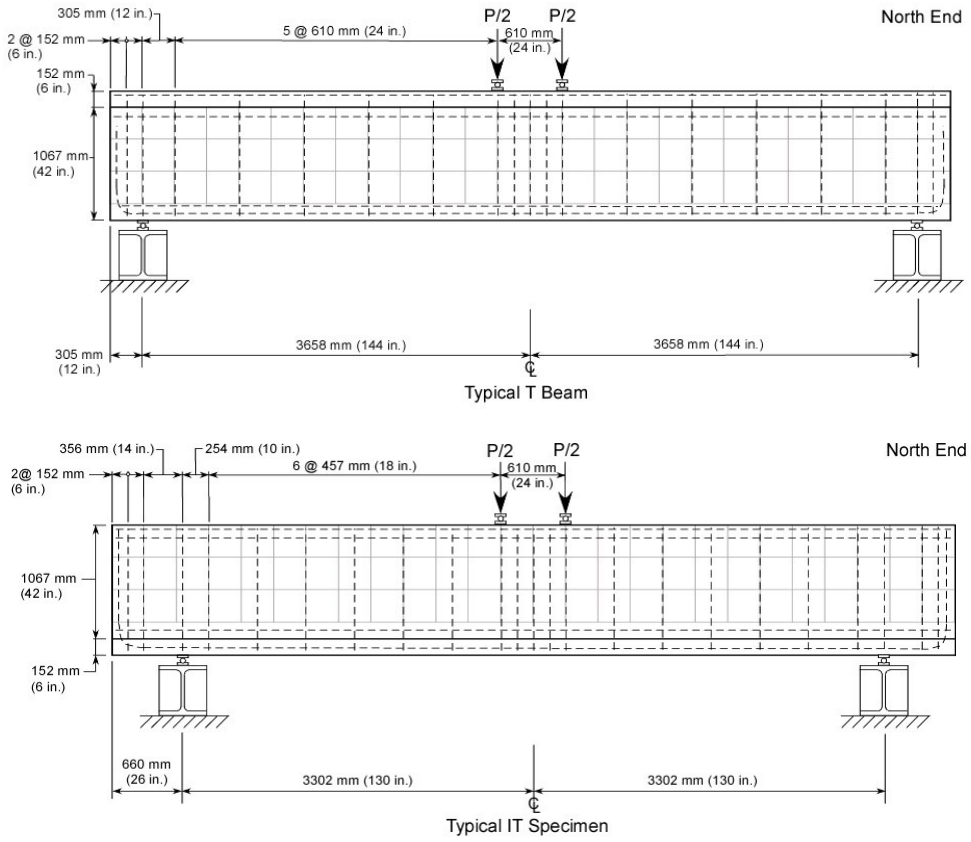

Fig. 3.2 – T and IT Beam Elevations.

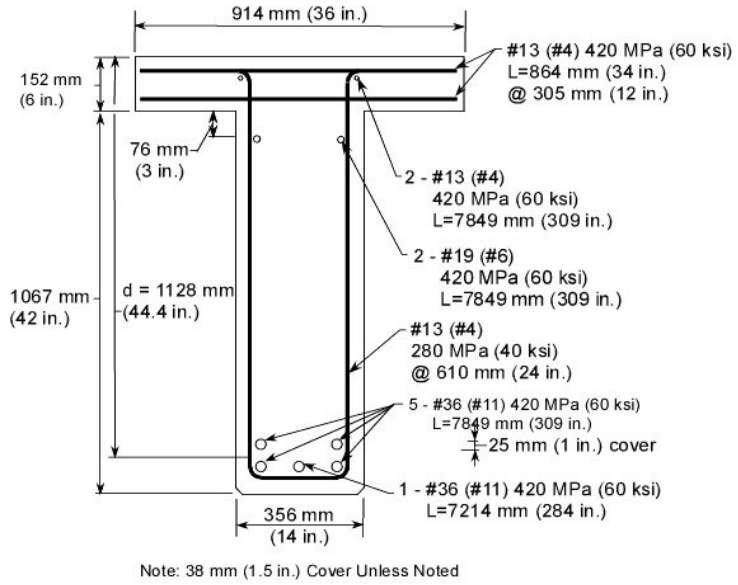

T Beam Typical Section

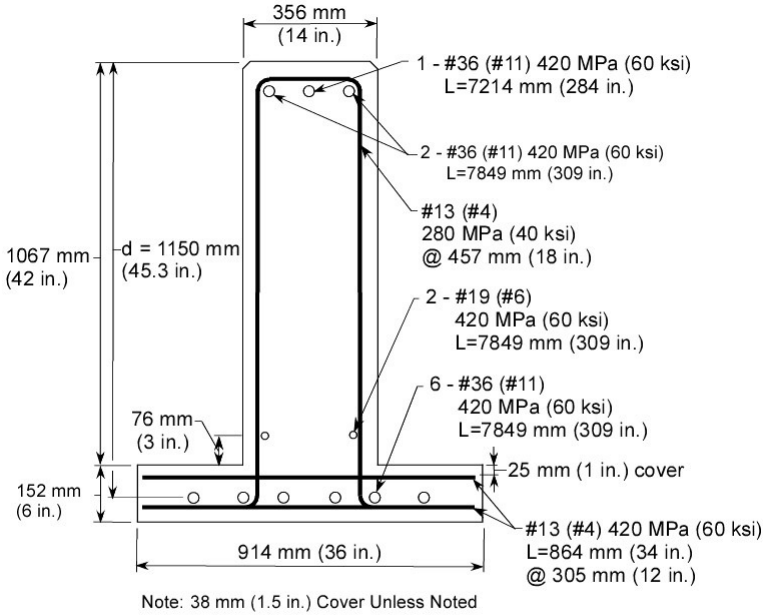

IT Beam Typical Section

Fig. 3.3 – T and IT Beam Typical Sections.

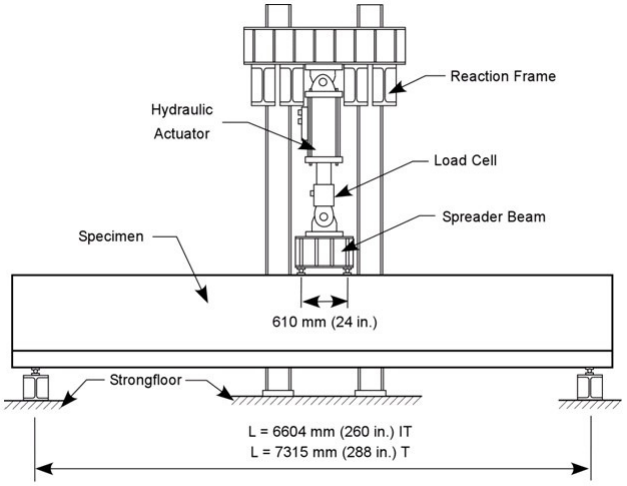

Fig. 3.4 – Typical beam loading setup (IT section shown).

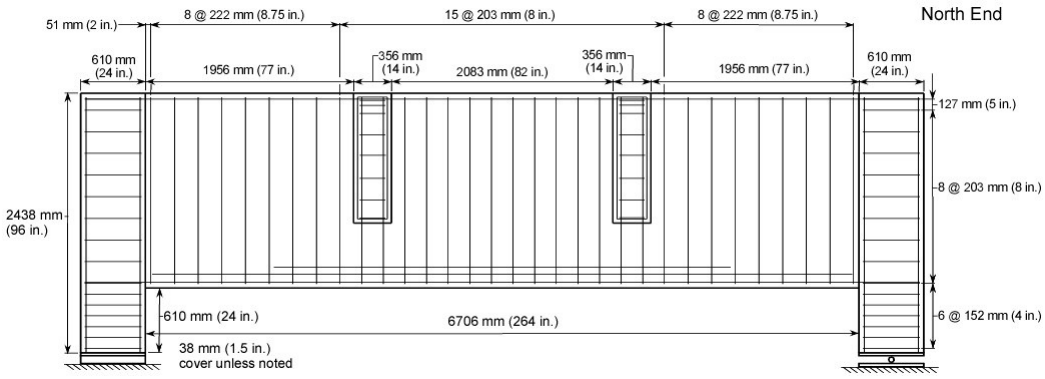

Fig. 3.5 – Bent cap elevation view of reinforcing details and geometry.

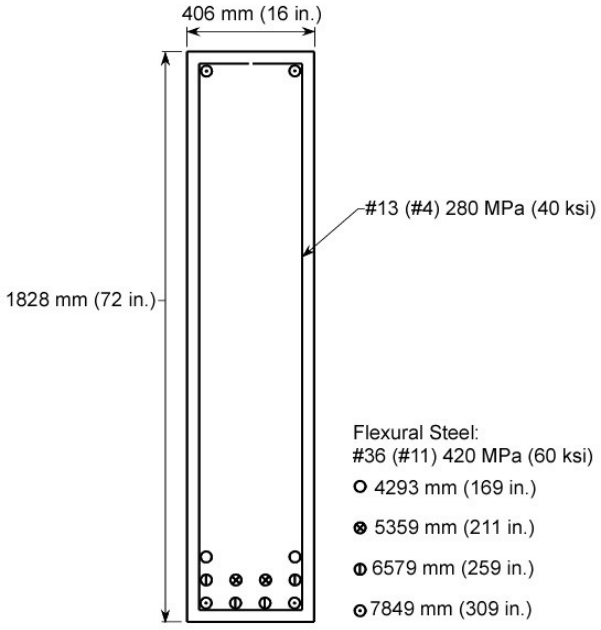

Typical Section at Mid Span

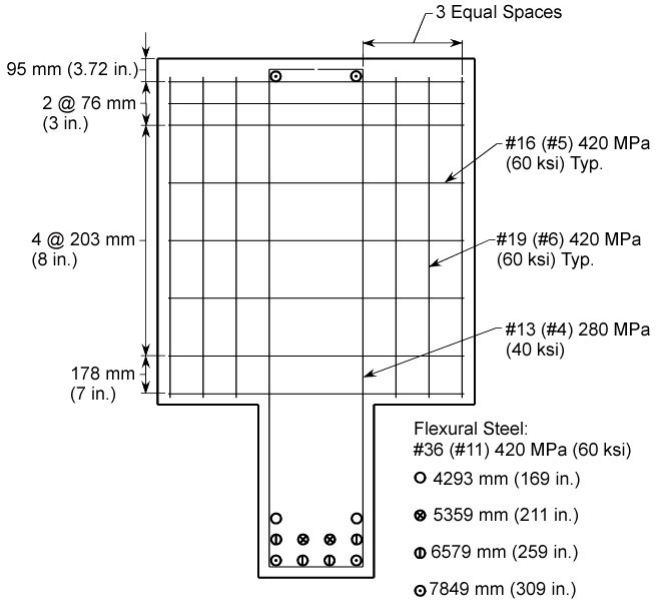

Typical Section at Stub Girder

Fig. 3.6 – Bent cap section at midspan and at stub girder.

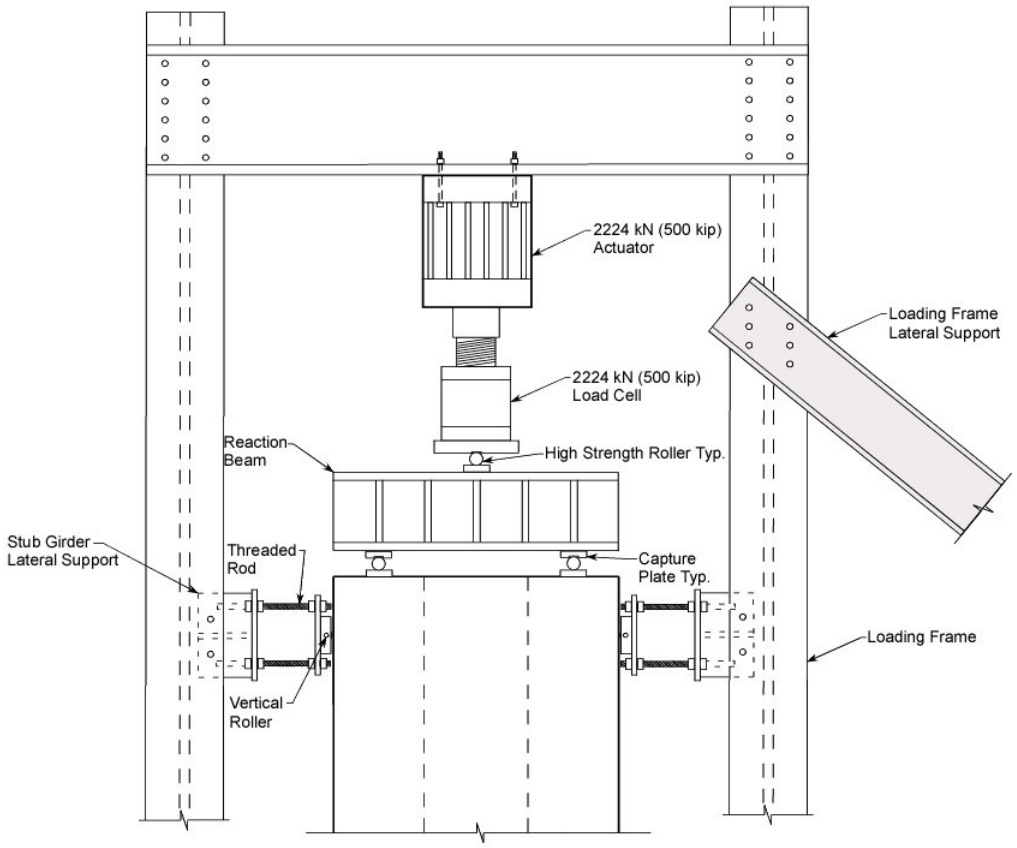

Fig. 3.7 – Bent cap indirect loading at stub girder location.

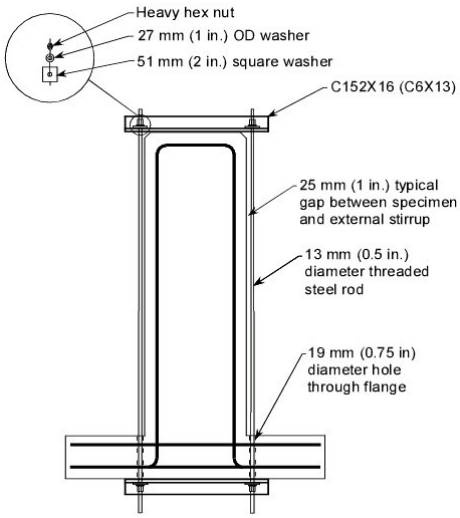

Fig. 3.8 – External stirrup typical section: channel repair.

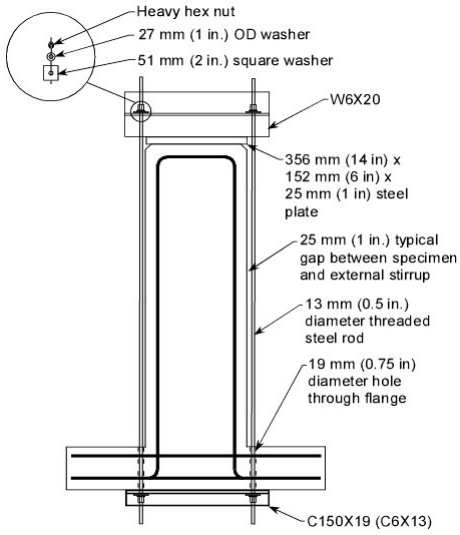

Fig. 3.9 – External stirrup typical section: WBeam repair.

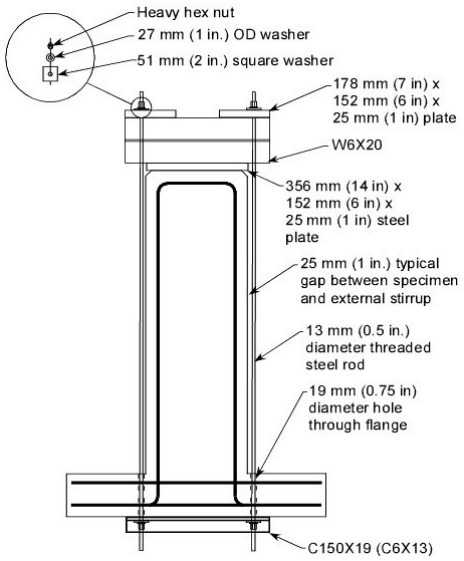

Fig. 3.10 – External stirrup typical section: strengthened WBeam repair.

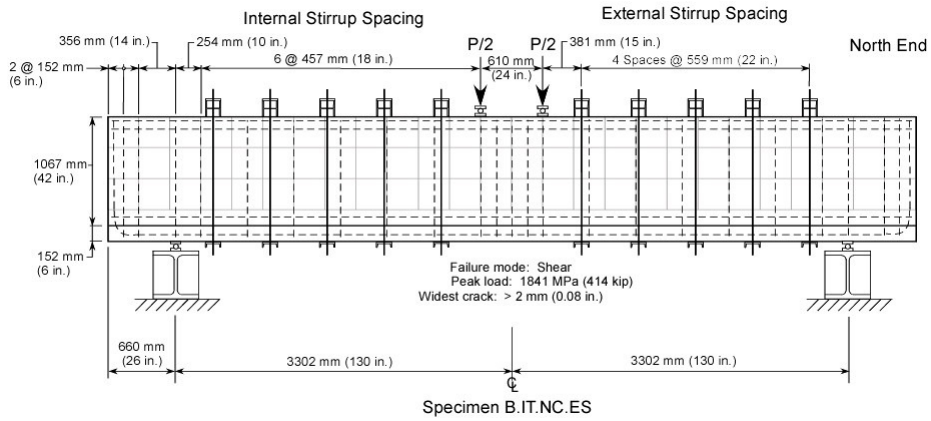

Fig. 3.11 – Specimen B.IT.NC.ES repair.

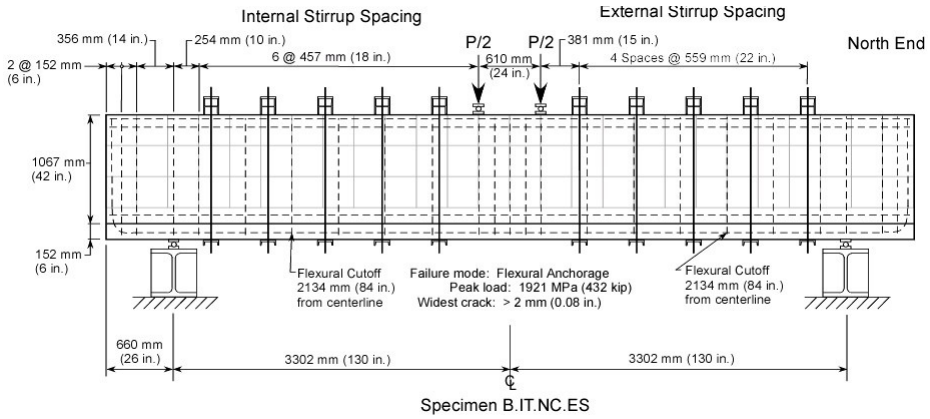

Fig. 3.12 – Specimen B.IT.C.ES repair.

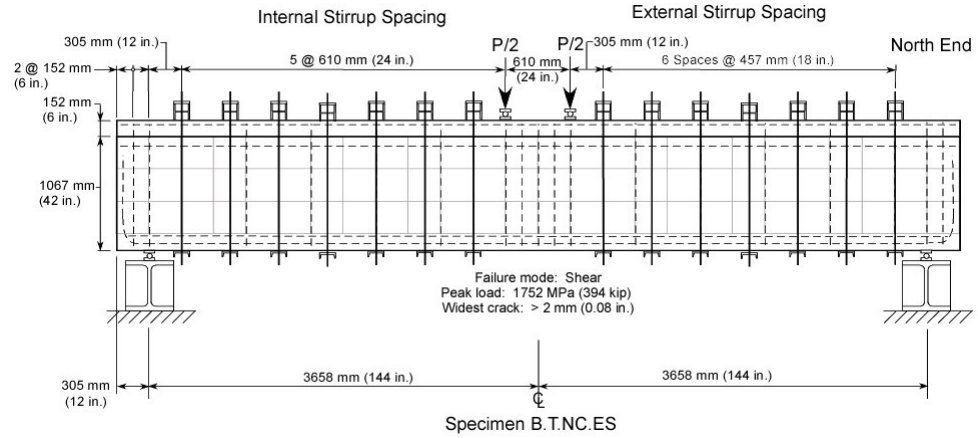

Fig. 3.13 – Specimen B.T.NC.ES repair.

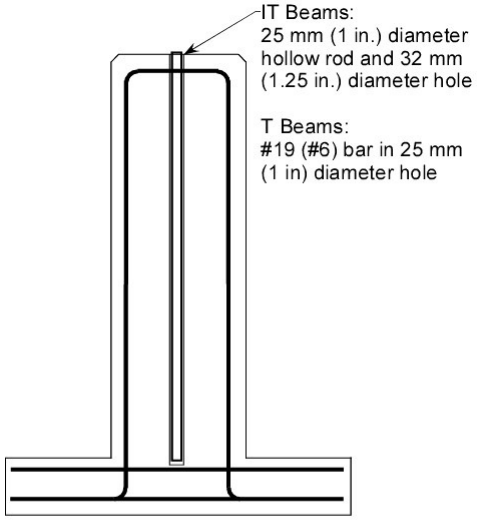

Internal Stirrup Repair: Typical Section

Fig. 3.14 – Internal stirrup typical section.

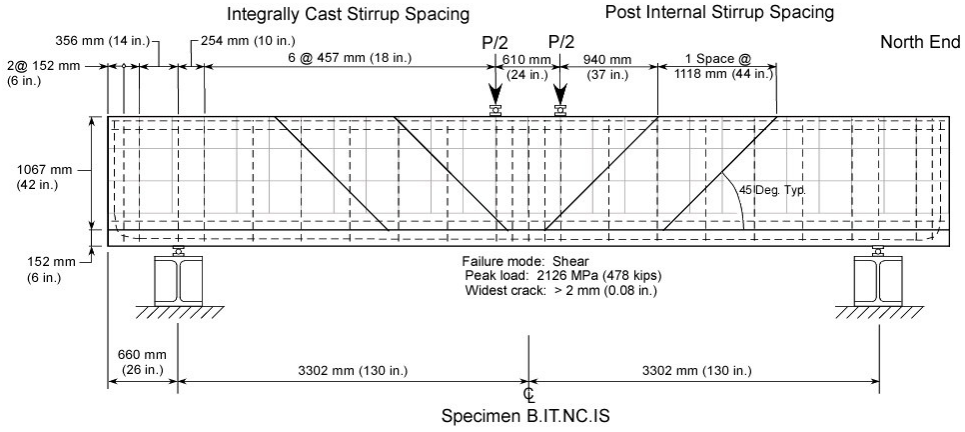

Fig. 3.15 – Specimen B.IT.NC.IS repair.

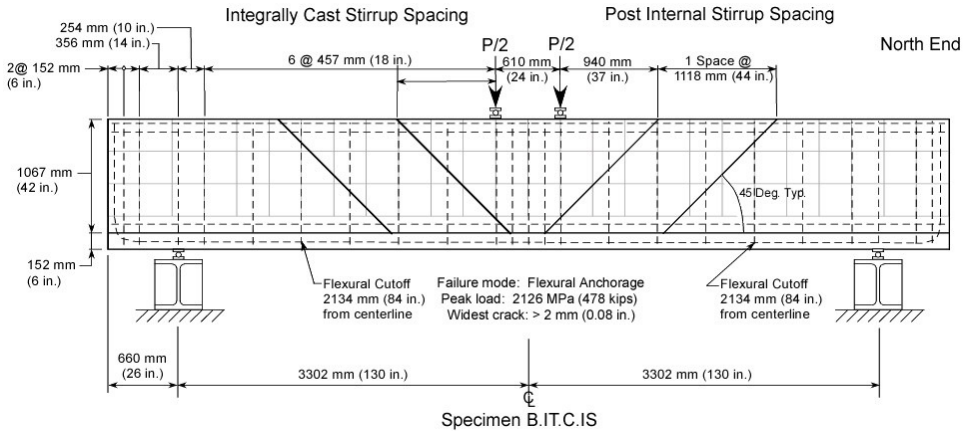

Fig. 3.16 – Specimen B.IT.C.IS repair.

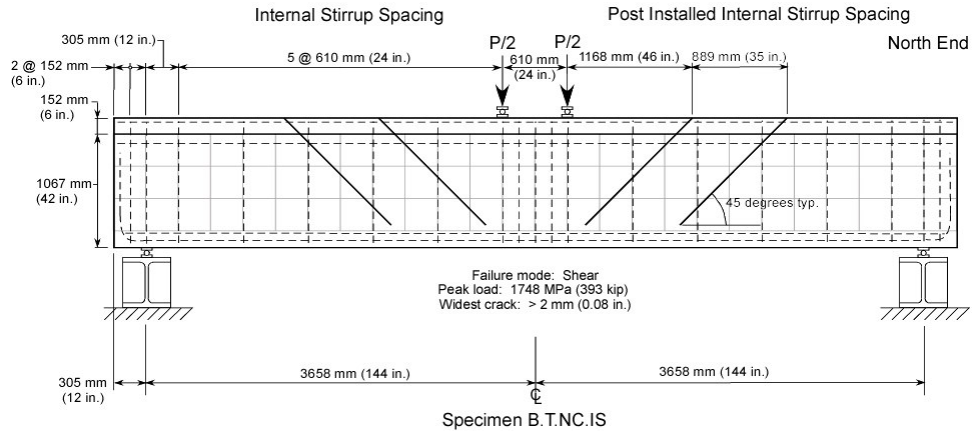

Fig. 3.17 – Specimen B.T.NC.IS repair.

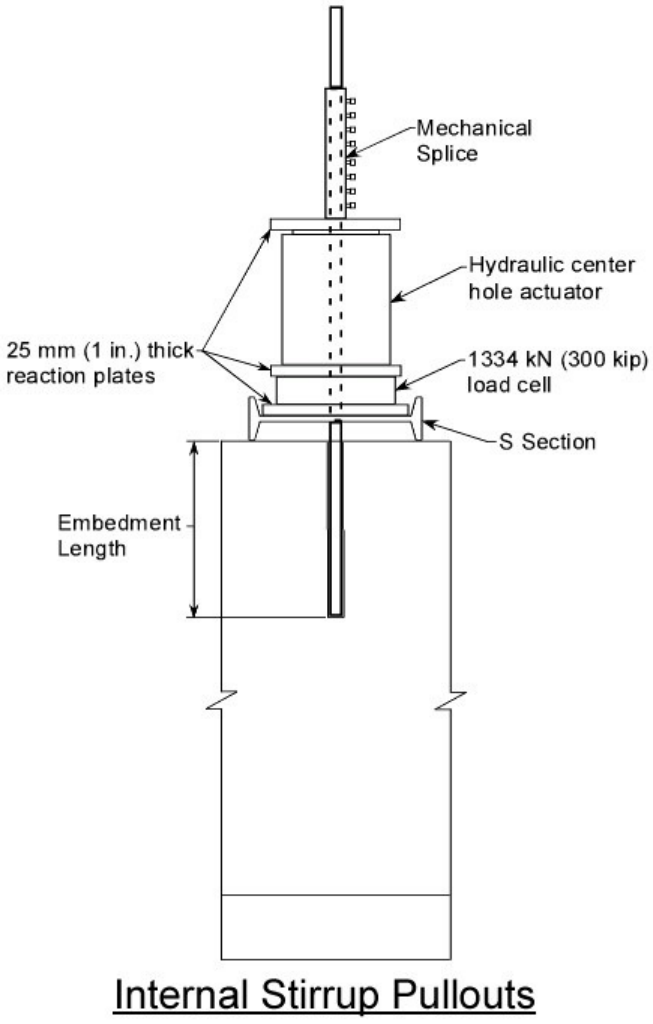

Fig. 3.18 – Internal stirrup pullout test setup.

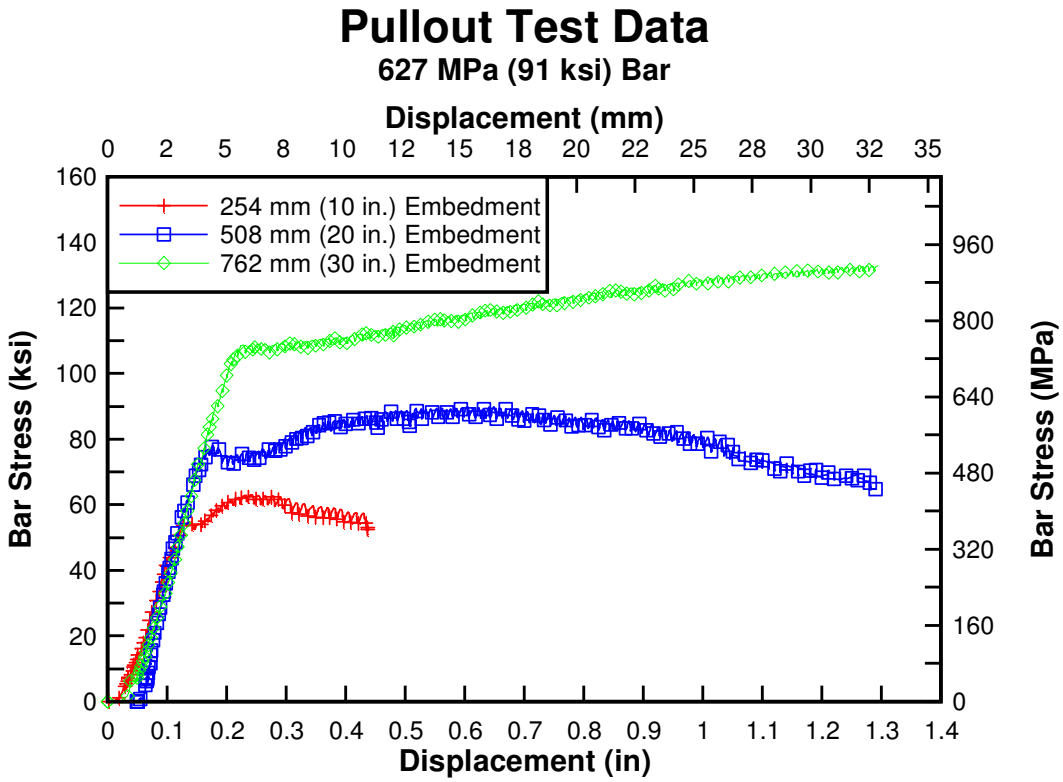

Fig. 3.19 – Internal stirrup 627 MPa (91 ksi): bar stress versus displacement.

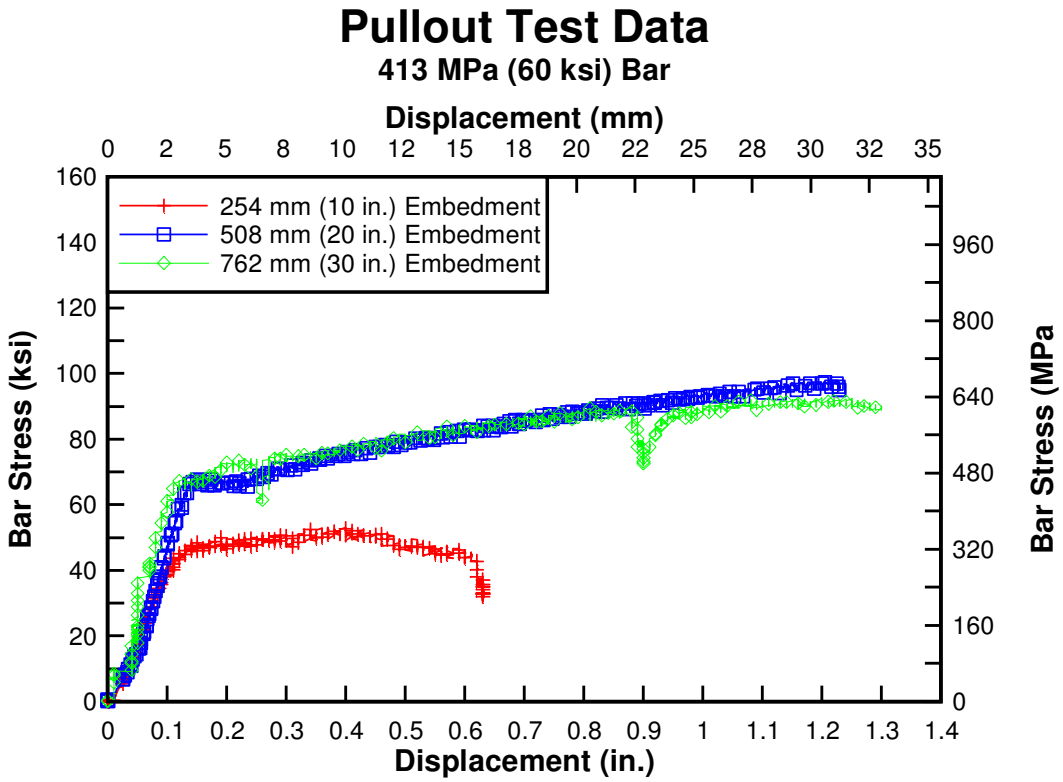

Fig. 3.20 – Internal stirrup 413 MPa (60 ksi): bar stress versus displacement.

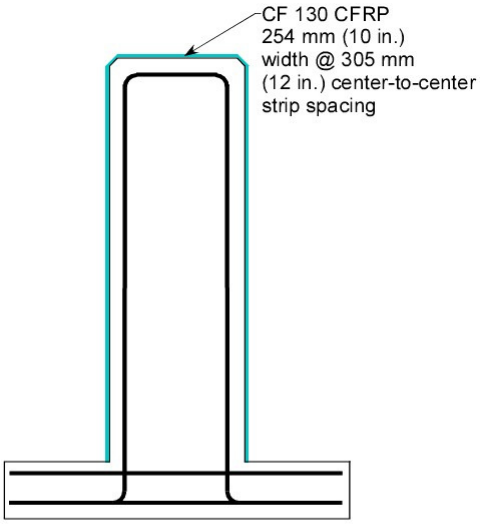

Fig. 3.21 – CFRP beam typical section.

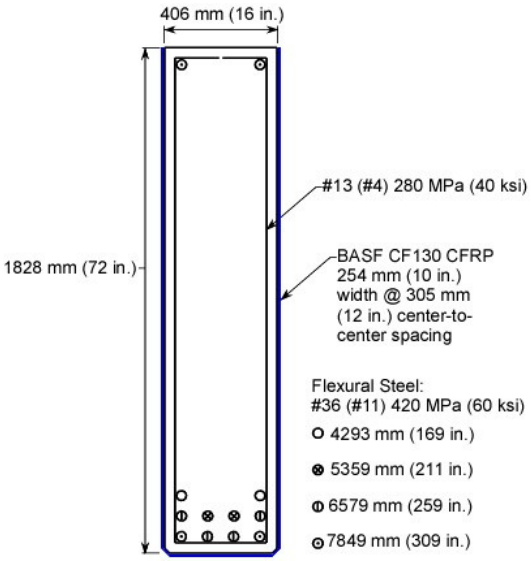

Fig. 3.22 – CFRP bent cap typical section.

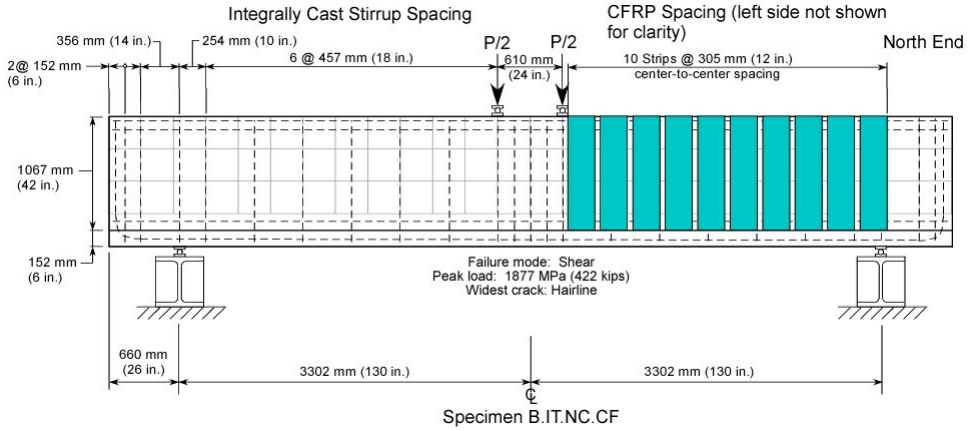

Fig. 3.23 – Specimen B.IT.NC.CF repair.

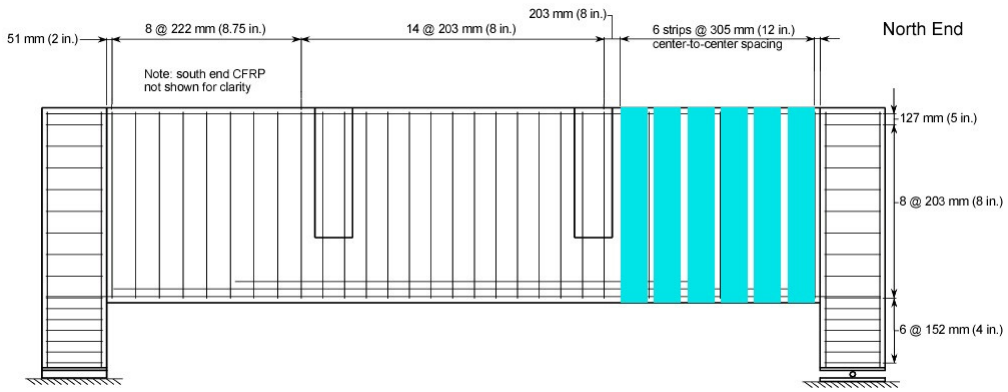

Fig. 3.24 – Specimen D.IT.C.CF repair.

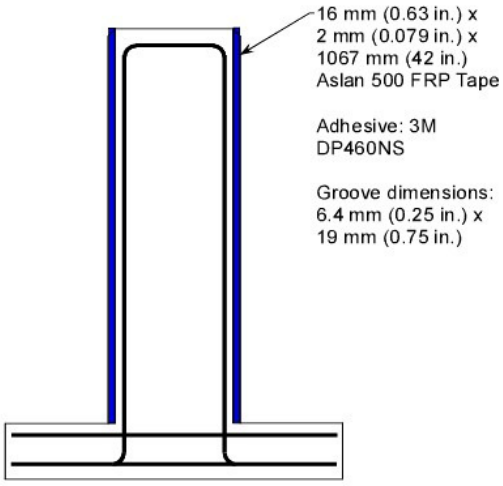

Fig. 3.25 – NSM FRP typical section.

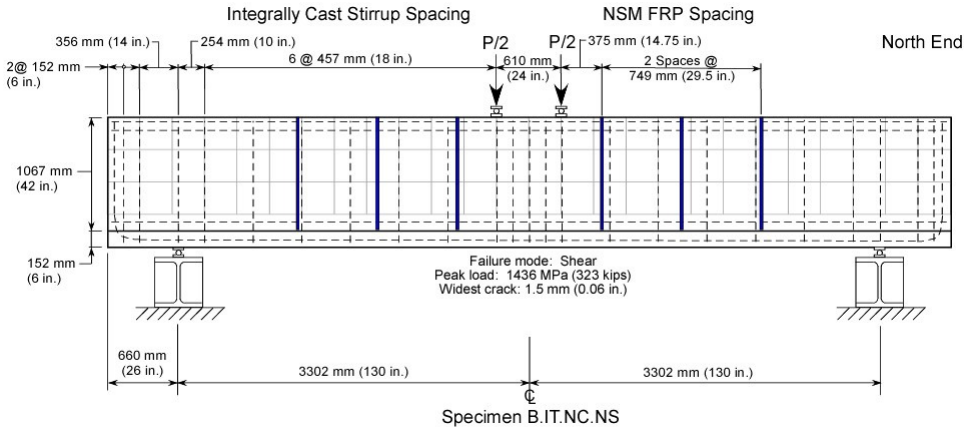

Fig. 3.26 – Specimen B.IT.NC.NS repair.

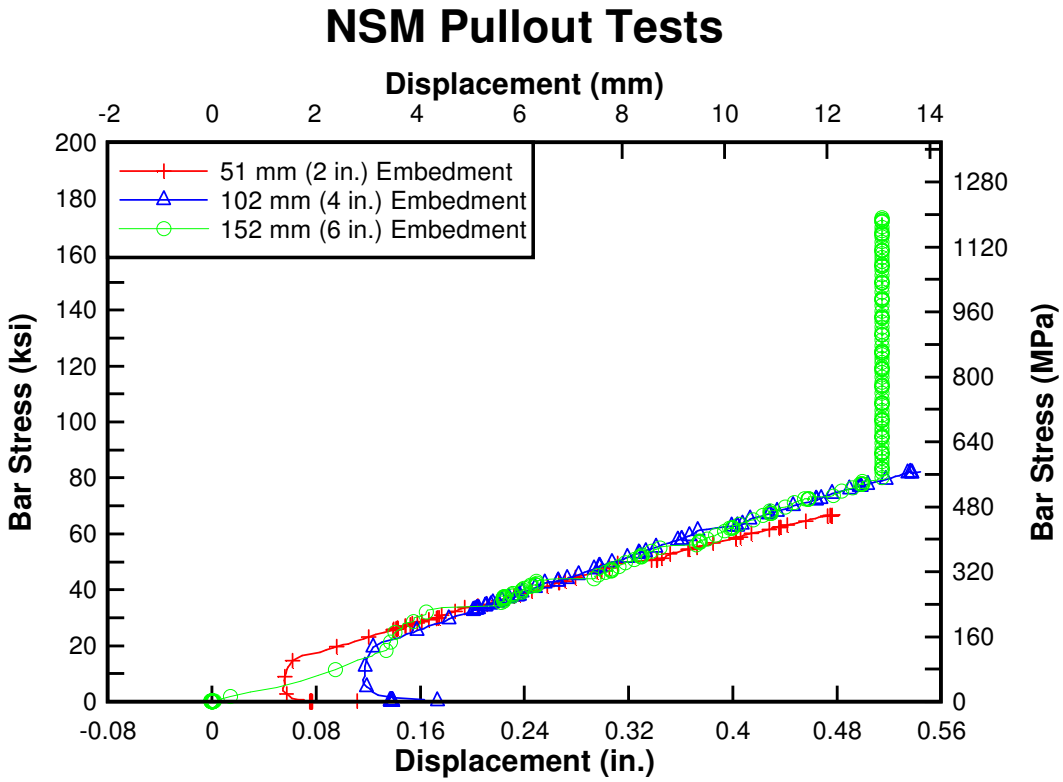

Fig. 3.27 – Specimen B.IT.NC.NS repair.

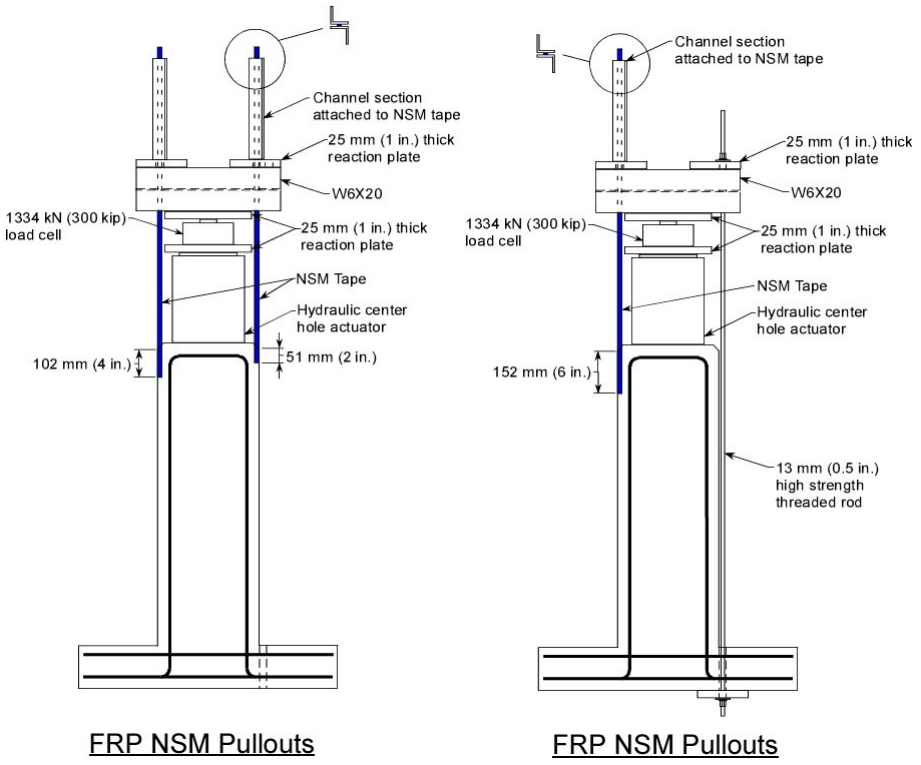

Fig. 3.28 – NSM pullout test setup.

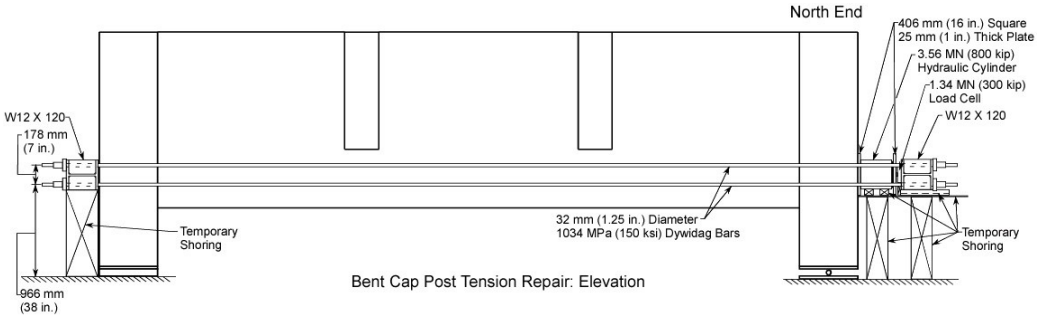

Fig. 3.29 – Specimen D.IT.C.PT repair elevation.

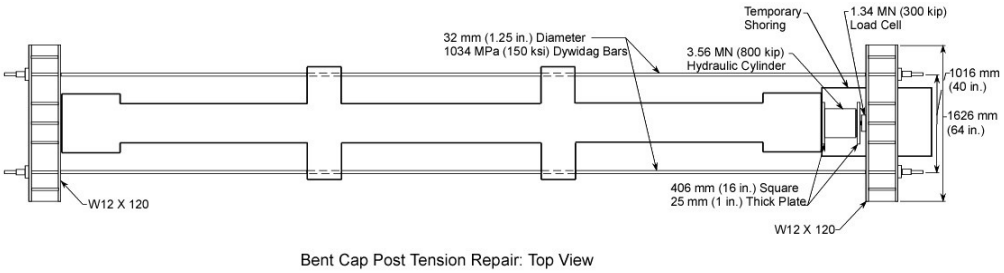

Fig. 3.30 – Specimen D.IT.C.PT repair top view.

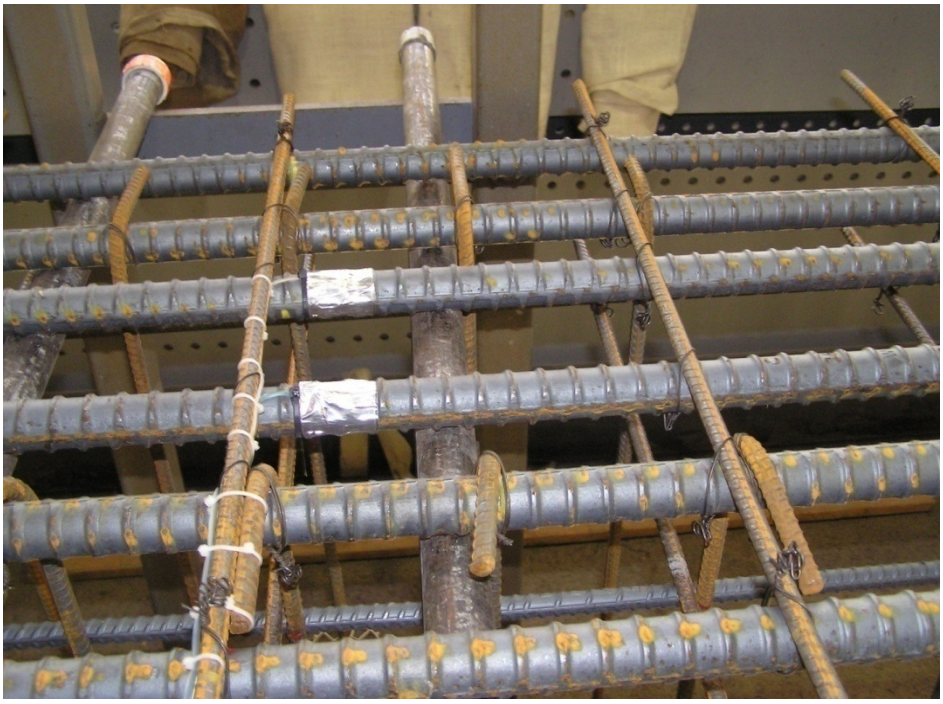

Fig. 3.31 – Typical strain gage locations along flexural steel.

Fig. 3.32 – Typical strain gage locations along stirrups.

Fig. 3.33 – Assembly of completed reinforcing cage adjacent to formwork (IT specimen shown).

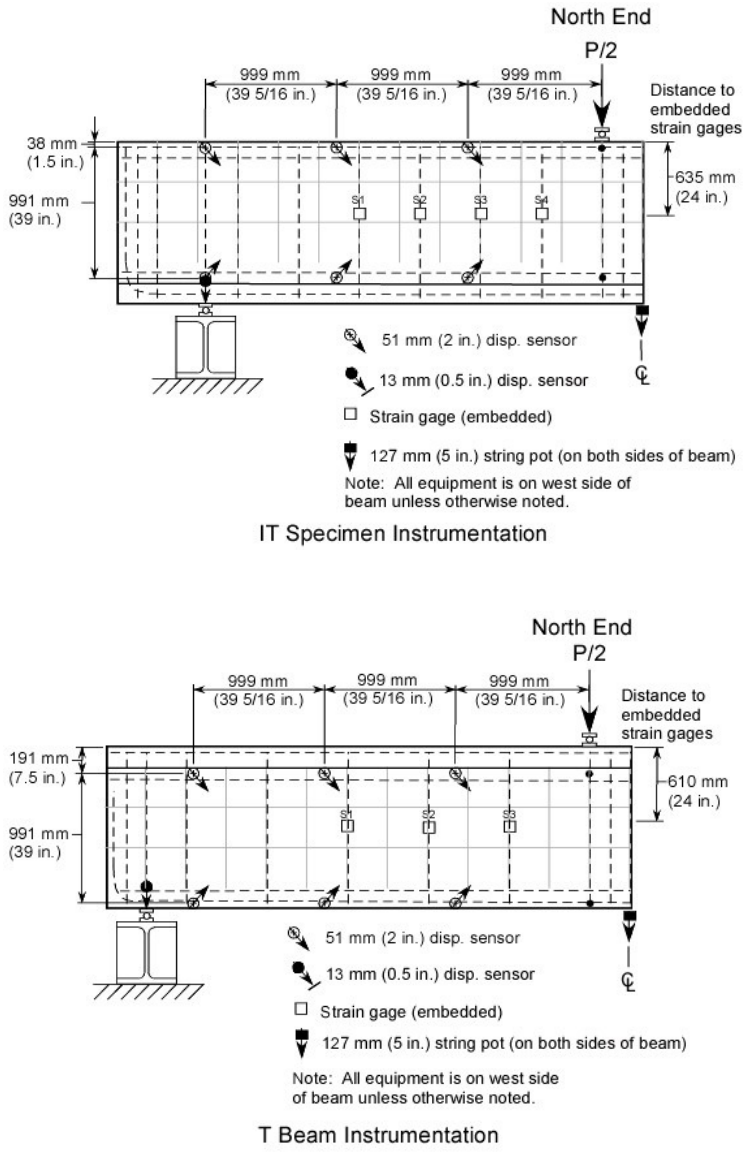

Fig. 3.34 – Schematic view of sensors for IT and T beams.

Fig. 3.35 – Typical bent cap stirrup assembly.

Fig. 3.36 – Typical bent cap stub girder assembly.

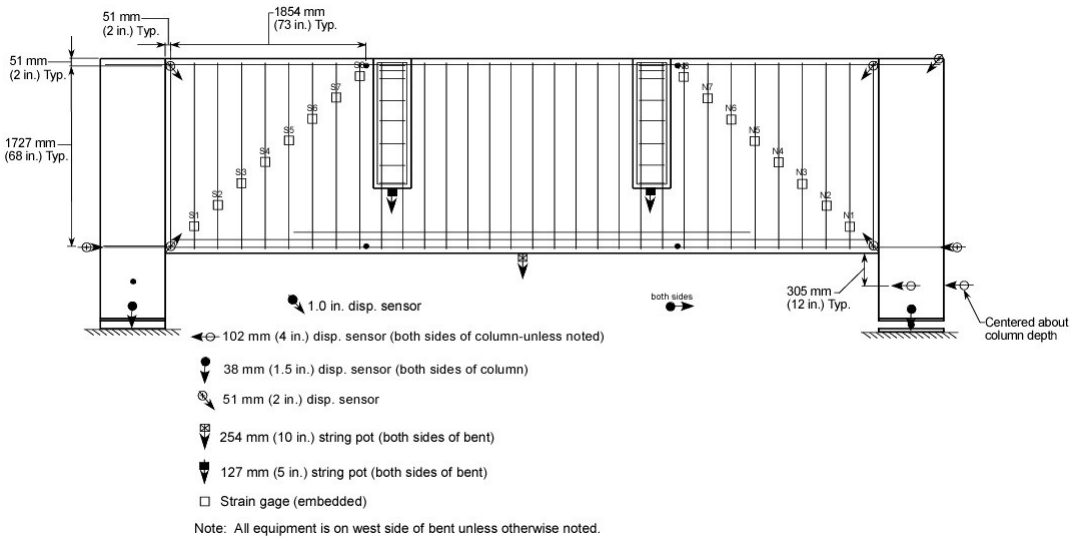

Fig. 3.37 – Schematic view of sensors for bent cap.

Fig. 3.38 – External stirrup installation.

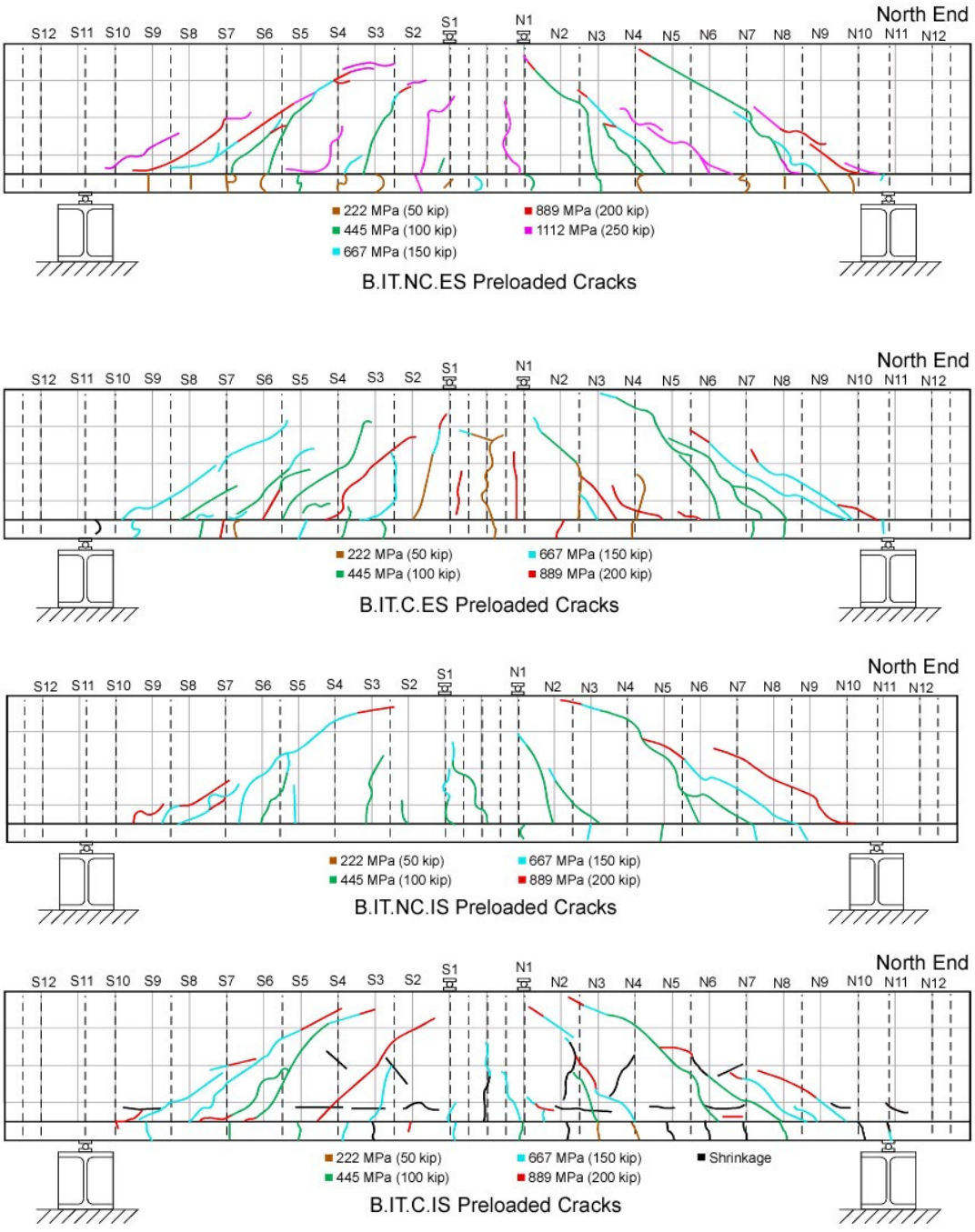

Fig. 3.39 – Beam preloaded crack maps.

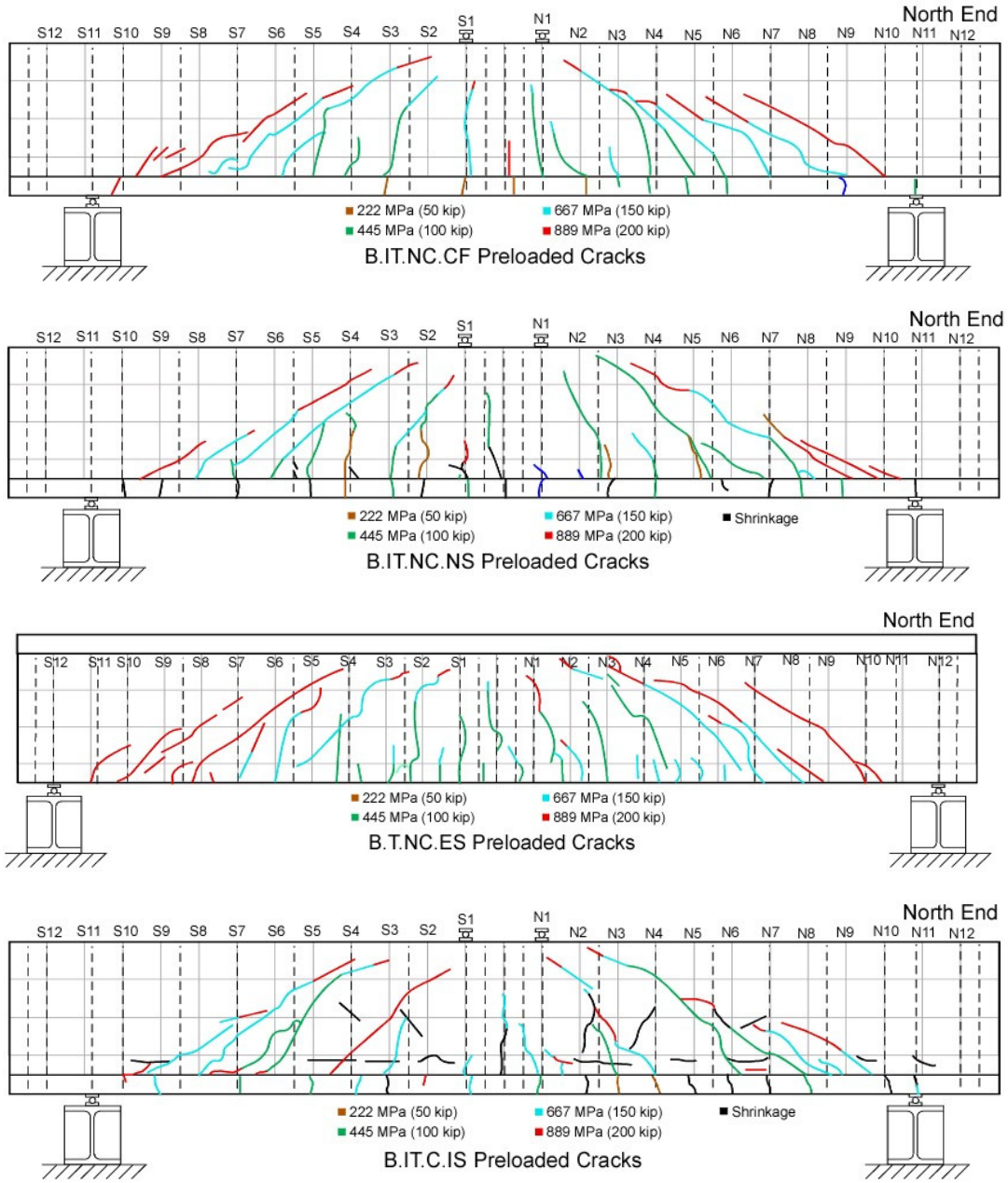

Fig. 3.39 Continued – Beam preload crack maps.

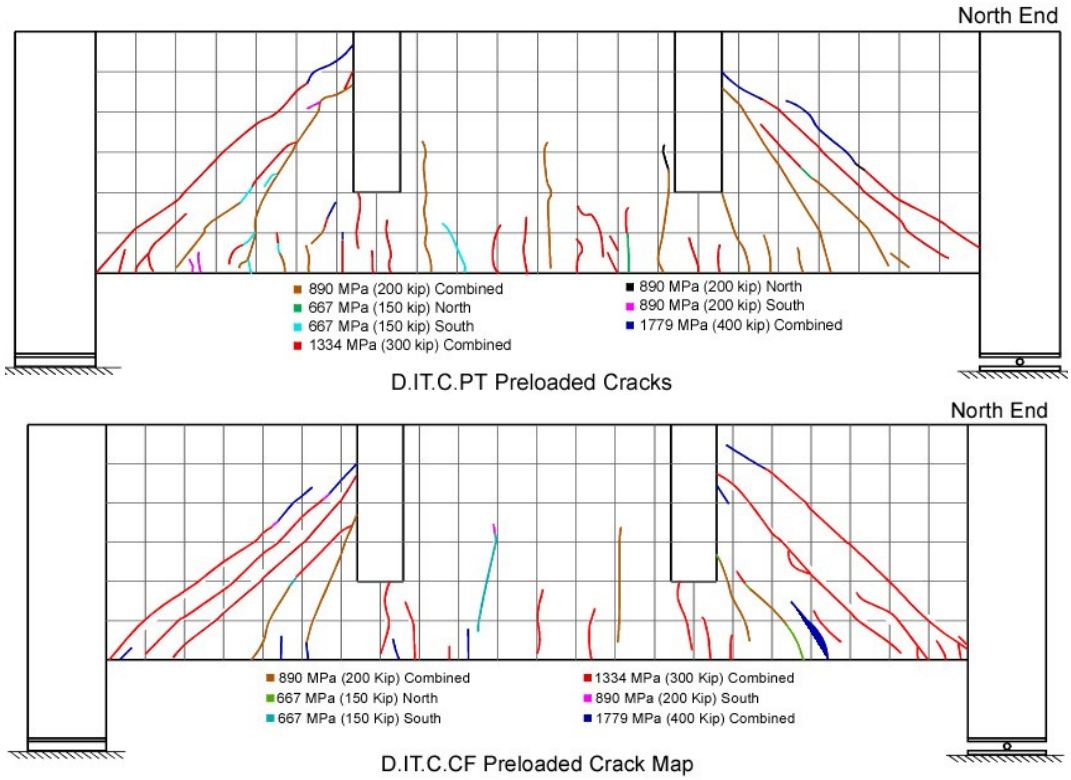

Fig. 3.40 – Bent cap preloaded crack maps.

Fig. 3.41 – Internal stirrup installation.

Fig. 3.42 – CFRP beam installation: epoxy injection.

Fig. 3.43 – CFRP installation: ground surface (left) and primer application (right).

Fig. 3.44 – CFRP installation: putty installation (left) and FRP strips with saturant (right).

Fig. 3.45 – NSM installation: cut grooves (left) and initial epoxy application (right).

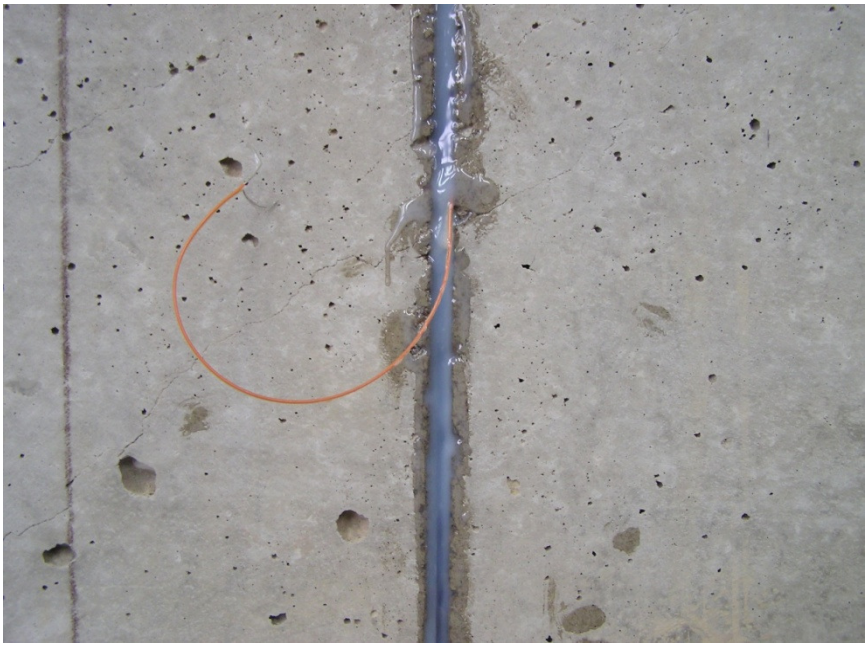

Fig. 3.46 – NSM installation: final product.

Fig. 3.47 – CFRP bent cap installation: epoxy injection.

Fig. 3.48 – CFRP bent cap installation: primer (left) and putty (right).

Fig. 3.49 – CFRP bent cap installation: strip installation.

Fig. 3.50 – Post tensioned bent cap installation: overall view (left) actuator and reaction beam (right).

Fig. 3.51 – Post tensioned bent cap installation: adjacent reaction beam.

4. EXPERIMENTAL RESULTS

In this section, the results from the experimental work for the beam and bent cap specimens are presented. Comparison of specimen global response, stiffness changes, and load sharing among the integrally cast stirrups and repair media are presented for the service and ultimate load range. For localized behavior, a numbering system has been adopted such that integrally cast stirrups are numbered increasingly from the support toward the center actuator (smaller numbers near support, larger numbers adjacent to actuator). Where not explicitly shown, strain gages for each repair media are numbered increasingly from bottom to top, then from the support toward the center of the specimen. For example, for surface bonded CFRP strips, a total of eight gages may be mounted on various strips. As such, the first numbered gage is located at the lowest level on the strip closest to the support, with the gage above it numbered next. Once all the gages on a particular strip have been accounted for, the sequence repeats on the next strip toward the actuator.

For each of the beam and bent cap specimens included in the current investigation, shear was applied under force control at 223 kN (50 kip) increments under quasi-static loading of 9 kN/sec (2 kip/sec). As noted previously, the bent cap specimens had two actuators, one located at the north stub girder and a second located at the south stub girder. Load was applied to each stub girder individually in a half load step, then combined in a whole load step. Each beam specimen was tested up to a service load condition equal to 890 kN (200

kip) of applied force or 445 kN (100 kip) of applied shear force, while the bent cap specimens were tested to a service load of 1779 kN (400 kip) or 890 kN (200 kip) of applied shear. The target shear values are representative of typical shear force experienced for the span length considered in the current study and provide a reasonable strain range for the integrally cast stirrups in order to perform additional tests on a specimen without loss of functionality. The results are provided according to specimen type with individual repair methods included for each type.

4.1. IT Beam Specimens

The first group of specimens under consideration is the IT beams which include four specimens with fully developed flexural steel within the shear span and two specimens with flexural cutoff details. All six beams have identical shear spans, support conditions, and integrally cast stirrup spacing. The beams also share the same concrete mix design, although actual strengths varied from specimen to specimen. Comparisons of the IT beams are divided into two groups: beams with fully developed flexural details and beams with cutoff flexural cutoff details. In addition, the specimens will be compared to previous IT beams of similar scale and integral stirrup spacing. Global behavior in terms of applied shear force versus mid span displacement, typical integrally cast stirrup strains, and center diagonal elongations will be compared to previously described SPR350 specimens.

4.1.1. IT Beams with Fully Developed Flexural Details

4.1.1.1 IT External Stirrup Repair Scheme

Prior to comparison of the four IT beams with fully developed flexural details, the first external stirrup repair specimen was investigated for the optimal repair scheme based on varying several subsequently described parameters. The initial test specimen included application of the external stirrups at two load levels—the beam self weight or no dead load condition, and a second superimposed service condition dead load level. Comparable tests performed in the available literature negated the use of a superimposed dead load on the repair method. However, a superimposed dead load force was included in the current investigation to document the effects on the clamping action related to the repair method. Crack widths due to the self weight of the beam were small in comparison to those at the first or second load step. Therefore, a superimposed shear force of 178 kN (40 kip) representative of the weight of the deck, intermediate diaphragms, superficial wearing surface, and traffic barrier was applied prior to attachment of the external stirrups. This value was determined from a typical interior girder of a three span continuous deck girder bridge with 15.2 m (50 ft) spans and a uniform dead load of 23.3 kN/m (1.6 kip/ft).

In addition to the two initial loading conditions for the external stirrups, the initial clamping force and resulting stress in each individual external stirrup leg was varied. The first loading case, denoted as the snug condition, was chosen to overcome any seating

losses associated with uneven bearing surfaces and to engage strain in the threaded rod prior to application of additional shear. Each of the two threaded rods required for the repair method was instrumented with common foil quarter bridge strain gages such that the two bars were stressed equally at the start of each test. The snug condition resulted in a 200 με value corresponding to a 34 MPa (5 ksi) stress in each external stirrup leg. The second post-tensioned stress condition was determined based on an assumed common failure strain between the external and internal stirrups. Uniaxial tension tests on the integrally cast stirrups resulted in a yield strength of 345 MPa (50 ksi). Similar tests on the external stirrups resulted in a yield strength of 586 MPa (85 ksi), thus the external stirrups were post tensioned to 207 MPa (30 ksi), corresponding to 1034 με, to provide essentially the same stress range prior to yielding between the two bars at failure, assuming no interaction or load sharing among the stirrups.

The first external stirrup specimen initially utilized two different repair sections at the base of the web, as shown in Figure 4.1a and 4.1b. Recall the external stirrup repair was chosen to investigate a current repair of an in-service bridge within Oregon's bridge inventory utilizing channel sections which react about the top surface of the deck and the bottom of the web. For this loading condition, the channel section at the base of the web is placed in weak axis bending due to edge bearing at the corners of the stem. Thus, the strain in the external stirrups was dependent upon the relative flexural stiffness of the reaction section and the moment arm from the corner of the stem to the external stirrup. To reduce the affect of the reaction section on the repair scheme, a W section in weak axis bending with mounting hardware reacting against the web of the section was placed at the base of the

concrete stem, providing approximately 13 times the stiffness of the channel section. Also, the external stirrups were positioned as close to the stem as possible (typically 12 mm (0.5 in.)) in order to minimize the affect of the moment arm. Initial testing of the W section indicated local bending of the web, as shown in Figure 4.1b. The W section apparatus was modified, as shown in Figure 4.1c, by placing a 25 mm (1 in.) thick steel plate atop the W section. For this loading condition, the top steel plates extend from the outside of the W section toward the centerline of the beam, which in turn changes the bending stiffness of the system significantly. Stiffness in this configuration comes from local deformation of the plate and flange, treated as a column section from the web to its terminal end. Local flange buckling due to compression is not problematic, as the maximum force in the external stirrups is significantly smaller then the Euler buckling load for the vertical portion of the flange. Thus, neglecting p-Δ effects, the deformation of the strengthened W beam was set equal to PL/AE. A testing matrix for specimen B.IT.NC.ES is shown in Table 4.1 taking into account the three repair sections, the two loading conditions, and the two stress levels in the external stirrups prior to testing.

Table 4.1 External stirrup specimen B.IT.NC.ES testing matrix

Test:	Channel Section:	W Beam:	Strengthened W Beam:	Post-Tensioned	Snug Tightened	Dead Load	No Dead Load
1	X				X		X
2	X			X			X
3	X				X	X	
4	X			X		X	
5		X			X		X
6		X		X			X
7		X			X	X	
8		X		X		X	
9			X		X		X
10			X	X			X
11			X		X	X	
12			X	X		X	

Applied shear force versus midspan displacement graphs illustrate changes in stiffness for the three reaction sections, taken for the case of no dead load, including snug and post tensioned stresses in the external stirrups as illustrated in Figure 4.2. The global stiffness improved slightly for the strengthened Wbeam case; the remaining repair sections did not show any appreciable change.

While midspan displacement provides a measure of the global stiffness of a section, the use of the diagonal sensors noted in Chapter 3 along the west face of the specimen provide a means to measure the average vertical strain over the height of the stem. This data can then be used to investigate strain compatibility between the external stirrups and the specimen. Diagonal displacement sensors were placed within the shear span, resulting in

three "panels" which measured the elongation and/or contraction of each sensor depending on its orientation with respect to a diagonal crack. In order to define the total average vertical strain over each panel, a third direction must be measured, analogous to a strain rosette which utilizes three strain gages at defined angles to determine principle strain values. In the case of a cracked concrete beam, the proposed failure crack indicates the orientation of principle strain in the concrete within the panel of interest. From this orientation, the average vertical strain over the panel length can be calculated using Mohr's circle for strain, following the procedure outlined below. It should be noted that Mohr's Circle for strain is similar to Mohr's Circle for stress, with the variation of the inclusive angle between the axis and the point of interest is taken as 2θ, not θ, as indicated in Figure 4.3.

The conversion of diagonal sensor data to average vertical strain in a specific panel is dependent on five known quantities, as identified in Figure 4.4 taken from Dawson [Dawson 2008]: diagonal tension displacement (L_t), diagonal compression displacement (L_c), diagonal displacement gage length (L_0), diagonal displacement gage orientation ($\theta_{diagonal}$), and crack angle (θ_{crack}). Variation in the orientation of the diagonal sensors was assumed to be negligible.

Once the quantities of interest are known, conversion to average vertical strains follows from the equations noted below, taken from Mohr's circle for strain. The diagonal displacements are converted to strains ε_t and ε_c from Equations [4.1] and [4.2] below.

$$\varepsilon_t = \frac{L_t}{L_0} \quad [4.1]$$

$$\varepsilon_t = \frac{L_c}{L_0} \quad [4.2]$$

The center of the circle is then denoted by Equation [4.3].

$$\varepsilon_{center} = \frac{\varepsilon_t + \varepsilon_c}{2} \quad [4.3]$$

Next, the orientation of the principle strain was calculated, as shown in Equation [4.4], assuming the crack angle was orthogonal to the principle strain. Recall from Figure 4.4, this value is measured with respect to the crack angle and the diagonal displacement gage orientation.

$$\theta_{principal} = 90° - \theta_{diagonal} - \theta_{crack} \quad [4.4]$$

Utilizing the angle of principal strain, the center of the circle, and the tensile strain, the radius of the circle can be found, as shown in Equation [4.5].

$$R = \frac{\varepsilon_t - \varepsilon_{center}}{\cos 2\theta_{principal}} \quad [4.5]$$

All quantities for Mohr's circle have been calculated, thus the principal strains, ε_1 and ε_2, as well as the vertical and horizontal strains, ε_x and ε_y can be calculated, as shown in Equations [4.6]-[4.9].

$$\varepsilon_1 = \varepsilon_{center} + R \quad [4.6]$$

$$\varepsilon_2 = \varepsilon_{center} - R \quad [4.7]$$

$$\varepsilon_x = \varepsilon_{center} - R\cos 2\theta_{crack} \quad [4.8]$$

$$\varepsilon_y = \varepsilon_{center} + R\cos 2\theta_{crack} \quad [4.9]$$

The average vertical strains were determined for panel 2S, corresponding to the center panel along the eventual failure crack. As a starting point for comparison of the three reaction sections, the change in average vertical strain due to post tensioning with and without dead load were compared for the static condition prior to application of additional load on the specimen. The results are shown in Figure 4.5 with the no dead load condition on the left and the dead load condition on the right for the channel, Wbeam and SWbeam, respectively. For the no dead load condition, each reaction section provides essentially the same reduction in average vertical strain. This is a result of the small diagonal crack widths when only the self weight of the specimen is used. For the superimposed bridge dead load condition, the channel section appears to be less capable of compressing the cracks over the depth of the stem compared to the other two methods.

Comparison of the average vertical strain for the no dead load snug and post tensioned conditions throughout the service loading range is presented in Figure 4.6. A best fit curve for each repair section is shown. For the no dead load case, the channel section appears to provide a higher reduction in average vertical strain compared to the other sections. However, for the post-tensioned case, the channel section and strengthened Wbeam provide a slightly higher reduction than the Wbeam alone.

Turning toward local behavior, the interaction of the integrally cast stirrups and strain compatibility of the section is investigated. The static reduction in strain for the integrally

cast stirrups due to clamping force was investigated for the three reaction sections. For both the self weight and the dead load case, the snug loading had a negligible effect on the internal stirrup strain, as the initial force in the external stirrups was unable to produce a measurable reduction in strain for the internal stirrups. However, the post tensioning case resulted in a reduction in internal stirrup stress for both the self weight and dead load cases. In both instances, the reduction in strain was similar for each of the three reaction sections. For the self weight case, the internal stirrups were placed into compression, while the dead load case resulted in a reduction of strain but was not sufficient to place the stirrups into a compressive state. Comparing the reduction in strain for the dead load and self weight cases resulted in a slight contradiction. For stirrups N1 and S2, the data indicated that the self weight case resulted in a higher strain reduction than the dead load case, but the opposite held true for stirrups N3 and N4, as shown in Figure 4.7. Upon further investigation, the reason for the discrepancy resulted from exposure of the steel stirrup legs from the surrounding concrete at stirrups N1 and S2 due to strain gage failure after the initial precrack load was applied. A rotary hammer was used to expose the stirrup steel at the location of the existing strain gage as shown in Figure 4.8, a new gage was mounted, and the baseline loading cycle was repeated. Due to the additional exposure of the stirrup leg, the strain data was more susceptible to larger reductions at the no dead load condition. For stirrups N3 and N4, which functioned successfully throughout the series of tests, the exposed length of steel was only equal to the width of the diagonal cracks crossing the stirrup over the height of the specimen. Therefore, they were subjected to a smaller length reduction at the self weight condition since the existing crack widths were small compared

to the loaded condition. Figure 4.7 also indicates the reduction in strain just after post tensioning was essentially equal across the three reaction sections.

In order to investigate the behavior of the integrally cast stirrups for each reaction section over the service loading range, the strain measurements for internal gage 3N are shown for the dead load snug and post tensioned cases in Figure 4.9. In each case, the shape and strain range was identical, but the starting strain value varied depending on the post tensioning force applied. The reduction in starting strain was proportional to the applied post tensioning force.

The investigation continues with a look into the external stirrup strain and corresponding strain compatibility with the average vertical strains previously described. External stirrup 3S (along the eventual failure crack) was chosen due to its location directly in the center of panel 2S, which was used to measure average vertical strains in the specimen. The strain range for this stirrup for the four loading conditions and three reaction sections is shown in Figure 4.10. The figure indicates that a stiffer reaction section results in a higher strain range for the external stirrups. For the realistic installation case of superimposed dead load for a typical bridge, the snug condition results in no advantage for the higher resistance sections. However, for the post tensioned dead load case, it is clear that the higher strain range in the stirrup is a function of the bending stiffness of the reaction section.

The external stirrup strain values indicate that strain compatibility of the external stirrups with the average vertical strain should be similar. For the realistic case of superimposed dead load with post tensioning, the applied shear versus average vertical strain in panel 2S and the external stirrup 3S is shown in Figure 4.11a. By focusing on the slope of the average vertical strain and external stirrup strain values, it is clear that the efficiency increases as the stiffness of the reaction section increases. This is evident for the case of no dead load snug and post tensioned cases shown in Figure 4.11b.

The external stirrup repair scheme can be idealized as elastic springs in series, as shown in Figure 4.12. In this figure, there are three primary springs, the first, K_1, relates to the elastic properties of the external threaded rod only. The second spring, K_2, relates to the reaction section at the base of the stem—which has been the focus of the current investigation—while the third spring, K_3, provides any additional inefficiency to seating of the reaction sections. Nonlinear elastic response associated with the third spring are assumed to be negligible for the current investigation, since the snug loading case induced a minor stress in the stirrups, thus minimizing the effect of seating which is a principle source of nonlinear elastic response.

An indication of the efficiency of each anchorage section can be shown by focusing on K_2 with respect to strain compatibility of the section. A graph of the ratio of the external stirrup strain to average vertical strain (as the values approach 100%, there is strain compatibility) versus reaction section stiffness, K_2 is shown in Figure 4.13 for all but the

dead load snug condition, as sensor malfunction resulted in insufficient data. The figure indicates what was shown previously for the external stirrup strain and strain compatibility figures—the higher the flexural resistance of the anchorage section, the higher the strain compatibility. The figure also indicates the snug post tensioning condition is inferior to the post tensioning for all three sections.

Returning to the remaining spring coefficients, an equivalent spring stiffness can be shown for each repair scheme, taking K_3 as essentially infinitely stiff, as shown in Equation [4.10]

.

$$K_{equivalent} = \frac{1}{\frac{1}{k_1} + \frac{1}{k_2}} \quad [4.10]$$

The equivalent spring stiffness for each section is calculated below. For each case, the stiffness of the external threaded rod is identical; the value is shown in Equation [4.11].

$$K_{ext\_stirrup} = \frac{AE}{L} \quad [4.11]$$

In the above equation, the L is the height of the section 1219 mm (48 in.), A is the area of the external stirrup of 129 mm^2 (0.2 in^2), and E is the modulus of elasticity of the rods. For ASTM A449 threaded rod, the modulus value is 199955 MPa (29000 ksi). The stiffness contribution for the second spring comes from the weak axis bending of the anchorage section. For the channel section, the loading is as shown in Figure 4.14. The resulting deflection term is shown below in Equation [4.12].

$$\Delta_{flexure} = \frac{\frac{1}{3}Pa^3 + \frac{1}{2}Pa^2L}{EI_{weak\_axis}} \quad [4.12]$$

Where P is the applied load, a is the distance from the edge of the web to the location of the external stirrup, L is the width of the web, E is the modulus of elasticity of the section, and I is the moment of inertia about the weak axis of the channel. The width of the web was held constant such that L was equal to 356 mm (14 in.); the distance from the edge of the web to the external stirrup was 13 mm (0.5 in.). The modulus of elasticity was taken to be 199948 MPa (29000 ksi) and the moment of inertia of the channel section was 437043 mm^4 (1.05 in^4). Comparison of the deflection estimate from Equation [4.12] with a commercially available finite element program indicated larger deformations then those from hand calculations. The finite element solution took into account the shear deformations of the section under weak axis bending, whereas the hand calculation did not. Thus, the hand calculation was modified to account for the shear deformations, as shown in Equation [4.13].

$$\Delta_{shear} = \frac{Pa}{GA_{shear}} \quad [4.13]$$

Where A_{shear} is the shear area in the weak axis direction and G is the shear modulus, defined in Equation [4.14].

$$G = \frac{E}{2(1+\nu)} \quad [4.14]$$

The total stiffness of the system is then the summation of the two equations, rearranged to indicate the stiffness term, as shown in Equation [4.15].

$$K_{weak\_axis} = \frac{EI_{weak\_axis}}{\frac{1}{3}a^3 + \frac{1}{2}a^2 L} + \frac{GA_{shear}}{a} \quad [4.15]$$

A similar scenario is presented for the W beam section, neglecting local web deformations, in order to estimate the stiffness term. For the strengthened W beam, the location of the top reaction plates changes the deformation of the system from bending to axial, thus the stiffness term is as shown in Equation [4.16].

$$K_{SWBeam} = \frac{AE}{L} \quad [4.16]$$

In which A is taken as the length of the length of the section times the two flange thicknesses and L is taken as the flange height. From these comparisons, the stiffness term is dominated by the external stirrup, with the three reaction sections providing significantly higher values. The data does illustrate effectively that the strengthened Wbeam is the most efficient repair scheme for each of the loading conditions and thus it was used for the remaining two external stirrup repair schemes

4.1.1.2 Comparison of IT beam Without Cutoff Bars: Service Loading

As noted previously, the behavior of the IT beams with fully developed flexural steel within the shear span included comparison with previous beam specimens without repairs, denoted in the current context as SPR350 beams. The SPR350 beams were part of a series of experiments to test the ultimate capacity of concrete beams with flexural cutoff details and varying stirrup spacing. Two beams are included in the current comparison, the first

specimen replicates the base specimens used in the current study with 457 mm (18 in.) stirrup spacing while the second beam exhibits 305 mm (12 in.) stirrup spacing representative of the repaired beams. The SPR350 loading history has been truncated for the service level range typical of the beams in the current study with a maximum applied shear force of 445 kN (100 kip).

Global behavior of the six beams is shown in Figure 4.15 in terms of applied shear force versus centerline displacement. The SPR350 beams show a decrease in stiffness after initial cracking with additional deflection of the 457 mm (18 in.) specimen in the higher load steps. The internal stirrup and carbon fiber fabric repair beams show little change in stiffness from the baseline specimens while the external stirrup and near surface mount specimens exhibit a slight decrease in stiffness over the baseline tests. Still, all the repaired specimens show a marked improvement between load steps in terms of permanent deformations; the external stirrup specimen is especially consistent throughout the loading cycles in this respect.

The centerline displacement of the four repair beams for the final loading step in the service range is compared to for the repaired condition in Figure 4.16. The plot indicates the internal stirrup specimen improved the baseline condition while the remaining beams exhibited slightly decreased stiffnesses. The external stirrup specimen shows a decrease over the baseline test, but the comparison of the baseline displacement was taken before the series of three repair sections were applied; therefore the comparison may not be

entirely accurate as the remaining repair specimens were only tested through one baseline test prior to repair and ultimately failure.

Panel strain provides a second measure of repair effectiveness that may not directly result in midspan displacement changes. Recall, two diagonal displacement sensors were used to calculate the average vertical strain data for one of three panels for a known crack angle. For the SPR350 beams, the compression diagonal data was not of sufficient resolution to make a comparison to the current beams. Thus, a comparison of the tension diagonal data is shown in Figure 4.17 for all six beams while the average vertical strain for the four repair beams is shown in Figure 4.18. Data included in the two previous figures were taken along the center panel along the eventual failure crack for the beam of interest. In Figure 4.17, the SPR350 beams exhibit linear behavior up to a shear of approximately 330 kN (75 kip) prior to cracking but showed similar displacement histories afterward. Of the repaired beams, the carbon fiber repair shows a small increase in stiffness relative to the baseline loading. The internal stirrup and carbon fiber strip specimens exhibit a much lower strain range throughout the loading history which is similar to the SPR350 305mm (12 in.) specimen, while the external stirrup and near surface mount specimen show larger strain values. Comparison of average vertical strain in Figure 4.18 indicates the baseline results were the least effective for the NSM beam, followed by the external stirrup, internal stirrup, and carbon fiber repaired beams. Relative changes due to repair were the greatest for the carbon fiber strip and external stirrup beam. The internal stirrup beam exhibited a minor improvement while the NSM beam was slightly worse than the baseline condition.

Average vertical strain ranges for the remaining panels for each of the repair beams is shown in Figure 4.19 based on a ratio of repaired to baseline strain range. The figure indicates the NSM repair was the least effective of the four beams with widely ranging strain values from one end of the beam to the other. The external stirrup repair beam exhibits minor changes along the north end but decreased strain ranges along the south end. The internal stirrup and carbon fiber strip beams exhibit significant reduction in average vertical strain throughout the service range.

Prior to comparisons of load sharing between internal and external stirrups, the local behavior of the integrally cast stirrups is shown for the baseline and repair condition in Figure 4.20 for a typical stirrup. Variability in cracking patterns resulted in strain histories for different stirrups within Figure 4.20 for each beam; the goal was to display a relevant strain history typical for the specimen of interest. The SPR350 beams again show a marked change in behavior on the onset of diagonal cracking, with large increases in strain after cracking. The external stirrup specimen repair illustrates a similar shape and range to the baseline test, with a reduction in strain due to post tensioning at the start of the test. The internal stirrup specimen indicates an increase in stirrup strain over the baseline specimen. The NSM and carbon fiber strip specimens show little to no difference in strain values over the service range.

The strain ranges of the remaining integrally cast stirrups for each repair method are shown in Figure 4.21. The near surface mount repair beam displayed a significantly larger strain

range for the repaired beam over the baseline specimen while the external stirrup beam included a reduction due to post tensioning for all but two stirrups. As with the average vertical strain, the carbon fiber strip and internal stirrup beam provide a significant reduction in internal stirrup strain over the service range. This provides evidence of load sharing between the integrally cast stirrups and the repair material.

The data analysis now turns toward each individual repair media with respect to load sharing. The data for the external stirrup specimen has previously been investigated and thus is not repeated. The internal stirrup repair beam included instrumentation of the supplemental steel at the location of a diagonal crack. Figure 4.22 illustrates the strain range of the north supplemental stirrups. The strain ranges of both bars are on the order of 200 με. As a point of comparison, the two supplemental stirrups are plotted against the strain range of the integrally cast stirrups before and after repair in Figure 4.23. The integrally cast stirrups show between 600 and 800 με reduction over the baseline specimen for an approximately 100 με range in the supplemental stirrups.

Load sharing and strain compatibility for the carbon fiber repaired beam can be expressed by investigating the integrally cast stirrup and carbon fiber strains and the average vertical and carbon fiber strains. Prior to comparisons, the location and identification of the surface mounted foil strain gages to the carbon fiber are identified in Figure 4.24. From this figure, the carbon fiber strain data can be compared to the average vertical strain as shown in Figure 4.25. The data indicates the average vertical strain is quite similar to

CFRP gage 3N which is located in the second panel of the beam at the location of a diagonal crack. Gages 2N and 5N, located along the same diagonal crack but along different CFRP strips, indicate additional strain when compared to the panel strain. Comparison of the integrally cast stirrup strain and carbon fiber strain is shown in Figure 4.26 for stirrup 1N and CFRP gages 1N, 2N, and 3N. The strain histories are similar for CFRP gage 3N and the internal stirrup strain, whereas CFRP gage 2N exhibits significantly higher strain for the service level loading. Bending of the CFRP strips combined with debonding makes direct comparison of strains with the internal stirrups difficult.

The NSM specimen thus far has shown little stiffness change or change in average vertical strain. However, strain data for the carbon fiber strips are presented which show the load contribution for the repair material. Strain gage locations for the near surface mount strips are shown in Figure 4.27 for the east and west face of the specimen. The cracking pattern was similar for both faces, thus comparison of carbon fiber strain data at the same crack location is shown in Figure 4.28 for gages NE2 and NW2B. The data indicates a similar strain history for the two strips. Load sharing among the integrally cast stirrups is shown in Figure 4.29 for stirrups 2N and 3N which are located adjacent to either side of the second NSM strip. Figure 4.29 indicates a higher strain along the lower crack (represented by NW2B) while the upper crack shows similar strain data to stirrup 2N. Average vertical strain data is shown in Figure 4.30 for the north end of the beam along with the NSM strains. Figure 4.30 indicates there is little correlation between the carbon fiber strips and average panel strain. The final comparison of NSM strain data is shown in Figure 4.31 as a distribution of strain away from a diagonal crack at NSM strip NW2. At this location, the

carbon fiber strip was instrumented at two cracks while a third gage was inserted between them. Figure 4.31 shows a significant reduction in strain at a distance of 114 mm (4.5 in.) from each crack throughout the service range. This indicates excellent stress transfer between the NSM and concrete substrate.

4.1.1.3 Comparison of IT beams without cutoffs: Strength Loading

Ultimate behavior of the IT beams is investigated in the following section, again with reference to the SPR350 beams. Crack map data for all the repaired beam specimens are shown in Figure 4.32 including crack formation for each load increment. The crack map data is replicated in Figure 4.33 for all the beam specimens with the cracks identified as precrack and repair. Also, a summary of the applied shear force at failure and failure mode for the beam specimens are shown in Table 4.2. The remainder of the comparisons mirrors those of the service level analysis.

Table 4.2 Beam specimen failure shear

Specimen:	V_{DL}		$V_{applied}$		V_{total}		Failure Mode
	kip	kN	kip	kN	kip	kN	
B.IT.NC.ES	4.8	21.17248	207	921	212	943	DT
B.IT.C.ES	4.8	21.17248	216	962	221	983	FA
B.T.NC.ES	3.4	14.94528	197	876	200	891	DT
B.IT.NC.IS	4.8	21.17248	239	1061	243	1082	FA
B.IT.C.IS	4.8	21.17248	237	1054	242	1075	DT
B.T.NC.IS	3.4	14.94528	197	875	200	890	DT
B.IT.NC.CF	4.8	21.17248	211	938	216	960	DT
B.IT.NC.NS	4.8	21.17248	162	719	166	740	DT

DT-diagonal tension
FA-flexural anchorage failure

Global behavior of the four beam specimens and two SPR350 beams is shown in Figure 4.35 in terms of applied shear versus centerline displacement. The SPR350 beams show a failure load of just over 445 kN (100 kips) for the 457 mm (18 in.) specimen while the 305 mm (12 in.) specimen reaches twice that shear force prior to failure. General trends for the repair beams include linear behavior to a shear force of 445 kN (100 kip) with larger permanent deformations occurring at subsequent load steps. The external stirrup repair beam maintains linear behavior up to a load of 668 kN (150 kip) while the internal stirrup repair beam maintains a linear behavior to between the 445 kN (100 kip) and 668 kN (150 kip) range. Beyond the linear stage, the displacement for a given applied shear force varied for each specimen. The displacement at 890 kN (200 kip) was smallest for the carbon fiber repair specimen, followed by the internal stirrup and finally external stirrup specimen; the near surface mount beam failed prior to this load, but still obtained a strength that was greater than SPR350 specimen with 457 mm (18 in.) stirrup spacing.

Tensile diagonal displacement and average vertical strain within the center panel along the eventual failure crack is shown in Figure 4.35 and 4.36 respectively. Tensile diagonal displacement data indicates the external stirrup repair behaved in a linear manner with little permanent deformation until a shear force of 667 kN (150 kip). After this load, the specimen begins to soften with larger permanent deformations with each subsequent load step. The internal stirrup specimen behavior is similar to that of the SPR350 beams, with an initial linear behavior which evolves into a nonlinear behavior with increasing permanent deformations as the loading increased. The carbon fiber repair provided the greatest stiffness increase over the higher load steps, until a shear force of 890 kN (200 kips), which was close to the eventual failure load. The near surface mount repair beam shows a linear behavior up to a shear force of 445 kN (100 kip), then stiffness begins to drop off sharply. Comparison of the average vertical strain among the four repair specimens show similar trends to the tensile diagonal data with the carbon fiber strip repair beam exhibiting the greatest reduction in strain with regard to the other specimens.

Typical integrally cast stirrup strain behavior for the ultimate loading case is shown in Figure 4.37. For this case, all typical stirrups previously investigated achieved yield, except for the carbon fiber strip repair specimen. The external stirrup repair beam exhibits an ‘S’ shaped curve which indicates as the applied shear force increases, there is more load sharing with the adjacent stirrups. The internal stirrup repair follows the baseline curve up to a shear force of 222 kN (50 kip) at which time the slope changes dramatically from the baseline curve and a compressive strain is experienced at the conclusion of each load step. The carbon fiber strip specimen shows a near vertical slope up to a shear force of 445 kN

(100 kip) at which time the behavior becomes nonlinear with minor permanent deformation at subsequent load steps.

Behavior of the repair beams is now investigated for the strength loading condition. Starting with the external stirrup repair beam, the average vertical strain and external stirrup strain data is shown in Figure 4.38 which indicates strain compatibility throughout the strain history. Turning toward the supplemental internal stirrup repair beam, the applied shear versus supplemental stirrup strain data is shown in Figure 4.39. Recall from the service level analysis, the data indicated a strain range on the order of 100 με. The first gage location now shows a strain range on the order of 600 με while the second gage achieves a strain range beyond the limit of the strain gage itself. Recall, the yield strength of the supplemental stirrups was 468 MPa (120 ksi) which results in a strain reading of 4138 με. The range of the foil strain gages for the selected gain setting, is on the order of 3800 με, therefore, there is no definitive way to know if the gages reached yield. However, the shape of the curve and horizontal nature near the end of the loading cycle in Figure 4.39 provides an indication this may be the case. A review of the integrally cast and supplemental stirrup strain data is shown in Figure 4.40. The integrally cast stirrups continue a similar slope from the service loading, with an increased slope at the higher load steps. This occurs as the strain in the supplemental stirrups begin to increase in both bars which indicates the integrally cast stirrups are taking more load as the beam approaches failure.

Comparison of the carbon fiber repair specimen for the strength loading condition is shown in Figure 4.41 in terms of average vertical strain and CFRP strain. The service load data in Figure 4.25 indicated the average vertical strain and CFRP gage 3N were in close alignment. Therefore, the remaining CFRP gages are not shown for the strength condition. The data indeed shows a similar behavior between the CFRP and panel strain throughout the strength loading. Local behavior of the CFRP repair during the strength loading is shown in Figure 4.42 as integrally cast stirrup and carbon fiber strain data. The service level analysis showed consistency between CFRP gage 3N and internal stirrup 1N, therefore the remaining CFRP gages are not included in Figure 4.42. The stiffness of CFRP gage 3N changes at a shear force of 396 kN (89 kip), which is evident for the final load step over the service range but emerges distinctly during the following two load steps. Afterward, the stiffness changes two additional times between load steps accompanied by ever larger permanent deformations until failure. The internal stirrup exhibits a slight decrease in stiffness before changing to a higher slope for the final load steps.

The strength loading condition for the near surface mount beam illustrates strain throughout the depth of the member, load sharing with integrally cast stirrups, comparison of average vertical strain to carbon fiber strain, and the distribution of strain within the carbon fiber at a fixed distance from a crack for the strength loading condition. The first comparison, shown in Figure 4.43 illustrates the strain data for two NSM strips at the same crack location. Figure 4.43 indicates the two curves begin to diverge from each other after the service level strains are exceeded with a maximum deviation of approximately 1200με for the gage located on the west side of the specimen. Comparison of the integrally cast

stirrup strain with that of the carbon fiber is shown in Figure 4.44. The service level range of data indicates consistent strain readings for internal stirrup 2N and the carbon fiber gages. However, as the applied shear increases, the carbon fiber begins to behave in a nonlinear fashion.

Average vertical strains are compared to the carbon fiber strains in Figure 4.45. The figure indicates reduced strain compatibility throughout the strain range, which was consistent with the service level loading analysis. The distribution of strain along the carbon fiber is shown in Figure 4.46 for NSM strip NW2. The top and bottom gage for this strip were located along diagonal cracks while the center gage was mounted equidistant from the previous two. The center gage shows little strain for the service level loading, but exhibits a significant increase in strain during the second load step above the service range. For this load step, the upper and lower gages do not change slope. The center gage experiences a large strain range for the last two load steps, but they are still less than the strain range of the remaining gages.

4.1.2 IT Beams With Flexural Cutoff Details

Flexural cutoff details are typical of vintage CRC bridges, but the repaired behavior of such members is not well understood as the moment-shear interaction changes within the shear span. Thus, two IT beams similar to the previous four were constructed to

investigate the internal and external stirrup repair methods. The repair schemes were similar to that used for the previous IT beams, thus the only change was the available flexural steel long the span length. No comparison to the SPR350 beams is included in this series of beams, as no comparable specimens were available. However, the beams do provide a comparison to each other and to the previously described IT beams.

The internal stirrup repair beam was damaged during handling which produced a large spall to the flange. However, the damage was contained within the outer portion of the flange at the terminal end of one of the flexural cutoff bars and did not continue through the depth of the stem, as shown in Figure 4.47. The beam was tested such that the damaged south end was loaded only through the stem. Also, the beam was repaired with four supplemental stirrup bars at the south end and only two at the north end as shown in Figure 4.48, as to force the failure on the north end of the beam where the bearing condition was identical to the previous IT beams. The beam did however fail on the south side and therefore the pertinent strain data is presented for this condition.

4.1.2.1 Comparison of IT Beam Specimens with Flexural Cutoff Details: Service Loading

Global behavior of the two repaired beams are shown starting with applied shear force versus displacement in Figure 4.49. In each case, the repaired specimens exhibited a minor decrease in midspan displacement over the baseline tests. Panel displacement is shown in

Figure 4.50 and 4.51 in terms of tensile diagonal displacement and average vertical strain. The tensile diagonal data is included for reference to the previous IT specimens. Nonetheless, the tensile diagonal displacements indicated a slight decrease for the external stirrup repair specimen but no relative change for the internal stirrup repair! Average vertical strain, shown in Figure 4.51, indicates a different result. While the external stirrup repair exhibits a simple linear offset in the repaired condition, the internal stirrup beam shows significantly reduced average vertical strains.

A similar trend is shown for the local behavior of the integrally cast stirrups, shown in Figure 4.52. The external stirrup beam provides an offset for the starting strain values but had similar slopes. The internal stirrup beam displays almost linear behavior with significantly reduced strain range compared to the baseline test.

A comparison of individual repair media to local beam behavior is presented, starting with the external stirrup repair beam. Specifically, a comparison of the reduction in the integrally cast stirrup strain for the external stirrup specimen is shown in Figure 4.53. The data indicated that for the dead load condition, the post tensioning reduced the stirrup strain but was not enough to place the stirrups into compression. Next, strain compatibility as measured by the external stirrup and panel strain, is shown in Figure 4.54 which indicates consistent strain compatibility was maintained throughout the service loading history.

A review of the internal stirrup repair method indicates load sharing among the supplemental and integrally cast stirrups. Strain data for the supplemental internal steel stirrups alone is shown in Figure 4.55 while Figure 4.56 includes the integrally cast stirrups. Figure 4.55 indicates small and non uniform distribution of the strain ranges in the supplemental stirrups along the south side. Comparison with the integrally cast stirrups indicated a significant reduction in integrally cast stirrup strains due to the presence of the supplemental bars as seen in Figure 4.56.

4.1.2.2 Comparison of IT beam specimens with flexural cutoffs: ultimate loading

Each of the two repaired beams failed due to flexural anchorage failure at the location of the cutoff within the flange however, the path of the failure crack varied significantly between the two specimens. The external stirrup repair beam exhibited a failure crack originating from the terminal end of the cutoff bar within the flange. The crack then propagated to the stem where it continued at approximately 45 degrees to within 50 mm (2 in.) to 100 mm (4 in.) of the top of the stem as shown in Figure 4.32. The crack then flattened out as it approached the actuator support plate. The internal stirrup specimen exhibited a similar starting point, but the crack continued along the flange instead of converging at the interface with the stem. Figure 4.57 illustrates the affect of the reinforced stem by diverting the crack around this area; the extents of the four internal stirrup bars are shown in the figure.

Global behavior of the two repaired beams for the failure loading case is shown in Figure 4.58 in terms of centerline displacement. Both beams exhibit linear behavior over the service level loading, then become non-linear with larger permanent deformations for each subsequent load step. The internal stirrup repair exhibits a lower displacement for each load step and a slightly higher ultimate load compared to the external stirrup repair.

Panel behavior in terms of tensile diagonal displacement and average panel strain for the two repaired beams is shown in Figures 4.59 and 4.60 respectively. The tensile diagonal displacement of the internal stirrup repair beam in Figure 4.59 exhibits a gradual decrease in stiffness for each subsequent load step beyond the service level. The external stirrup beam on the other hand, displays almost a bilinear behavior over the loading range. The average vertical strain data in Figure 4.60 exhibits a similar behavior to the previous graph with the internal stirrup specimen exhibiting a gradual softening after each load step while the external stirrup repair exhibits almost bilinear behavior above 667 kN (150 kip).

Local behavior of the integrally cast stirrups are shown in Figure 4.61 for the two repair beams. The internal stirrup repair specimen continues the dramatic change in slope for the repaired case above the service level loading before showing signs of softening between 667 kN (150 kip) and 890 kN (200 kip), but the stirrup does not achieve yield. The external stirrup repair beam exhibits a offset value in strain that is typical of the repair thus far. However, the strain history indicates a point where additional shear force results in

little to no addition of strain in the steel. This phenomenon occurs for three load steps prior to failure resulting in a lower strain at zero load.

Strain compatibility for the external stirrup repair beam is shown in Figure 4.62 in terms of external stirrup strain and average vertical panel strain. Compatibility between the two responses is consistent throughout the loading history, even when strain is beyond the limits of the foil strain gages, denoted by the vertical line on the curve.

Supplemental stirrup strain history is shown in Figure 4.63 while load sharing among the supplemental and integrally cast internal stirrups are detailed in Figure 4.64. Figure 4.63 indicates a strain range for the supplemental stirrup on the order of 600 με -800με which is higher than the measuremens experienced during the service level loading, but still far below yield. The supplemental and integrally cast stirrups show significant load sharing throughout the failure loading history with the integrally cast stirrups exhibit higher strain for majority of the gages, often until the final load step is achieved.

4.2. T Beam Specimens

Two T beams were repaired as part of the current study based on the results from the IT internal and external repair beams. The T beams used grade 420 (60 ksi) steel with a

smaller area to achieve the goal of increasing the base specimen 610 mm (24 in.) spacing to that of 457 mm (18 in.). Two specimens from the SPR350 work are included in the comparison; however, one of the specimens was part of a fatigue study, thus only the precrack data for the service level analysis is presented here—the final post fatigue behavior is not directly comparable with the present work.

Prior to comparison of the two repair beams, the data for the external stirrup repair must be documented, because a sequence of tests was performed on this specimen prior to the failure loading event. After baseline loading of the external stirrup repair beam, the initial failure loading sequence resulted in excessive midspan displacement, indicative of a flexural failure and so the test was halted. Further investigation indicated that the shear force required to initiate flexural failure of the strengthened beam was lower than the anticipated shear failure load, thus the test setup was modified to decrease the length of the shear span by moving the outer bearings and reaction sections inward 457 mm (18 in.) for each shear span as shown in Figure 4.65. After which time, a second baseline loading sequence was completed due to the changes in the moment shear interaction due to the decreased shear span. The specimen was retested and as the theoretical failure load was achieved, the specimen did not exhibit imminent shear failure. Additional shear force would have resulted in a flexural failure, thus the specimen was unloaded a second time. A third baseline test was completed due to any accumulated damage and/or permanent deformations associated with the previous testing sequence. The contribution of the external stirrups was higher than anticipated for the given shear span, therefore a shear failure mode was only possible if the contribution from the external stirrups was reduced.

Thus, every other external stirrup was removed as shown in Figure 4.66, and post tensioned for the third and final loading sequence, resulted in shear failure of the specimen. The sequence of three tests performed on the T beam were unintended but provide data for two different shear span to depth ratios and two different external stirrup spacing. The following comparison between the internal stirrup and SPR350 beams reference the third baseline and subsequent failure noted above. In addition, comparisons for the three tests on the external stirrup repair beams are included after the service level comparison is descrbed.

4.2.1 Comparison of T Beam Specimens: Service Loading

Global behavior among the T beams in terms of midspan displacement is shown in Figure 4.67. The repaired beams show little variation between the baseline and repaired conditions but exhibit increased stiffness over the SPR350 beams. The internal stirrup beam shows an increased stiffness compared to the external stirrup repair.

Tension diagonal displacement for the three beams is shown in Figure 4.68. The repaired beams exhibited reduced diagonal displacement for the repaired condition. The internal stirrup displacement is slightly less than that of the external stirrup beam throughout the service load. Comparison of average vertical strain for the two repair beams is shown in

Figure 4.69. The external stirrup specimen shows similar shape although shifted response for the repaired condition compared to the internal stirrup repair.

Local behavior of the integrally cast stirrups are shown in Figure 4.70. The SPR350 beams show a large deviation in strain for the 334 kN (75 kip) load step, with the 610 mm (24 in.) specimen reaching yield prior to failure. The 457 mm (18 in.) specimen exhibits reduced strain through for the final two service load steps. The external stirrup specimen shows a significant initial reduction in amplitude of strain due to post tensioning, although the range is not reduced as much. The internal stirrup repair beam shows similar strain behavior although the strain amplitudes are reduced slightly for the repaired case. The strain ranges were similar to that of the larger spaced stirrup SPR350 beam.

Strain compatibility of the external stirrup repair is shown in Figure 4.71 for two of the north panels. Comparison of panel 3N and external stirrup 7N (located adjacent to the spreader beam near midspan) indicates a large differential between the panel shear and the external stirrup strain. This is due to the location of the stirrup relative to the panel—as the external stirrup is located near the start of the panel not in the center of the panel as was the case for the previous IT beams. The second comparison of panel 2N and external stirrup 5N shows a better agreement and shows that the unbonded external stirrups correspond to average vertical strain in the section.

The reduction in strain due to post tensioning for the external stirrup repair is shown in Figure 4.72. The plot includes the three tests performed on the external stirrup specimen. The graph indicates several of the gages were placed into compression after post tensioning. Figure 4.72 also illustrates the reduction in strain for case C is less than that of case B since the stirrups were reduced by two. A comparison of the absolute reduction in strain for the three external stirrup repair specimens is shown in Figure 4.73. The graph is interesting because the three specimens had different cracking patterns, stirrup spacing, and concrete strengths, but the reduction in strain varied consistently between 100 με to 300 με among all three specimens.

The supplemental stirrup strain data and load sharing among the integrally cast stirrups are shown in Figures 4.74 and 4.75 respectively. For the supplemental stirrups alone, the strain range for 1S is on the order of 1800 με while bar 2S is on the order of 1000 με. These values are higher than the previous internal stirrup repair beams for the service range. A comparison of load sharing with the integrally cast stirrups in Figure 4.75 reveal little change for the baseline and repair condition.

Attention is now turned toward the external stirrup specimen in terms of the three testing configurations mentioned previously. Global behavior is shown in Figure 4.76 for applied shear versus centerline displacement. The plot is noteworthy as it displays an improvement for test A for the repaired condition as well as an overall reduction in displacement between test A and B baseline values as would be expected with a shorter

shear span. Comparing the baseline and repaired conditions of tests B and C indicate test C provides less reduction which is proportional to the number of active external stirrups used for the final condition.

Local behavior of the internal and external stirrup strain ranges are shown for the sequence of three tests in Figures 4.77 and 4.78. The internal stirrup strain ranges follow a similar trend to the centerline displacement. Comparison of the baseline curves for tests A and B indicate essentially the same strain range for the two cases as well as reduction in strain due to the repair. The second observation relates to the reduction in strain for tests B and C which again is related to the number of post tensioned stirrups used in each test. External stirrup strain for each test is shown in Figure 4.78. Each curve displays an 'S' shape with a higher strain range for each subsequent test. This is consistent with the testing sequence as test B resulted in the same shear force but different moment-shear interaction and test C differed from test B with fewer external stirrups indicating the same load shared by fewer elements results in higher strain for the remaining external stirrups. Strain compatibility among the three external stirrup tests are shown in Figure 4.79 with similar shape and slope for each case.

4.2.2 Comparison of T Beam Specimens: Strength Loading

Global response of the two repaired beams and that of SPR350 beams are shown in Figure 4.80. Recall, the SPR350 457 mm (18 in.) specimen was used for fatigue analysis in the previous study; therefore the service loading cycle is echoed in the following graphs for reference only. The remaining SPR350 beam with 610 mm (24 in.) stirrup spacing failed at a displacement of 25 mm (1 in.) with nonlinear progressive permanent deformations for each subsequent load step. The external stirrup repair specimen exhibited a near bilinear behavior with a limited permanent deformation throughout the higher load steps with diminished midspan deflection at failure compared to the internal stirrup repair beam. The internal stirrup repair beam exhibited an initial linear behavior followed by a progressively softer behavior until failure.

Tensile diagonal displacement is shown for the beams in Figure 4.81. The 610 mm (24 in.) SPR350 beam failed at a quite large displacement that was not evident in any of the repair beams in the current study. The repair beams did not exhibit a strain of 0.2 until the last and second to last load step for the external and internal stirrup repairs respectively. Also, as in the previous comparisons, the external stirrup repair exhibited a reduced permanent deformation at the higher load steps when compared to the internal stirrup repair beam. A second trend is shown for the internal stirrup specimen in terms of an initial linear curve followed by a gradually softening nonlinear behavior whereas the external stirrup specimen exhibits a near bilinear behavior until failure.

Average vertical strain for the two repair beams is shown in Figure 4.82. In each case, the repaired curves exhibited a slight decrease in strain over the service load values. However, the internal stirrup specimen exhibits significant permanent deformations once the behavior turned nonlinear. The external stirrup repair specimen exhibited behavior similar to the tensile diagonal strain in Figure 4.81 with minor permanent deformation throughout the service level load steps with large deformation prior to failure.

Integrally cast stirrup strain is shown in Figure 4.83 for the two repaired beams and the SPR350 specimens. The SPR350 specimen exhibited similar strain at the service level comparison, as the beam failed on the subsequent load step just beyond the 445 kN (100 kip) of applied shear. The external stirrup specimen exhibited a similar trend that was evident on the previous two specimens—that of initial strain reduction due to post tensioning coupled with a similar shape and slope to that of the baseline test. The stirrup of interest in this case did not achieve yield prior to specimen failure. The internal stirrup specimen exhibited yielding strain values after the service level loading. The loading history exhibited minor hysteresis at the onset of load with a linear behavior prior to yield.

Strain compatibility for the external stirrup repair specimen is shown in Figure 4.84 for the strength condition. The two curves are very similar for each load step, reproducing a trend that was evident in the previous two external stirrup repair specimens.

The supplemental internal stirrup strain values and behavior with the integrally cast stirrups is shown in Figures 4.85 and 4.86 respectively. For the supplemental stirrup strain in Figure 4.85, the two gages achieve yield strain, with a noted change in slope. The south supplemental stirrup exhibits a change in behavior at a shear force of 600 kN (150 kip) with strain values less than yield but a noted offset after the loadstep. Load sharing among the integrally cast stirrup is shown in Figure 4.86. The integrally cast stirrups showed lower strains compared with the diagonal supplemental stirrups.

4.3. Bent Cap Specimens

Repair of the bent cap specimens included two methods: external surface bonded carbon fiber strips and longitudinal post tensioning. The geometry and materials used for concrete, flexural, and integrally cast stirrup steel were identical for each bent cap. Flexural cutoff details were present in the three layers of reinforcing steel as shown previously in Chapter 3. The two repaired specimens were compared with a previous specimen tested at OSU with identical geometric and material properties, but which was not repaired prior to failure. The bent cap specimens provide a large array of data to investigate global behavior in terms of midspan and stub girder displacement, average vertical strain data, and column lateral displacements. The specimens also provide a great deal of local behavior for the integrally cast stirrups, flexural slip of the bars embedded into the column, as well as flexural strains within the column and at midspan; however,

only the data pertaining to the integrally cast stirrup strains are investigated in the current study. The results of interaction with the repair media provide a measure of effectiveness for each repair over the service and strength loading cycles.

4.3.1 Bent Cap Specimen: Service Level Performance

The post tensioned bent cap repair specimen includes baseline loading histories that are less than the applied shear in the remaining baseline tests. As the post tensioned repair specimen was the first to be cast, the reduction in initial cracking shear was meant to limit the probability of specimen and/or gage failure. Also, the loading sequence prevented reduction in the service level shear in the two remaining specimens for equal comparisons. For example, if the final service load step included a 890 kN total shear force, this would have been applied at 445 kN per actuator. If the post tensioned specimen was only subjected to a total shear force of 779, it would result from two equal actuator forces of 389.5 kN.

Global displacement for the bent cap specimens was measured at three locations: midspan of the section and at the north and south stub girder locations. The results of the applied shear versus midspan, south, and north stub girders are shown in Figures 4.87 through 4.89. The midspan displacement graph indicates both repair specimens exhibited decreased displacement throughout the service level loading history with the post tensioned

specimen exhibiting the lowest displacement value at the final load step. Global displacement and stiffness trends are evident for both stub girders in Figures 4.88 and 4.89.

Another measure of global behavior that is interrelated to midspan displacement is column displacement. Recall, the bent specimen is fixed at one end but rests on a roller on the other. Thus, displacement between the two columns as well as displacement of the roller end from a fixed point away from the specimen can be compared. The behavior between the two columns is shown in Figure 4.90. Again, the two repair specimens exhibit decreased column displacement over the control specimen. The response history shows hysteresis of similar shape but the post tensioned specimen exhibited a significant reduction due to the large applied post tensioned force. Absolute column displacement is shown in Figure 4.91 with similar trends. Both repair specimens exhibit lower displacement values compared to the control specimen. Also, the carbon fiber repair showed little difference in column displacement for the repaired condition. The post tensioned specimen does show a marked difference in column displacement, but this is due primarily from the post tensioned force applied at the level of the internal flexural reinforcing.

Tensile diagonal displacement data for the north and south panels is shown in Figure 4.92 and 4.93 respectively, due to the absence of compressive diagonal displacement data for the control specimen. In each graph, the control specimen exhibited no displacement for the first load cycles, prior to first cracking. For the north panel data in Figure 4.92, the

displacement values for the control specimen exhibited changes in slope for the final two load steps after initial cracking. The two repair specimens exhibit a similar displacement for the baseline tests, which are smaller in relation to the control specimen. The carbon fiber specimen exhibited a reduced displacement over the baseline test for each subsequent load step, but the changes were minor compared to the behavior change for the post tensioned specimen. The data indicates the post tensioned specimen exhibits little to no movement until the final two load steps, similar to the control specimen except the post tensioned case was cracked prior to testing. Results of the south tensile diagonal are shown in Figure 4.93 with similar results.

Average vertical strain data for the two repair specimens is shown in Figure 4.94. The carbon fiber specimen exhibits a similar shape with a nominal decrease in displacement at the higher load steps. The post tensioned specimen exhibits a dramatic change in slope and starting strain value, which supports the behavior of the previous figures.

Local behavior of the bent cap specimens, in terms of integrally cast stirrup strain, is shown in Figure 4.95 and 4.96 for typical north and south stirrups. For the typical north end stirrup in Figure 4.95, the control specimen exhibited little to no strain prior to cracking, as would be anticipated, followed by a large increase in strain. The stirrup maintained a linear relationship prior to the last load step in which it achieved yield. The post tensioned specimen exhibited hysteresis for the repaired case which reduced the strain range for each load step. This reduction is not the shown for the carbon fiber repair

specimen. However, the gradually increasing slope of the baseline curve is not evident for the repair case, indicating a consistent response for the service load case which was not obtained in the baseline test. The repaired condition shows little strain in the integral stirrups, indicating the load sharing between the CFRP is quite sufficient. However, once the strain in the carbon fiber began to falter due to debonding of individual strips, load is again taken by the integrally cast stirrups with a nonlinear response up to yield at the service level.

The behavior of the south integrally cast stirrup in Figure 4.96 exhibit similar trends with several notes. The control specimen again exhibited no strain within the stirrups prior to cracking but eventually achieves yield of the stirrups for the service level load range. The post tensioned specimen exhibits a reduced strain range but does not exhibit the degree of hysteresis that was present on the north end as well as the fact that the stirrup achieves yield in the baseline and repaired condition. The carbon fiber repair specimen exhibits decreased stirrup strain for the first few load steps, ultimately giving way to strain values in the final load step.

The previous two graphs provide a snapshot of the behavior of the integrally cast stirrups, but providing graphs for each of the individual 16 stirrups is not warranted. Instead, the service level strain ranges for the north and south stirrups are shown in Figures 4.97 and 4.98 respectively, keeping in mind the post tensioned baseline condition resulted in a slightly lower shear force within the stirrups. All but one of the gages in Figure 4.97 for

the north side operates below the yield plateau. The gages near the centroid of the cross section indicate the carbon fiber repair significantly reduced the service level strain values for each gage. The post tensioned specimen exhibited a reduction in strain, but it was minor in comparison to the carbon fiber repair. It is also interesting to note the baseline strain readings for the carbon fiber repair are higher than the control and post tension specimen but the repair strain values are lower. Strain ranges at the south end are typically higher due to the fixed constraint at the base of the column. The control specimen does not show much strain range for this case, but this may be due to the location of the diagonal crack just above or just below the gage locations. The post tensioned repair specimen exhibits significant strain ranges for the baseline specimen and significant reduction in strain for the repair case. The carbon fiber repair specimen shows a mixed result with little to no strain readings for all but four of the gages. However, three of those gages experienced a reduction.

The effectiveness of the carbon fiber repair can be shown by comparing the surface carbon fiber strain range data to that of the panel and integrally cast stirrup strain. The orientation and numbering scheme for the carbon fiber repair specimen is shown schematically in Figure 4.99. A closer view of the north panel—where failure occurred—is shown in Figure 4.100 with the integrally cast stirrups numbered below the targets and the surface mounted foil strain gages numbered at or above the targets. A graph of the average vertical strain and CFRP strain data is shown in Figure 4.101 which indicates carbon fiber strain is larger than the panel strain for gages 3N, 6N, and 7N but less for the remaining gages. For gages 6N and 7N, the carbon strain appears to be twice that of the panel strain. This may

be due to membrain stresses on the outer surface of the carbon fiber due to debonding away from the crack. Evidence for this behavior is typically found as permanent strain after unloading that is not indicative of actual strain in the remainder of the carbon fiber strip. A further view of local behavior can be seen from Figure 4.102 which compares integrally cast stirrup and surface mounted foil strain gage data. The reduction in integrally cast stirrup strain for the north end of the bent was evident in Figure 4.97, however the interaction between the integrally cast stirrup is seen clearly in Figure 4.102. The carbon fiber reduced the stirrup strain by half for the service level loading.

4.3.2 Bent Cap Specimen: Strength Level Performance

Crack map data for the repair specimens is shown for the baseline and repair case in Figure 4.103; failure shear for each specimen is shown in Table 4.3. Global load versus displacement graphs for midspan, south and north stubs are shown in Figures 4.104 through 4.106. The control specimen failed before the next full load step (recall each stub was loaded first individually in a half step loading sequence then together in a full step sequence) with a large displacement at failure. The carbon fiber specimen failed at just over 1335 kN (300 kip) due to abrupt bond failure between the CFRP and concrete but failed at a larger displacement than the post tensioned specimen. Video evidence of the failure showed debonding of one strip resulted in a domino affect for the remaining strips and eventually the specimen itself. It was odd that the failure occurred on the north end, as all previous unrepaired specimens failed at the south end, presumably where the additional

restraint of the fixed support resulted in failure. However, by removing the added strength gained by the CFRP at the north end, the base specimen was insufficient to maintain the resulting applied shear. The post tensioned specimen failed at a slightly lower shear than the carbon fiber repair, but failure occurred at the south end. Prior to failure, the specimen was unloaded and an additional post tensioned force was applied to the specimen, which was again loaded to essentially the same load and failure soon followed.

Table 4.3 Bent cap specimen failure shear

Specimen:	Failure Shear:	
	kN	[kips]
D.T.C.PT	1398	314
D.T.C.CF	1527	343

Column displacement data is shown in Figures 4.107 and 4.108 for relative and absolute displacement. The relative column data in Figure 4.107 indicates the carbon fiber specimen failed at a similar displacement to the control specimen whereas the post tensioned specimen failed at a reduced displacement. Both repair sections followed a linear behavior through the failure loading cycle. Similar trends are evident for the absolute column displacement in Figure 4.108.

Tensile diagonal displacement and average vertical strain is shown in Figure 4.109 for the north end and 4.110 for the south end of the bent caps respectively. The tensile diagonal

data in Figure 4.109 indicates the carbon fiber repair specimen showed lower displacement values compared to the control specimen for all but the last load step. The post tensioned specimen exhibited a similar behavior compared to the service level loading, with gradually increasing displacement until failure. Average vertical strain data in Figure 4.110 indicates the south end of the carbon fiber repaired bent cap progressed through the loading cycle with a near linear behavior (as the south end remained intact throughout the test). The behavior of the post tensioned specimen along the eventual failure side shows an improvement over the baseline curve. The second post tensioning cycle is close to specimen failure, as the horizontal line indicates significant panel elongation with no additional shear.

Data for the south tensile diagonal is shown in Figure 4.111. The behavior of the post tensioned specimen mirrors the initial load steps of the north end, discounting the eventual failure event with typical strain less than 0.05. The strain range is well below the other two specimens. The carbon fiber repair specimen exhibits behavior that is similar to the average vertical strain, with minor initial strain followed by a near linear behavior until failure occurred at the north end.

Local behavior of the north and south integrally cast stirrups are shown in Figures 4.112 and 4.113 respectively. For the north end, the internal stirrup achieves yield during the service level range and continues into strain hardening as is evident in the figure. The post tensioned specimen does not achieve yield, yet this may be due to the fact failure did not

occur at the north end for this specimen. As would be expected, the post tensioned specimen does achieve yield and continue into strain hardening, as this was the failure end of this beam. The carbon fiber repair specimen also achieves yield just prior to failure. The slope of the repair curves for the two repair specimens are quite different, which indicates the carbon fiber repair specimen provides greater load sharing between the integrally cast stirrups and the carbon fiber.

Strain compatibility and load sharing of the carbon fiber repair specimen are shown in Figure 4.114 and 4.115. The average vertical strain values are significantly less than that experienced in the carbon fiber for the higher load steps. This is supported in Figure 4.115 which compares the integrally cast stirrup strain with carbon fiber strain. In the higher load steps, the carbon fiber strain is essentially twice that of the internal stirrup for the whole step values.

a)

b)

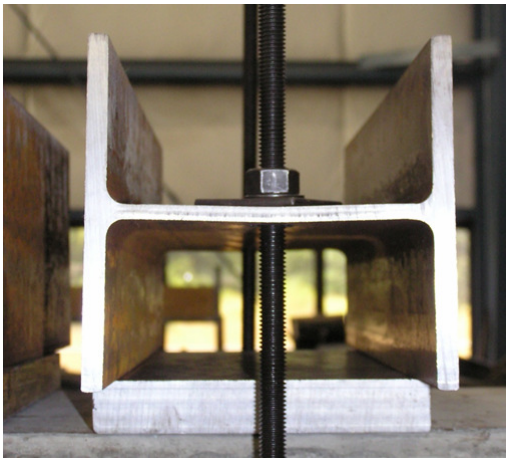

c)

Fig. 4.1 – External stirrup repair: a) channel section, b) Wbeam, c) Strengthened Wbeam (note deformation of the web for case b)

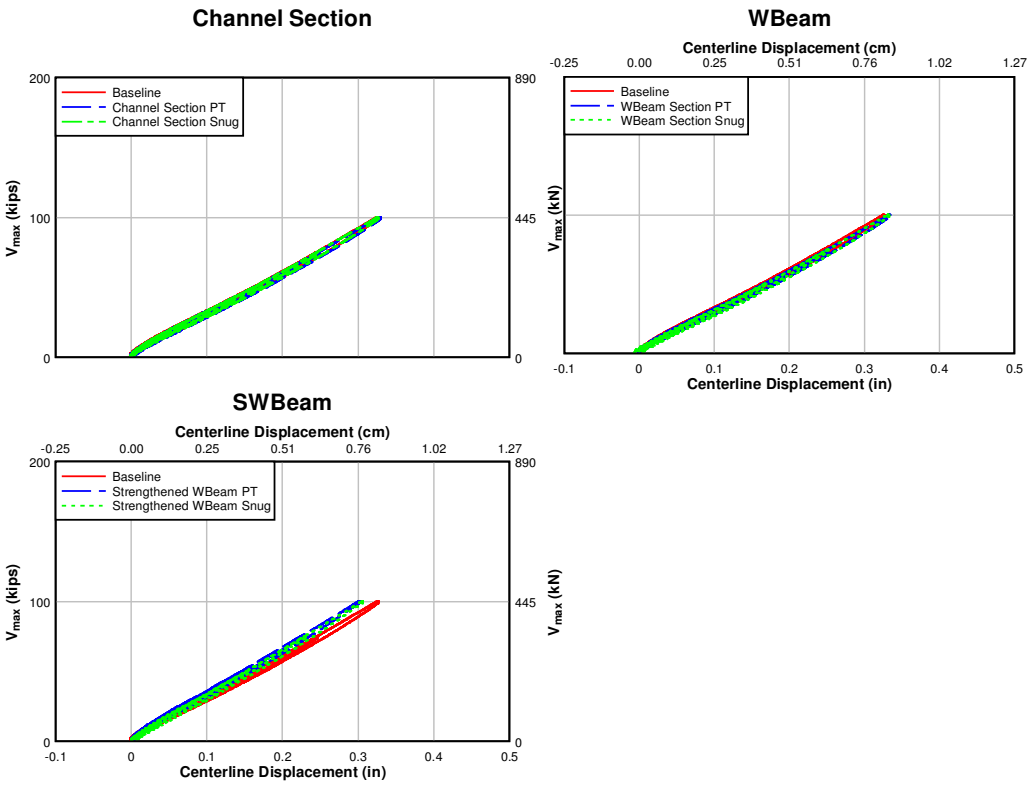

Fig. 4.2 - Maximum shear force versus centerline displacement:

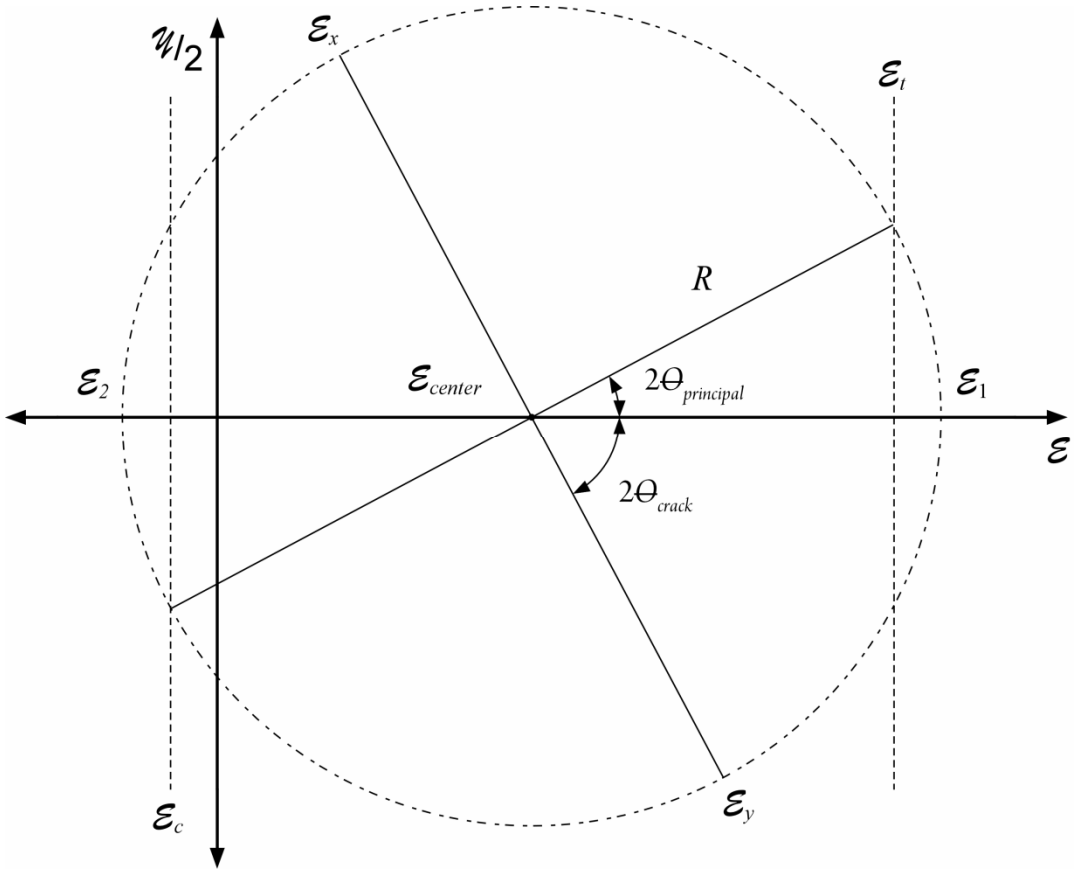

Fig. 4.3 - Mohr's circle for strain.

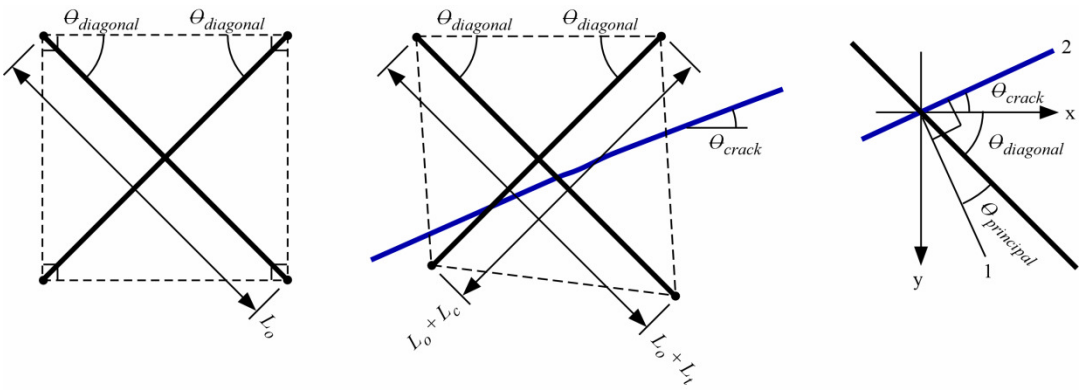

Fig. 4.4 – Diagonal displacement geometry

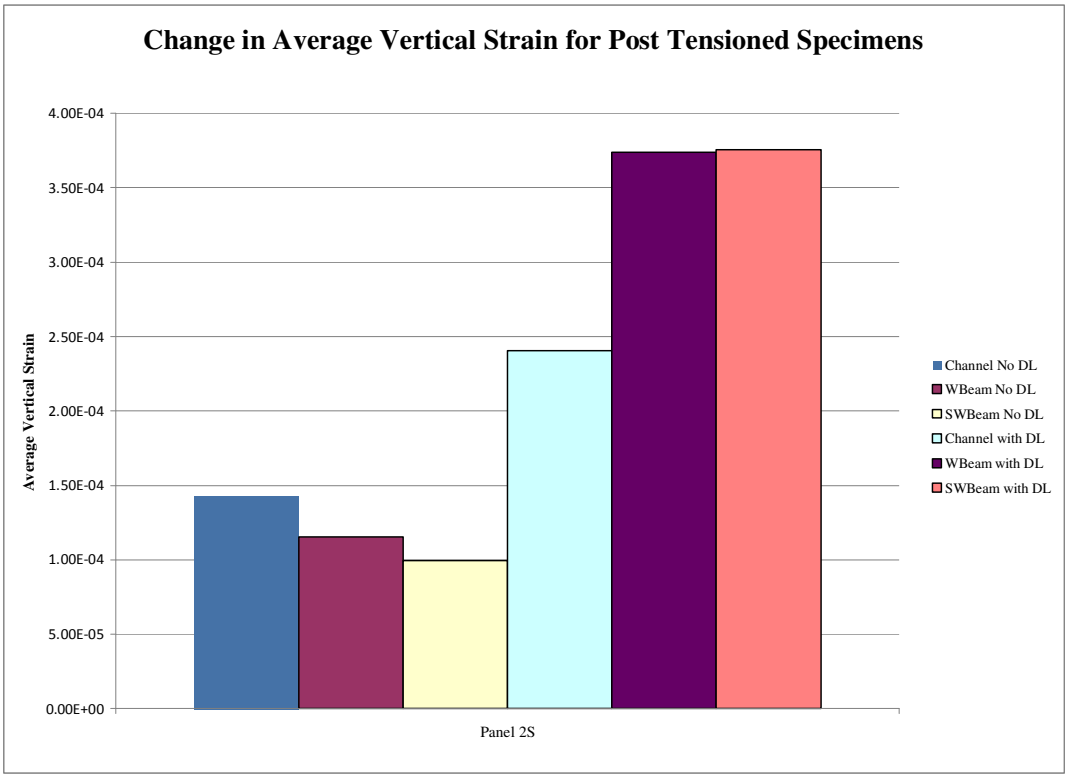

Fig. 4.5 – Average vertical strain comparison between different dead load and external stirrup support conditions at installation of external stirrups due to post tensioning condition

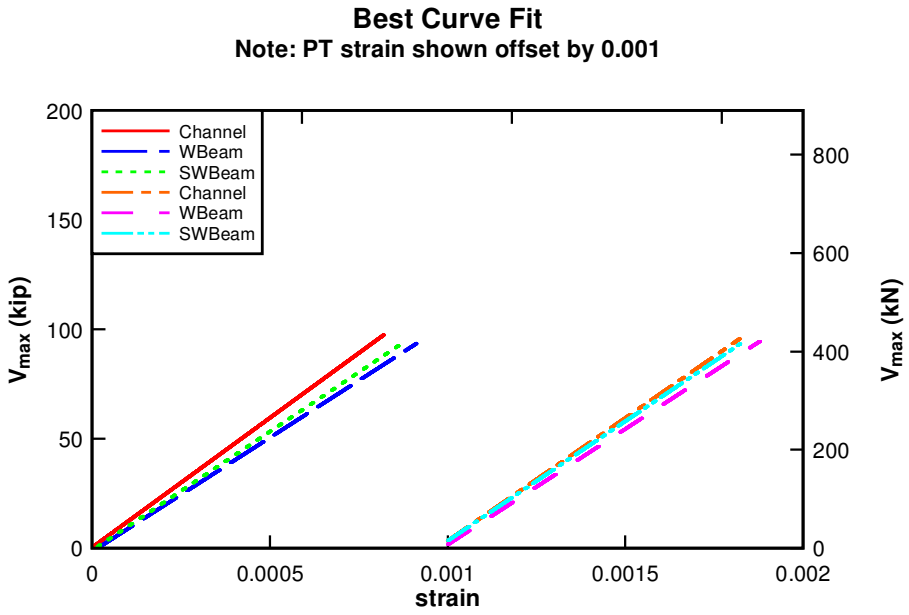

Fig. 4.6 – Best fit curve of shear versus average vertical strain for panel 2S: beam self weight

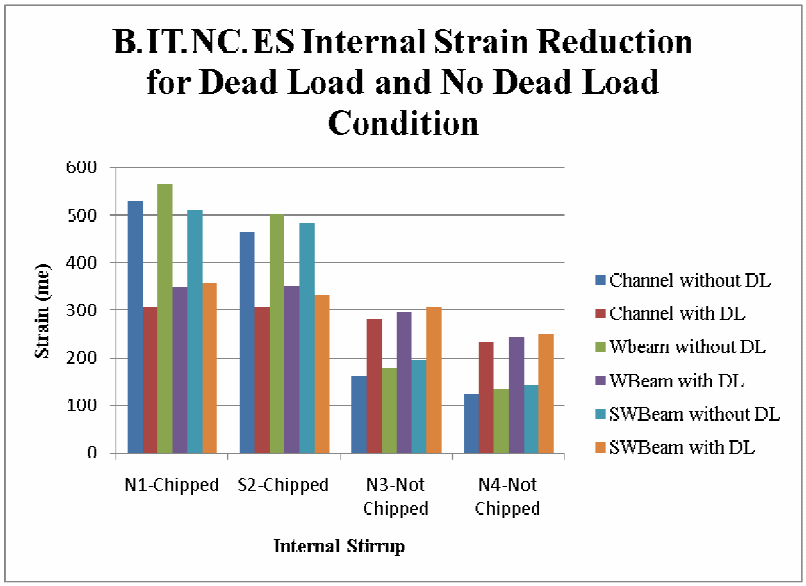

Fig. 4.7 – Integrally cast stirrup absolute strain reduction due to post tensioning

Fig. 4.8 – Exposure of integrally cast stirrup leg to replace failed strain gage

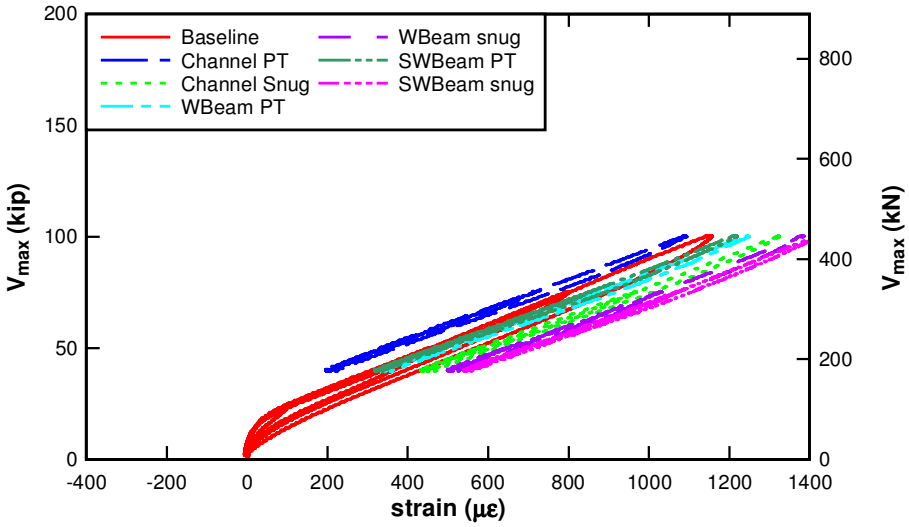

Fig. 4.9 – Shear force versus internal stirrup 3N strain range for three reaction sections: service loading

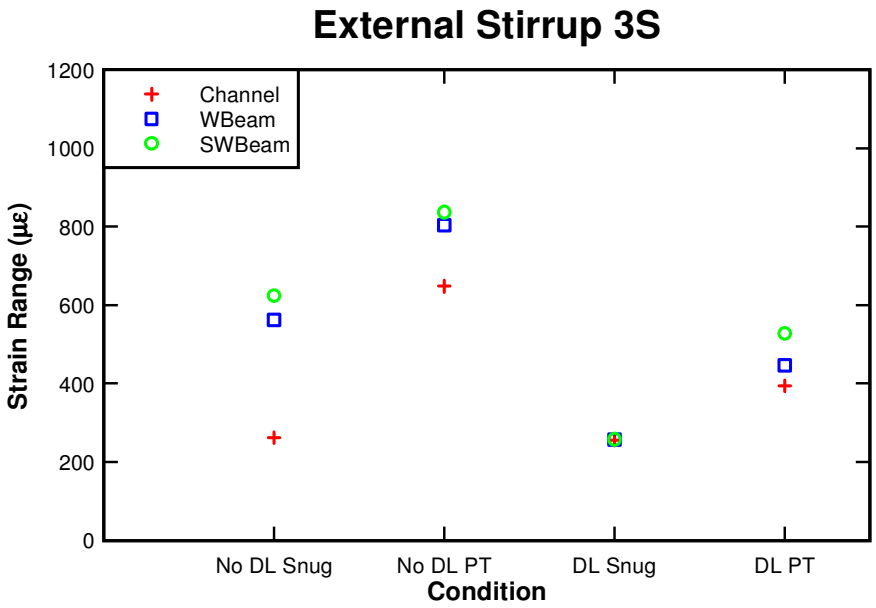

Fig. 4.10 – External stirrup 3S strain range for various loading conditions: service loading

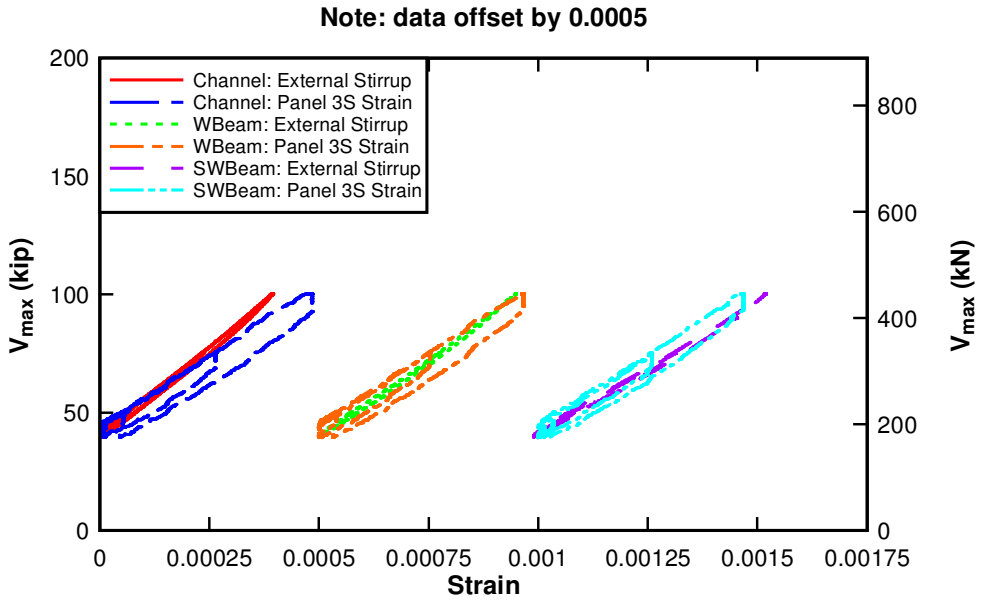

a)

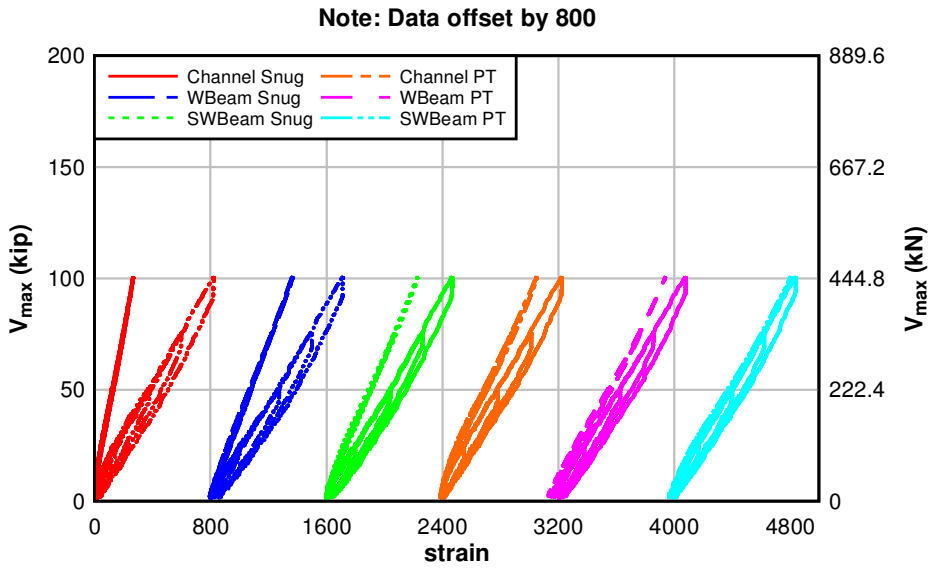

b)

Fig. 4.11 – Shear versus external stirrup 3S and average vertical strain in panel 2S a) with dead load, and b) without dead load

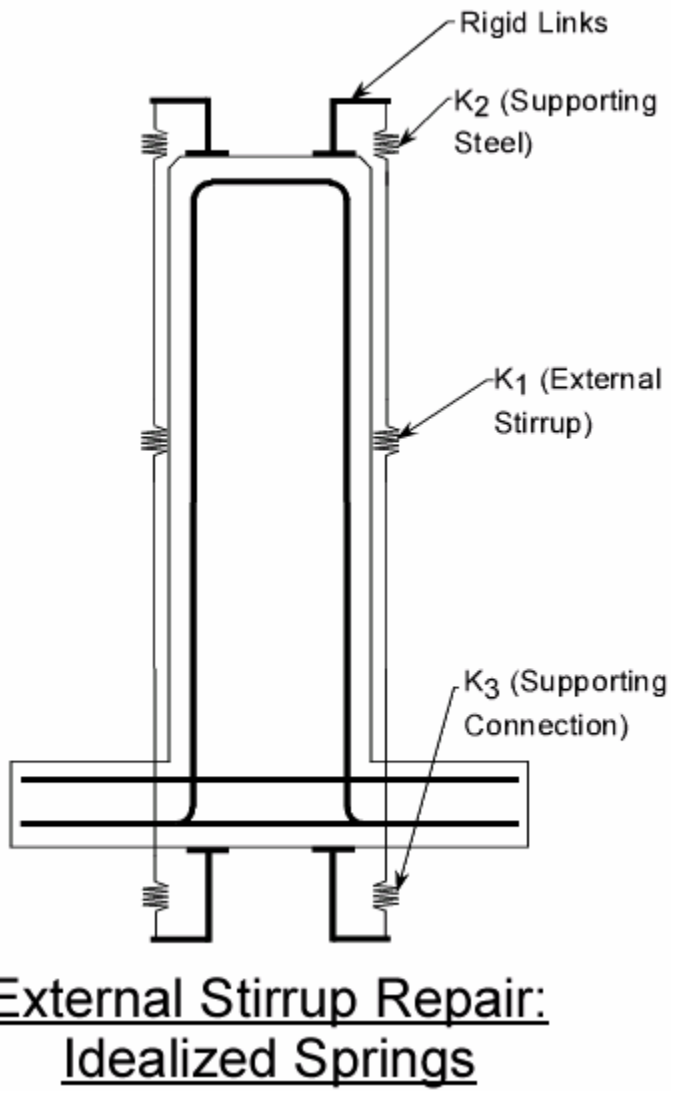

Fig. 4.12 – External stirrup and supports idealized as springs

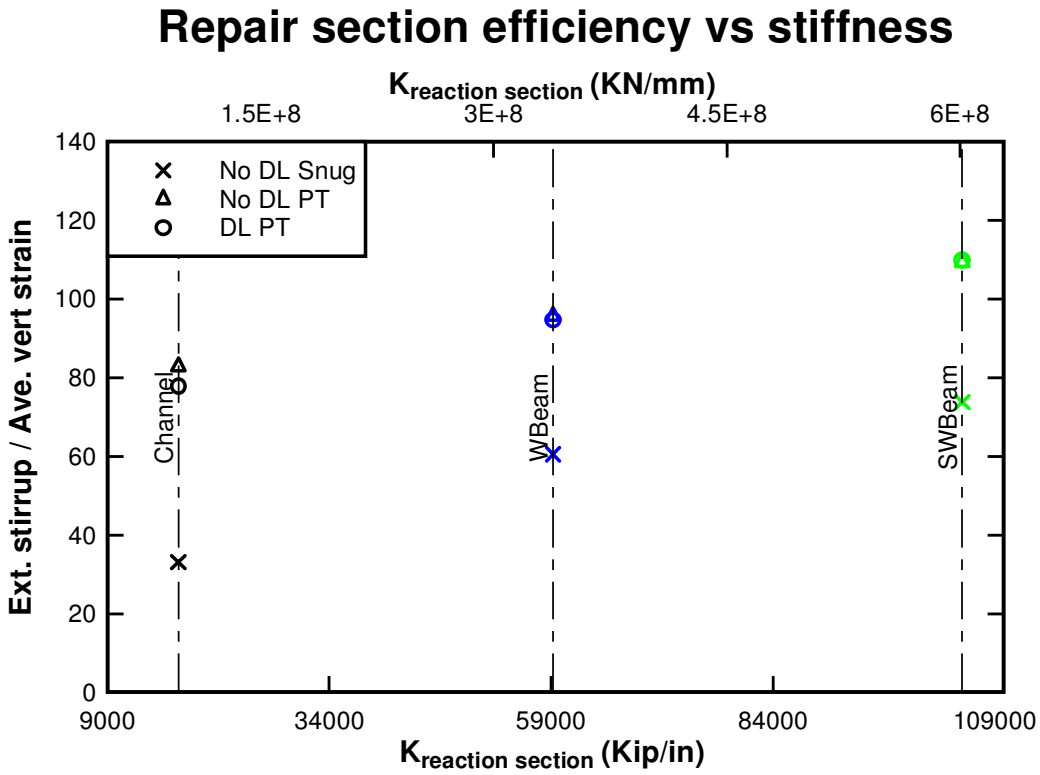

Fig. 4.13 – Repair section efficiency versus repair section stiffness

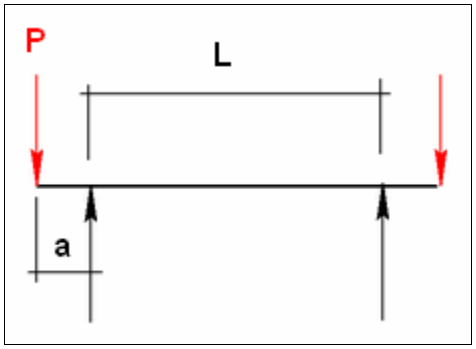

Fig. 4.14 – Weak axis bending of reaction section

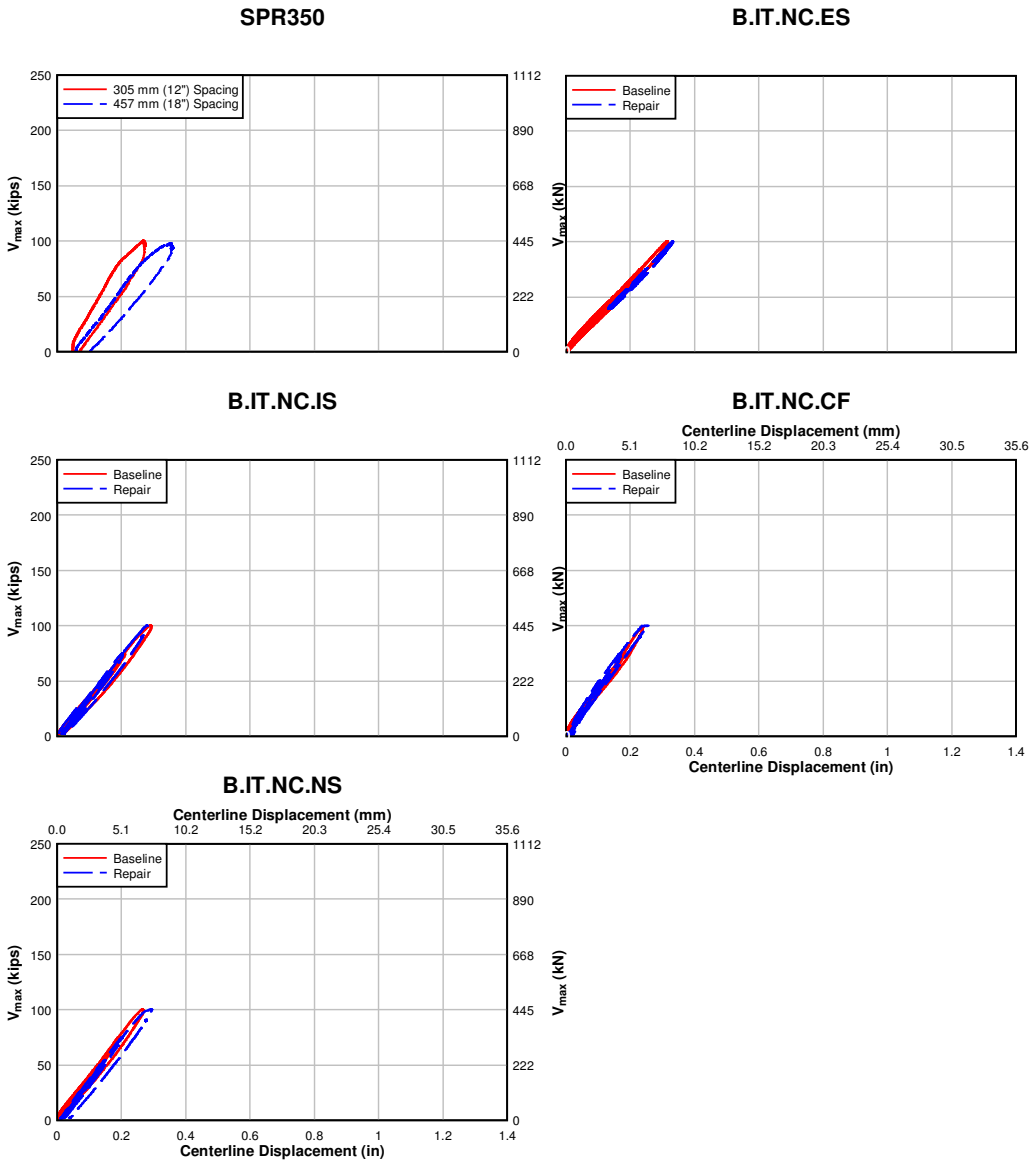

Fig. 4.15 – IT Beam shear force versus centerline displacement: service loading condition

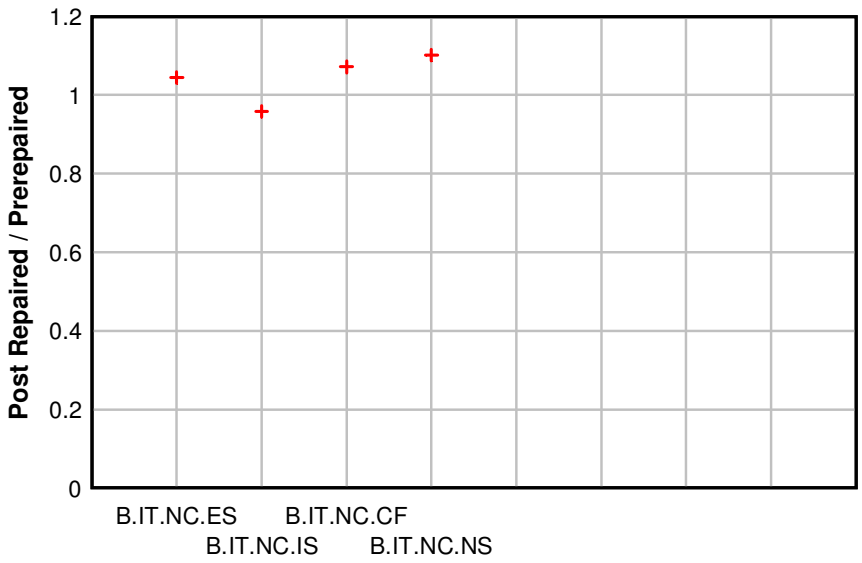

Fig. 4.16 – IT Beams without cutoffs centerline displacement: service range

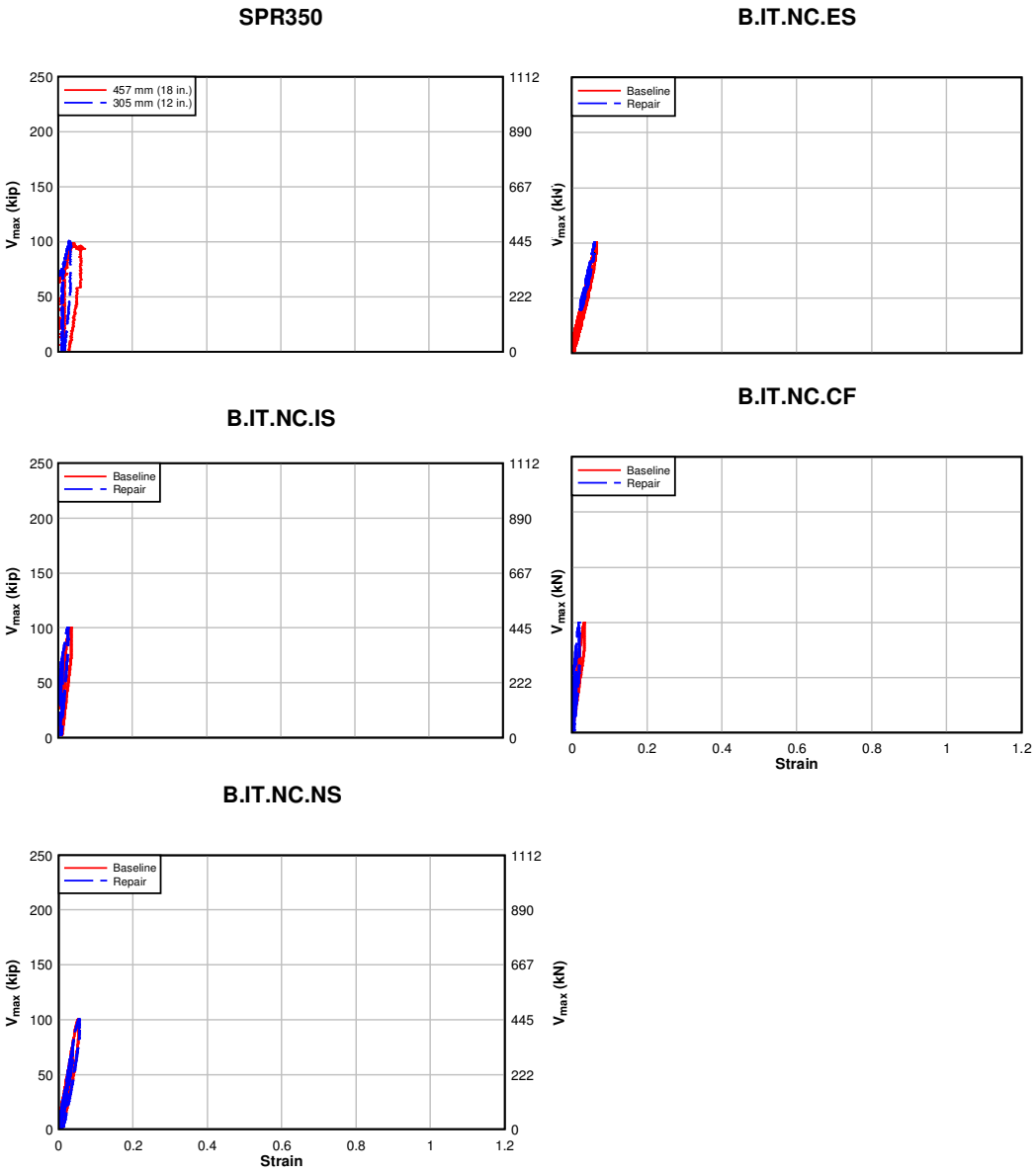

Fig. 4.17 – IT Beam shear force versus tensile diagonal displacement: service loading condition

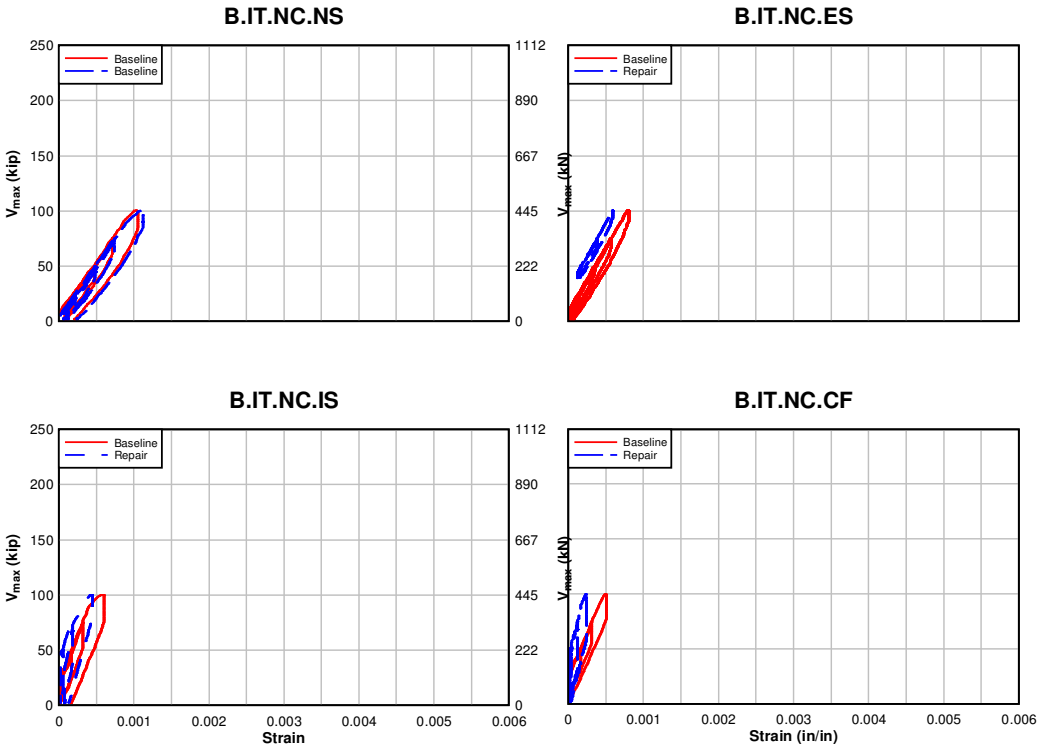

Fig. 4.18 – IT Beam shear force versus average vertical strain: service loading condition

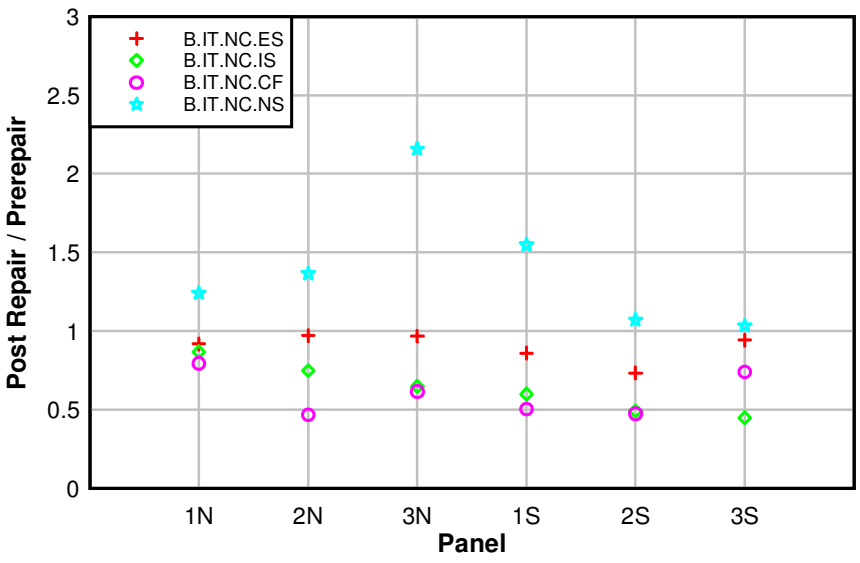

Fig. 4.19 – IT Beam shear force versus typical internal stirrup strain: service loading

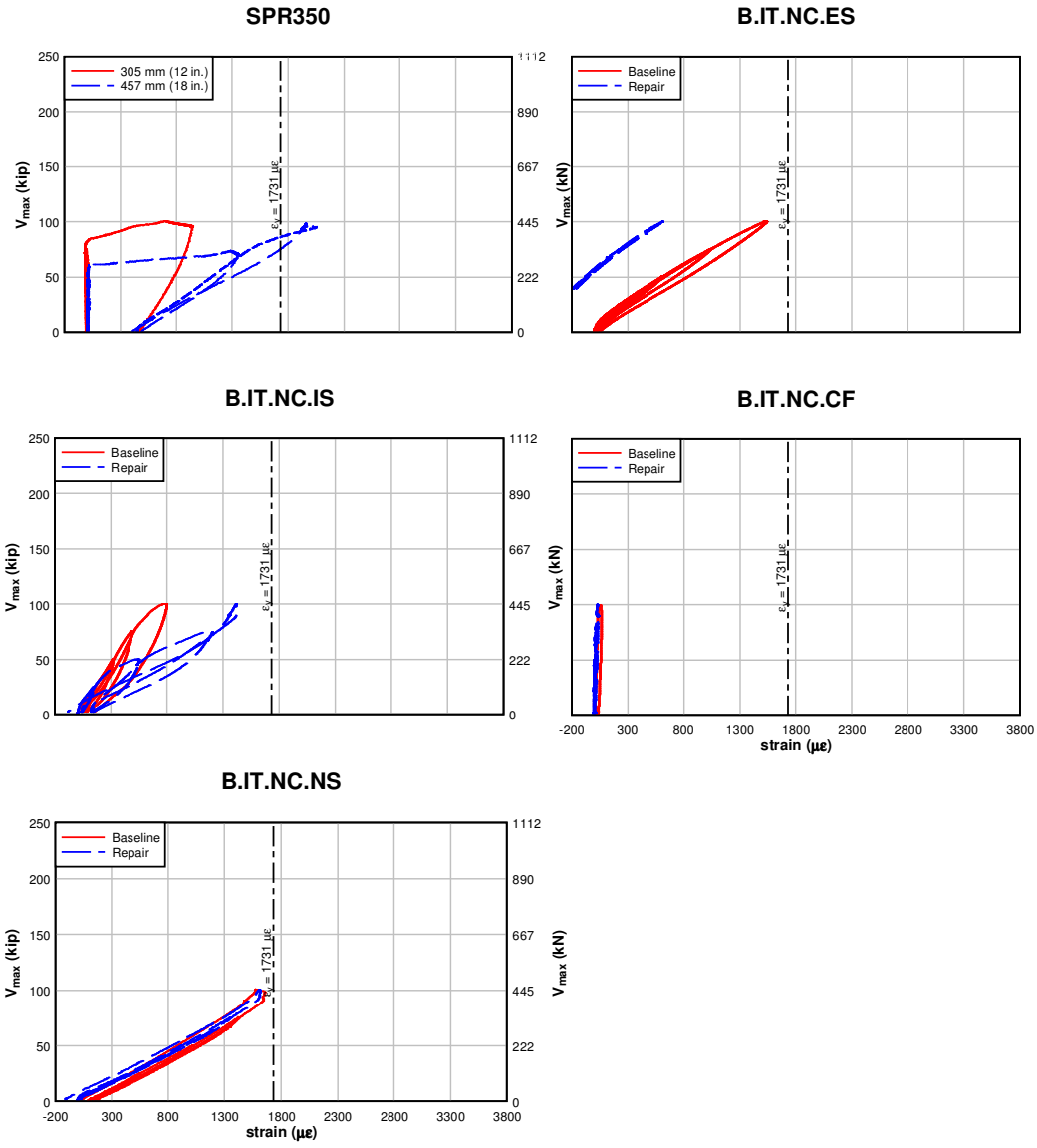

Fig. 4.20 – IT Beam shear force versus typical internal stirrup strain: service loading condition

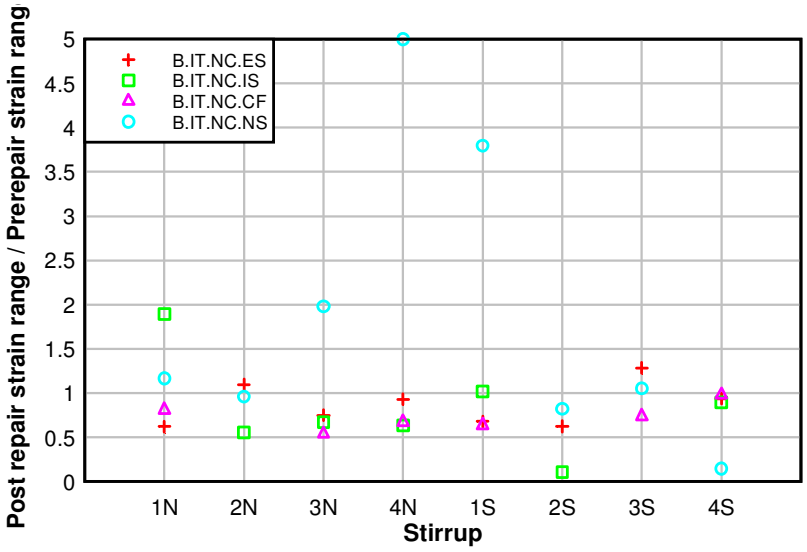

Fig. 4.21 – IT Beam shear force versus typical internal stirrup strain: service loading

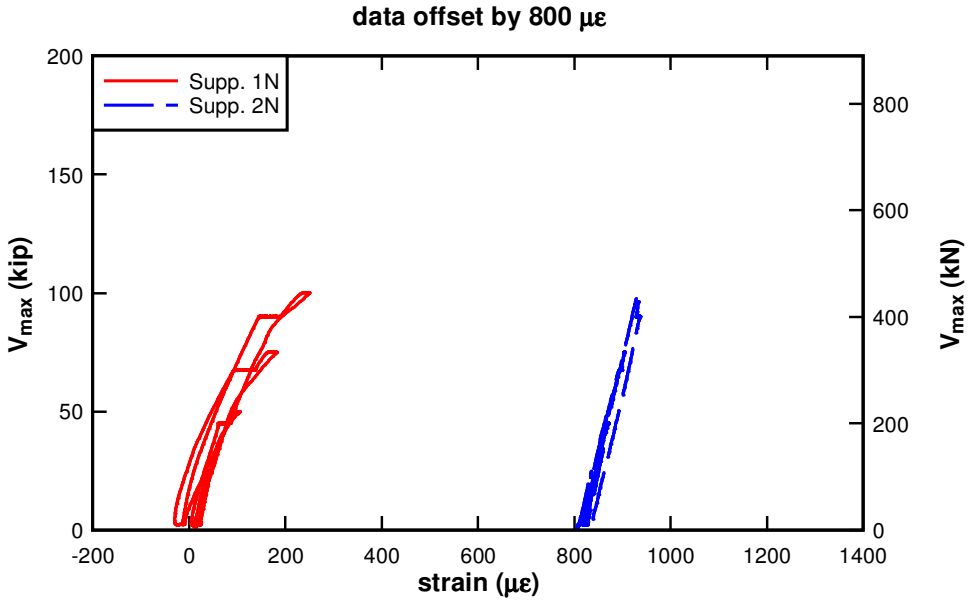

Fig. 4.22 – Specimen B.IT.NC.IS shear force versus supplemental internal stirrup strain: service loading

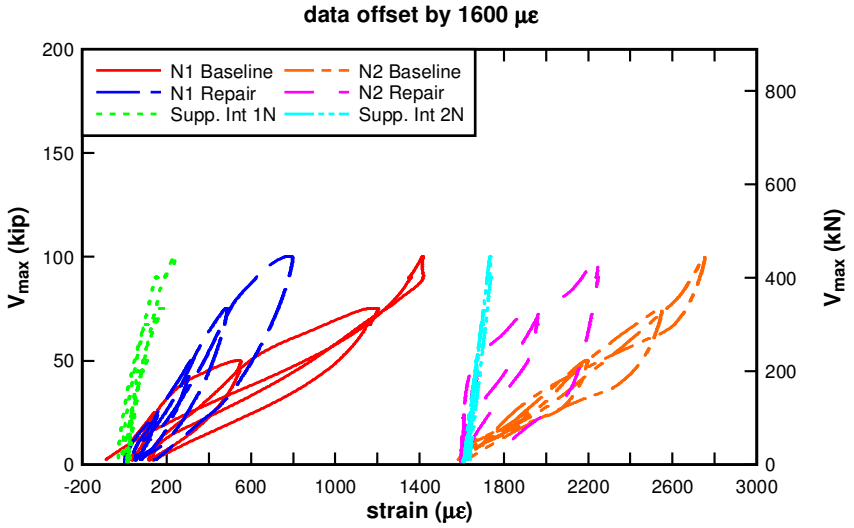

Fig. 4.23 – B.IT.NC.IS shear force versus internal and supplemental internal stirrup strain: service loading

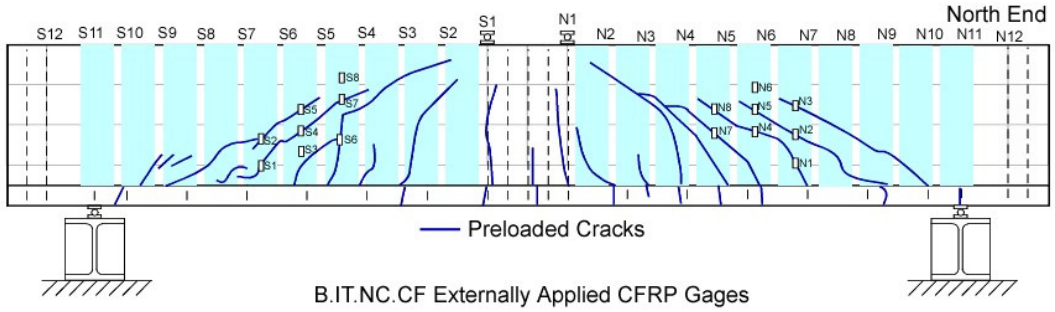

Fig. 4.24 – B.IT.NC.CF CFRP Strain Gage Locations

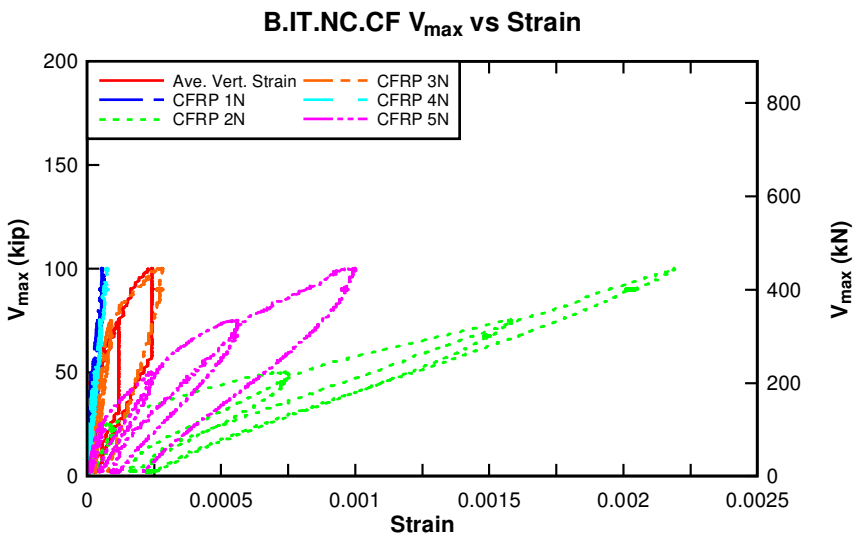

Fig. 4.25 – B.IT.NC.CF shear force versus average vertical strain and CFRP strain: service loading

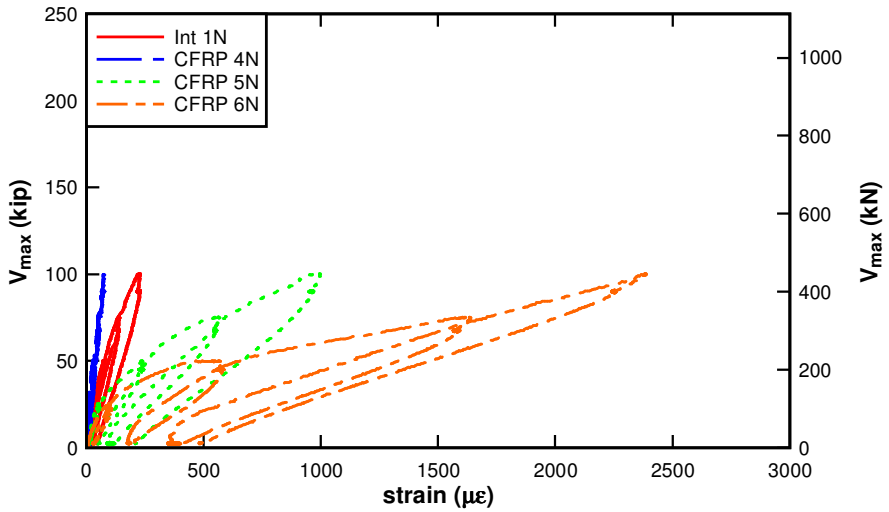

Fig. 4.26 – B.IT.NC.CF shear force versus integral stirrup strain and CFRP strain: service loading

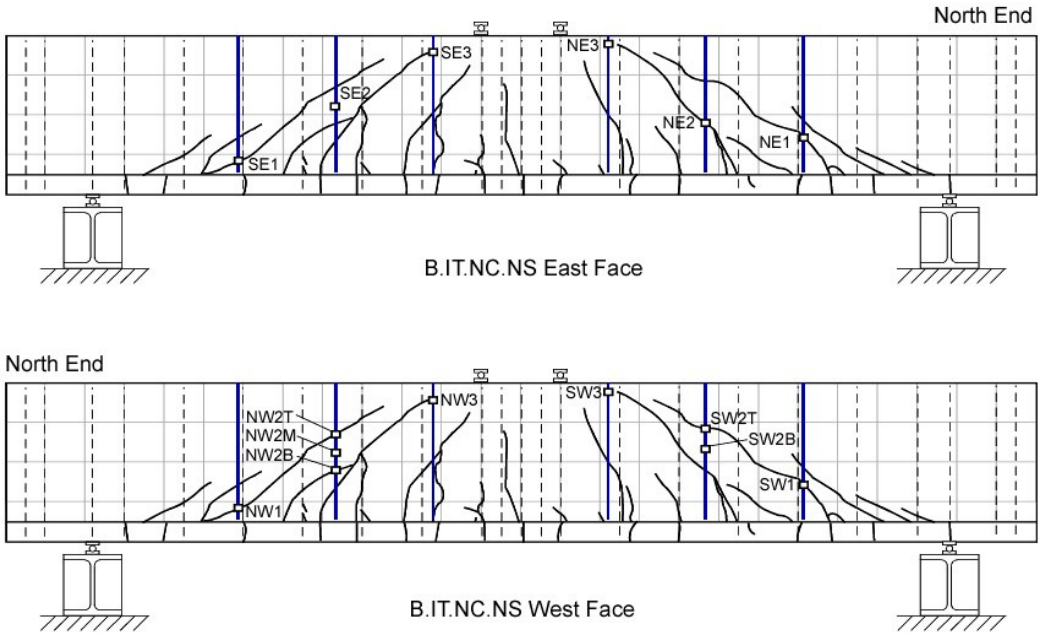

Fig. 4.27 – B.IT.NC.NS Near Surface Mount Strain Gage Locations

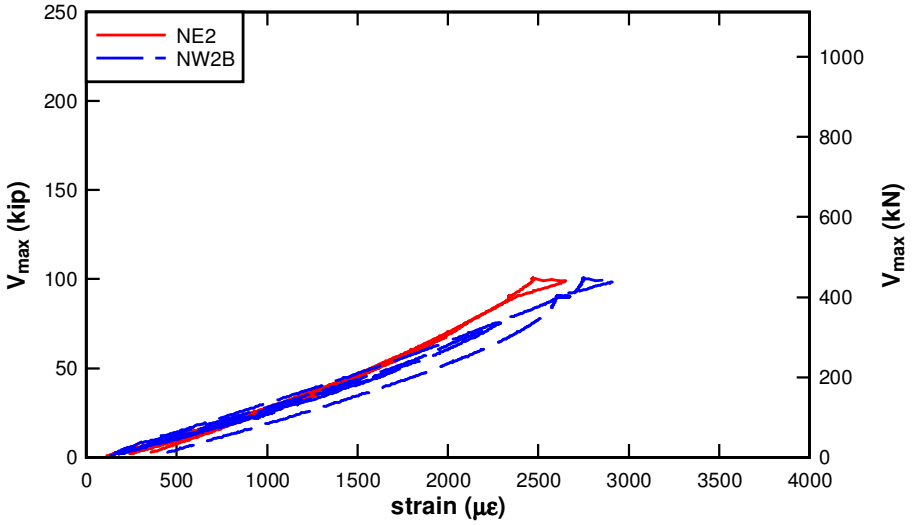

Fig. 4.28 – B.IT.NC.NS shear force versus NSM strain: service loading

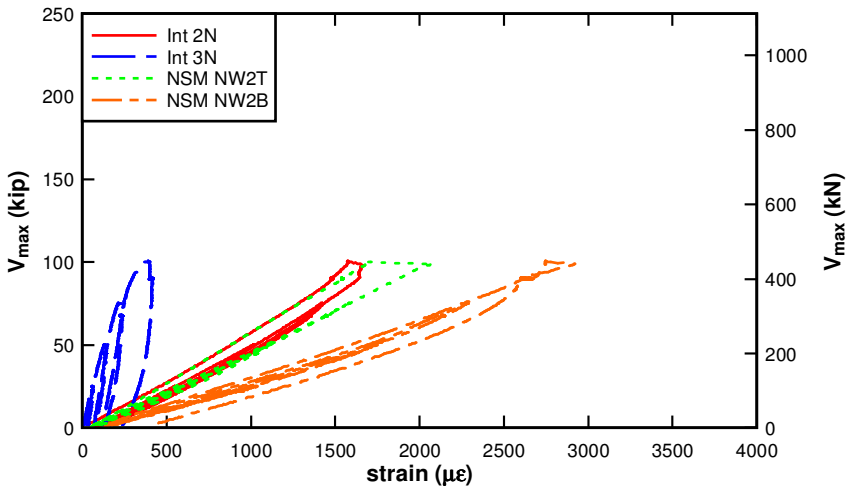

Fig. 4.29 – B.IT.NC.NS shear force versus NSM and integrally cast stirrup strain: service loading

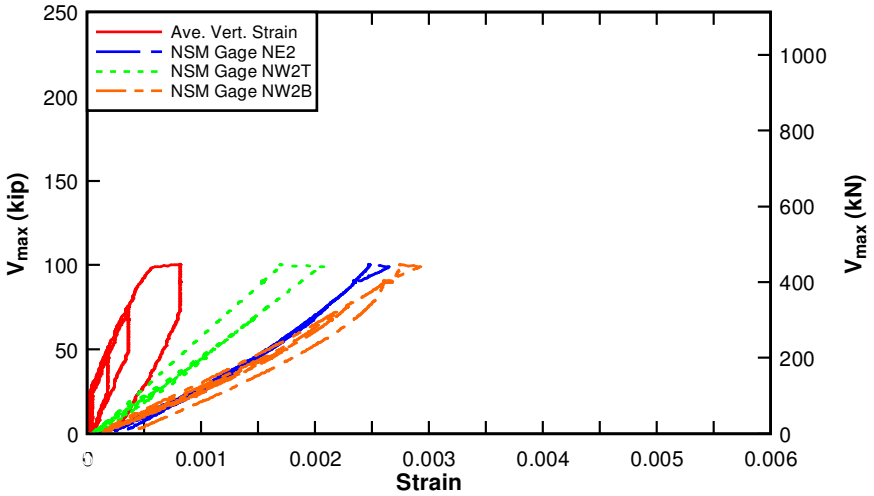

Fig. 4.30 – B.IT.NC.NS shear force versus NSM and average vertical strain: service loading

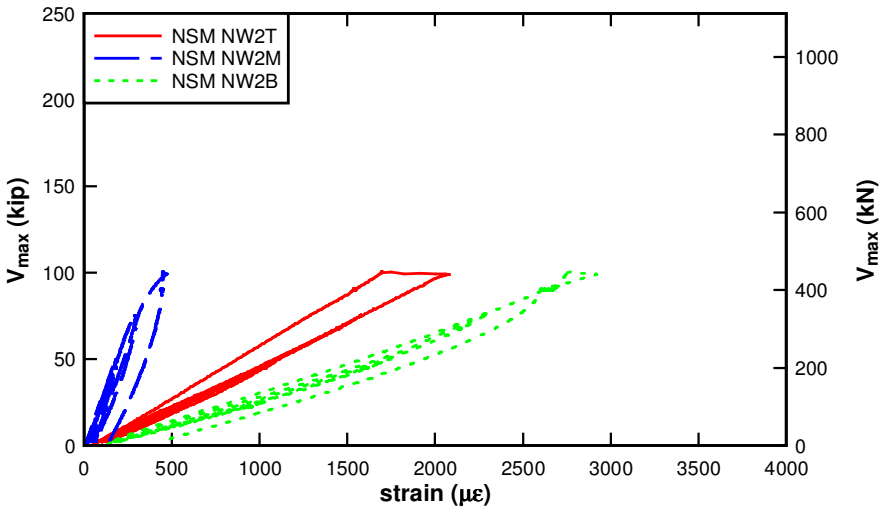

Fig. 4.31 – B.IT.NC.NS shear force versus NSM strain distribution: service loading

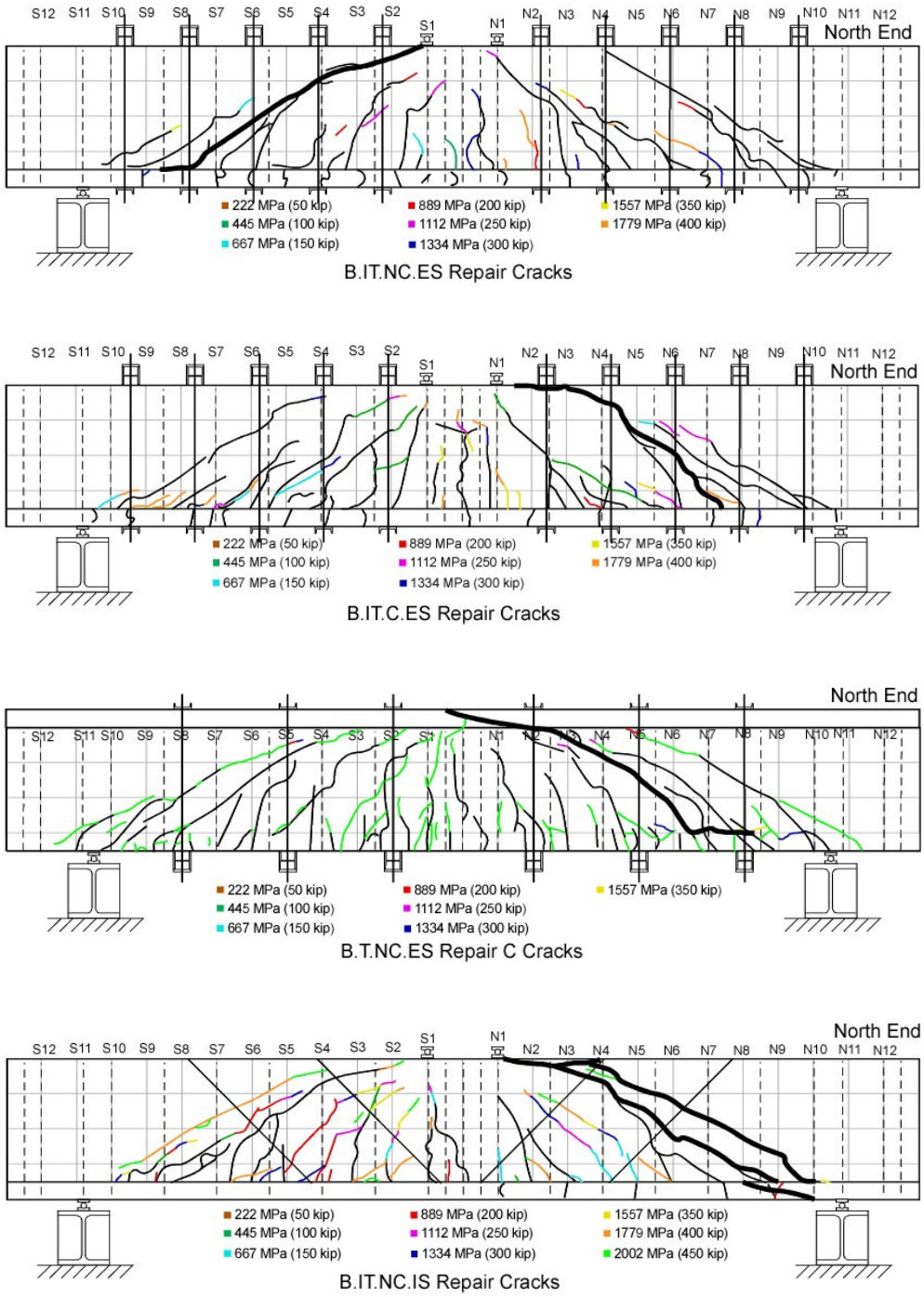

Fig. 4.32 – Beam specimen crack maps: individual load steps indicated

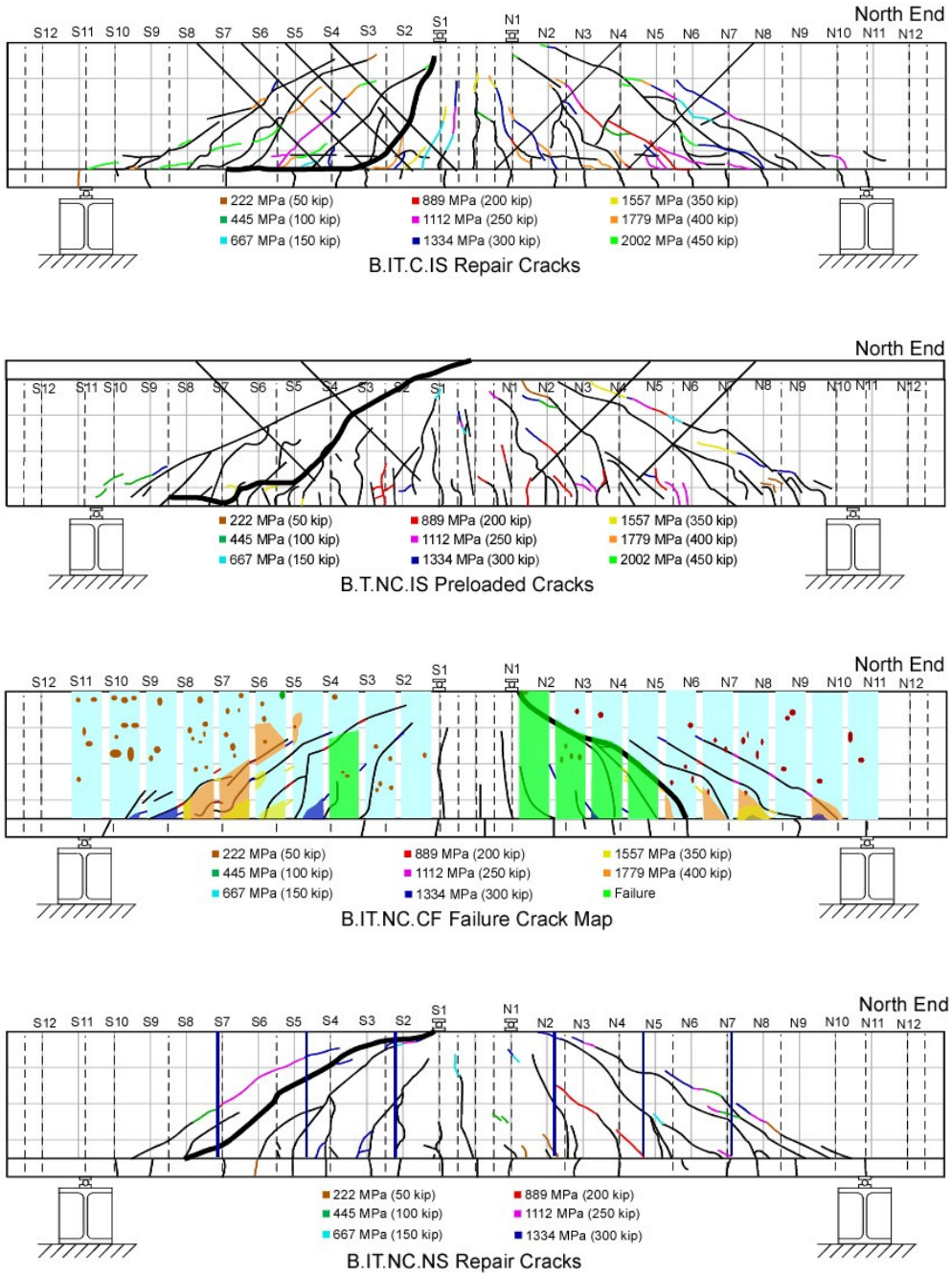

Fig. 4.32 – Beam specimen crack maps: individual load steps indicated continued

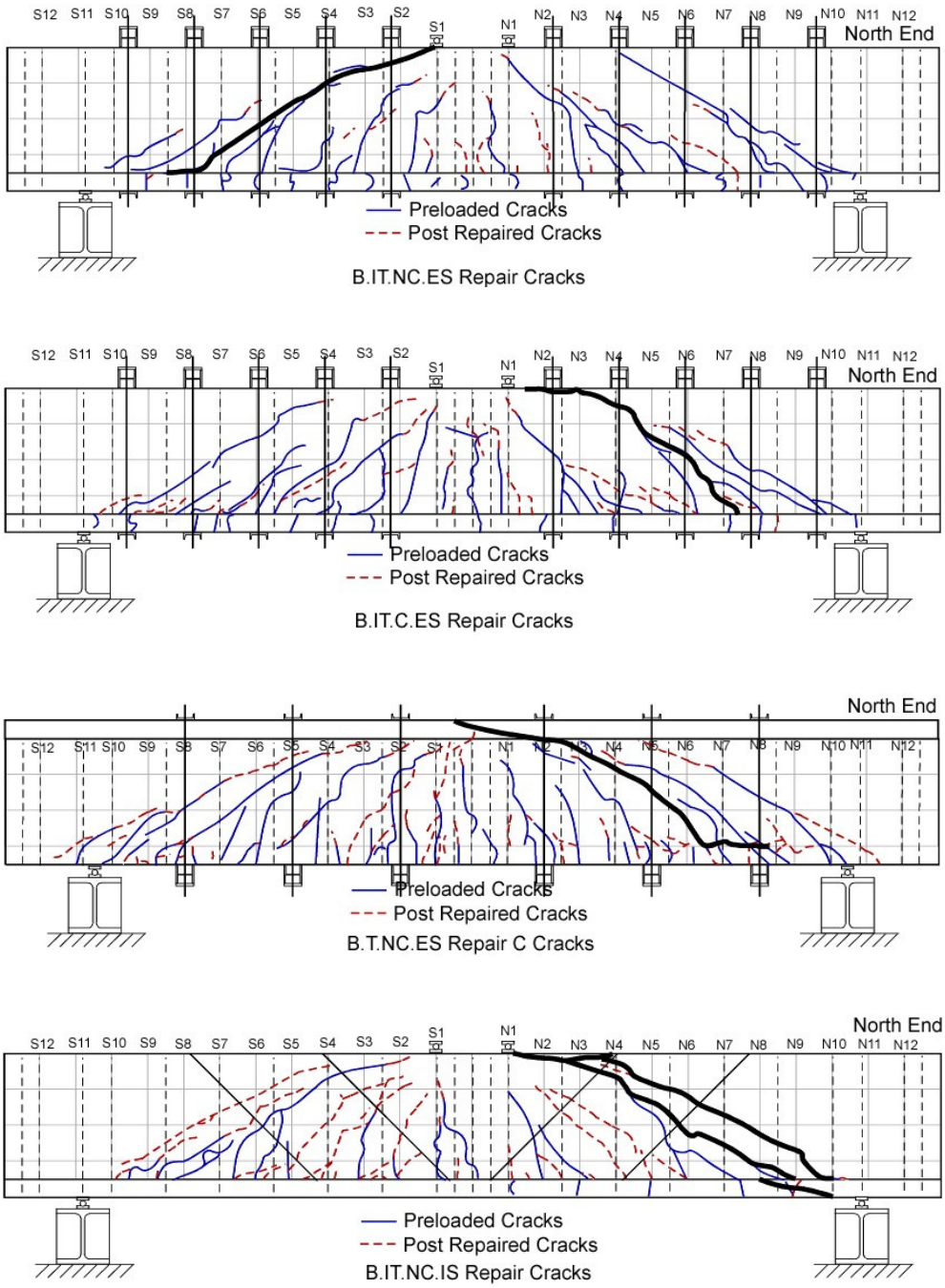

Fig. 4.33 – Beam specimen crack maps: precrack versus repair

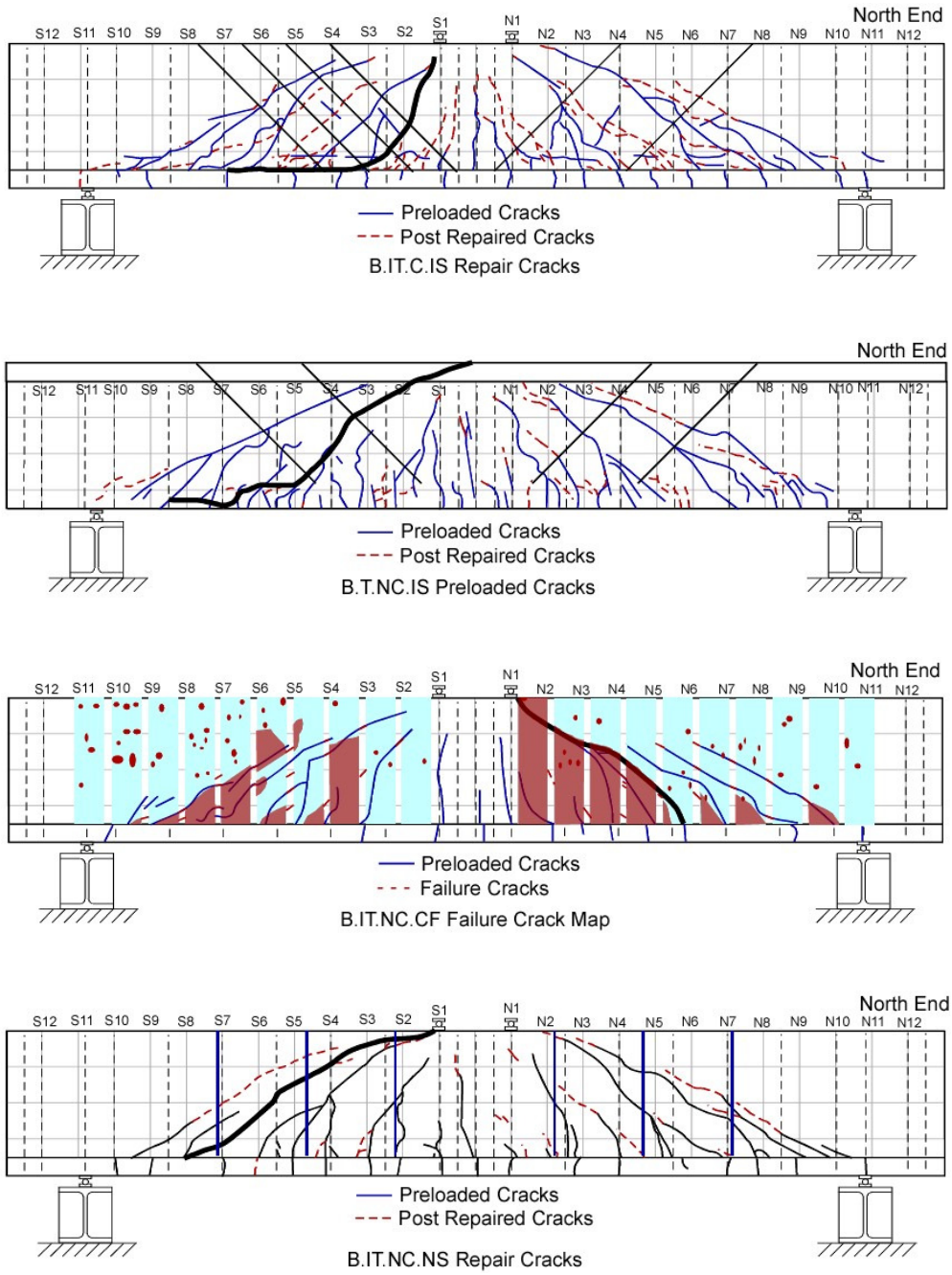

Fig. 4.33 – Beam specimen crack maps: precrack versus repair continued

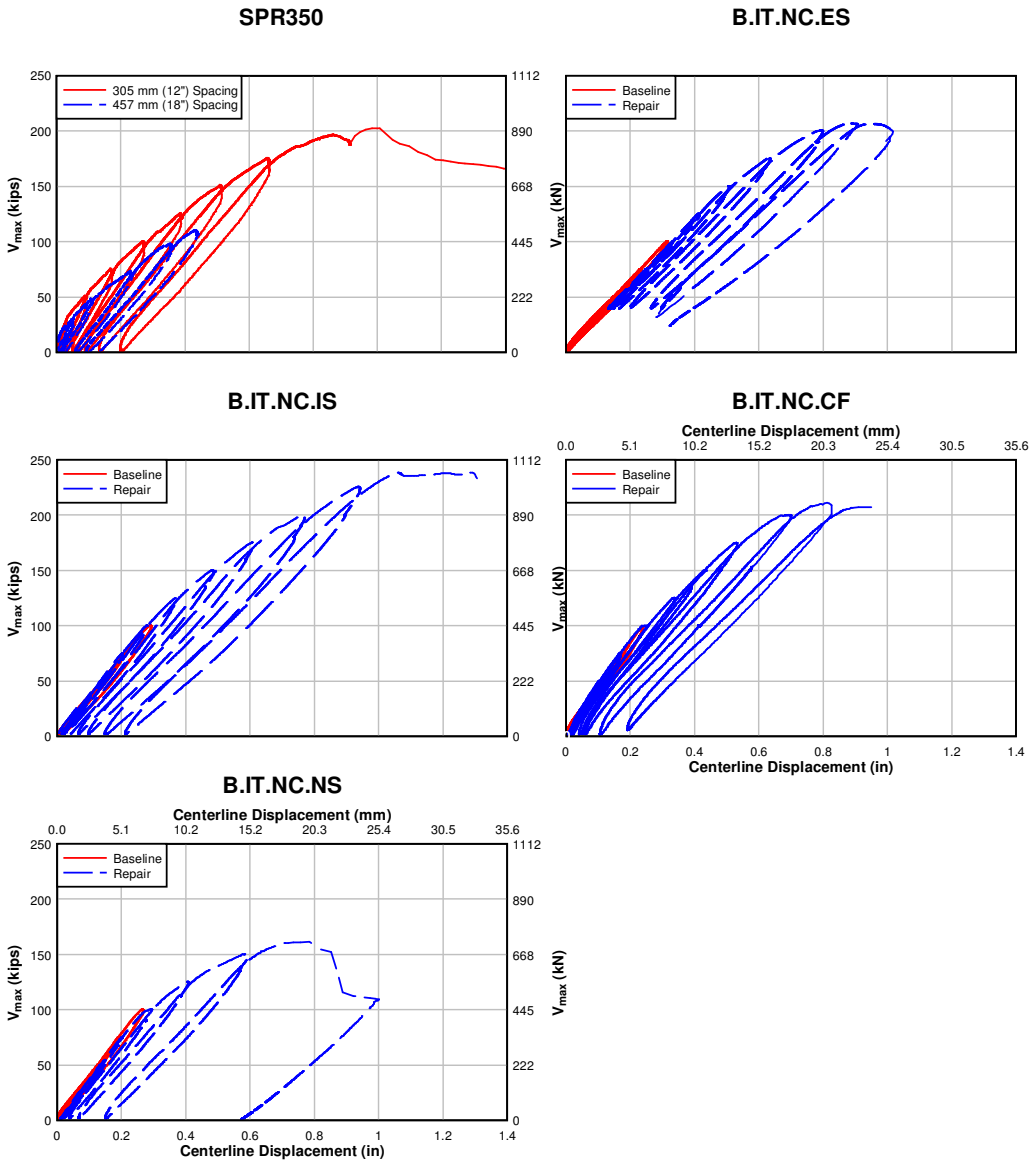

Fig. 4.34 – IT Beam shear force versus centerline displacement: strength loading condition

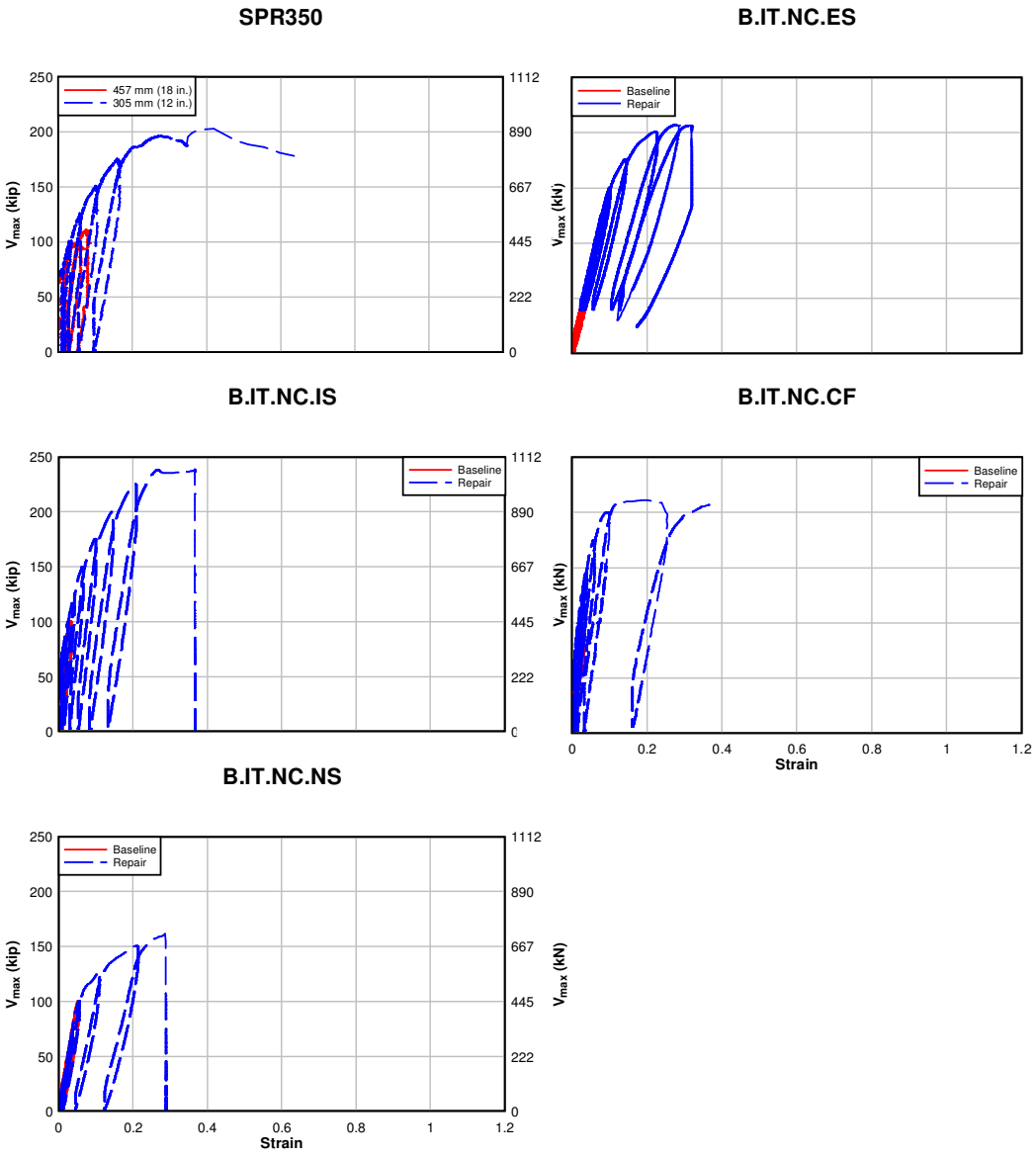

Fig. 4.35 – IT Beam shear force versus tensile diagonal displacement: strength loading condition

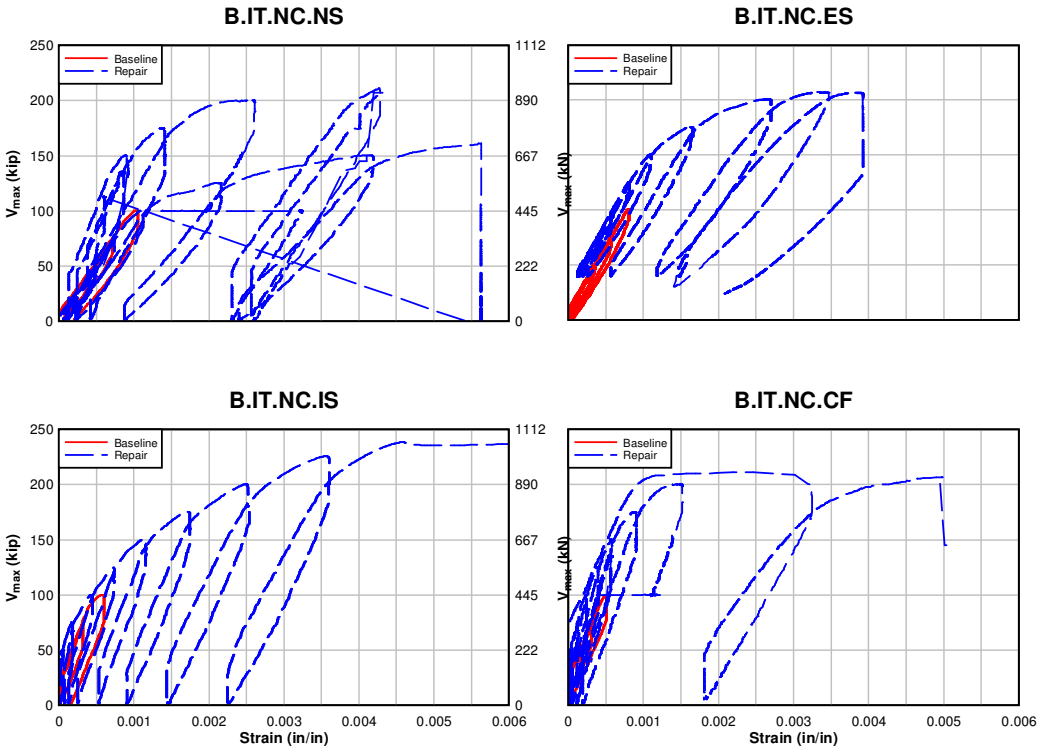

Fig. 4.36 – IT Beam shear force versus average vertical strain: strength loading condition

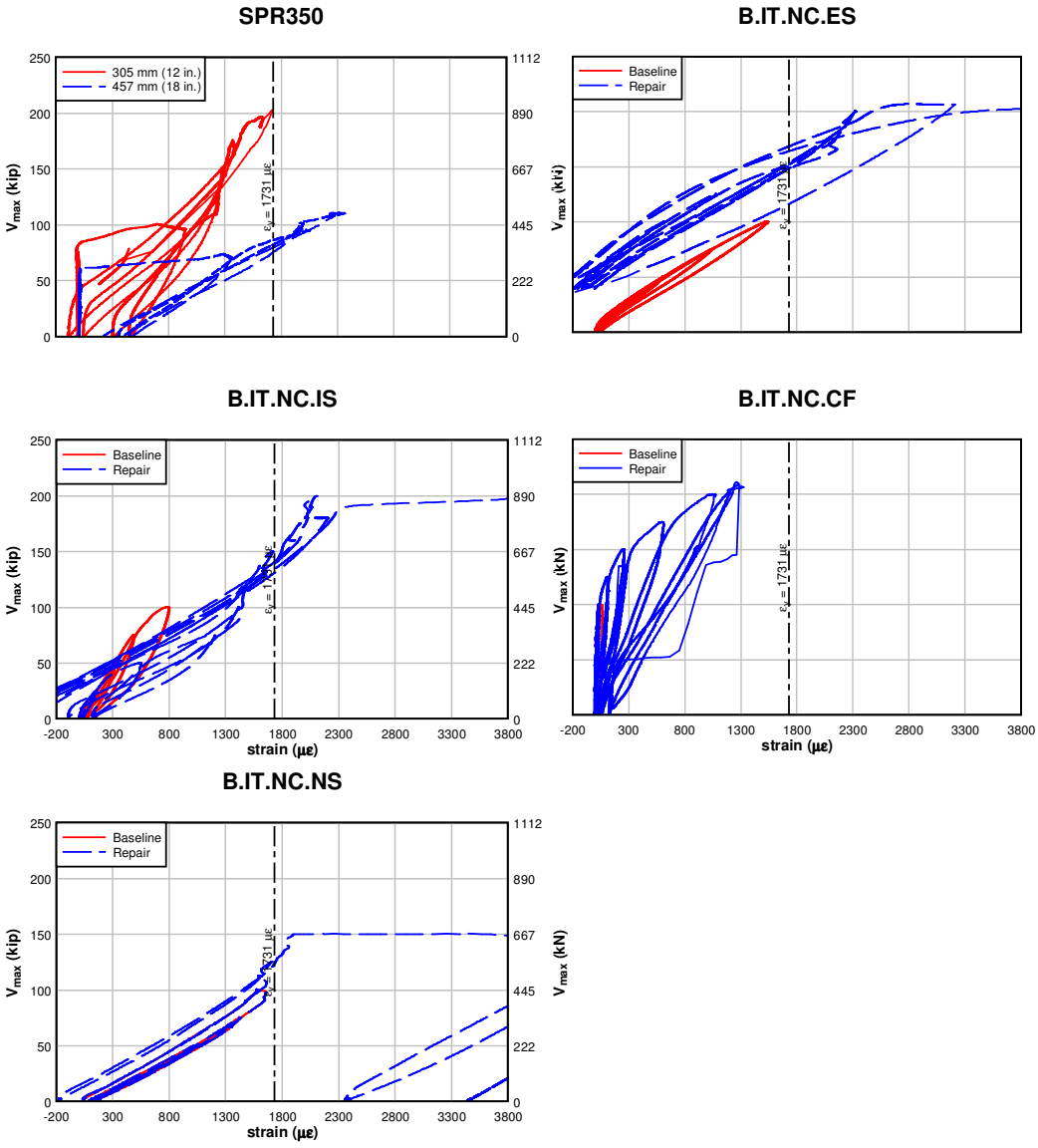

Fig. 4.37 – IT Beam shear force versus typical internal stirrup strain: strength loading condition

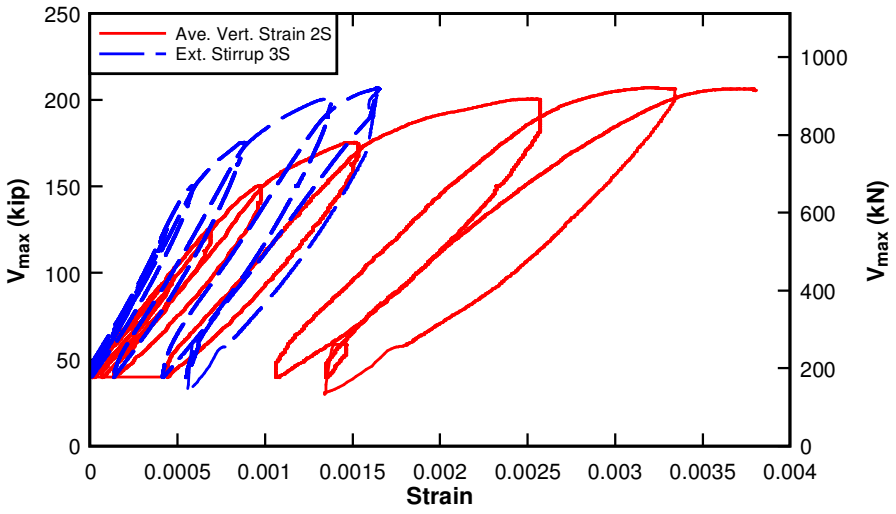

Fig. 4.38 – Specimen B.IT.NC.ES shear force versus external stirrup and average vertical strain: strength loading

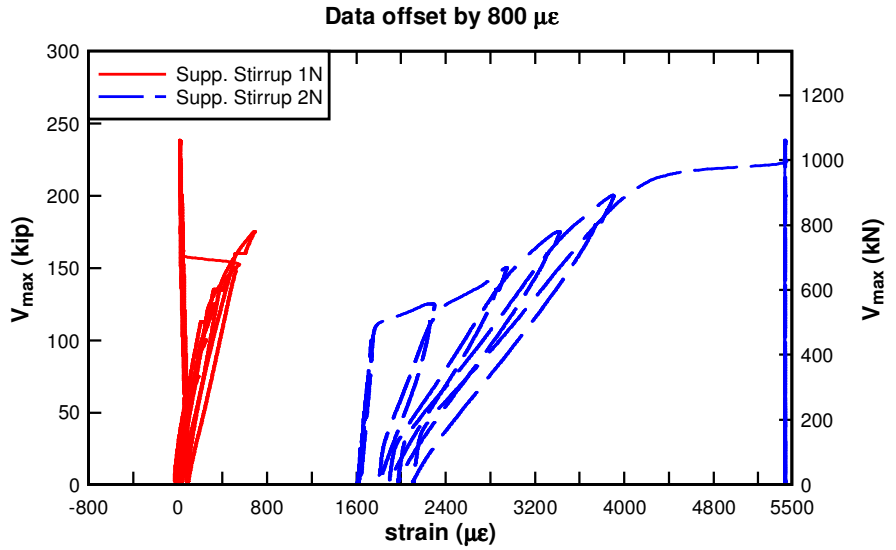

Fig. 4.39 – Specimen B.IT.NC.IS shear force versus supplemental internal stirrup strain: strength loading

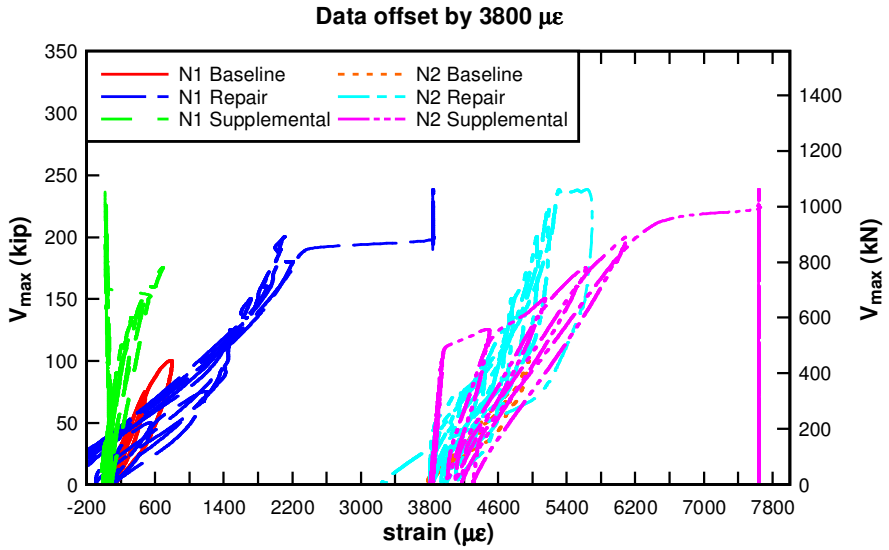

Fig. 4.40 – B.IT.NC.IS shear force versus internal and supplemental internal stirrup strain: strength loading

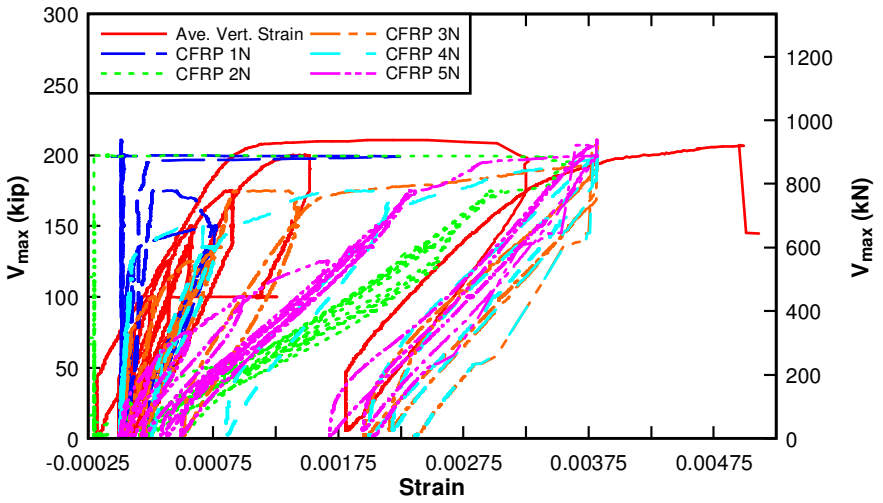

Fig. 4.41 – Specimen B.IT.NC.CF shear force versus average vertical strain and CFRP strain: strength loading

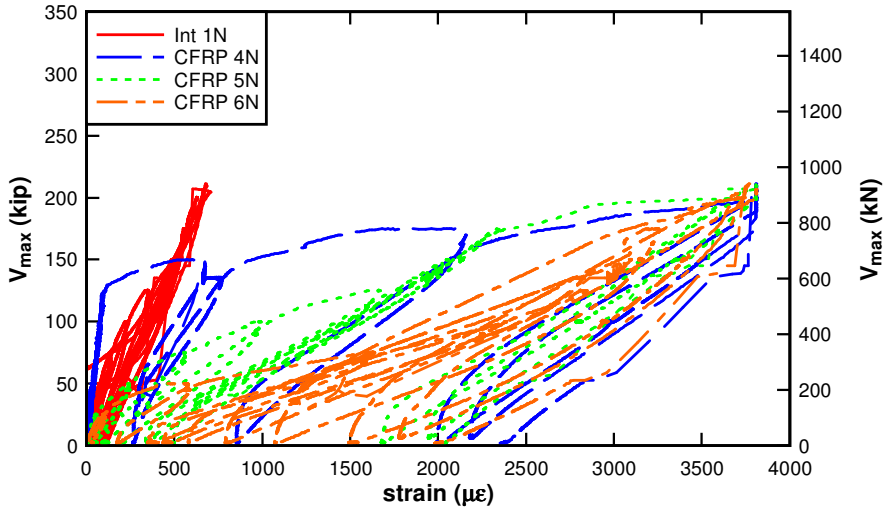

Fig. 4.42 – B.IT.NC.CF shear force versus integral stirrup strain and CFRP strain: strength loading

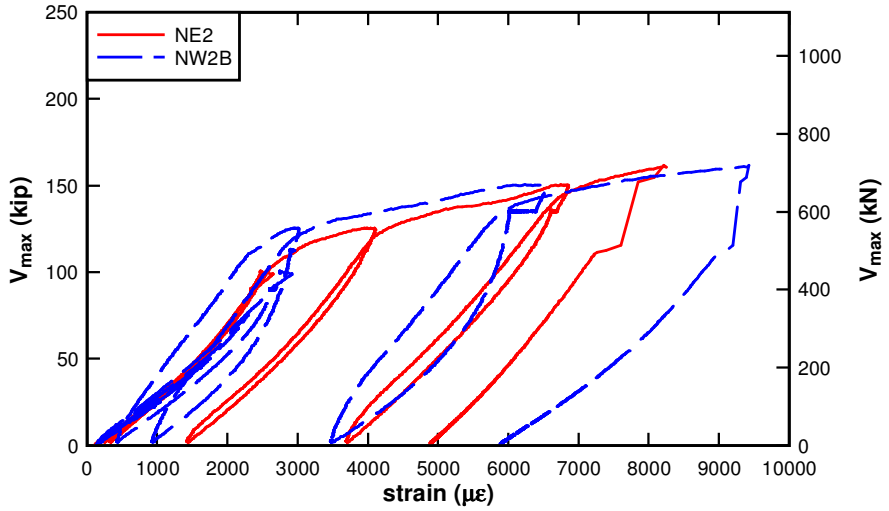

Fig. 4.43 – B.IT.NC.NS shear force versus NSM strain: strength loading

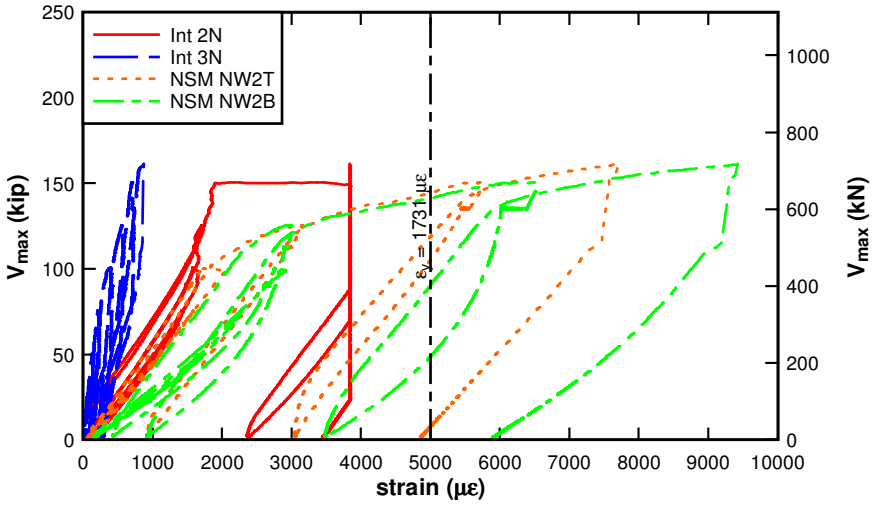

Fig. 4.44 – B.IT.NC.NS shear force versus NSM and integrally cast stirrup strain: strength loading

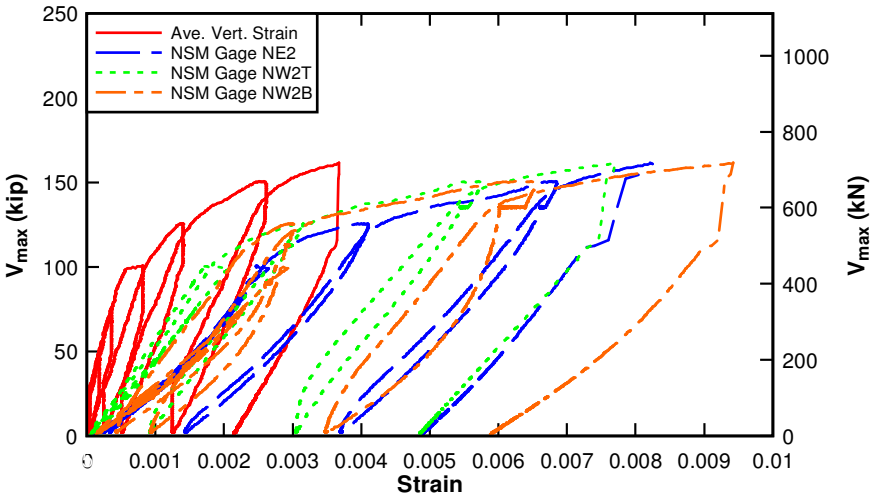

Fig. 4.45 – B.IT.NC.NS shear force versus NSM and average vertical strain: strength loading

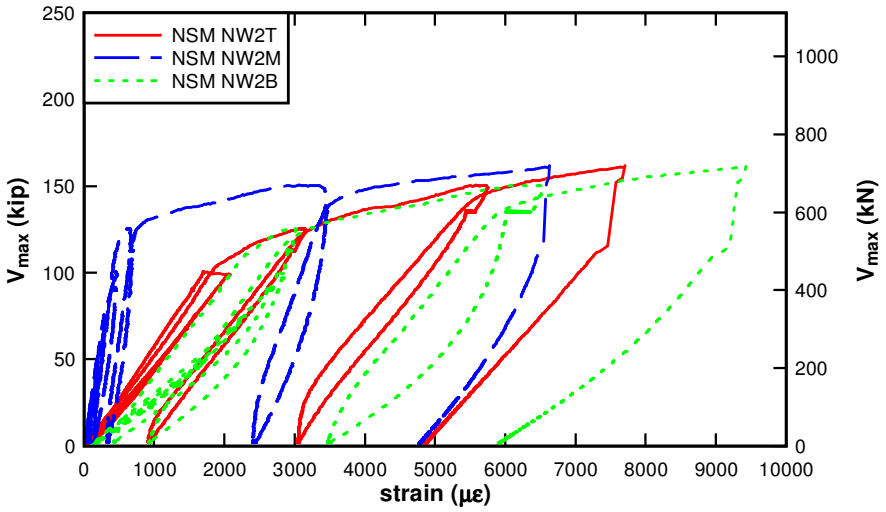

Fig. 4.46 – B.IT.NC.NS shear force versus NSM strain distribution: strength loading

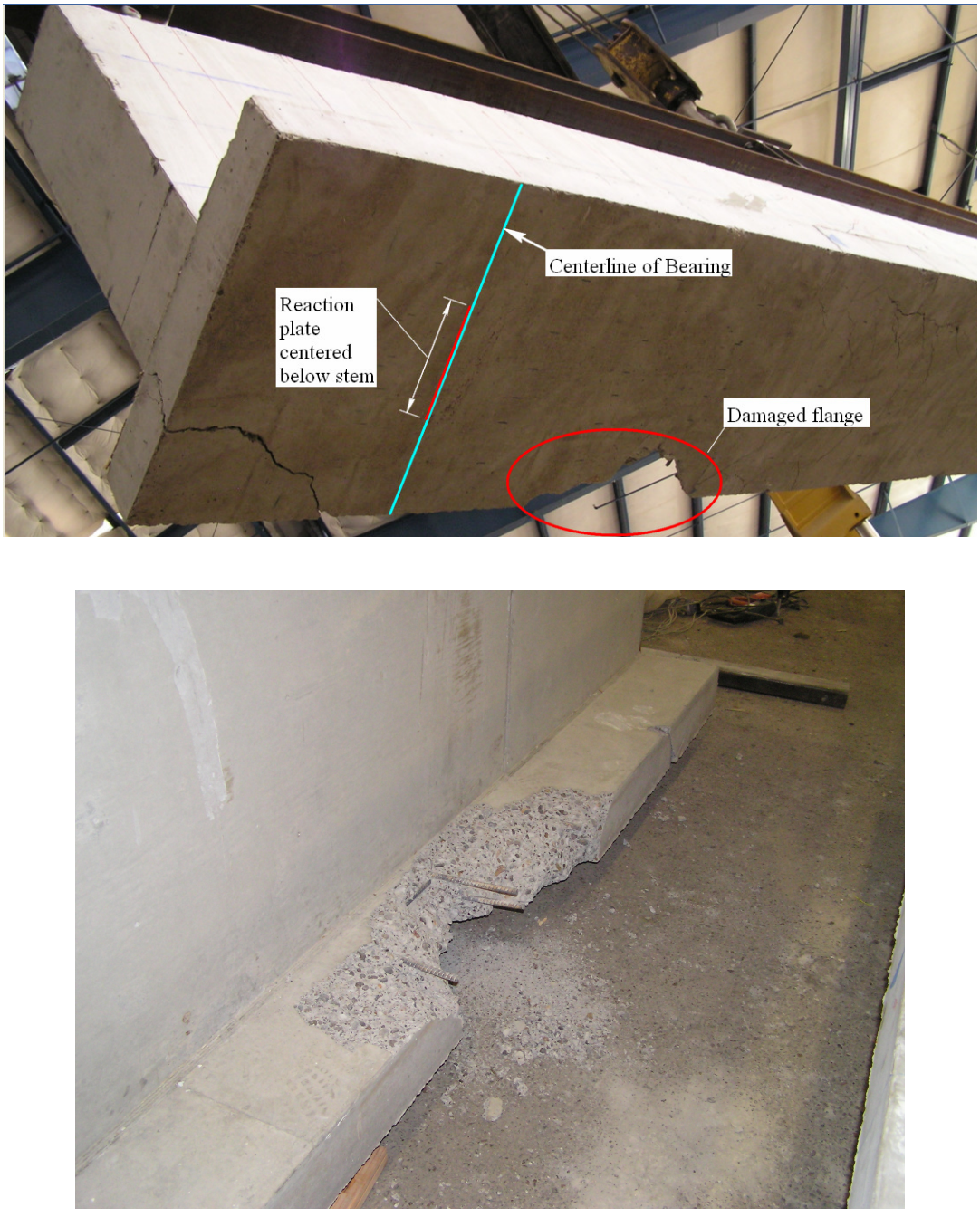

Fig. 4.47 – B.IT.C.IS flange damage: a) top of flange and b) side of flange

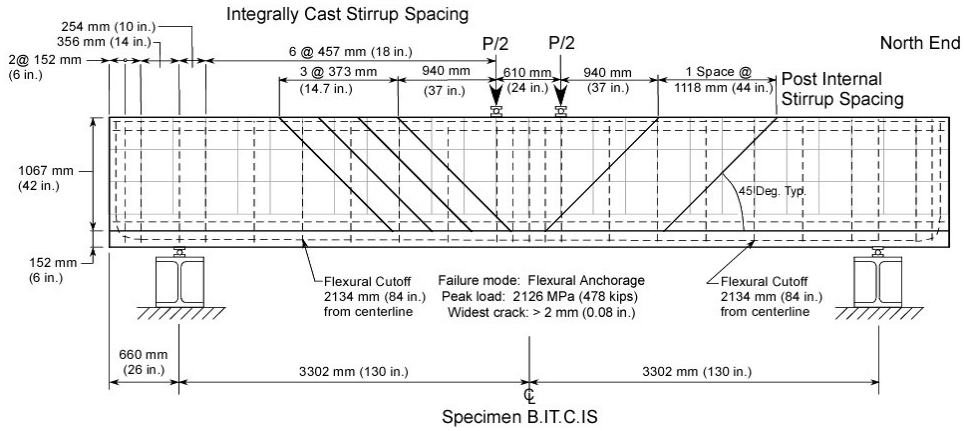

Fig. 4.48 – B.IT.C.IS revised repair

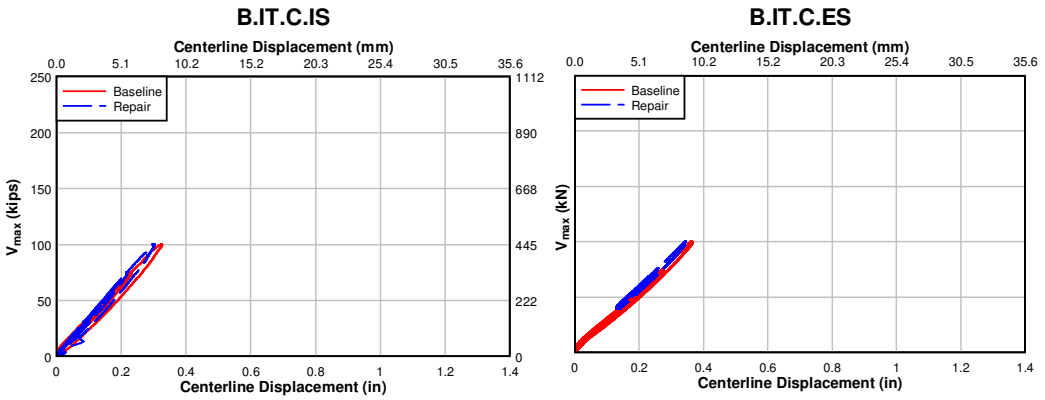

Fig. 4.49 – IT Beam with flexural cutoff details shear force versus centerline displacement: service loading condition

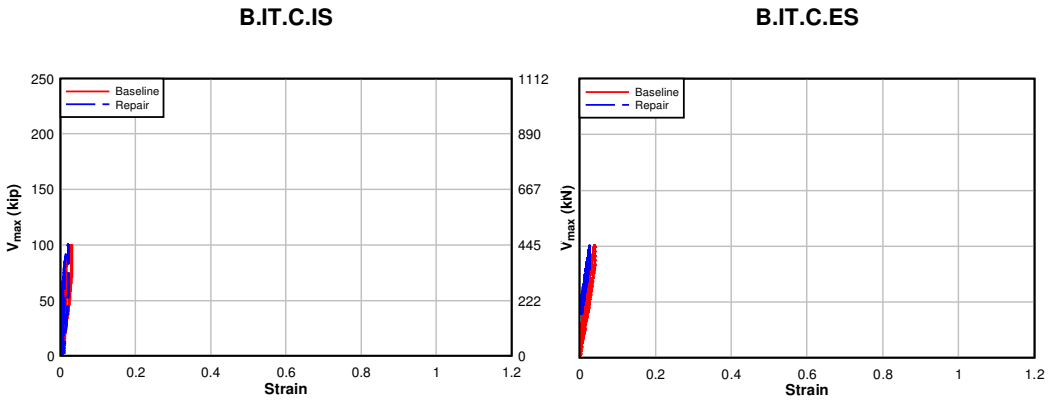

Fig. 4.50 – IT Beam with flexural cutoff details shear force versus tensile diagonal displacement: service loading condition

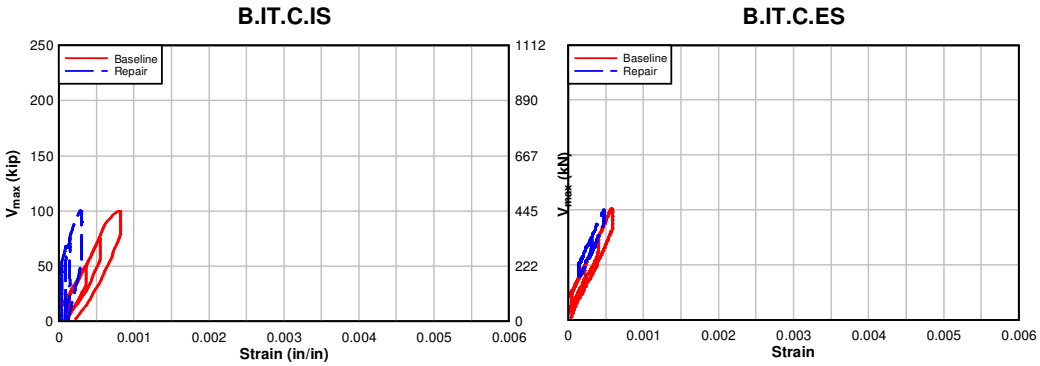

Fig. 4.51 – IT Beam with flexural cutoff details shear force versus average vertical strain: service loading condition

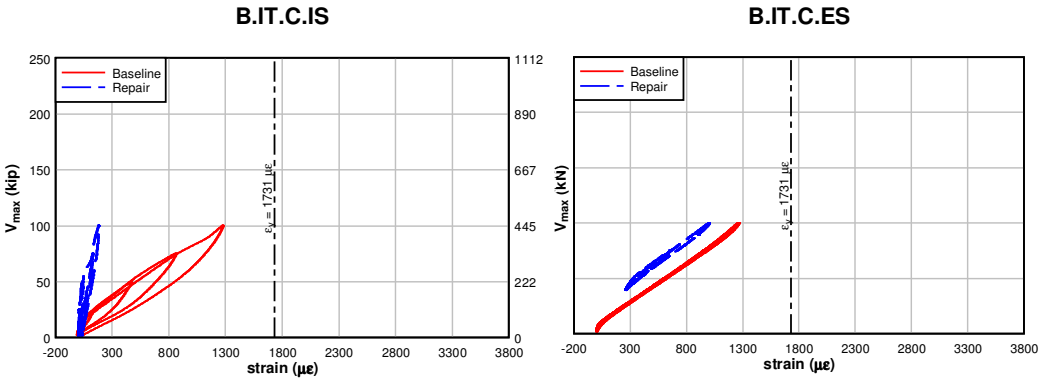

Fig. 4.52 – IT Beam with flexural cutoff details shear force versus typical integrally cast stirrup strain: service loading condition

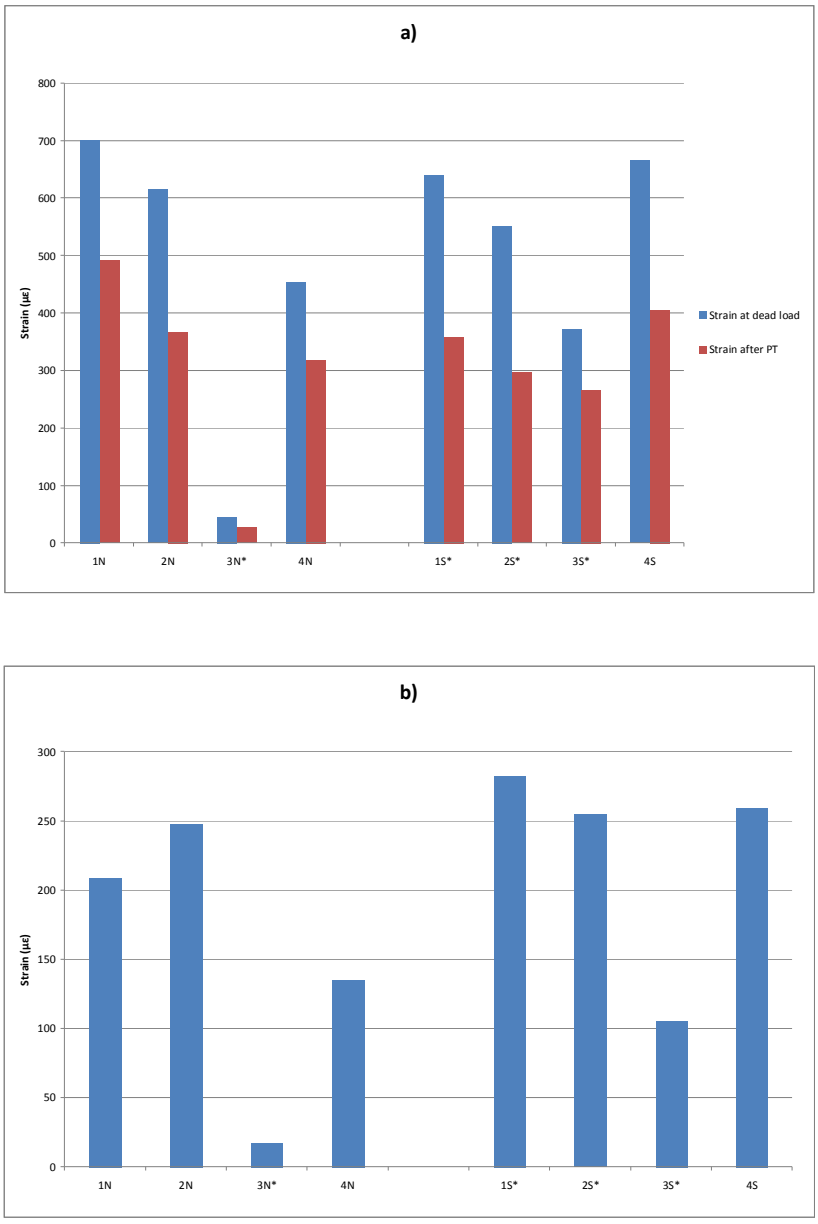

Fig. 4.53 – Specimen B.IT.C.ES integrally cast stirrup strain: a) before and after post tensioning, b) strain reduction due to post tensioning. Note: asterisk denotes chipped in stirrups.

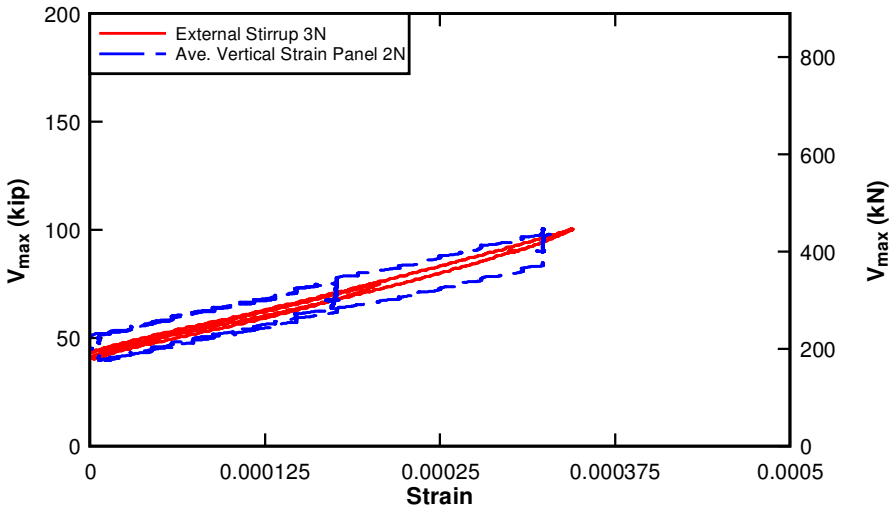

Fig. 4.54 – Specimen B.IT.C.ES shear versus external stirrup 3N and average vertical strain in panel 2N

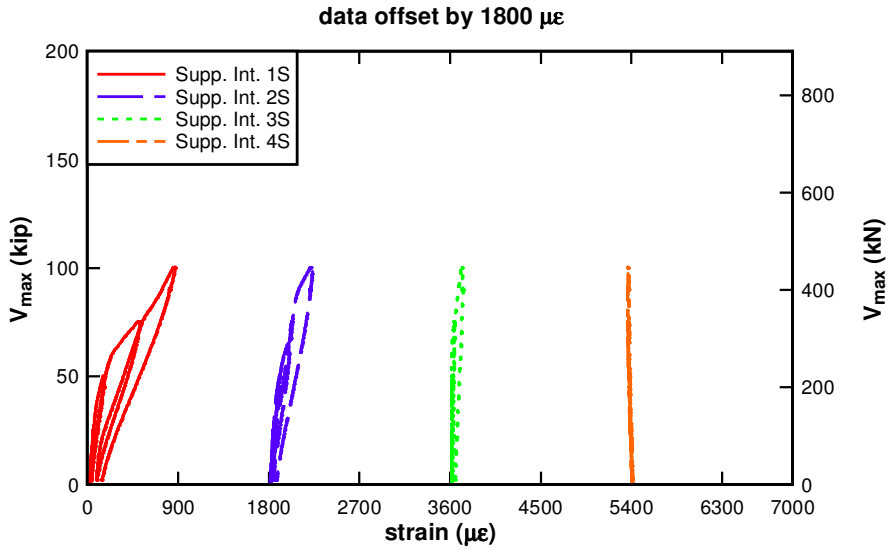

Fig. 4.55 – Specimen B.IT.C.IS shear force versus supplemental internal stirrup strain: service loading

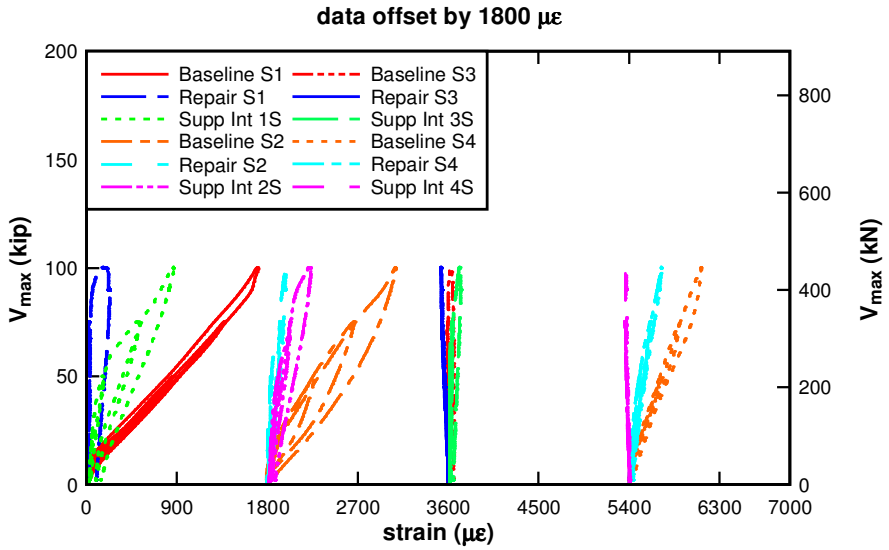

Fig. 4.56 – Specimen B.IT.C.IS shear force versus internal and supplemental internal stirrup strain: service loading

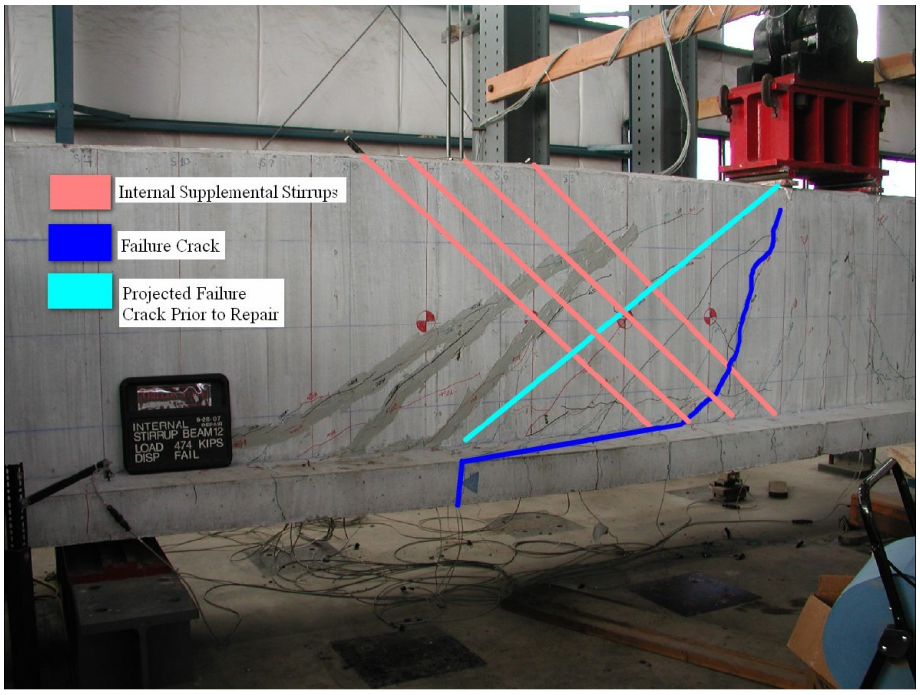

Fig. 4.57 – Specimen B.IT.C.IS failure crack projection and actual location

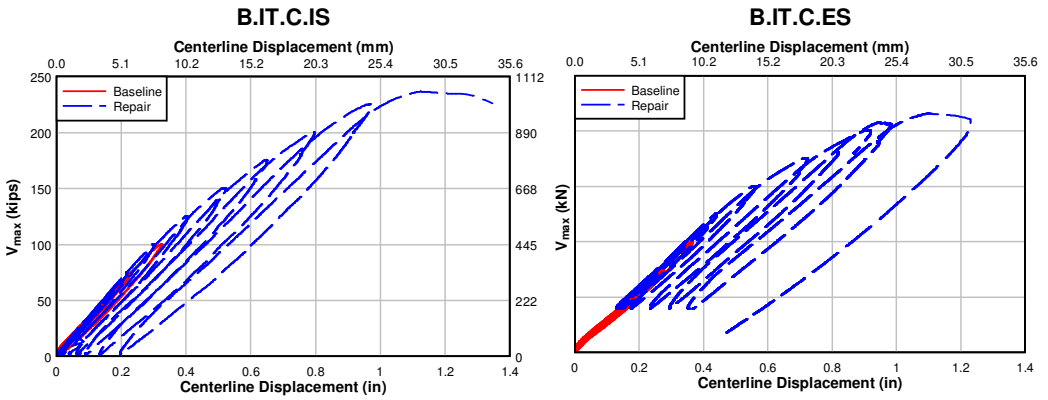

Fig. 4.58 – IT Beam with flexural cutoff details shear force versus centerline displacement: strength loading condition

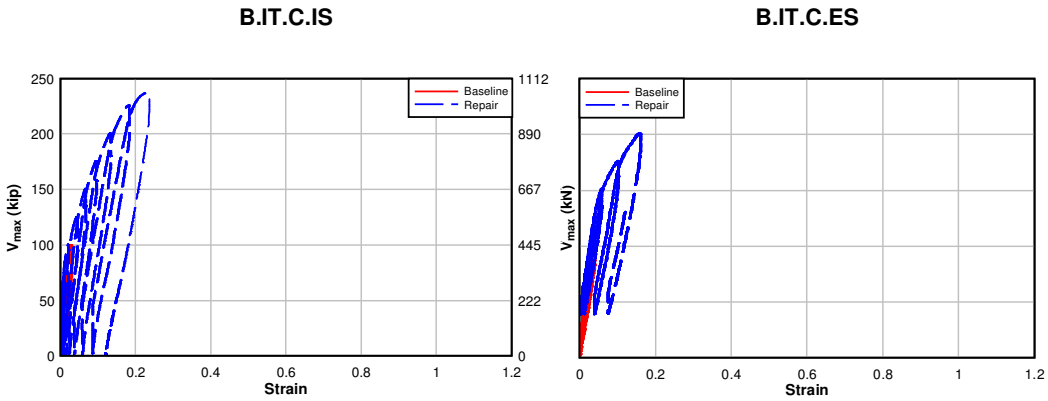

Fig. 4.59 – IT Beam with flexural cutoff details shear force versus tensile diagonal displacement: strength loading condition

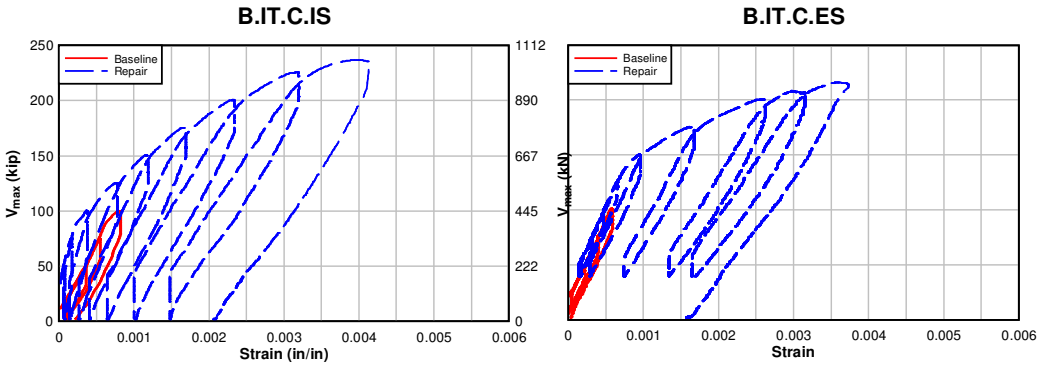

Fig. 4.60 – IT Beam with flexural cutoff details shear force versus average vertical strain: strength loading condition

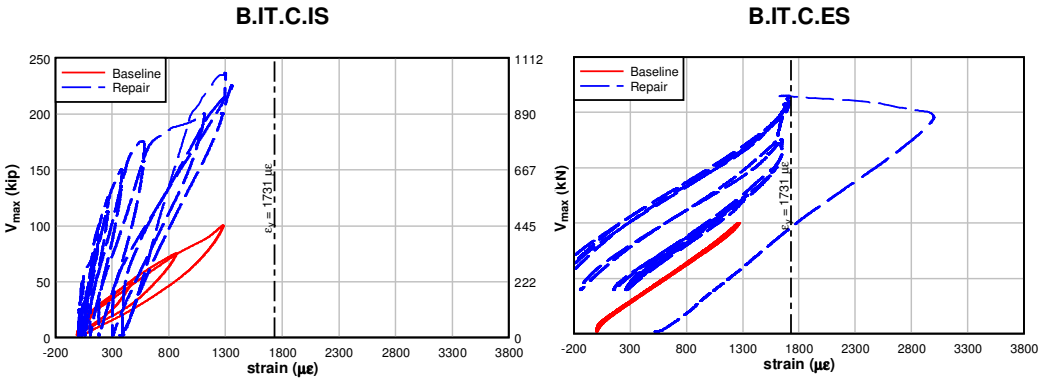

Fig. 4.61 – IT Beam with flexural cutoff details shear force versus typical integrally cast stirrup strain: strength loading condition

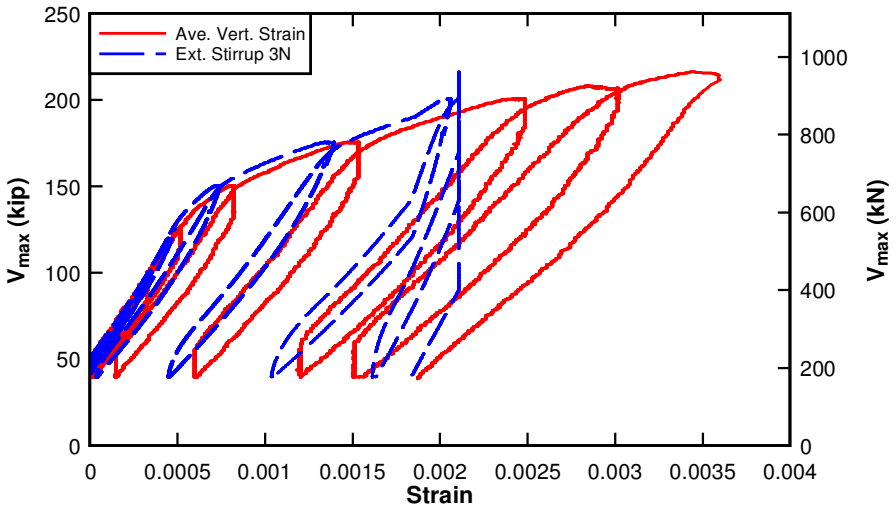

Fig. 4.62 – Specimen B.IT.C.ES shear force versus external stirrup and average vertical strain: strength loading

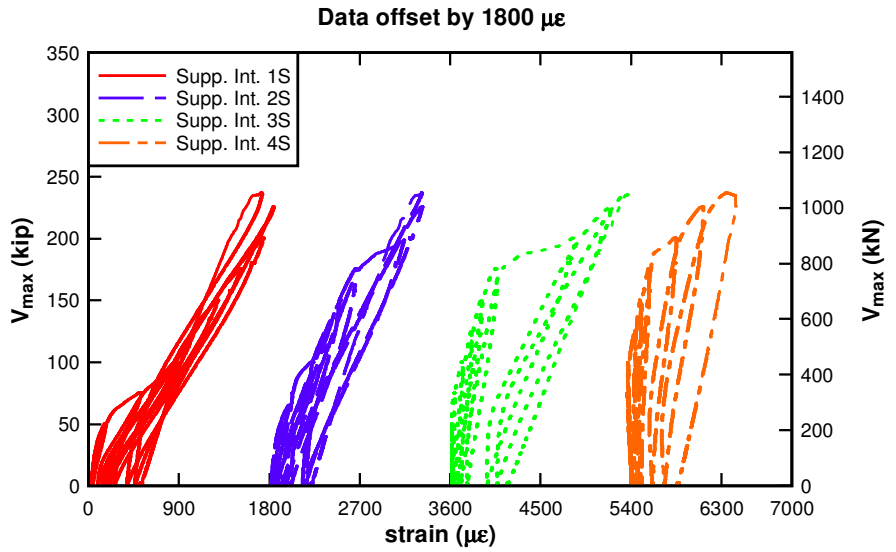

Fig. 4.63 – Specimen B.IT.NC.IS shear force versus supplemental internal stirrup strain: strength loading

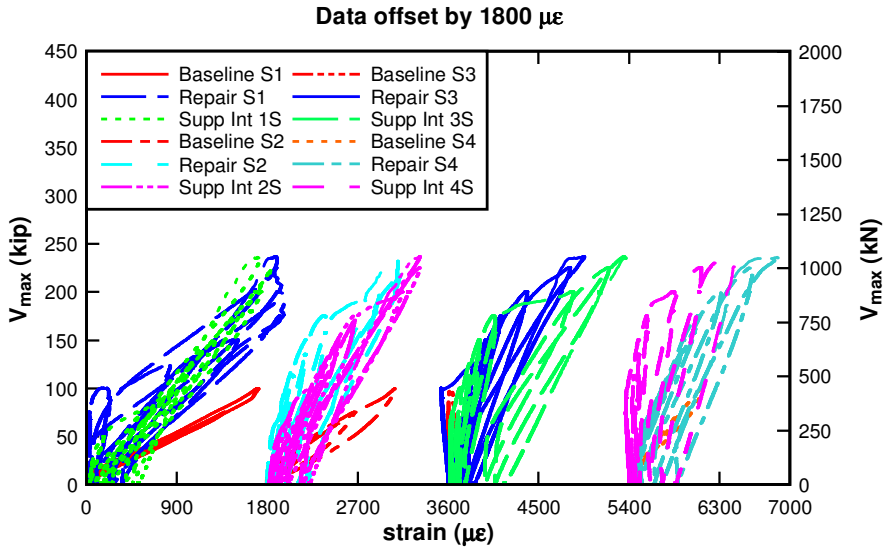

Fig. 4.64 – Specimen B.IT.NC.IS shear force versus internal and supplemental internal stirrup strain: strength loading

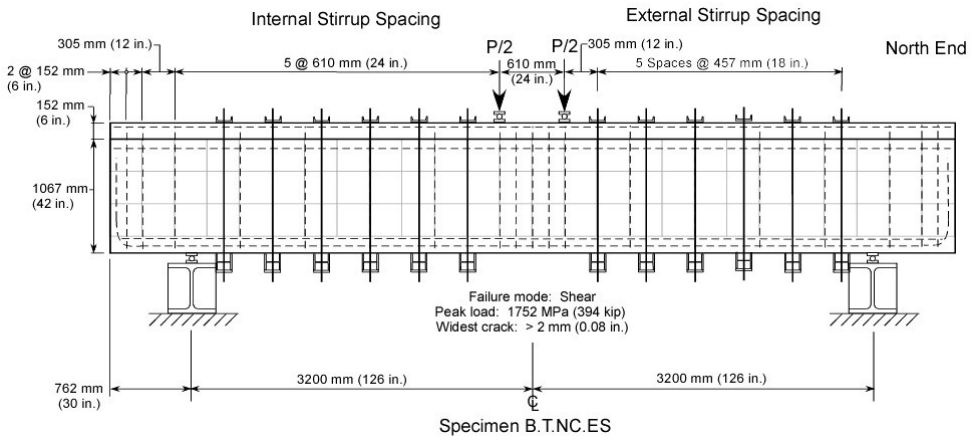

Fig. 4.65 – B.T.NC.ES revised test setup B

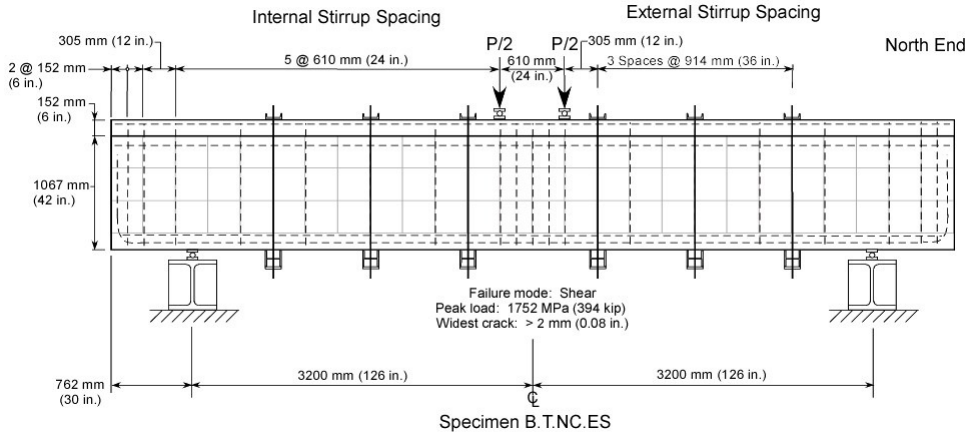

Fig. 4.66 – B.T.NC.ES revised test setup C

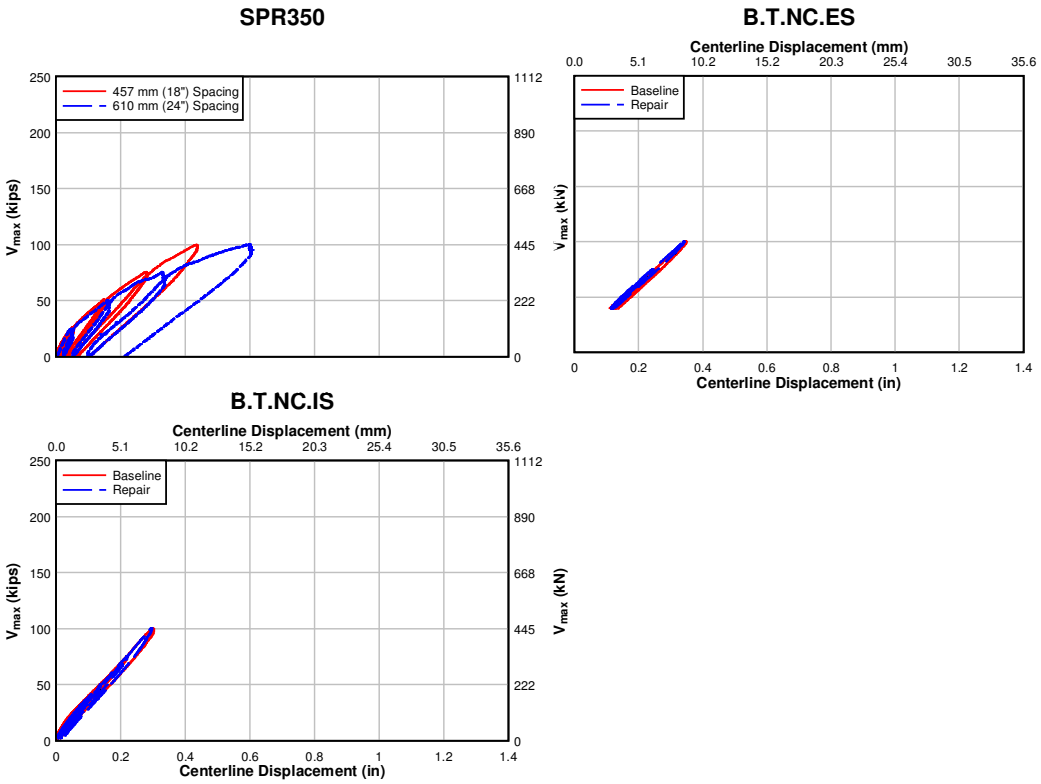

Fig. 4.67 – T Beam shear force versus centerline displacement: service loading condition

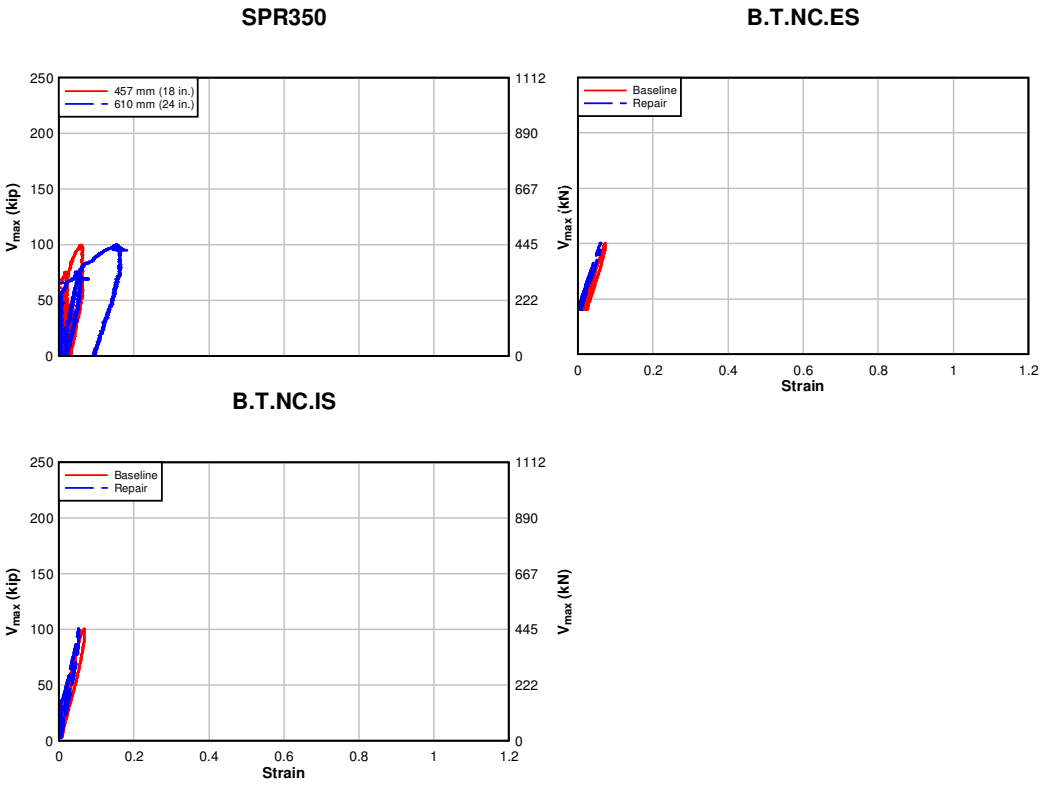

Fig. 4.68 – T Beam shear force versus tension diagonal strain: service loading condition

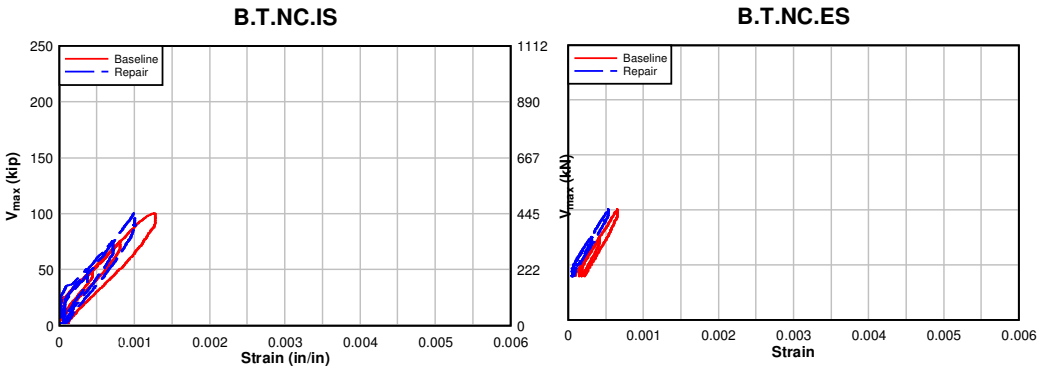

Fig. 4.69 – T Beam shear force versus average vertical strain: service loading condition

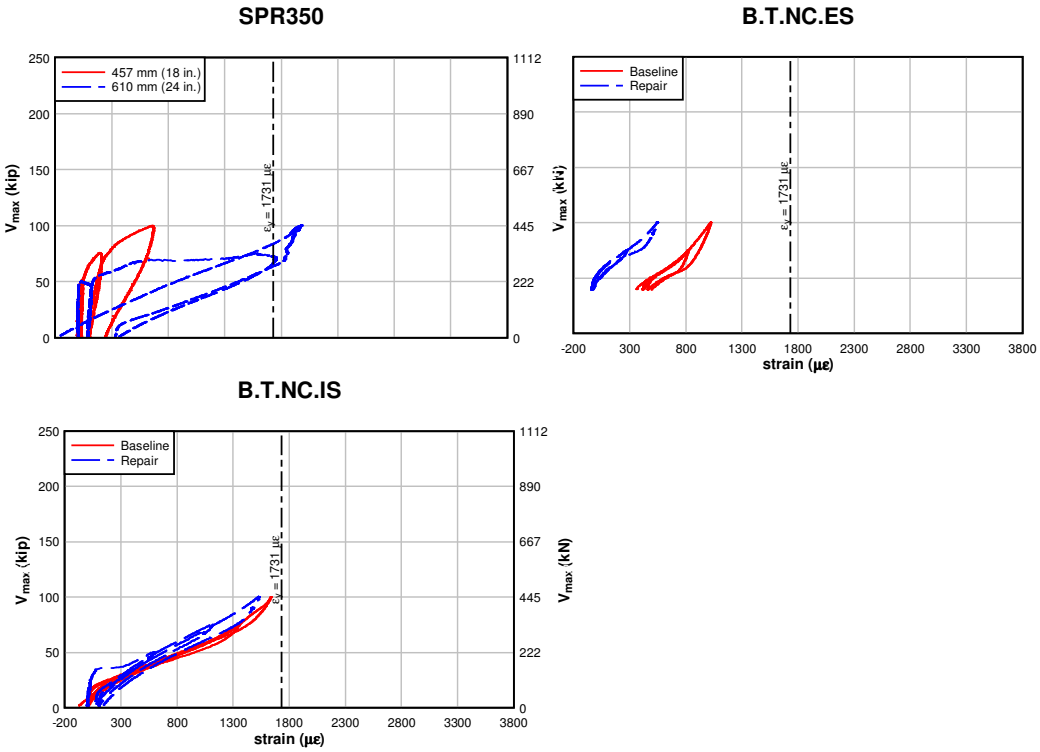

Fig. 4.70 – T Beam shear force versus typical internal stirrup strain: service loading condition

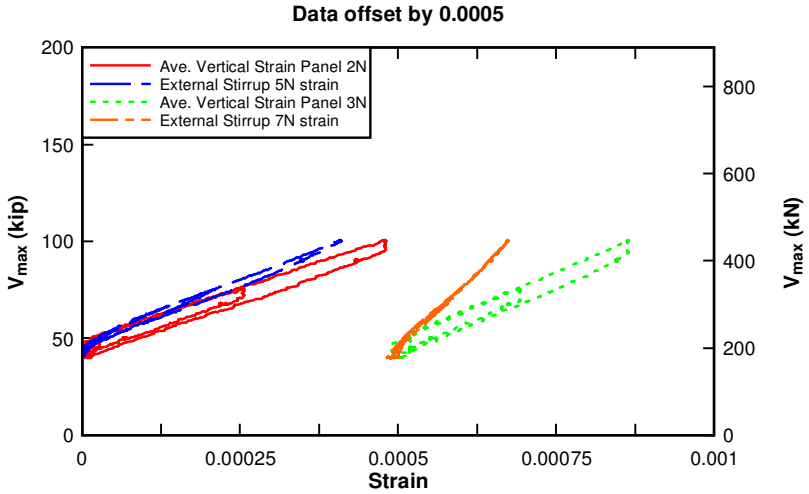

Fig. 4.71 – B.T.NC.ES shear force versus average vertical strain and external stirrup strain: service loading condition

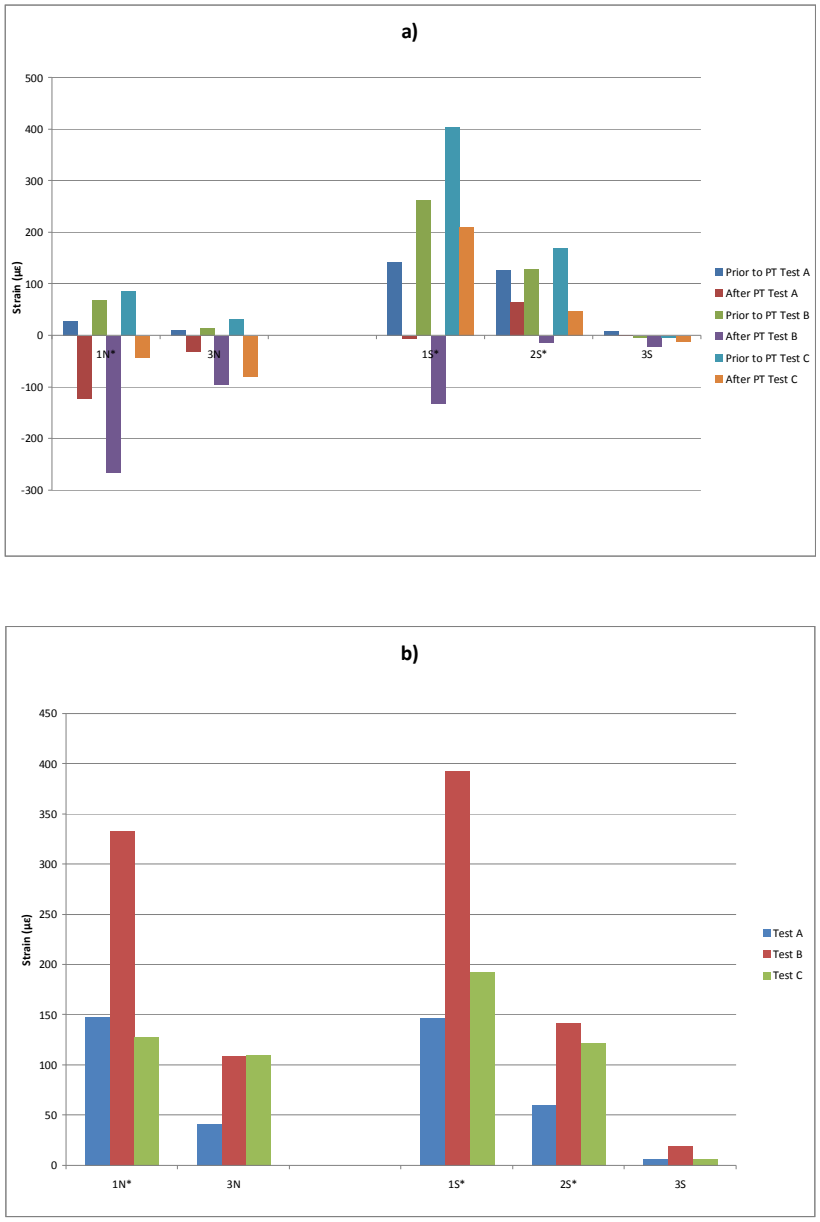

Fig. 4.72 – Specimen B.T.NC.ES integrally cast stirrup strain: a) before and after post tensioning, b) strain reduction due to post tensioning. Note: asterisk denotes chipped in stirrups.

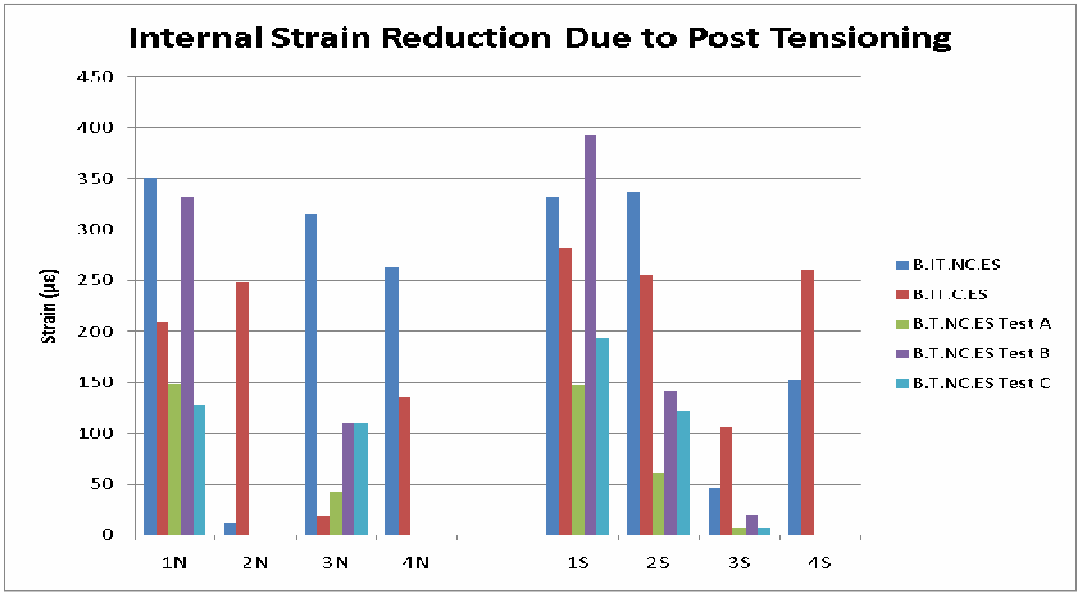

Fig. 4.73 – Comparison of specimens B.IT.NC.ES, B.IT.C.ES, and B.T.NC.ES integrally cast stirrup absolute strain reduction due to post tensioning

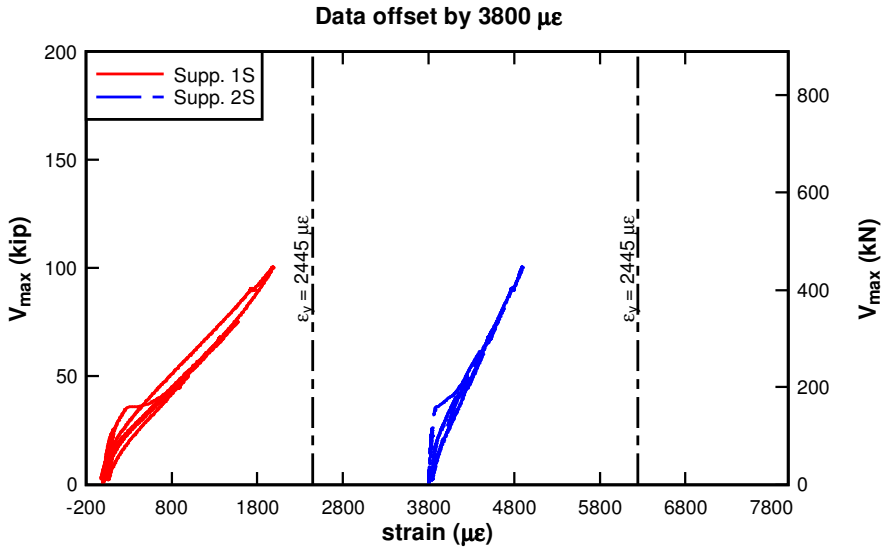

Fig. 4.74 – Specimen B.T.NC.IS shear force versus supplemental internal stirrup strain

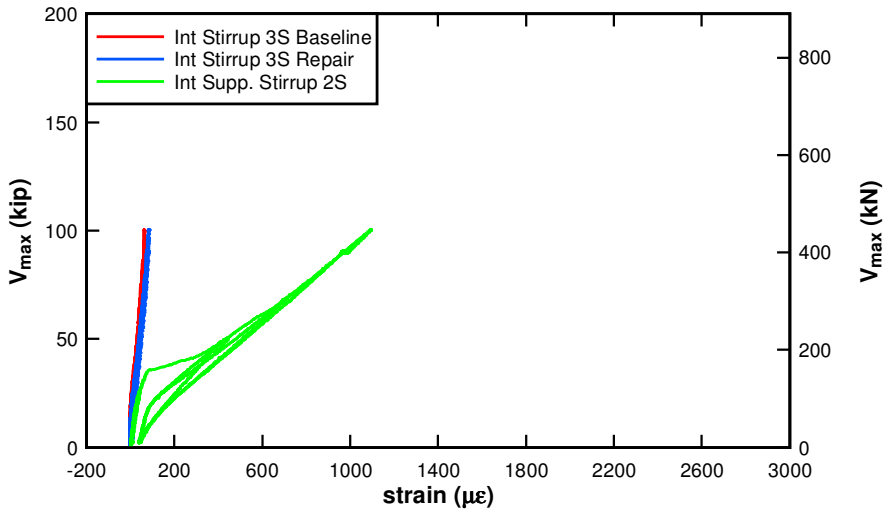

Fig. 4.75 – Specimen B.T.NC.IS shear force versus internal and supplemental internal stirrup strain

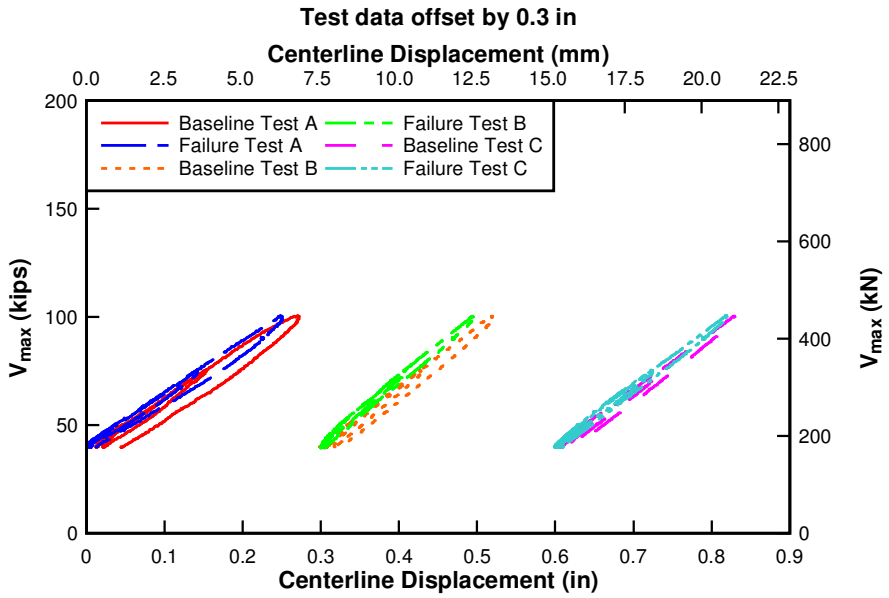

Fig. 4.76 – B.T.NC.ES shear force versus centerline displacement for tests A, B, and C

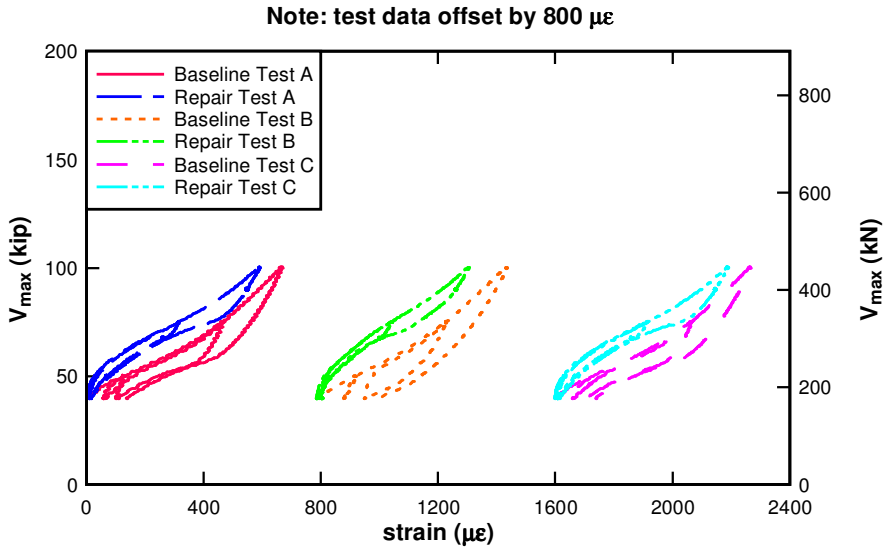

Fig. 4.77 – B.T.NC.ES shear versus internal stirrup 1N strain range for tests A, B, and C

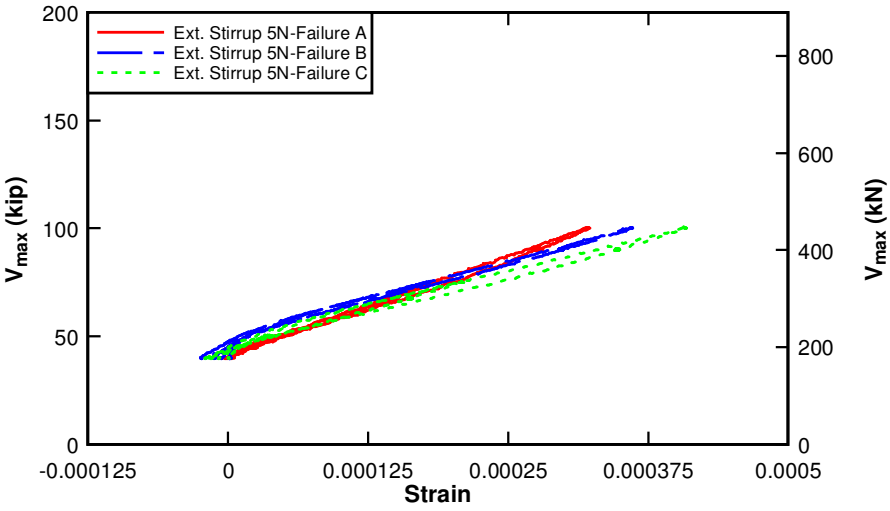

Fig. 4.78 – B.T.NC.ES shear versus external stirrup 5N strain for tests A, B, and C

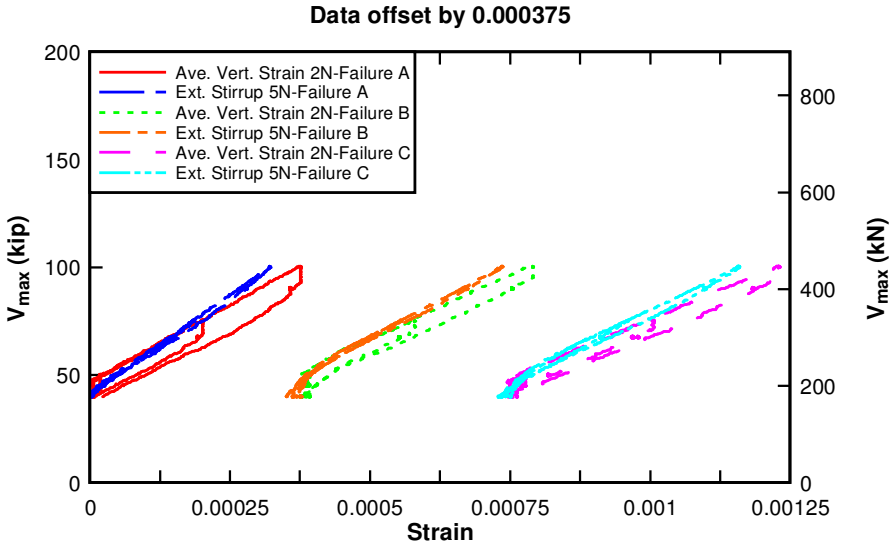

Fig. 4.79 – Specimen B.T.NC.ES shear versus external stirrup 5N and average vertical strain in panel 2N for tests A, B, and C, offset for clarity

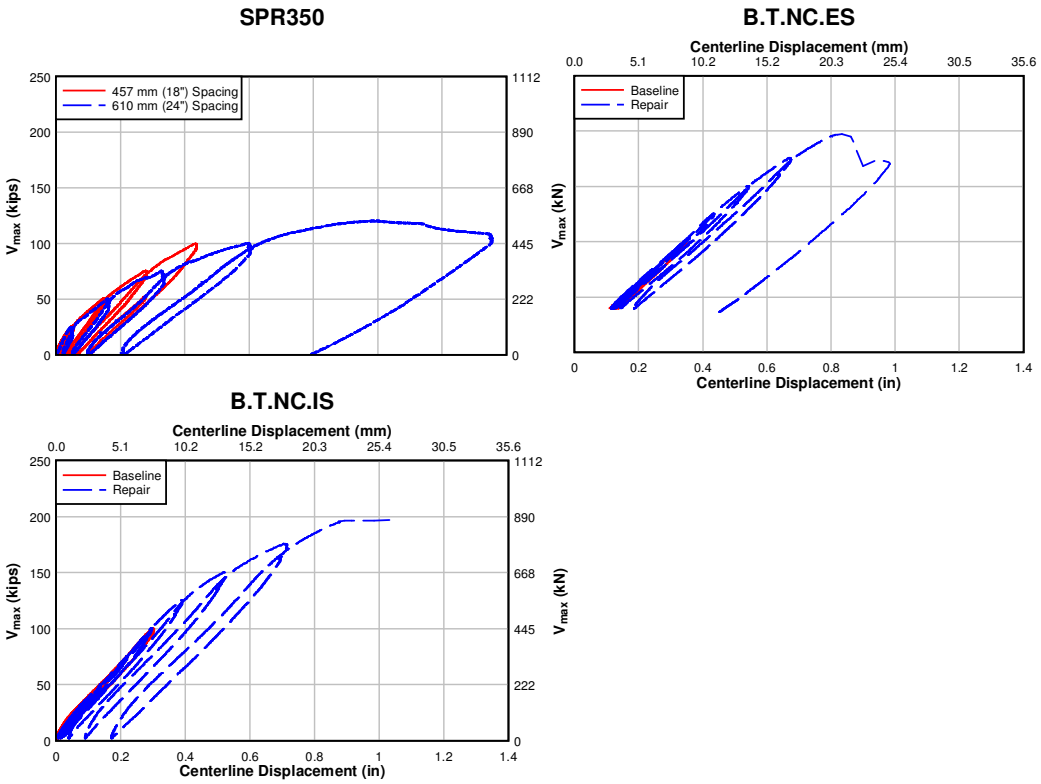

Fig. 4.80 – T Beam shear force versus centerline displacement: strength loading condition

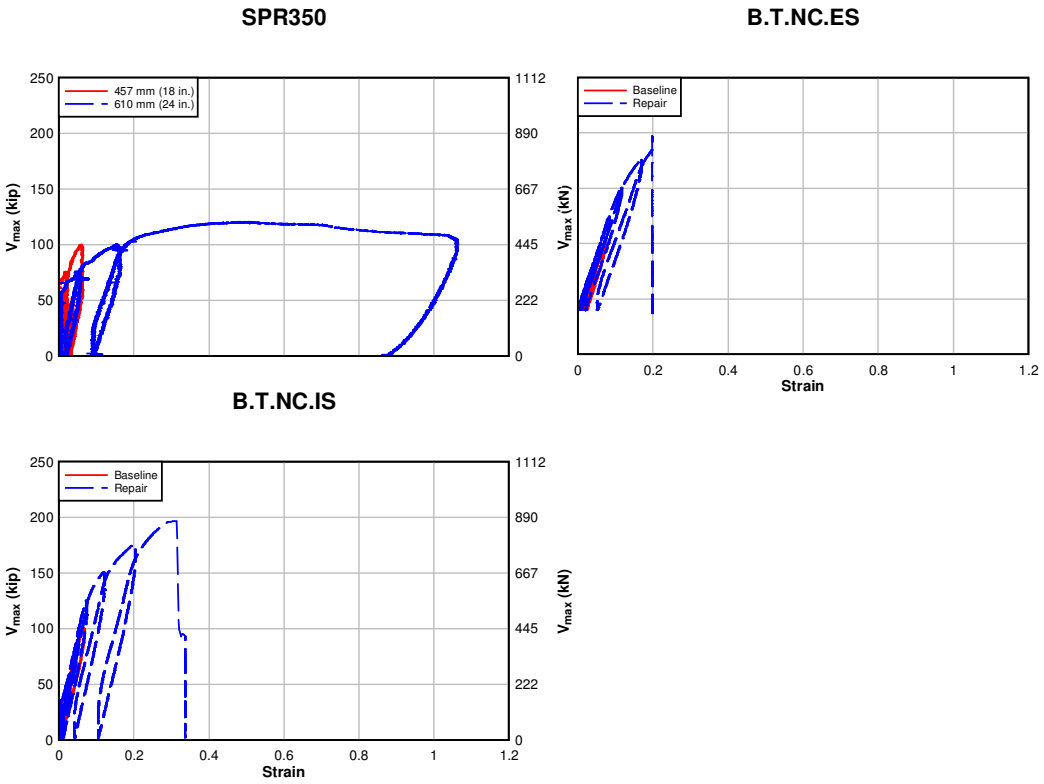

Fig. 4.81 – T Beam shear force versus tension diagonal strain: strength loading condition

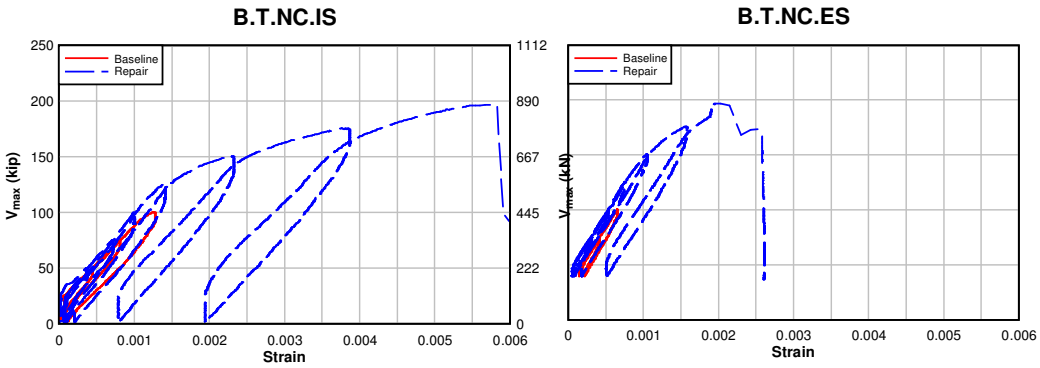

Fig. 4.82 – T Beam shear force versus average vertical strain: strength loading condition

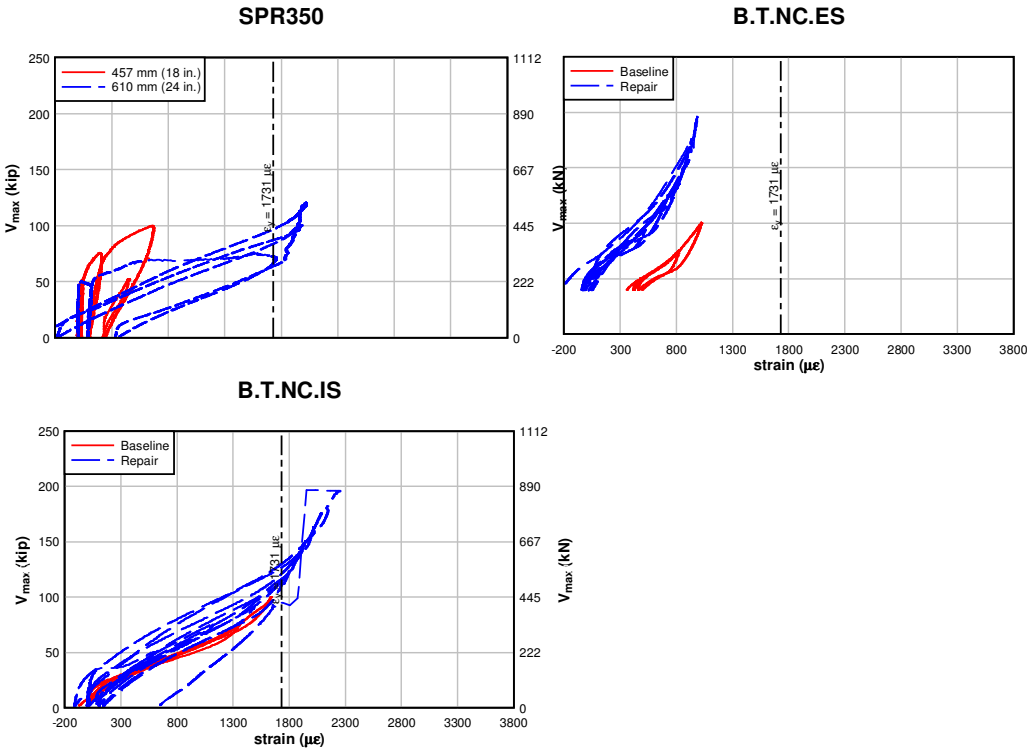

Fig. 4.83 – T Beam shear force versus typical internal stirrup strain: strength loading condition

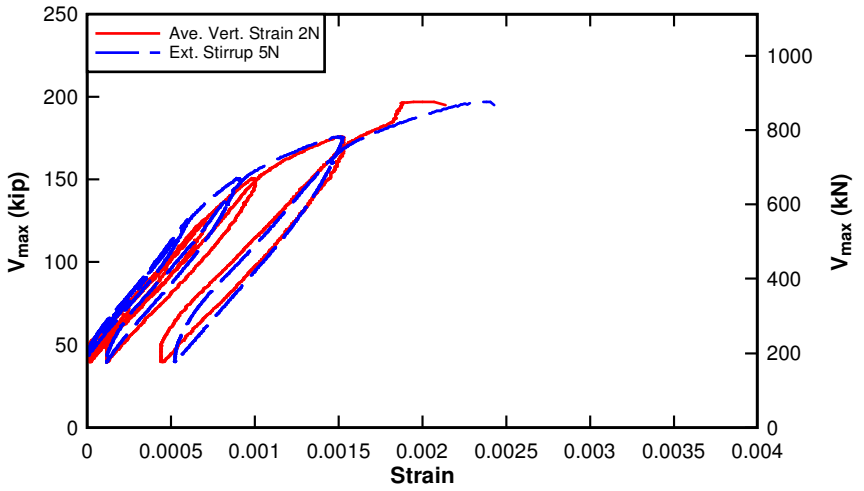

Fig. 4.84 – Specimen B.T.NC.ES shear force versus external stirrup and average vertical strain: strength loading

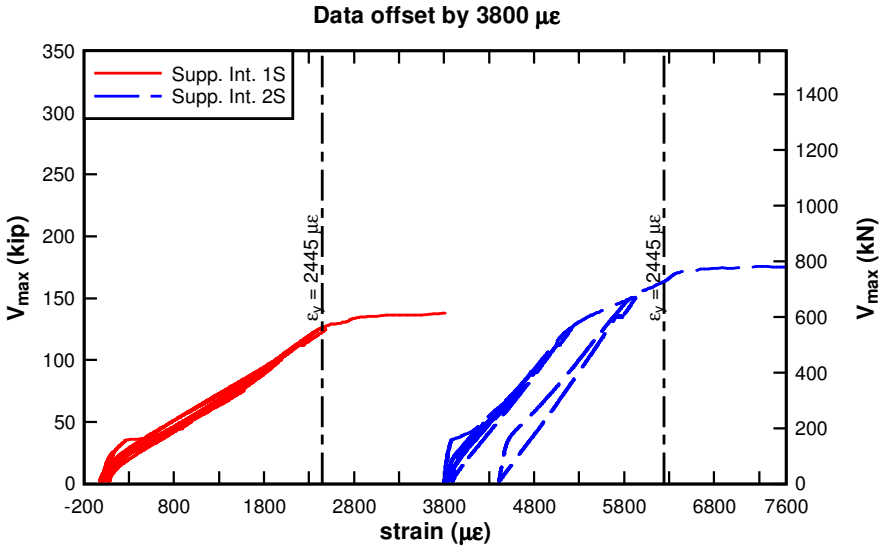

Fig. 4.85 – Specimen B.T.NC.IS shear force versus supplemental internal stirrup strain: strength loading

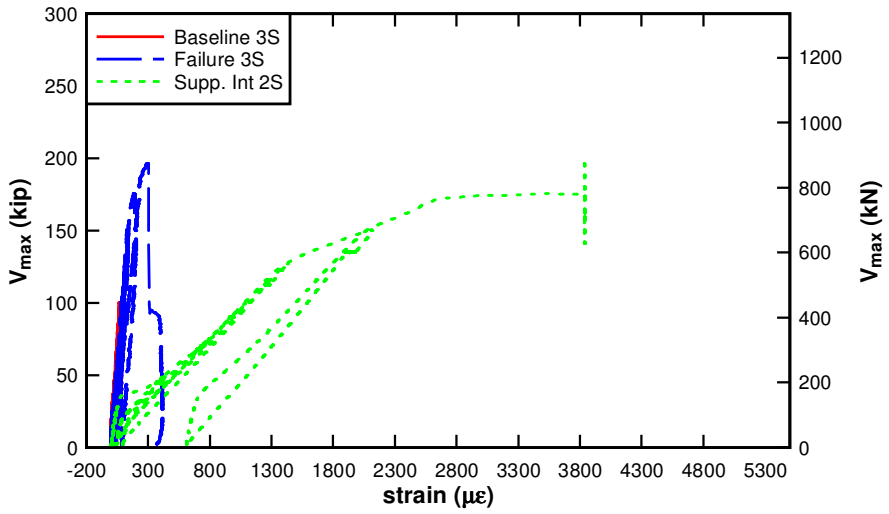

Fig. 4.86 – Specimen B.T.NC.IS shear force versus internal and supplemental internal stirrup strain: strength loading

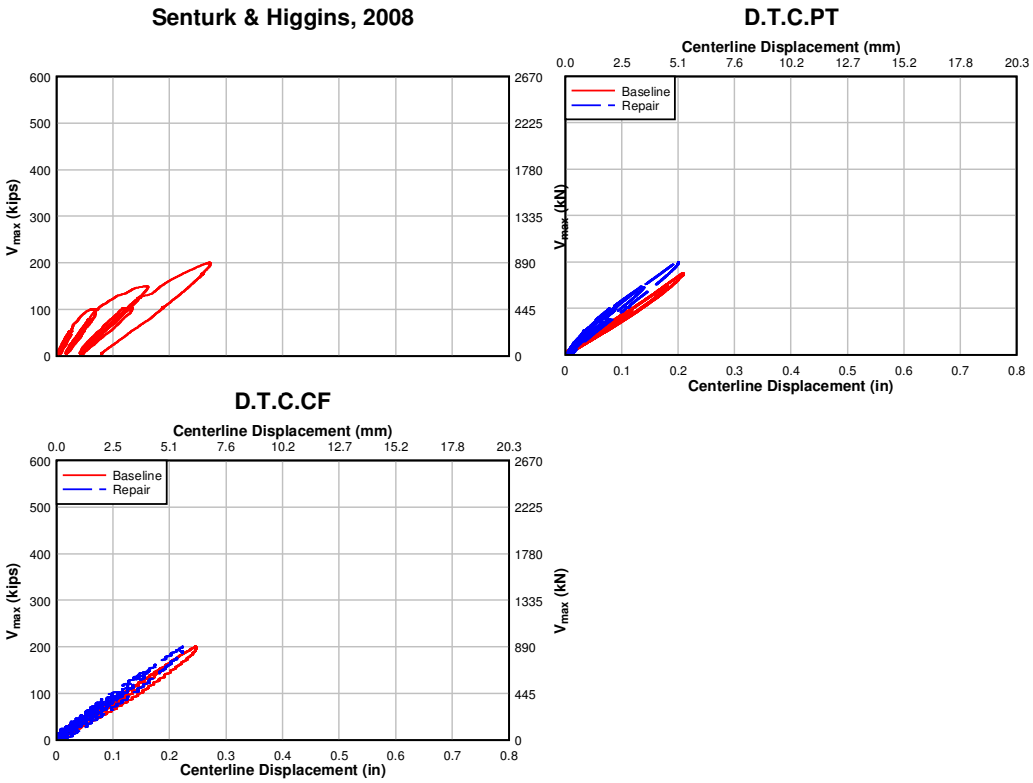

Fig. 4.87 – Bent cap shear force versus centerline displacement: service loading condition

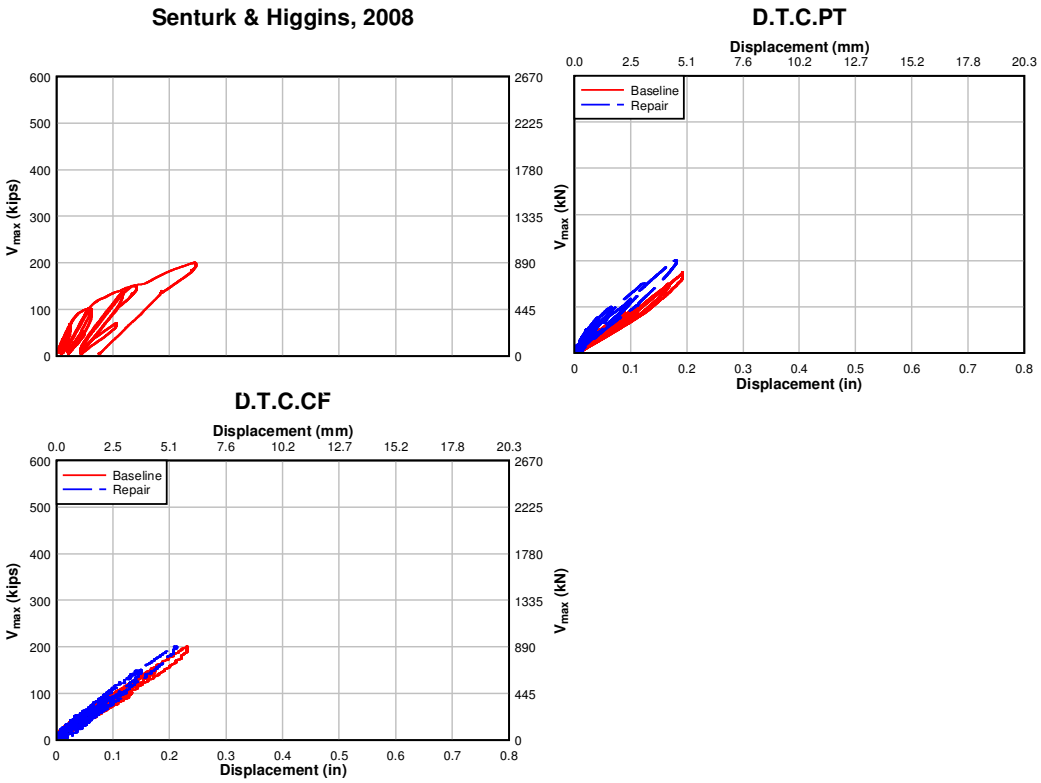

Fig. 4.88 – Bent cap shear force versus south stub girder displacement: service loading condition

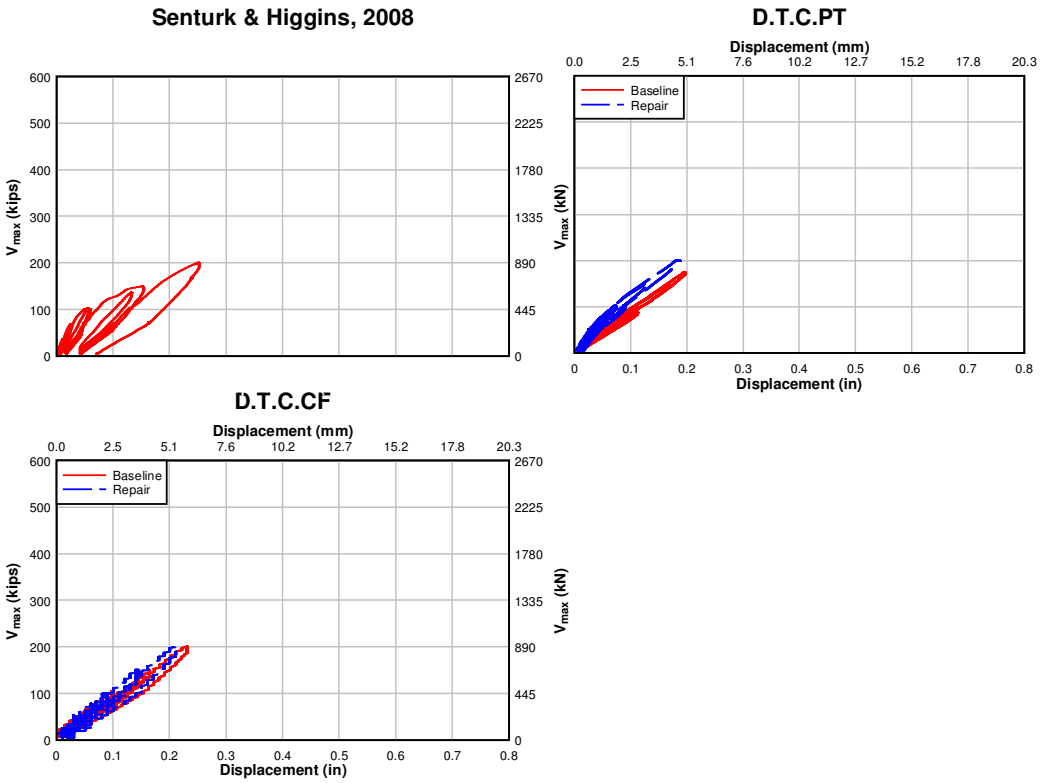

Fig. 4.89 – Bent cap shear force versus north stub girder displacement: service loading condition

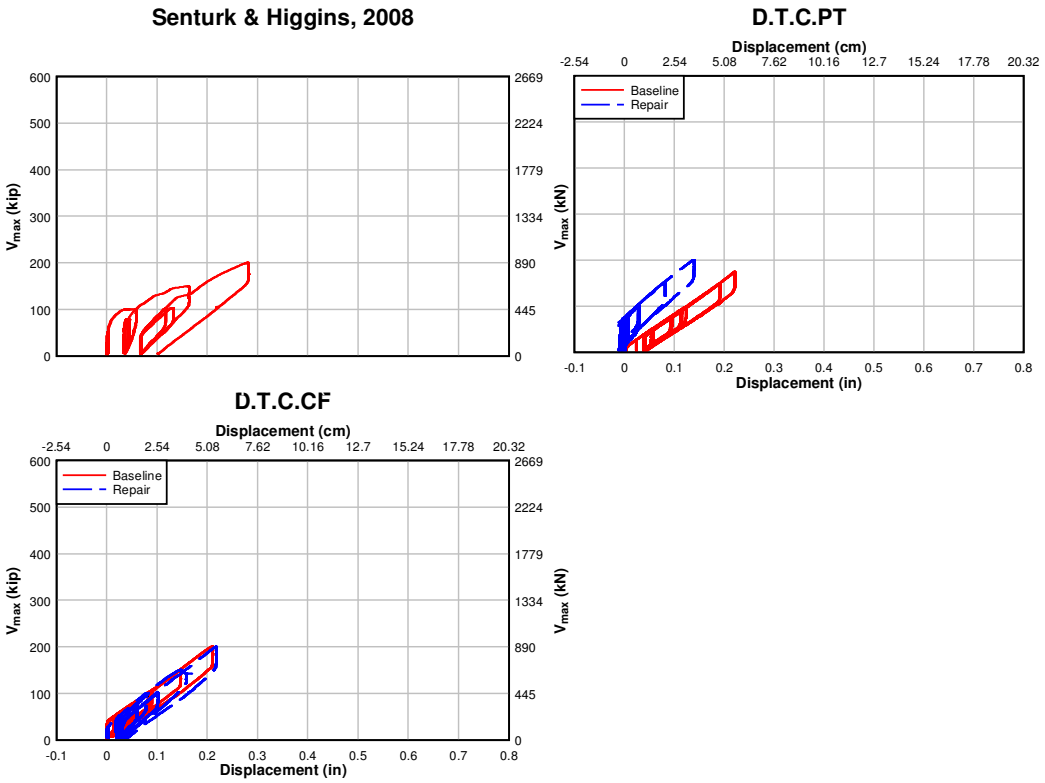

Fig. 4.90 – Bent cap shear force versus relative column displacement: service loading condition

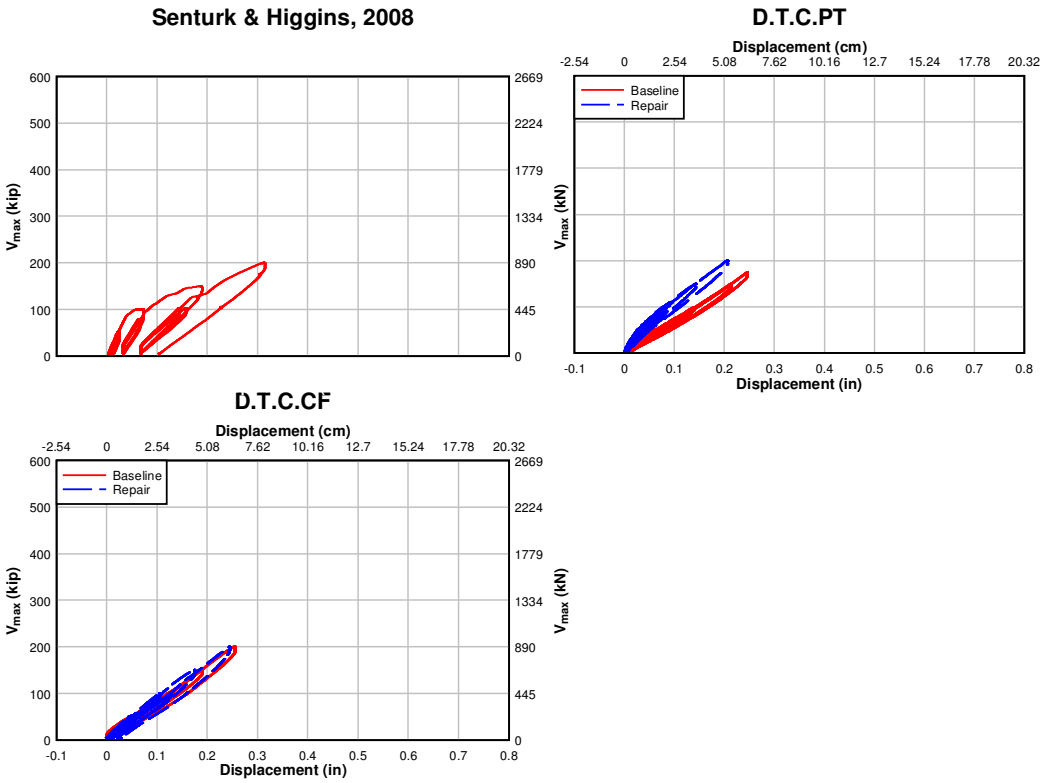

Fig. 4.91 – Bent cap shear force versus absolute column displacement: service loading condition

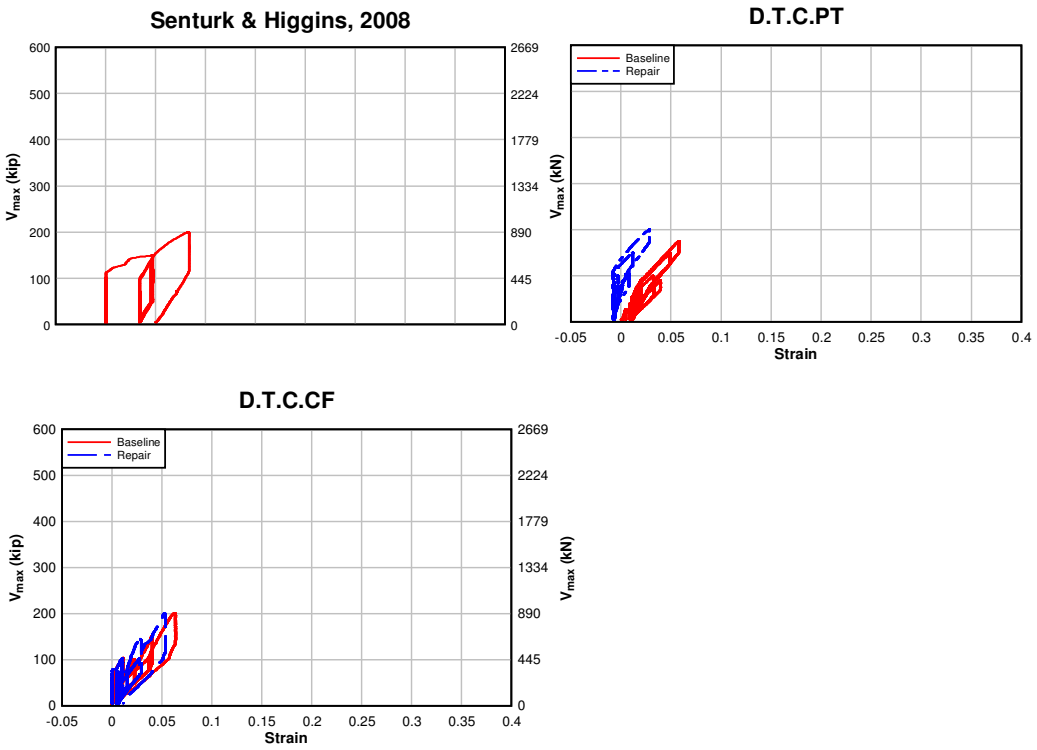

Fig. 4.92 – Bent cap shear force versus north tension diagonal: service loading condition

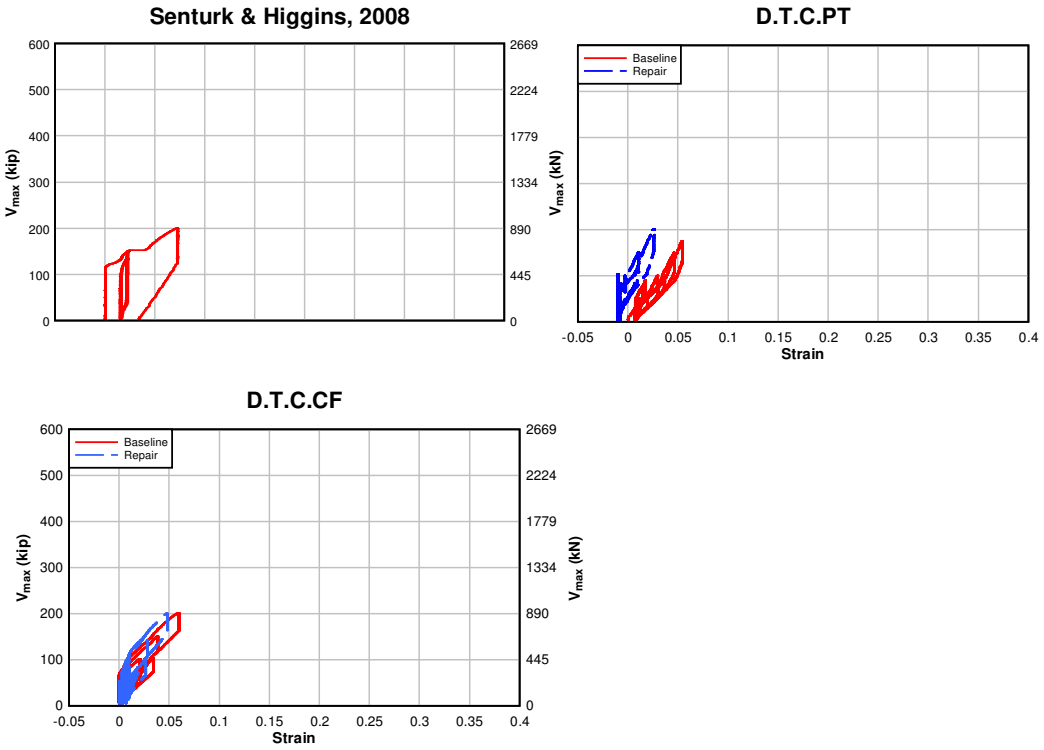

Fig. 4.93 – Bent cap shear force versus south tension diagonal: service loading condition

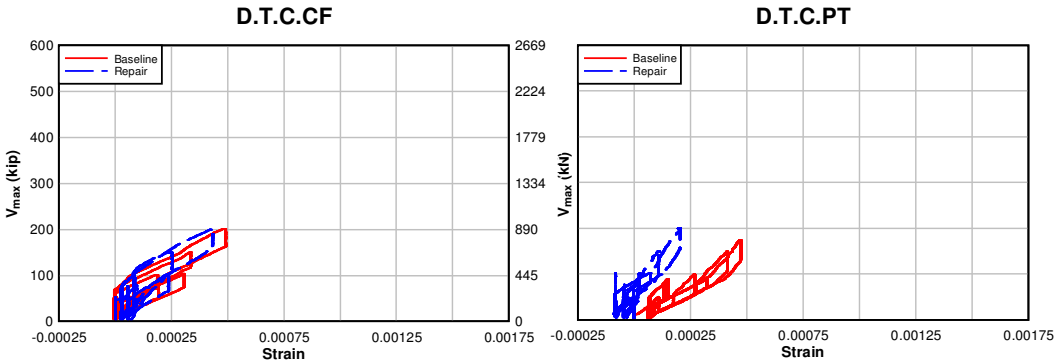

Fig. 4.94 – Bent cap shear force versus south average vertical strain: service loading condition

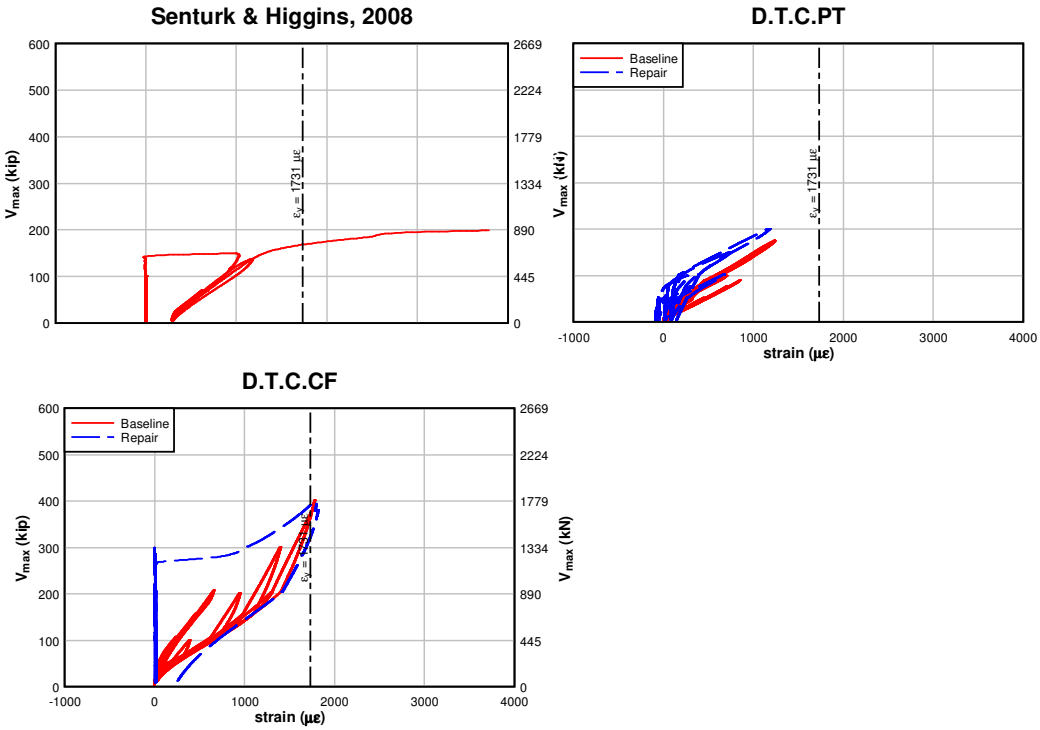

Fig. 4.95 – Bent cap shear force versus typical north internal stirrup: service loading condition

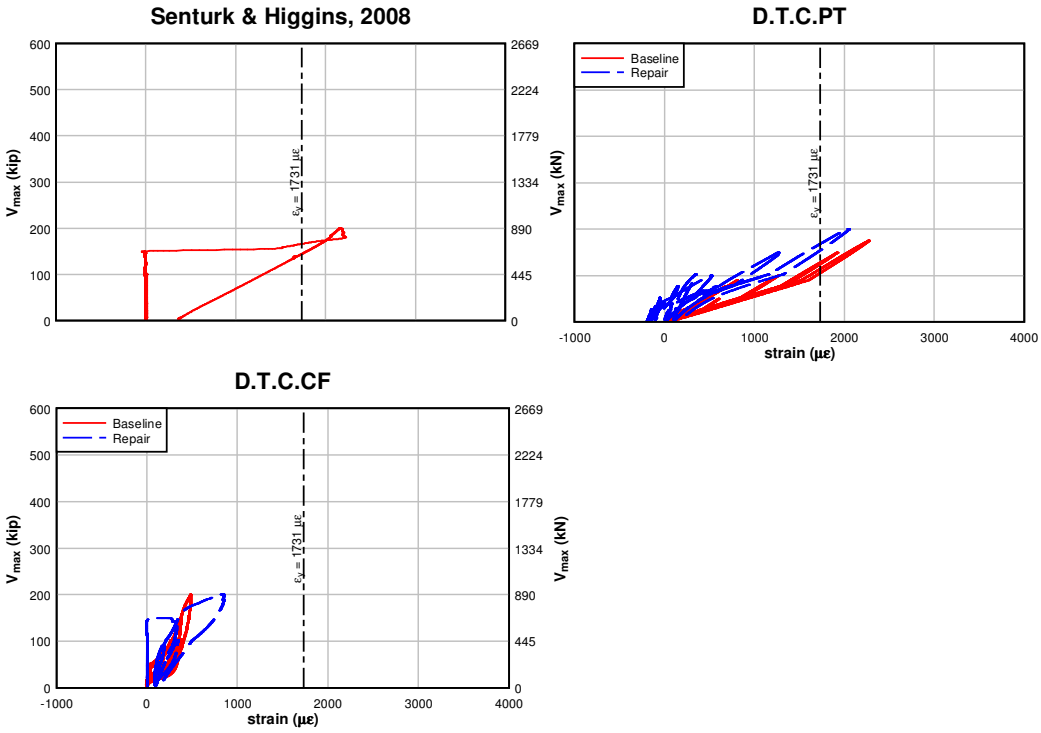

Fig. 4.96 – Bent cap shear force versus typical south internal stirrup: service loading condition

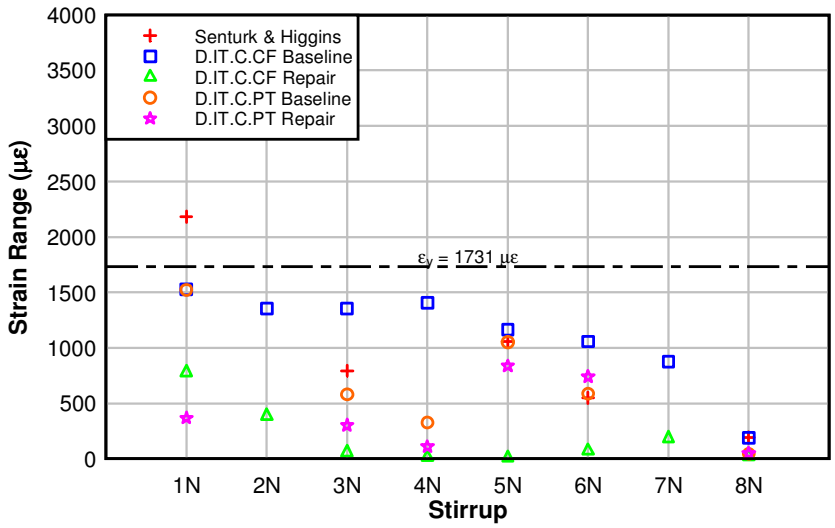

Fig. 4.97 – Bent cap north integrally cast stirrup strain: service loading condition

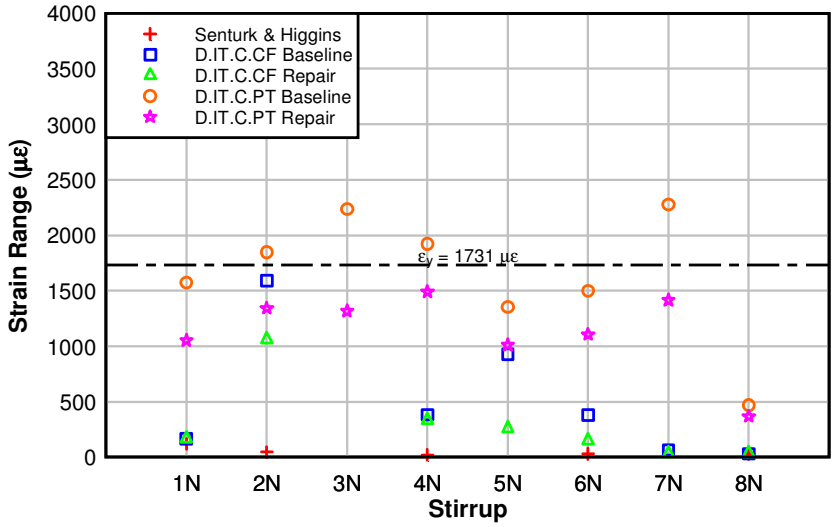

Fig. 4.98 – Bent cap south integrally cast stirrup strain: service loading condition

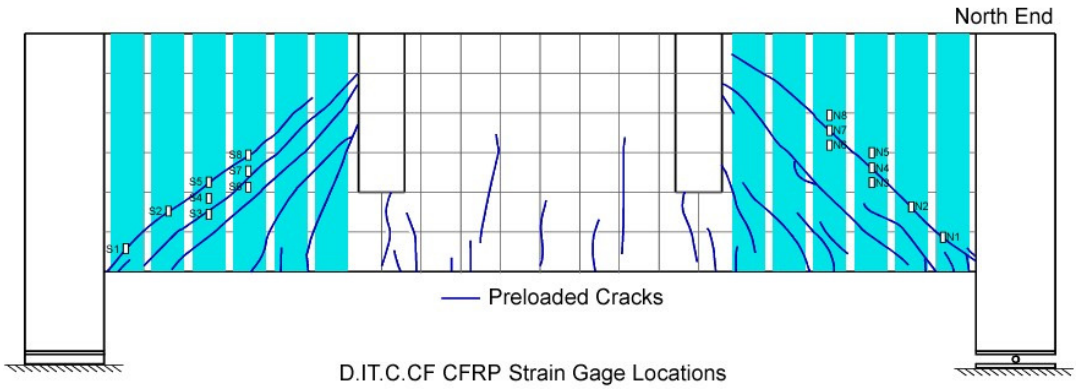

Fig. 4.99 – Bent cap CFRP strain gage locations

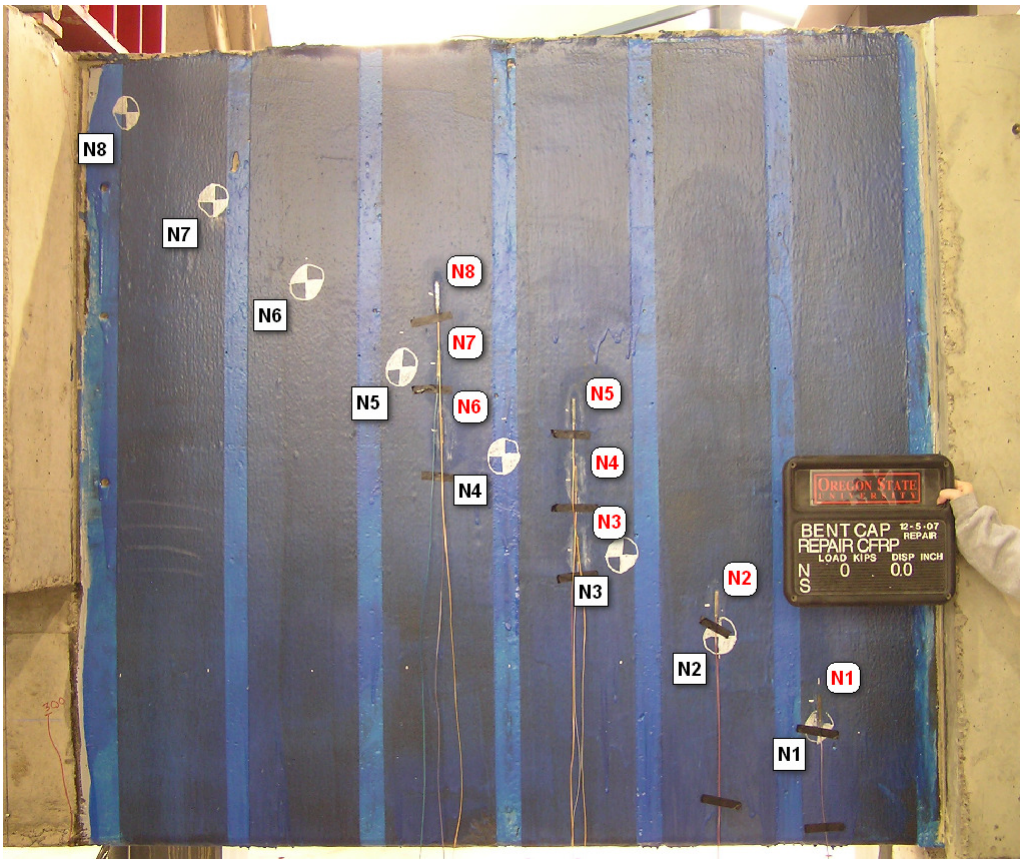

Fig. 4.100 – Bent cap north end integrally cast stirrup and CFRP strain gage locations

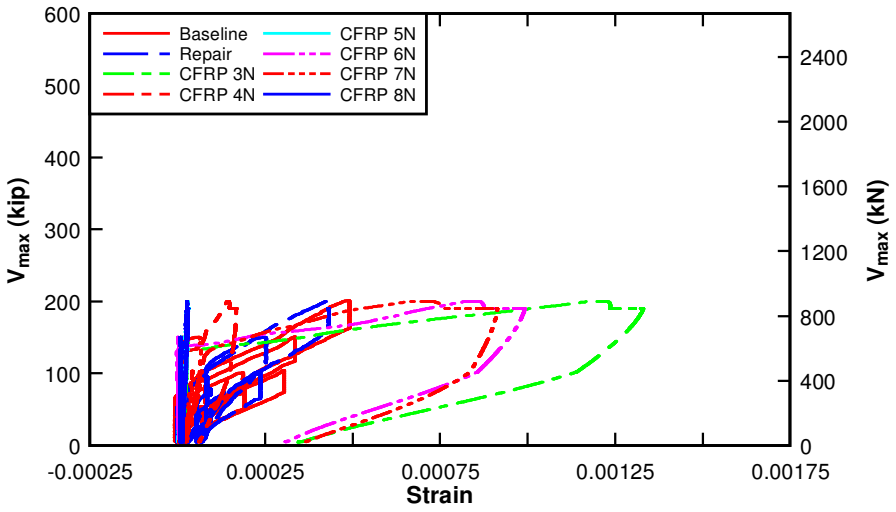

Fig. 4.101 – Bent cap D.T.C.CF shear force versus CFRP and average vertical strain: service loading condition

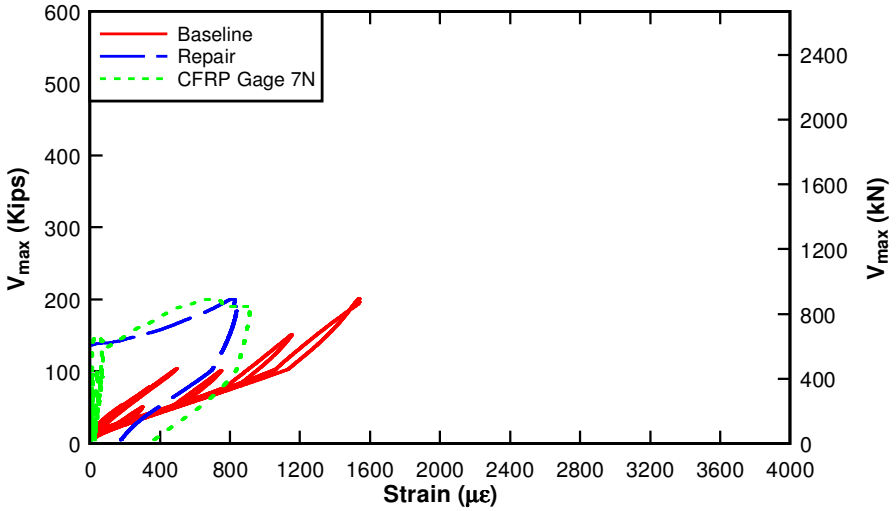

Fig. 4.102 – Bent cap D.T.C.CF shear force versus CFRP and integrally cast stirrup strain: service loading condition

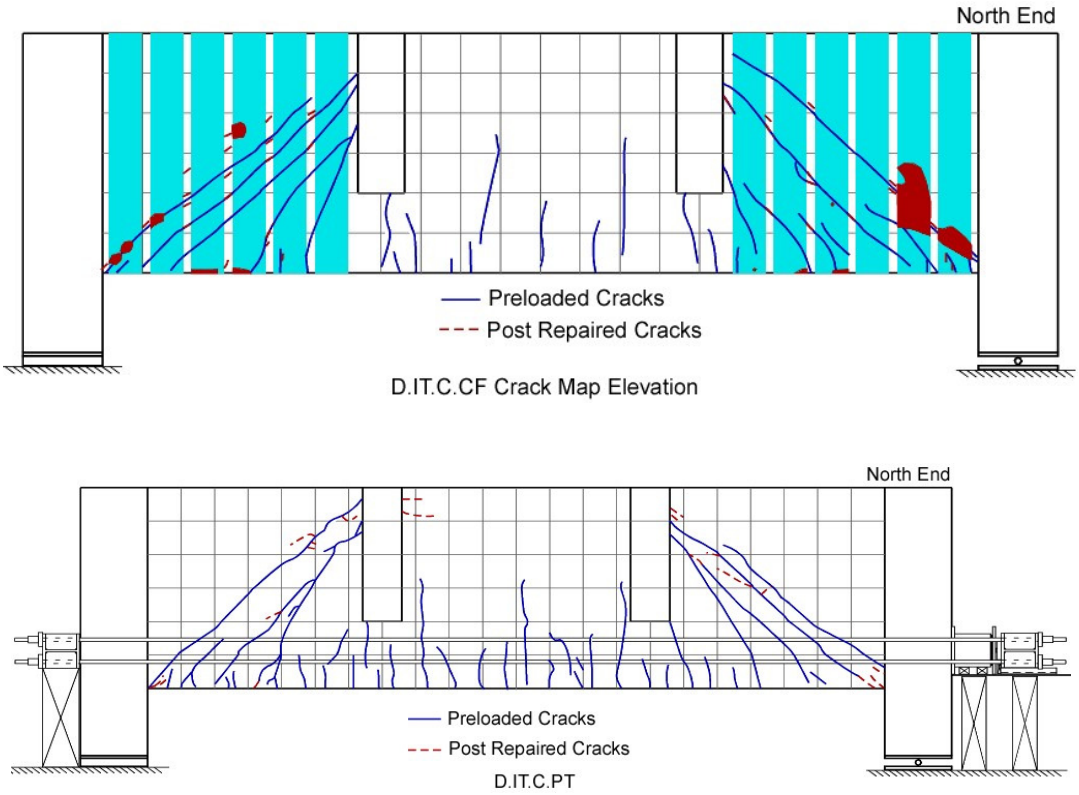

Fig. 4.103 – Baseline and strength loading crack maps for bent cap specimens

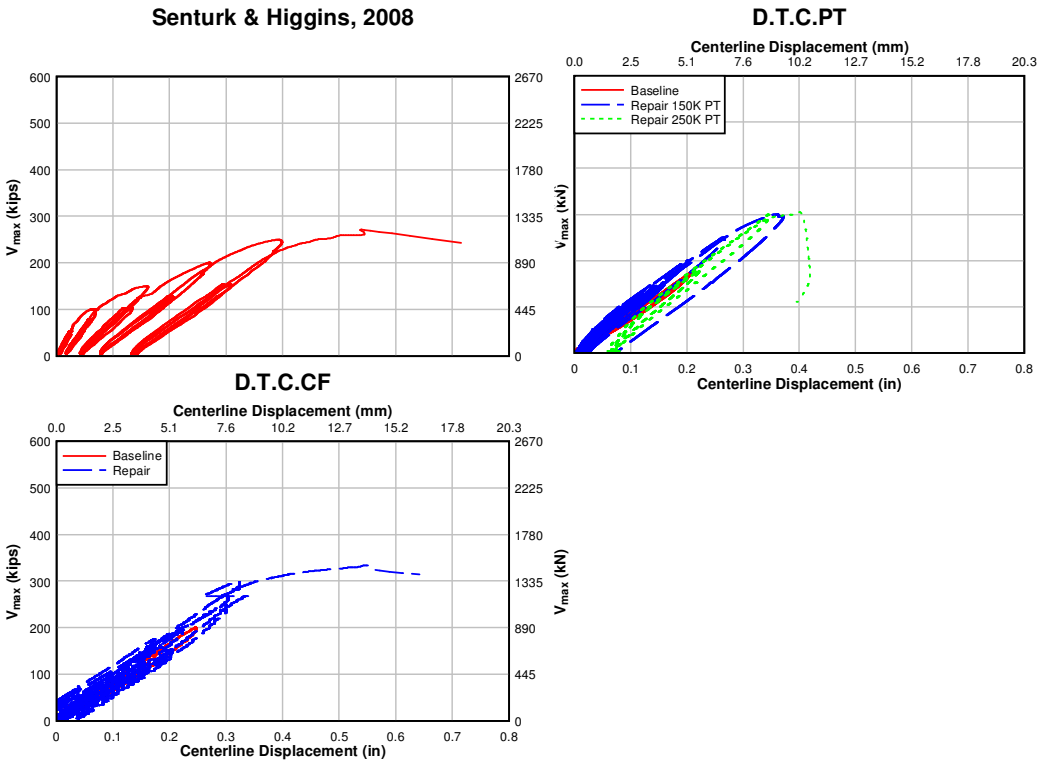

Fig. 4.104 – Bent cap shear force versus centerline displacement: ultimate loading condition

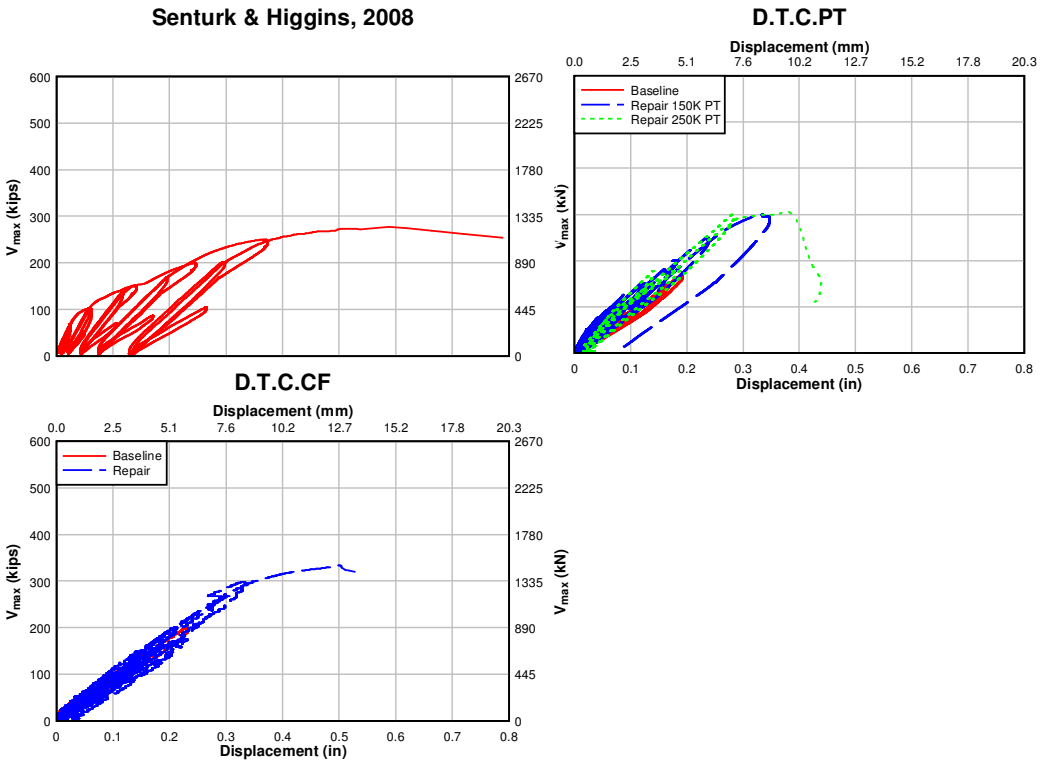

Fig. 4.105 – Bent cap shear force versus south stub girder displacement: ultimate loading condition

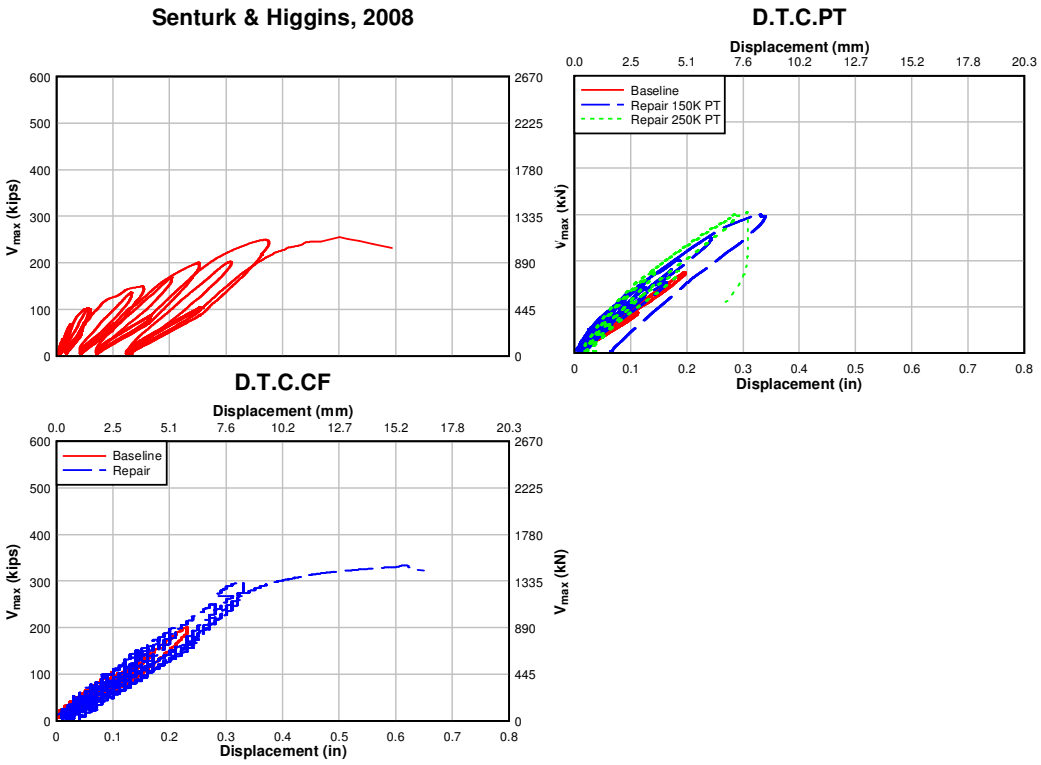

Fig. 4.106 – Bent cap shear force versus north stub girder displacement: ultimate loading condition

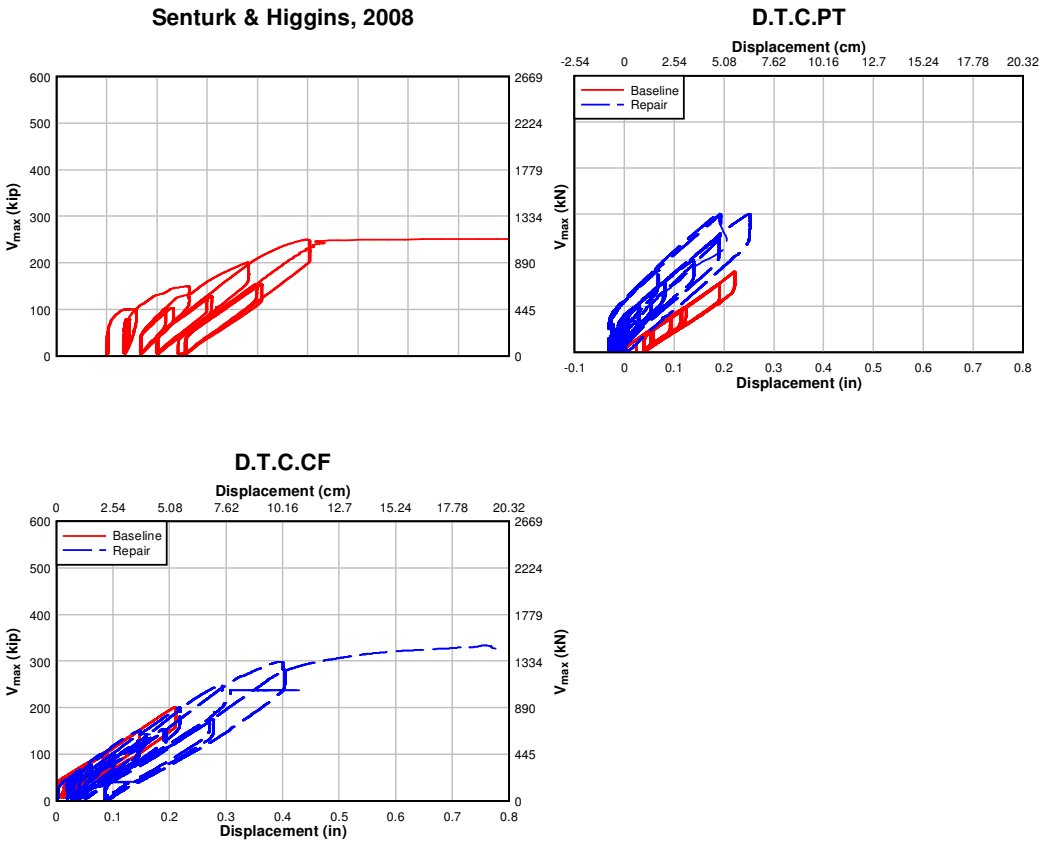

Fig. 4.107 – Bent cap shear force versus relative column displacement: service loading condition

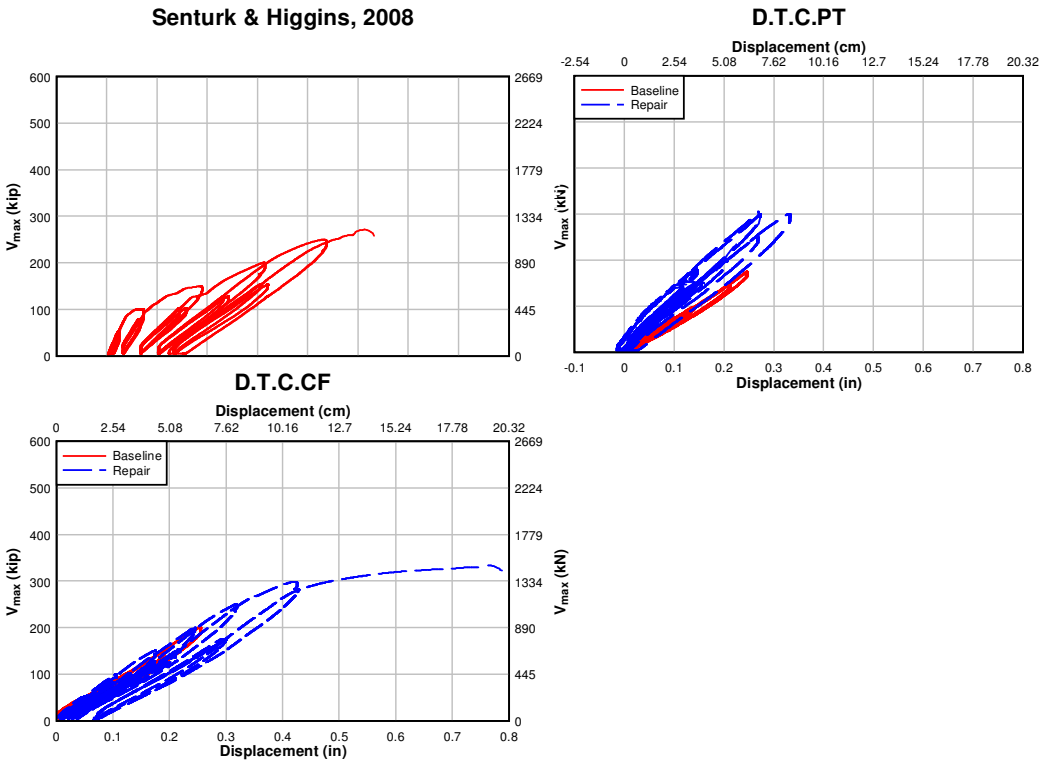

Fig. 4.108 – Bent cap shear force versus absolute column displacement: service loading condition

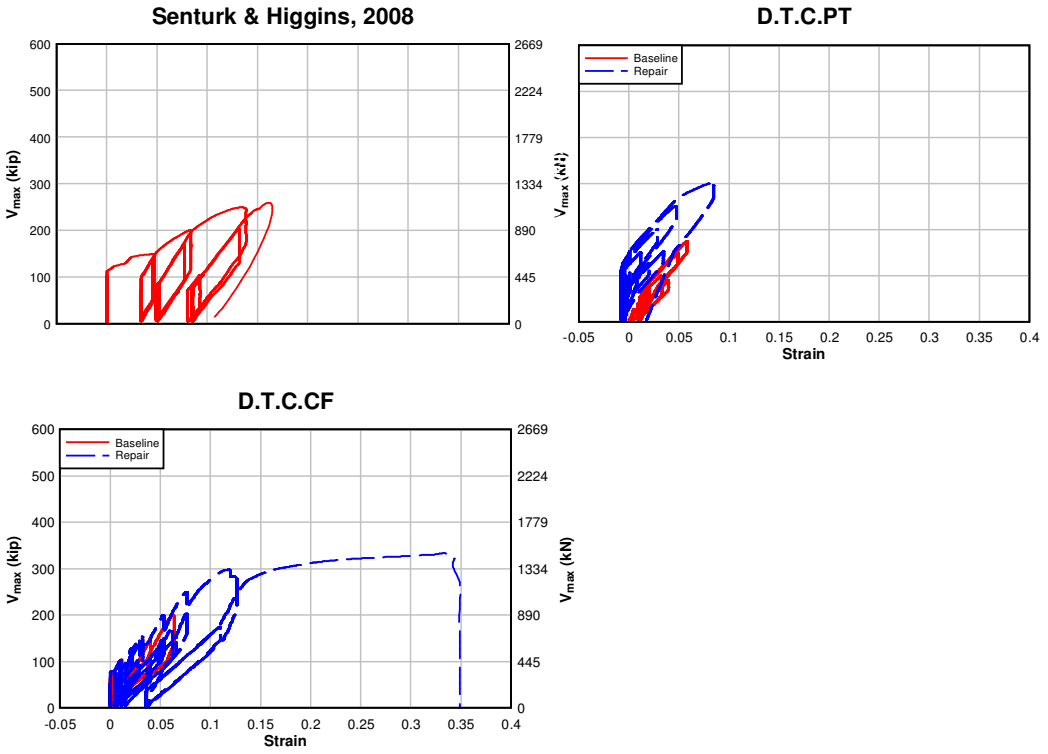

Fig. 4.109 – Bent cap shear force versus north tension diagonal: ultimate loading condition

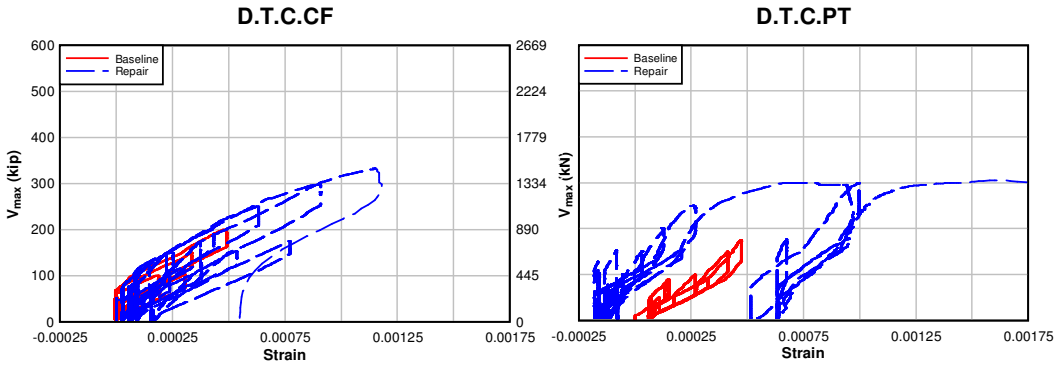

Fig. 4.110 – Bent cap shear force versus south average vertical strain: ultimate loading condition

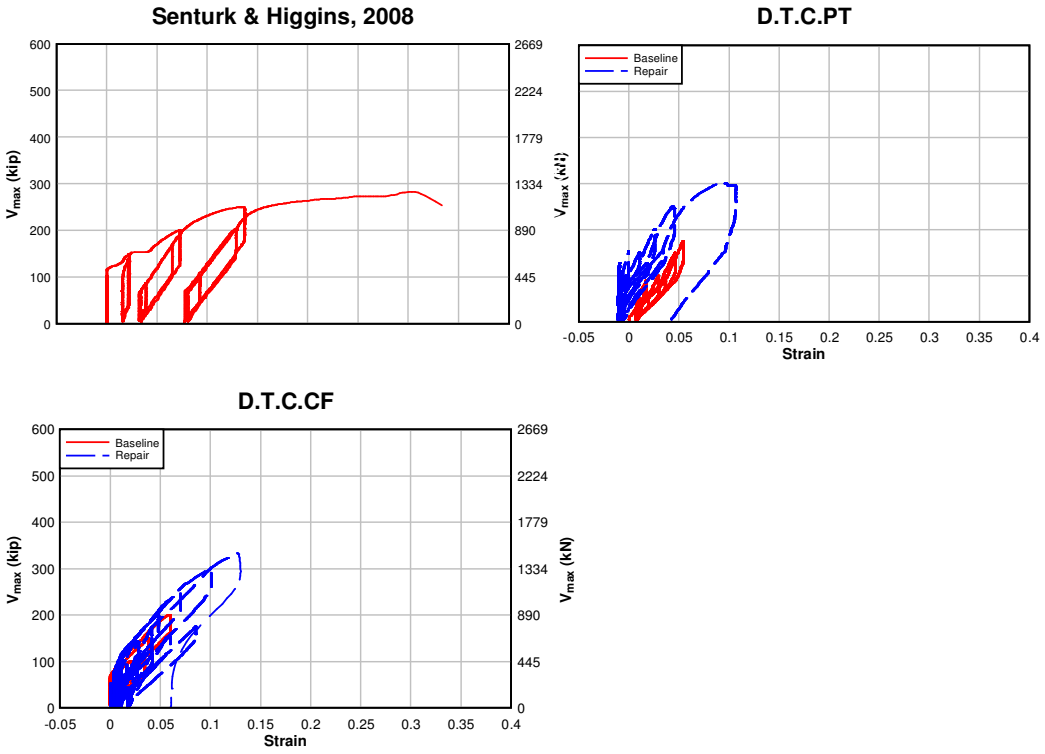

Fig. 4.111 – Bent cap shear force versus south tension diagonal: ultimate loading condition

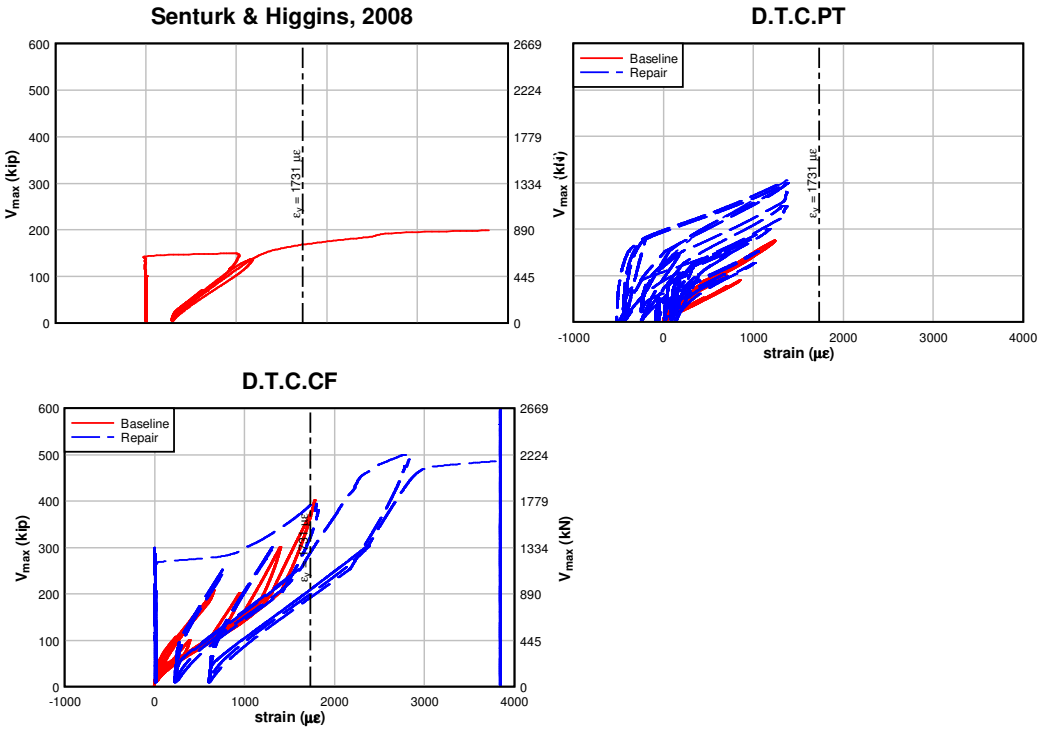

Fig. 4.112 – Bent cap shear force versus typical north internal stirrup: ultimate loading condition

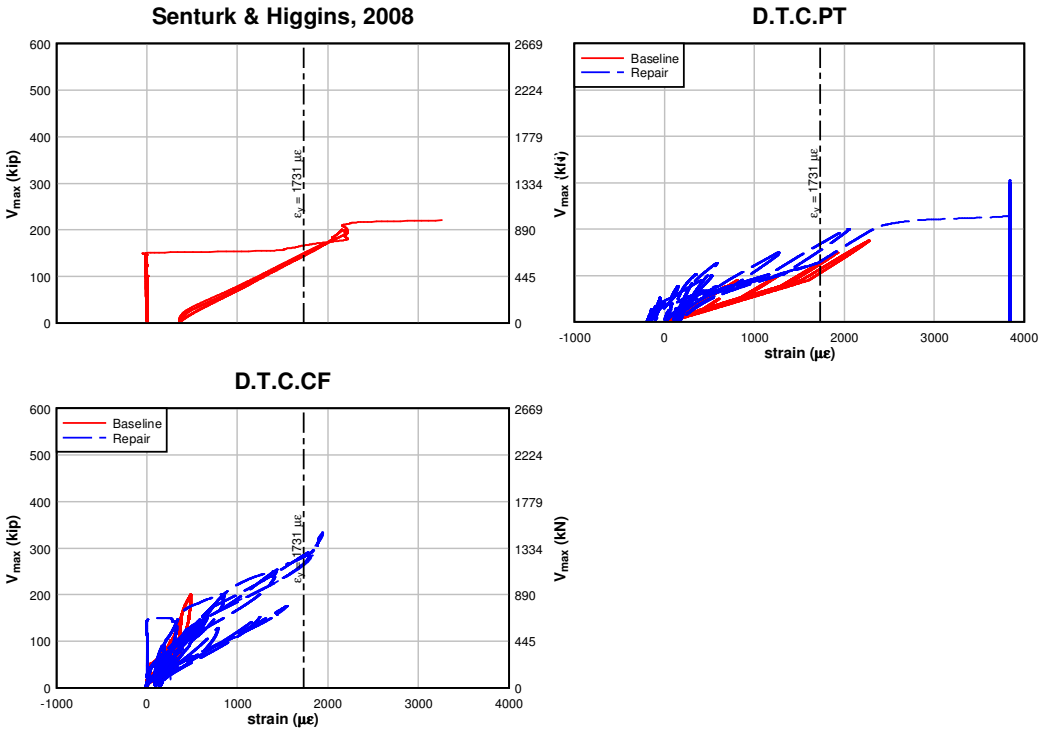

Fig. 4.113 – Bent cap shear force versus typical south internal stirrup: ultimate loading condition

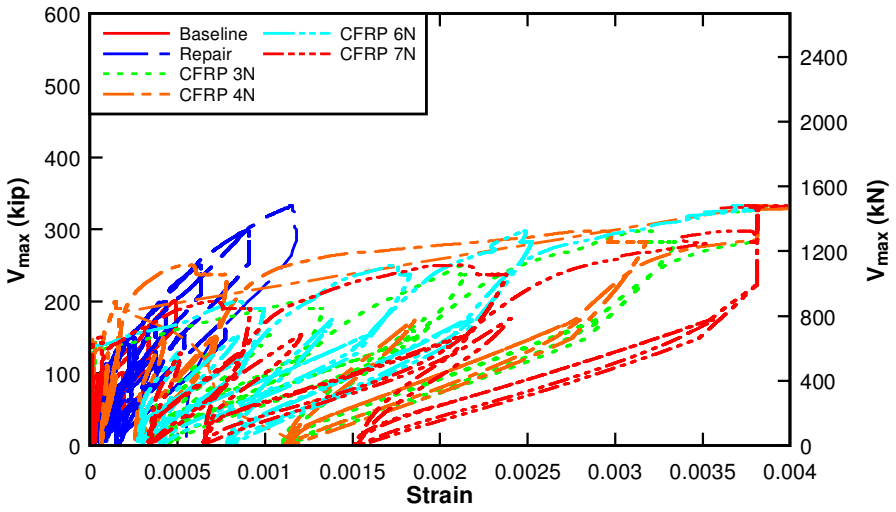

Fig. 4.114 – Bent cap D.T.C.CF shear force versus CFRP and average vertical strain: strength loading condition

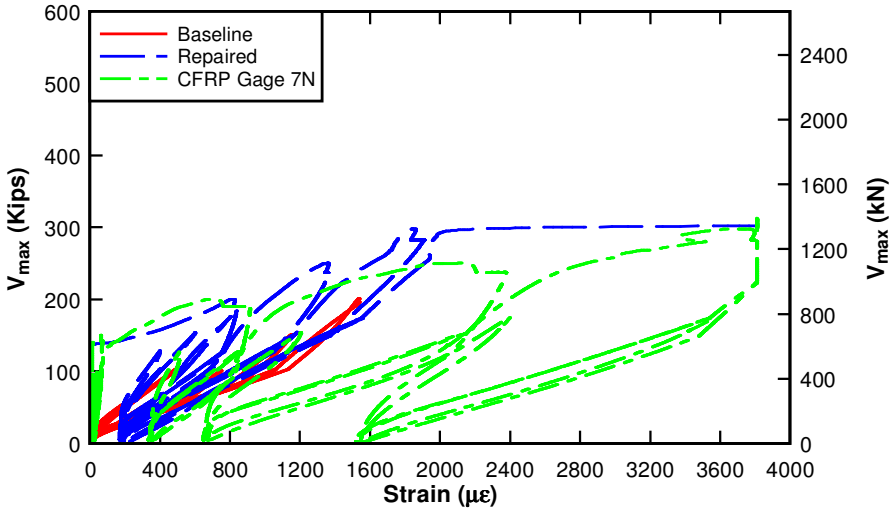

Fig. 4.115 – Bent cap D.T.C.CF shear force versus CFRP and integrally cast stirrup strain: strength loading condition

5. ANALYTICAL METHODS

In this section, the results of the experimental data will be compared among the available literature where applicable and code provisions noted previously in Chapter 2. In addition, two computer programs will be used for estimating the repaired specimen capacity. The results will then be compared across the available codes and literature (where applicable) for similarities and differences.

5.1. Analysis Programs

Analysis of the beam specimens was performed using two computer programs: Response2000 (R2K) and VecTor2. R2K is a sectional analysis program based on the Modified Compression Field Theory (discussed in section 5.2). The program takes into account the longitudinal strain of a section of interest by discretizing the section vertically. The resulting crack inclination angle calculated internally is similar to those used in the AASHTO LRFD and Canadian code through the use of tables to determine β and θ values. They differ in the fact that the code provisions take the cross section as one element, not a discretization of several elements vertically. R2K is a free program that is easy to modify and accurately models the behavior of reinforced concrete beams, based on the previous work of Higgins, et al. 2004. However, the program is limited to specimens with an a-to-d ratio of less than 2.0 (it does not accurately model deep beam specimens).

VecTor2 is a non-commercially available non-linear finite element (NLFEM) program based on the previous work of modified compression field theory, but it includes an update denoted as the Distributed Stress Field Model (DSFM-covered in section 5.3). The program predicts the response of concrete elements subjected to in-plane normal and shear stresses only. The cracked concrete is modeled as an orthotropic material with smeared, rotating cracks. Material stiffness contributions are determined from a secant stiffness algorithm (as opposed to a tangent stiffness calculation).

Finite elements used by VecTor2 are relatively simple and low-powered used in conjunction with a fine mesh. The program includes a three node constant strain triangle, a four node plane stress rectangular element, a four node quadrilateral element for modeling concrete with smeared reinforcement, a two node truss bar for modeling discrete reinforcement, a two node link element for modeling bond-slip relationships, and a four node element for modeling contact problems.

VecTor2 features a pre and post processor in a convenient Microsoft Window's based work environment and provides accurate modeling of deep beam specimens, based on the work of Senturk; however, the program is not available in the public domain and requires a non-commercial site license. The preprocessor program is denoted as Formworks. Model geometry, material properties, and loading are all prepared within the Formworks environment while post processing of data is performed in a separate program denoted as Augustus. VecTor2 supports the use of seed files, which replicates past loading cycles on

a specimen. For the specimens in the current study, a precrack load can be applied in VecTor2, then the repair media can be added to the model, and the model can be reloaded till failure, thus capturing the post cracked load deflection behavior of the specimen with the appropriate repair media. It should be noted that the ultimate capacity of the section is not contingent on the presence of the precracking load.

5.2. Analytical Methods: Modified Compression Field Theory

Three relationships are used in modified compression field theory to model the behavior of a concrete element: compatibility, equilibrium, and constitutive relationships. The method assumed the following:

- reinforcement is uniformly distributed
- cracks are uniformly distributed and rotated
- shear and normal stresses are uniformly applied
- strains and stresses are averaged over a distance that includes several cracks
- There is a unique stress state for each strain state without consideration of strain history
- Orientation of principal stress and strain are the same
- Perfect bond is assumed between the reinforcement and the concrete

- Independent constitutive relationships exist for concrete and reinforcement
- There is negligible shear stress in the reinforcement

Compatibility is assumed such that the strain in the panel is equal to the strain in the concrete which is equal to the strain in the steel. With the assumption of perfect bond, the strain in the concrete and reinforcement are equal over a given distance. Using Mohr's circle for strain, the average vertical tensile/compressive strains and orientation of the principal strain axis can be determined. This results in the orientation of the principal stress, as the two are assumed to be coincident. Equilibrium of an element subjected to normal and shear stresses results in internal forces in the reinforcement and concrete. Equilibrium is assumed such that average vertical and horizontal stresses are taken by the steel and concrete, whereas externally applied shear forces are balanced by the average shear stresses in the concrete (by summation of moments, assuming no dowel action of the reinforcement). The orientation of the principal tensile stress axis was determined from compatibility, thus the average concrete stresses in the vertical and horizontal directions can be related to the average principal concrete tensile stress. Relating the strains from compatibility with the stresses from equilibrium require constitutive relationships taken from laboratory tests for cracked concrete in compression and tension.

Constitutive relationships were taken from a panel tester created by the University of Toronto in the mid 1980s. The panel tests indicate that for concrete in compression, the compressive strength and stiffness decreased as the coexisting tensile strains increased. This is known as compression softening. A relationship was introduced which reduces the

strain in the concrete after the peak compressive stress is obtained, although compression softening is not limited to the post peak response. For concrete in tension, the relationship relates the principal tensile stress to the principal tensile strain. Prior to cracking, concrete behaves in a linear-elastic manner. The modulus values (taken as the initial tangent stiffness) can be evaluated as can the strain based on the cracking strength. After cracking, tensile stresses may continue to exist in the concrete between cracks due to bond interaction between the concrete and reinforcement. The concrete tensile strength decays from the tensile strength prior to cracking as the principal concrete tensile strain increases. This is known as tension stiffening. After yielding of reinforcement, the behavior is taken as bilinear.

In addition to the three conditions noted, additional limitations are implemented locally at the cracks. Across a crack, the additional stress not taken by the concrete in tension is transferred to the reinforcement. Thus, for equilibrium, the tensile stress in the concrete *between* the cracks is a function of the stress in the reinforcement *at* the crack. If the reinforcement yields at this location, the concrete tensile stress is reduced. Thus a reduction in tensile strength in the concrete is included. Shear stresses at the crack are absent for the concrete, but may exist for reinforcement oriented at an angle to the longitudinal axis of the member. Local shear stress along the crack can become large to induce sliding. This is prevented in turn by aggregate interlock which relates to maximum aggregate size and crack width. Thus, shear stress on the crack is limited. If either of the two previous conditions is violated, the strain state of the element is modified to result in a lower average concrete tensile stress.

5.3. Analytical Methods: Disturbed Stress Field Model

Disturbed Stress Field Model (DSFM) was devised in 2000 to address a few of the systematic deficiencies of MCFT in predicting the response of certain structures/loading conditions. In lightly reinforced elements, where crack shear slip is significant, the rotation of the principal stress field tends to lag the rotation of the principal strain field. Recall, MCFT assumes the rotations are the same, thereby resulting in an overestimation of results where crack shear slip is significant. The converse also holds true, for elements with limited rotation of principal stress/strain fields, MCFT results in an underestimation of shear stiffness and strength, partially due to the over softening affect of the principle tensile strains. The method builds upon that of MCFT, but includes crack shear slip deformations which are differentiated from the strains due to applied stress. Also, by calculating the crack slip deformations explicitly, the method eliminates the crack shear check currently present in MCFT.

Compatibility of DSFM is similar to that of MCFT prior to cracking. Once a section cracks, the rotation of the strain field occurs at a larger rate than that of the stress field resulting in a differential lag between the stress and strain axes. Thus, the total strain in each direction for an element is now defined as the average vertical strain in the concrete plus a strain due to shear slip. The principal net concrete tensile and compressive strains are found from Mohr's circle for strain. The crack slip strain components are calculated from the average crack slip shear strain, which is resolved into strain components in the

vertical, horizontal, and shear strain orientations. The difference between the orientation of the principal concrete stresses and the orientation of the total strain field is the rotation lag.

Equilibrium relationships for the two methods are the same, with one exception. MCFT utilizes Walraven's aggregate interlock equation to limit shear stress at the crack location, whereas DSFM does not have this limit as the deformations are explicitly determined due to shear slip.

Constitutive relationships for DSFM are similar to MCFT. However, for concrete in compression, the term for compression softening provides a reduction term to account for the effect of element slip deformations. The softening effect is thus reduced for DSFM compared to MCFT. The post-cracking tensile stress in the concrete is taken as the larger of the values predicted by tension stiffening (described previously for MCFT) and a term denoted as tension softening. The latter is based on fracture mechanisms which may be significant in lightly reinforced concrete structures.

5.4. Beam Specimen Analytical Methods

The base capacity of the beam specimens was determined using R2K. The program is capable of determining the capacity of a section based on the interaction of shear and

moment, by introducing a ratio of flexure to shear at the section under consideration. For a given M/V ratio, the program models the interaction between shear and moment for a given stirrup spacing. The relationship can be shown in Fig. 5.1 for the IT beams with and without cutoffs and the T beams (without cutoffs). The average shear stress over the effective web area is displayed on the vertical axis while a shear "pressure" term, as shown below in Equation [5.1], is located on the horizontal axis.

$$\frac{A_v f_y}{b \cdot s} \qquad [5.1]$$

For a specific beam with a given M/V ratio, the stirrup spacing was varied such that the failure shear over a wide range of spacing was shown. The figure also includes a curve which represents 98% of the R2K capacity, which removes the program bias based on the results of the SPR350 series of experiments [Higgins, *et al.* 2004a]. The graph indicates for an increase in shear strength along the vertical axis, the corresponding required shear "pressure" varies depending on the beam behavior within the shear span. For the IT beams, the specimens without cutoffs include a constant sloped portion of the curve which indicates additional shear strength is possible with little increase in shear pressure, as the specimens were lightly reinforced to start with. On the other hand, the curve for the cutoff specimen indicates for a unit increase in shear, additional shear pressure is required compared to the flexurally fully developed specimen. The T beams exhibit a different M/V ratio than the IT beams as well as a different effective depth. Thus, the curve has a similar shape to that of the fully developed IT.

Fig. 5.1 provides insight into overall beam behavior for shear retrofit. For a specimen with a fixed M/V ratio and two vastly different flexural steel ratios, a similar shear repair would result in different behaviors. For the specimen with a low flexural steel ratio, the curve is relatively flat indicating a significant shear pressure term is required for an incremental increase in shear strength. On the other hand, a beam with an excessive flexural steel ratio exhibits a higher sloped design curve indicating the same unit increase in shear strength requires a much smaller shear pressure increment. Thus, the design curve accurately assesses the moment-shear interaction of the beams at the point of interest.

Results from Fig. 5.1 are shown individually for each repair beam type (IT, IT with cutoffs, and T beam) in Fig. 5.2-5.4 respectively. Each of the repair beams are shown within the graphs to provide an indication of base specimen capacity. The IT and T beams indicate the base specimens are located on the steeper sloped portion of the curve, while the IT cutoff base specimen is located on a flatter portion of the curve.

M-V Interaction plots for the IT beams without cutoffs including the failure shear are shown in Fig. 5.5-5.8 for the four repair types. The external stirrup repair in Fig. 5.5 indicates an increase beyond the initial linear portion of the base curve. The internal stirrup repair in Fig. 5.6 indicates a significant increase over the remaining three beams, as the horizontal axis was increased to include the experimental failure shear. The curve becomes asymptotic beyond the failure shear, indicating additional shear capacity would not be economical. The carbon fiber strip repair in Figure 5.7 is similar to that of the

external stirrup repair, with failure occurring along the flatter portion of the curve relative to the base capacity. The near surface mount beam, shown in figure 5.8 indicates little increase over the base specimen, even though failure occurred within the higher sloped portion of the curve.

Interaction plots for the IT beams with cutoffs and the T beams are shown in Fig. 5.9-5.12 for the external and internal stirrup repairs respectively. For the external IT with cutoffs repair beam, shown in Fig. 5.9, the resulting failure shear is beyond the limits of the generated R2K analysis. The same result is shown in Fig. 5.10 for the internal stirrup repair beam. Recall both of the cutoff specimens failed due to anchorage of the cutoff bars. Further investigation of the flexural capacity versus demand—accounting for the additional flexural bars based on the current ACI development length equations—shown in Fig. 5.11 indicates the failure does originate from flexure. The interaction of the external stirrup T beam repair is shown in Fig. 5.12 with a minor increase in shear for the failure event compared to the baseline specimen. This is expected, as the repair resulted in half of the external stirrups than originally planned. The internal stirrup T beam repair in Fig. 5.13 indicates a significant increase in shear along the flatter portion of the curve compared to the baseline specimen.

The previous series of plots display graphically the increase in shear from the theoretical R2K baseline to the experimental failure shear. The results are also illustrated in Table 5.1.

The values shown for the increase due to repair will be used as a reference in the subsequent analysis.

Table 5.1 Total shear increase for beam specimens

Specimen:	Response Estimated Capacity:				Failure:		Difference	
	Base Specimen:		0.98*Base Specimen					
	kip	kN	kip	kN	kip	kN	kip	kN
B.IT.NC.ES	173.3	770.8	169.8	755.4	211.9	942.5	42.1	187.1
B.IT.C.ES	133.2	592.5	130.5	580.6	220.9	982.7	90.4	402.1
B.T.NC.ES	147.8	657.4	144.8	644.3	173.4	771.1	28.5	126.8
B.IT.NC.IS	168.9	751.3	165.5	736.2	243.4	1082.4	77.8	346.2
B.IT.C.IS	133.1	592.0	130.4	580.2	241.7	1074.9	111.2	494.7
B.T.NC.IS	148.2	659.2	145.2	646.0	200.0	889.8	54.8	243.8
B.IT.NC.CF	174.5	776.2	171.0	760.7	215.7	959.5	44.7	198.9
B.IT.NC.NS	164.8	733.0	161.5	718.4	166.3	739.8	4.8	21.4

5.4.1 External Stirrup Repair

5.4.1.1 External Stirrup Repair: Comparison with Literature

Recall from Chapter 2, there were four primary investigations dealing with external strengthening of traditionally reinforced concrete beams. The first, published by Mihn et al., included one external stirrup repair specimen as one of the several repair techniques. The specimens had realistic shear span to depth ratios for slender beams, but lacked integrally cast stirrups. The lone repair specimen was over reinforced for shear resulting in a flexural failure. The investigation provided no clear indication of the efficiency of the

repair, as the exact shear contribution was not measured. Still, a plot of the interaction for this specimen is shown in Fig. 5.14. Note, the shear span was cast devoid of stirrups; however, stirrups were used outside of the shear span in order to construct the specimens. The stirrups noted in this area were used for constructing the interaction graphs. As the specimen failed in flexure, the interaction curve provides little indication of the effectiveness of the method, which is similar to the cutoff specimens previously noted.

The second investigation by Altin et al., consisted of 13-half scale T specimens with varying integrally cast steel and externally applied shear reinforcement ratios. The paper provides sufficient information for reproduction of the beam specimens in R2K; a sample of a typical beam interaction graph is shown in Fig. 5.15. However, the specimens in the study were over reinforced for shear, resulting in flexural failures in each case. Therefore, comparison of the additional shear "pressure" term is not possible in this case.

The third investigation, by Kim et al., utilized flexible high strength wire rope units in lieu of mild or high strength steel as an external stirrup repair. The beam specimens included three shear span-to-depth ratios, covering deep and slender specimens. The orientation of the wire rope units varied from 45 to 90 degrees to the longitudinal axis of the members, as did the pre-stressing force in the wire rope units. The specimens were cast devoid of integrally cast stirrups within the shear span, loaded to failure, repaired with the wire rope units, then tested to failure a second time. Similar to the specimens constructed by Minh et al., the integrally cast stirrups were provided outside of the shear span. However, they

were not identified in the paper, which negates creation of interaction plots as numerous combinations of steel size and grade would lead to quite different interaction plots which may or may not be consistent with the final failure load.

The final investigation for the external stirrup repair, by Shamsai et al. included mild steel external stirrups attached by channel sections and associated hardware. However, the channel sections also included an elastomeric bearing pad and associated steel plate intended to distribute the post tensioning force of the external stirrups equally throughout the shear span. This is not a feasible option for a full scale specimen, thus the data for this experimental program is not included.

A consensus for estimating the strength gain from external stirrup repair is mixed among the researchers. Three of the four researchers provided extensions of the existing ACI shear capacity equation by taking the area of steel/wire rope times the yield strength. Two researchers distributed the reinforcement over a ratio of d/s whereas the third investigator provided a ratio of h/s. Another point that is not agreed upon by two of the researchers is the influence of post tensioning on the ultimate capacity of the member. Shamsai et al. contends that the increase in post tensioning force had no affect on the resulting shear. Kim et al. provides contrary evidence. Based on the results of the current experiment, post tensioning does not change the strain range for the internal stirrups, it simply changes the initial strain value. Although no direct comparison can be made for a specimen with a

snug post tensioning condition at failure, the evidence at the service load provides insight into the advantage of post tensioning beyond the snug position.

Another issue raised by Shamsai et al. relates to the reduction in crack widths due to post tensioning. The authors conclude that post tensioning is sufficient to close existing cracks in concrete components. The current investigation provided evidence that crack openings are much more difficult to close under the self weight of the specimen, which may otherwise be possible for small-scale specimens. Also, static crack width reduction is a function of the stiffness of the reaction section.

Another item that was investigated in the current study related to the deformation of the reaction section due to weak axis bending. The stiffness ratio of the reaction section to that of the entire repair setup for each of the researchers is shown in Table 5.2. The results indicate that the reaction section is sufficiently stiff with regard to the external stirrup or rod used in each case. However, the stiffness is highly dependent on the 'a' distance from the edge of the specimen to the centroid of the stiffening element. Also, the results for the OSU specimens were taken from the channel section. Data presented in Chapter 4 indicate for the service level loading, the stronger reaction section was superior to the channel section. Similar results would be expected at ultimate load.

Table 5.2 External stirrup reaction section efficiency

Investigator:	OSU	Altin et. al.	Kim et. al.	Mihn et. al.*
K_{eq} / $K_{extstirrup}$	0.9893	0.9700	0.9923	0.9403
*Investigator did not list 'a' distance; 12 mm (0.5 in) assumed				

5.4.1.2 External Stirrup Repair: Comparison with National/International Codes

Comparison of the external stirrup repair with the international codes is shown in Table 5.3. The table provides estimates of the base specimen capacity, differentiated between steel and concrete contribution where applicable. The table also indicates the R2K predicted base specimen capacity, adjusted to remove bias, as noted previously. The additional shear contribution follows the appropriate code equations noted in Chapter 2, but utilizes the external stirrup area of steel, yield strength, and spacing. The values are taken over the entire height of the beam, not restricted to the effective depth 'd' as in many of the code equations. Also of note, the AASHTO and Canadian code provide simple and alternative methods to calculate the capacity of a specimen based on MCFT from a series of tables of beams meeting the minimum area requirements noted in Chapter 2. The subsequent estimation of the inclination of the concrete compressive component was used in the Eurocode2 and CEB-FIP estimations in order to provide a more realistic estimate. The comparisons are shown graphically in Fig. 5.16.

Table 5.3 External stirrup strength estimates based on international codes

Specimen:	Method:	A_{s_min}	Base Specimen Capacity						Strengthened				Failure		V_{exp} / V_{code}
			V_c		Vs_int		Vs_tot		Vs_ext		Vs_tot				
			kN	kip	kN	kip	kN	kip	kN	kip	kN	kip	kN	kip	
B.IT.NC.ES	R2K	-	-	-	-	-	755	170	-	-	-	-	943	212	-
	AASHTO Simple	OK	349	78	223	50	572	129	327	74	899	202			1.049
	AASHTO MCFT	OK	410	92	337	76	746	168	327	111	1074	279			0.760
	ACI 318-05	OK	349	78	223	50	572	129	327	74	899	202			1.048
	Canadian Simple	OK	387	87	203	46	590	133	299	67	889	200			1.061
	Canadian MCFT	OK	420	94	313	70	733	165	460	103	1193	268			0.790
	Eurocode 2	OK	-	-	-	-	282	63	-	-	696	156			1.355
	CEB-FIP	NG	449	101	282	63	731	164	414	93	1145	257			0.823
B.IT.C.ES	R2K	-	-	-	-	-	581	131	-	-	-	-	983	221	-
	AASHTO Simple	OK	307	69	223	50	530	119	327	74	857	193			1.146
	AASHTO MCFT	OK	327	73	296	67	623	140	327	98	950	238			0.930
	ACI 318-05	OK	307	69	223	50	530	119	327	74	857	193			1.146
	Canadian Simple	OK	340	77	203	46	544	122	299	67	842	189			1.167
	Canadian MCFT	OK	309	69	280	63	589	132	411	92	1000	225			0.983
	Eurocode 2	OK	-	-	-	-	252	57	-	-	622	140			1.580
	CEB-FIP	OK	336	76	252	57	588	132	370	83	958	215			1.026
B.T.NC.ES	R2K	-	-	-	-	-	644	145	-	-	-	-	890	200	-
	AASHTO Simple	NG	375	84	164	37	539	121	200	45	739	166			1.203
	AASHTO MCFT	NG	263	59	106	24	369	83	200	29	569	112			1.783
	ACI 318-05	OK	376	84	164	37	540	121	200	45	740	166			1.203
	Canadian Simple	OK	416	94	150	34	566	127	182	41	748	168			1.189
	Canadian MCFT	OK	387	87	191	43	579	130	234	52	812	183			1.095
	Eurocode 2	NG	-	-	-	-	172	39	-	-	382	86			2.326
	CEB-FIP	NG	500	112	172	39	672	151	210	47	882	198			1.009

The first external stirrup specimen exhibited fully developed flexural steel within the shear span. The ACI, Simplified AASHTO, and Simplified Canadian code predict the capacity well, with a conservative strength estimate that is below the capacity of the laboratory specimens. However, taking into account varying theta angles from MCFT taken from the longitudinal strain noted in AASHTO and the Canadian code, the capacity of the specimen is overestimated by 20-30%. The CEB-FIP code also displays a similar behavior. The Eurocode2 estimate produced the most conservative estimation ($V_{EXP} / V_P = 1.36$), a common theme among the specimens tested.

The second external stirrup specimen exhibited flexural cutoffs within the shear span. For this specimen, the opposite conditions hold true. The ACI and AASHTO/Canadian Code simplified methods underestimate the capacity of the section. The MCFT approach of AASHTO and the Canadian code provided a more accurate, although slightly unconservative strength estimate. The CEB-FIP estimate utilizing the inclination angle from MCFT provided the most accurate conservative estimate of the strength. Again, the Eurocode2 provided the most conservative ($V_{EXP} / V_P = 1.58$) estimate.

The final external stirrup repair beam exhibited fully developed flexural steel but was tested in the 'T' position. For this beam, the AASHTO requirement for minimum area of steel was not met; therefore the second table within AASHTO was used for the strength estimate. However, the Canadian code indicated the area of steel provided was sufficient, therefore the resulting values were taken from the initial table. Otherwise, the AASHTO and Canadian code simple methods as well as the ACI approach provide a conservative strength estimate. For the MCFT Canadian code, the capacity estimate increases slightly, but it is still on the conservative side. The CEB-FIP code resulted in a slightly unconservative design based on the inclination found from the Canadian Code. Again, the Eurocode2 produced the most conservative ($V_{EXP} / V_P = 2.33$) estimate of capacity.

5.4.1.3 External Stirrup Repair: Comparison with R2K

Comparison of the external stirrup repair with R2K was used in conjunction with the previously noted interaction plots. The difference in shear pressure from the R2K calculated unrepaired specimen capacity to the experimental failure shear was recorded for each specimen. The corresponding shear pressure term taken from the measured material properties of the external stirrup repair were then compared to the experimental results. Table 5.4 indicates the efficiency of each repair beam with respect to an equivalent internal stirrup repair by a ratio of experimental to calculated delta shear pressure. For a value of 1.0, the repair was equivalent to adding integrally cast stirrups to the specimen. For a value greater than 1.0, the experimental repair performed better than the experimental data suggest. The converse, for a value less than 1.0, implies the repair is not efficient. A comparison of the cutoff specimens is not provided, as they failed due to anchorage within the shear span. The external stirrup repair exhibits a efficiency rating of 0.84 and 1.21 for the fully developed IT and T specimens, respectively. This implies the IT repair performed below expectations while the T beam performed better than expected. If these efficiency ratings are applied to the AASHTO and Canadian MCFT strength estimates for the IT beam only, the ratio of V_{EXP} / V_P changes from 0.760 and 0.790 to 1.04 and 0.94 respectively. For the T beam, the Canadian code is exceptionally close to the target strength. However, using an efficiency rating greater than 1.0 (1.21 in this case) results in an unconservative design shear. Therefore, conservatively assume the efficiency of the repair is limited to 1.0.

Table 5.4 R2K shear pressure comparison for different repair methods

R2K Prediction	
Specimen:	$\Delta x_{EXP} / \Delta x_P$
B.IT.NC.ES	0.84
B.IT.C.ES	-
B.T.NC.ES	1.21
B.IT.NC.IS	1.34
B.IT.C.IS	-
B.T.NC.IS	1.01
B.IT.NC.CF	0.85
B.IT.NC.NS	0.73

5.4.1.4 External Stirrup Repair: Comparison with VecTor2

All specimens in the current study were modeled with the previously mentioned VecTor2 nonlinear finite element package. A few notes about the location of elements and idealized boundary conditions are warranted prior to explanation of results. First, the analysis package provides an upper limit on the number of elements in a particular model. Therefore, the use of rectangular, quadrilateral, or triangular elements as well as the smallest mesh size resulted in the maximum number of elements the program would permit. Therefore a mesh size for the concrete elements ranging from 80 mm (3.14 in.) to 120 mm (4.72 in.) was used. Next, the program was run in SI units, with locations rounded to the nearest 10 mm (0.39 in.) which corresponds to a maximum error of $\pm$ 5 mm ($\pm$ 0.20 in.). The truss elements representing the flexural steel reinforcing bars were extended to the limits of the specimen longitudinally, when in reality concrete cover was provided in the experimental beams. Also, the location of the repair media on some beam

and/or bent cap specimens exceeded the minimum mesh size required by the program. Furthermore, the presence of the repair media resulted in concentrated mesh regions near the repair media, so that the limit on the maximum number of elements was exceeded. As such, the integrally cast stirrup and/or repair media were moved laterally a nominal distance to permit the mesh size of interest. Support conditions were modeled as one roller and one pin, in order to provide the required number of known degrees of freedom for the models to run. Recall, the boundary conditions for the beam specimen were rollers on each end and the bent cap was treated as fixed at one end with a roller at the adjacent end. However, the bent cap specimen at the fixed end did not provide ultimate fixity, as there was limited rotation between the steel plates. Still, the plates provided a larger degree of fixity when compared to the roller section. Senturk indicated that modeling the bent cap specimens in VecTor2 with a pin/roller combination provided a good indicator of cracking with the laboratory specimen, thus this assumption is valid for the current investigation.

The external stirrup specimens were modeled as unbonded reinforcement within VecTor2. The meshing schemes for the external stirrups are shown in Fig. 5.17. The load-deflection curves for the external stirrup beams are shown in Fig. 5.18 whereas the capacity estimations are shown in Table 5.5. The load deflection curves approximate the experimental data quite well. The fully developed IT beam exhibits the uncracked response of the VecTor2 model, whereas the remaining plots account for the baseline loading. The Table comparisons indicate VecTor2 consistently under estimated the specimen of each specimen. Therefore, modeling of unbonded steel within VecTor2 is

generally acceptable and conservative. It is worth noting no reduction was taken into account within the model to account for weak axis bending.

Table 5.5 External stirrup VecTor2 comparison

Specimen:	V_p (VecTor2)		V_{exp}		V_{exp} / Vp
	kN	kip	kN	kip	
B.IT.NC.ES	878	197	943	212	1.07
B.IT.C.ES	832	187	983	221	1.18
B.T.NC.ES	810	182	771	173	1.10

5.4.1.5 External Stirrup Repair: Design Recommendations

The design recommendations for the external stirrup repair are based on laboratory tests, previous work, and comparisons with the various international codes. For service level performance, the following design recommendations are provided:

- Selection of appropriate reaction section under weak axis bending has a direct effect on strain compatibility between the specimen and the external stirrups
- Reduction in crack size due to self weight is not as effective compared to the no dead load condition
- Post tensioning of external stirrups provides better strain compatibility over the service level loading

- From evidence from the literature, a higher post tensioned force results in higher specimen capacity.

- The amount of post tensioning should be limited based on a combination of the yield strength of the external stirrups and the dead load strain in the internal stirrups. A stress range for the external stirrups should be provided such that they are consistent with the remaining stress in the integrally cast stirrups.

For ultimate design of external stirrups, the following design guidelines are proposed.

- As specimens near failure, the ductile nature of the repair resulted in larger crack widths than the other repair methods. This point should be articulated for field inspection of structures repaired with this method, as it may result in false negative reports on the condition of a structure.

- From the available literature, the resulting shear strength of each external stirrup repair resulted in a variation with regard to the international codes.

- The current investigation provided a wide range of strength estimates based on either a simple 45 degree truss analogy or an approach following MCFT.

- The effectiveness of the repair is dependent on the reaction section used; however, if the external stirrup is positioned close to the web, this affect is minimized with a typical reduction due to weak axis bending on the order of 0.95.

- The lowest efficiency rating for the current study resulted in a factor of 0.84. Therefore, taking into account the reduction from weak axis bending and the efficiency factor, a strength reduction factor for external stirrups can conservatively be taken as 0.80.

5.4.2 Internal Stirrup Repair

Recall from Chapter 2, the available literature for supplemental internal stirrup repair was limited for shear repair. The major work was performed by Stratton et. al. through Kansas DOT, with the remainder of the literature review based on the various bond models for anchorage of attachments and doweling into existing structures. The work from Kansas lacked any laboratory specimens in order to verify the claimed increase in capacity.

5.4.2.1 Internal Stirrup Repair: Comparison with National/International Codes

Comparison of the supplemental internal stirrup repair with the international codes is shown in Table 5.6 and graphically in Fig. 5.19. The table is similar in format to the external stirrup table. The initial specimen in the table exhibits an overestimated capacity for each code but the Eurocode and CEB-FIP. The AASHTO and Canadian MCFT equations provide an overestimated capacity compared to the simple equations. The comparison of the second repair specimen is included even as it was damaged and repaired

with double the shear reinforcement along the south end. As a result, the specimen failed due to anchorage and the capacity estimates are off by as much as a factor of two. The data is shown for information purposes only.

Table 5.6 Supplemental internal stirrup strength estimates based on international codes

Specimen:	Method:	A_{s_min}	Base Specimen Capacity						Strengthened				Failure		V_{exp}/V_{code}
			V_c		Vs_int		Vs_tot		Vs_sup		Vs_tot				
			kN	kip	kN	kip	kN	kip	kN	kip	kN	kip	kN	kip	
B.IT.NC.IS	R2K	-	-	-	-	-	736	166	-	-	-	-	1082	243	-
	AASHTO Simple	OK	352	79	223	50	575	129	588	132	1163	261			0.931
	AASHTO MCFT	OK	399	90	324	73	723	163	605	136	1329	299			0.815
	ACI 318-05	OK	351	79	223	50	574	129	588	132	1163	261			0.931
	Canadian Simple	OK	390	88	203	46	593	133	624	140	1217	274			0.890
	Canadian MCFT	OK	400	90	302	68	702	158	654	147	1356	305			0.799
	Eurocode 2	OK	-	-	-	-	271	61	-	-	539	121			2.008
	CEB-FIP	NG	451	101	271	61	723	163	268	60	990	223			1.093
B.IT.C.IS	R2K	-	-	-	-	-	580	130	-	-	-	-	1075	242	-
	AASHTO Simple	OK	339	76	223	50	562	126	1761	396	2323	522			0.463
	AASHTO MCFT	OK	363	82	297	67	660	148	1658	373	2318	521			0.464
	ACI 318-05	OK	338	76	223	50	561	126	1761	396	2322	522			0.463
	Canadian Simple	OK	375	84	203	46	579	130	1866	420	2445	550			0.440
	Canadian MCFT	OK	355	80	280	63	635	143	1817	408	2452	551			0.438
	Eurocode 2	OK	-	-	-	-	252	57	-	-	996	224			1.080
	CEB-FIP	OK	409	92	252	57	661	149	744	167	1404	316			0.765
B.T.NC.IS	R2K	-	-	-	-	-	646	145	-	-	-	-	890	200	-
	AASHTO Simple	NG	342	77	164	37	506	114	231	52	737	166			1.207
	AASHTO MCFT	NG	244	55	95	21	339	76	94	21	433	97			2.053
	ACI 318-05	OK	342	77	164	37	506	114	231	52	737	166			1.207
	Canadian Simple	OK	379	85	150	34	529	119	463	104	992	223			0.897
	Canadian MCFT	OK	295	66	191	43	486	109	419	94	905	204			0.983
	Eurocode 2	NG	-	-	-	-	172	39	-	-	340	77			2.614
	CEB-FIP	NG	414	93	172	39	587	132	168	38	755	170			1.179

The final internal stirrup repair specimen provides a good estimation from the Canadian code, with the MCFT version indicating slight unconservatism. The AASHTO simple equation provides an over strength estimate for the simple equation. Recall, the spacing of the integrally cast stirrups indicate the section does not meet the AASHTO requirements

for minimum steel, therefore the second design equation is used whereas the specimen meets the Canadian code requirements for minimum steel.

5.4.2.2 Internal Stirrup Repair: Comparison with R2K

Comparison of the internal stirrup repair with R2K follows that of the external stirrup specimens as previously noted in Table 5.4. The additional shear pressure term for the IT without flexural cutoffs is not included in the table, as the specimen failed due to anchorage. The initial IT beam exhibits an efficiency ratio greater than 1.0, indicating the repair is superior to the estimate using the shear pressure coefficients, which is in opposition to the code estimates. The T beam also exhibits an efficiency ratio slightly greater than 1.0, indicating the repair is equivalent to treating the supplemental stirrups as equivalent integrally cast stirrups. This is similar to the Canadian MCFT curve, which calculated the specimen capacity within 1.7%.

5.4.2.3 Internal Stirrup Repair: Comparison with VecTor2

The internal stirrup repair was modeled within VecTor2 utilizing perfect bond between the concrete, epoxy, and steel. The objective was to obtain an ultimate strength value based on the assumption of perfect bond. If the program over-estimated the strength, a reduction or different bond model based on the literature review noted in Chapter 2 would be followed.

The results of the VecTor2 models are shown in Table 5.7. For the fully developed IT and T beams, the program provided a slightly conservative strength estimation that was within 3%-9% of the repair. These estimations are closer than the code comparisons, except for the Canadian code estimation of the T beam. The comparison of the damaged IT specimen with flexural cutoffs resulted in an underestimation of the strength by 26%. While this is a large margin, it is half of the value estimated by the available codes.

Table 5.7 Internal stirrup VecTor2 comparison

Specimen:	V_p (VecTor2)		V_{exp}		V_{exp} / Vp
	kN	kip	kN	kip	
B.IT.NC.IS	1052	237	1082	243	1.03
B.IT.C.IS	854	192	1075	242	1.26
B.T.NC.IS	817	184	890	200	1.09

Load-displacement graphs from VecTor2 are shown in Fig. 5.21. The behavior of all specimens matches the backbone curve of the experimental data. The initial precrack loading on two of the specimens indicates the relative change in stiffness of the base specimen. The base specimen loading cycle was completed with the area of the supplemental stirrups set to a minimal value, then the program was run with the full supplemental area till failure. The cutoff specimen illustrates a slight offset from experimental work.

5.4.2.4 Internal Stirrup Repair: Design Recommendations

As with the external stirrup repair, design recommendations are based on experimental data and information from the literature review. For the service level performance, the following recommendations are provided:

- Quality control of supplemental internal stirrup installation is paramount for its success
- Knowledge of existing flexural steel and stirrups is required for coring purposes in order to avoid severing critical steel components
- The exterior faces of the web should be patched at the location of the cracks, as seepage of the epoxy will eventually penetrate from the cored hole location to the exterior fiber of the beam
- Once a hole is created without interference with the surrounding steel, the interior concrete surface should be free and clear of any debris in order to provide a clean bonded surface for the epoxy. Also, seepage of epoxy through the depth of the section reduces the epoxy within the cored hole. Providing additional epoxy throughout the installation due to seepage ensures complete encapsulation of the steel rebar.
- Spacers located around the reinforcing bar are required to position the bar such that it is sufficiently embedded in epoxy, and not skewed to one side of the hole.

- Selection of epoxy and size/grade of steel is important in the repair. The question of using a larger higher strength bar with fewer holes or more common mild steel with more holes is open to debate. Both methods were used in the current study. Cost and installation configuration (top down or bottom up) will provide an indication of the optimal repair combination. For a top down installation, the use of mild steel is acceptable and this configuration provides sufficient anchorage of the steel. For a bottom up installation, the use of a hollow rod in which to pump epoxy through may provide the best quality control.

For ultimate loading the following items are noteworthy:

- Post failure investigation of the internal stirrup specimens indicate a horizontal offset of the previous vertical grid lines on the specimen. Dowel action—the resistance of a reinforcing bar to movement perpendicular to its longitudinal axis—is likely the cause of this phenomenon. Dowel action may also provide insight as to the efficiency of the method.

- Crack widths at ultimate were smaller than those of the external stirrup repair.

- Providing supplemental stirrups close to the principle strain axis of the member provides the best use of materials.

- The efficiency factors from R2K indicate the method performs better than anticipated (possibly due to the orientation of rebar with respect to the principle strain axis and the influence of dowel action).

- Comparison with international codes indicates an overestimation of strength for the IT beam by as much as 20%. For the T beam, the majority underestimated the strength, with one code overestimate of approximately 10%. Conservatively, a reduction factor of 0.80 is recommended for this repair.

5.4.3 Surface Mounted CFRP Beam Repair

5.4.3.1 CFRP Stirrup Repair: Comparison with Literature Review

Using CFRP in repair for shear began to gain prominence in the mid 1990s; the evolution of the current design recommendations from ACI 440 were documented previously in Chapter 2 and are not revisited at this time. Comparisons to the existing literature are not included, as the current ACI 440 recommendations incorporate the work of the early pioneers.

5.4.3.2 CFRP Stirrup Repair: Comparison with Codes

The contribution from CFRP to shear is shown in Table 5.8. Recall from Chapter 2, ACI 318 is used for design and construction of concrete members, whereas the recommendations from ACI 440 include strengthening guidelines. Therefore, the strength

contribution includes the base specimen capacity from R2K, adjusted for bias from the previous SPR350 data, and ACI 318. Utilizing the ACI 440 approach outlined in Chapter 2, the shear contribution from CFRP was limited by bond and thus the strain in the CFRP was limited to 0.0038 in/in. Results indicate the base specimen capacity is underestimated using ACI 318, but the composite capacity with ACI 440 results in a conservative strength estimate. On the other hand, the base specimen capacity from R2K coupled with the ACI 440 strength estimate is unconservative, by overestimating the shear contribution of the CFRP by approximately 10%. It should be noted that the ACI equation requires a 0.85 reduction factor on just the CFRP contribution; with the 0.85 reduction factor, the strength overestimate decreases to approximately 7%. A second overall reduction factor for the integrally cast stirrups and concrete contribution is provided in the code.

Table 5.8 CFRP beam code comparison

Specimen:	Method:	$V_{baseline}$		ACI 440 $V_{strengthened}$		V_{s_tot}		V_{EXP}		V_{EXP}/V_{calc}
		kN	kip	kN	kip	kN	kip	kN	kip	
B.IT.NC.CF	0.98*R2K	761	171	310	70	1071	241	960	216	0.90
	ACI 318	579	130			889	200			1.08

5.4.3.3 CFRP Stirrup Repair: Comparison with R2K

As with the previous beam analysis, a shear design curve utilizing R2K was produced for the CFRP beam with varying stirrup spacing. The results as noted previously, as shown in

Table 5.4. The results indicate the repair is 85% efficient, which compares well to the 10% overestimate from ACI 440 in conjunction with R2K. Coincidentally, the reduction factor from ACI 440 is set to 0.85 as well.

5.4.3.4 CFRP Stirrup Repair: Comparison with VECTOR

The CFRP specimen was modeled in VecTor2, as shown in Fig. 5.22. {Initially, the specimen was modeled utilizing the bond strength parameters from ACI 440, with limited success. Upon further inquires to the developers of VecTor2, Dr. Vecchio of the University of Toronto provided guidance in the form of a recently published paper which explains modeling the bond-slip relationship with FRP [Kim and Vecchio 2008]}. Within VecTor2, bond elements can be modeled as link or one dimensional contact elements. In the current study, the elements are connected with link elements. As outlined in a previous paper by Wong and Vecchio, to accurately model the behavior, two sets of nodes are assigned for each bond element; one node is assigned to the concrete and the other is assigned to the repair media [Wong and Vecchio 2003]. The bond between the two nodes are assigned based on constitutive relationships. The link elements have no dimensions, but are represented by two orthogonal springs which are independent of each other. Movement in the two directions represent the shear and normal stresses for the bond material. Internally, selecting the bond material model for externally applied carbon fiber strips places a significantly higher stiffness value to the normal direction, as a shear

dominated failure within the epoxy is most common in shear repair with CFRP. This limits the link element to displace in shear direction.

The constitutive relationship for bond-slip of CFRP strip is noted in the initial paper by Kim and Vecchio. VecTor2 requires three unique points in order to model the bond-slip relationship accurately, as shown in Fig. 5.23 [Vecchio and Wong 2002]. The relationship utilizes a bilinear approximation of the bond-slip behavior taking into account the compressive strength of the concrete and the carbon fiber material. For CFRP, the following equations are presented, based on the fracture energy G_f of the concrete.

$$\tau_{bFy} = \left(54 \cdot f_c^{'}\right)^{0.19} \text{ Kim \& Vecchio 2008} \quad [5.2]$$

$$G_f = \left(\frac{\tau_{bFy}}{6.6}\right)^2 \text{ Kim \& Vecchio 2008} \quad [5.3]$$

$$s_{Fy} = 0.057 \cdot G_f^{0.5} \text{ Kim \& Vecchio 2008} \quad [5.4]$$

$$s_{Fu} = \frac{2 \cdot G_f}{\tau_{bFy}} \text{ Kim \& Vecchio 2008} \quad [5.5]$$

Where τ_{bFY} in Eq. [5.2] is the maximum bond shear stress (MPa), f'_c (MPa) is the compressive strength of the concrete, s_{FY} in Eq. [5.4] is the bond slip at maximum shear stress, and s_{Fu} in Eq. [5.5] is the ultimate bond slip. Utilizing these parameters, the bond stress parameters τ_1 and τ_2 were assigned the value of τ_{bFy} whereas τ_3 was set to zero. The corresponding slip values Δ_1 and Δ_2 were assigned the value of s_{FY} and Δ_1 was set to s_{Fu}.

Modeling FRP within VecTor2 requires entering the area of FRP corresponding to a particular model. It is not noted explicitly in the manual, but the two modeling papers indicate the area is based on the tributary height of the truss element. Thus, it is directly dependent on the mesh size. The width per vertical height of CFRP based on the mesh size was used in the current investigation. Also, modeling a U-wrapped scheme as opposed to a side wrapped specimen presented an initial challenge in VecTor2. However, as bond failure originates at the free end, or in some cases from an existing crack toward a free end, the bottom of the U shape rarely governs the initial debonding that results in failure. As such, the lower portion of the U shape was modeled with a higher bond strength when entering the constitutive models.

Results of this modeling method are shown Table 5.9. The results are more consistent with the ACI 318 and ACI 440 combined strength, with a conservative strength estimate 15% below the experimental failure shear. The VecTor2 results are more consistent than the R2K combined with ACI 440 strength estimate. The load-deformation behavior taken from VecTor2 is shown in Fig. 5.24. The initial stiffness is taken as that of the uncracked beam, thus the initial slope for the VecTor2 graph would be closer to the experimental data for this case. The ultimate load is below that of the experimental data, and the load-deflection curve deviates from the experimental data for the latter load steps.

Table 5.9 CFRP beam VecTor2 comparison

Specimen:	V_p (VecTor2)		V_{exp}		V_{exp} / Vp
	kN	kip	kN	kip	
B.IT.NC.CF	834	188	960	216	1.15

5.4.3.5 CFRP Stirrup Repair: Design Recommendations

No modifications to the existing design codes are recommended for CFRP beam repair. However, to estimate the repaired specimen capacity, ACI 318 in conjunction with ACI 440 provides a conservative strength estimate. Estimation of repaired capacity using ACI 440 and R2K is not recommended, as the base specimen capacity is overestimated resulting in an unconservative design. VecTor2 provided a more conservative strength estimate than that of ACI 318 and ACI 440 combined. Thus, using the design equations is recommended.

5.4.4 NSM Beam Repair

5.4.4.1 NSM Stirrup Repair: Comparison with Literature Review

The bulk of the information for NSM repair have come from the available literature documented in Chapter 2. The issue related to the capacity estimates for NSM is focused

on the local bond properties of the specific type of carbon fiber and epoxy. In the current investigation, the results from French and Shield's work which investigated the bond properties of several epoxy products, produced a clear frontrunner with the 3M DP460NS epoxy. The problem of relating the bond properties to the repair is outside the scope of work in the current project. However, work of De Lorenzis and that of Barros and Nanni provide two differing values for the bond strength parameter used in design. As the library of other researchers continues to populate the literature, a better indication of the actual bond strength parameters and limits will be shown.

5.4.4.2 NSM Stirrup Repair: Comparison with Codes

The use of CFRP as a near surface mount application is a new and emerging technology. ACI 440 in conjunction with ACI 318 or R2K, similar to that of the CFRP repair specimen, was used as the primary comparison for the repair, as there is no additional guidance among the available international codes. The shear contribution from ACI 440 coupled with R2K and ACI 318 is shown in Table 5.10. As per ACI 440 guidelines, the FRP contribution to shear was dominated by bond strength and thus related to strain the carbon fiber. The reduction in strain was based on the repair scheme—the NSM was discretely repaired on 2 sides as opposed to the three sided U-wrap of the CFRP beam. The resulting increase in shear strength accounted for approximately 12 kN (3 kip) of shear. The R2K and ACI 440 strength estimate was close to the failure shear, although the base specimen

estimated by R2K was only 7 kN (1.5 kip) from the repair. The ACI 318 and ACI 440 strength estimate was ultra conservative, based on the base specimen capacity estimate.

Table 5.10 NSM beam code comparison

Specimen:	Method:	$V_{baseline}$		ACI 440 $V_{strengthened}$		V_{s_tot}		V_{EXP}		V_{EXP}/V_{calc}
		kN	kip	kN	kip	kN	kip	kN	kip	
B.IT.NC.NS	0.98*R2K	733	165	12	3	744	167	740	166	0.99
	ACI 318	509	115			521	117			1.42

5.4.4.3 NSM Stirrup Repair: Comparison with R2K

Comparison of the strength gain utilizing R2K design curves was provided, similar to the previous specimens, as shown in Table 5.4. The additional shear pressure term from the baseline to failure curve resulted in a 73% efficiency rating. The result is lower than the 85% provided in the CFRP model, but again the small increase in load can result in varied results depending on the assumed intersection on the design curves.

5.4.4.4 NSM Stirrup Repair: Comparison with VecTor2

The NSM beam was modeled with VecTor2 following the method outlined for CFRP. The meshing scheme for the NSM beam is shown in Fig. 5.25. The primary difference between

modeling the NSM and the CFRP was based on the effective width of NSM per unit height. The dimension for this value was taken as the three inside faces of the rectangular groove. Also, no increase in bond strength was provide at the bottom of the FRP strips, as the NSM repair scheme resulted in discrete strips, not 'U' shaped repairs.

Results of the VecTor2 comparison for the NSM repair are shown in Table 5.11. The analysis results in a slight under estimate of the beam strength (3%). Load-deformation response is shown in Fig. 5.26. Similar to previous graphs, the initial stiffness of the VecTor2 graph is higher than the experimental data to account for lack of precracking. However, after this initial phase of the graph, the program corresponds well with the experimental data until premature softening occurs. The identical response was noted for the CFRP beam in which the VecTor2 response does not match that of the experimental data as slip becomes more prevalent, although ultimate load is comparable to the experimental work.

Table 5.11 NSM VecTor2 comparison

Specimen:	V_p (VecTor2)		V_{exp}		V_{exp} / Vp
	kN	kip	kN	kip	
B.IT.NC.NS	720	162	740	166	1.03

5.4.4.5 NSM Stirrup Repair: Design Recommendations

No design recommendations are provided at this time for NSM repair method. As of the publication of this document, additional work has been funded by Oregon Department of Transportation regarding additional beam tests involving NSM. The population of available test data within the literature coupled with the future work may result in additional modifications to ACI 440 to include NSM retrofits. However, at the present time, there is still a dearth of consistent constitutive bond models as well as a lack of a national code which to follow—directed solely for use of NSM.

With the noted deficiencies of the method, behavior of the repair beam provided excellent crack restraint at the NSM locations. Fig. 5.27 illustrates the specimen under load with cracks reducing in size in the vicinity of the NSM. Also, the epoxy used in the program bonded well to the surrounding concrete. Failure photographs indicate the failure occurred in the concrete section, not due to degradation of bond between the FRP and the epoxy or epoxy and concrete interface.

5.5. Bent Cap Analytical Methods

5.5.1 Bent Cap Comparison: Literature Review

The single research paper included in Chapter 2 for post tensioning of bent cap specimens illustrated a significant strength gain if the dominant shear crack was epoxy injected prior to post tensioning, although no strength estimates due to post tensioning were provided. Validation of this conclusion is not applicable to the current study, as only one bent cap specimen was included, whereas a minimum of two are needed for validation: a control specimen repaired with epoxy injection, then post tensioned, and a second specimen post tensioned without epoxy injection. For the scaled specimens in the literature, the post tensioning repair is based on several factors related to aggregate interlock across the crack. For a shallow crack angle with wide crack widths, the application of post tensioning resulted in a reduction in strength, as the authors suggest the post tensioning induced additional slip along the failure crack. For the current study, the crack angle was approximately 45 degrees; the degree of aggregate interlock was not measured. It is worth noting that the Zararis Method assumes no aggregate interlock and crack widths open perpendicular not along the eventual failure crack. Thus, for an epoxy injected repair specimen, a diagonal rack will form at a higher load adjacent to the repaired crack. Thus, according to Zararis' Method, the capacity should be the same with or without epoxy injection, as the new crack provides no aggregate interlock and the capacity is again

governed by the steel crossing the crack. The two conflicting observations suggest future investigation with different crack inclinations and varying level of post tensioning.

5.5.2 Bent Cap Modeling: ACI 440

ACI 440 was used to model the shear contribution for the bent cap repair specimen, similar to that of the CFRP repair beam. However, the base specimen capacity in this case was modeled after the Modified Zararis Method (see section 5.5.5). Results are shown in Table 5.12. The shear capacity was limited by bond stress and thus strain in the carbon fiber was limited. The results indicate a good estimation of the specimen capacity, with a slightly conservative strength value; this is the opposite of what was found for the beam specimen.

Table 5.12 STM capacity predictions

Analysis Method:	Specimen:	Base Specimen V_P kN [kips]	Repaired ACI 440 V_P kN [kips]	Repaired Total V_P kN [kips]	V_{EXP} kN [kips]	Bias V_{EXP} / V_P
The Modified Zararis Method	D.T.C.PT	1143 [257]	- -	1517 [341]	1398 [314]	0.92
	D.T.C.CF	1119 [252]	343 [77]	1462 [341]	1527 [343]	1.04
Nominal STM	D.T.C.PT	1022 [229]	- -	1030 [231]	1398 [314]	1.36
	D.T.C.CF	837 [188]	- -	1244 [279]	1527 [343]	1.23
VecTor2	D.T.C.PT	-	- -	1344 [302]	1398 [314]	1.04
	D.T.C.CF	-	- -	1035 [233]	1527 [343]	1.48

5.5.3 Bent Cap Modeling: Strut-and-Tie Method

STM provides a general framework for discretization of a structure into regions that follow Bernoulli beam behavior and those that do not. Recall from Chapter 2, that sections with complex nonlinear stress distributions are referred to as D regions whereas sections which conform to the Bernoulli beam behavior are denoted as B regions. Within a given structure, D and B regions may both be present or only one may be present. For deep beams, the modeling of the D regions can be a complex task if performed by hand. Changes in the inclination of a truss or additions of more complex elements are rapidly re-evaluated by a computer.

Senturk utilized the Computer Aided Strut-and-Tie (CAST) software developed by Tjihn and Kuchma at the University of Illinois at Urbana-Champaign to evaluate the STM models used in his study. The program permits a graphical working environment for engineers to manipulate the size of the D regions, solve for internal member forces, and select the dimension of struts and reinforcement for ties. On-the-fly changes to the location of nodes can be accomplished at any stage of the analysis. The program contains a basic capacity estimation tool based on the ratio of the applied stress to the limits provided for the components. CAST follows the ACI 318-05 Appendix A method as well as user modifiable parameters to simulate the other international codes.

Senturk investigated three STM models for the specimens in the research. The first model was the simplest, with only two nodes and no representation of the vertical reinforcing. The second model included the effects of the vertical reinforcing, lumped as one vertical tension tie. The last model utilized a series of struts and ties in order to capture the arching affect of the specimen. Results for all three cases were conservative with respect to the laboratory specimens. The simple example provided the most conservative results, whereas the second model predicted a lower but still conservative ultimate shear load. The complex model was sensitive to minor changes in nodal geometry, resulting in quite different results for modest differences in nodal locations. Overall, each model provided a conservative design, but may be cost prohibitive for evaluation of existing structures that by analysis require additional capacity that may in reality be sufficient.

Senturk's work provided the basis for the STM models in the existing study using CAST. The ambiguity of STM leaves many possibilities for the complexity of the model. The primary components of the second model used by Senturk was used in the current study, as it resulted in a closer estimate of the base specimen with little sensitivity to nodal locations. The model consisted of four nodes, as shown in Fig. 5.28. The method was defined based on the requirements of Table 2.3 for various international codes.

The procedure for constructing the STM models in CAST followed the work of Senturk and are subsequently summarized. The first step in creating a model in CAST is to define a series of vertical and horizontal guidelines which aid in constructing the member boundaries and the intersection of interior nodes. The use of guidelines guarantees that the nodal points between elements are coincident and it provides easy modification of the location of the nodes by simply moving the guidelines as opposed to manually moving each individual node. Once the guidelines are complete, the STM elements are created, material properties for concrete and steel are entered, and boundary conditions and loads are applied. Member widths are also assigned within the model.

Member and node assignments for the base STM model are shown in Fig. 5.28. A common issue regarding the development of any STM relates to the effective width of the elements. The effective width of the top horizontal prismatic strut, representing the compression block, denoted as element S4, was set equal to:

$$w_c = k \cdot d \qquad [5.6]$$

In the above equation, d (mm or in.) is the effective depth of the section at midspan and k is taken from classical beam theory as:

$$k = \sqrt{(\rho \cdot n)^2 + 2 \cdot \rho \cdot n} - \rho \cdot n \qquad [5.7]$$

In the above equation, n is the modular ratio between steel and concrete, and ρ is the longitudinal reinforcement ratio taken at midspan. Next, the effective width of the vertical prismatic strut at the application of load was taken equal to the width of the stub girders that framed into the bent—406 mm (16 in.). The final prismatic strut representing the vertical column at the base of the specimen was given a width equal to half the column width (305 mm (12 in.)), coincident with its centerline.

Assignment of the tension ties was based on their relative location in the section. For the longitudinal steel, the effective width was taken as twice the distance bounded by the cross section and the centroid of the lowest row of steel. The effective width for the internal stirrups was taken as the total steel width for the lumped stirrups within the shear span. However, the program provides only one material property identification for steel. In other words, there was no way to differentiate the different yield strength of the flexural and transverse steel. This was resolved by reducing the lumped stirrup area to coincide with the reduction in yield strength.

As a side note, the flexural cutoffs were modeled following the ACI requirement for development length such that the node locations for the flexural bars coincide with their fully developed strength. Also, inversion of the stiffness matrix created by the program failed if an STM node attached only two elements. This condition is not explicitly described in the accompanying literature; however, it can be resolved. By attaching an additional STM member from the 2 member node to a second node, without assigning the element as either a strut or tie, the program will internally assign it as a zero force member; it is used for assembly and inversion of the stiffness matrix only. These members are denoted as 'stabilizer' elements in the program documentation.

The remaining compressive strut elements were constructed assuming bottle shaped for the ACI condition. The location of node N13, which connects the lumped stirrup tie to the two compression struts was arbitrarily placed at 1/3 the height from the top of the bent. It was positioned horizontally at the midpoint of the shear span. The effective width of the struts was taken from Senturk to be:

$$w_d = w_c \cdot \cos\theta + b_{wgirder} \sin\theta \qquad [5.8]$$

Where θ is the angle between the strut and the x-axis, w_c was previously shown, and $b_{w\ girder}$ (mm/in) is the width of the stub girders that frame into the bent.

The initial locations of the nodes were modified in order to obtain the highest strength capacity while providing the failure mode observed in the experimental program. Senturk

experienced specimen failure as a result of yielding of flexural bars within the column and stirrup failure simultaneously. By modifying the model to include failure of both elements provides the failure mechanism to be representative of the laboratory specimens. Senturk achieved the largest specimen capacity by increasing the inclination of the first strut from the beam-column connection. This was accomplished by moving the vertical prismatic strut representing the column member horizontally toward the shear span which in turn increased the angle of the first compression strut and reduced the effective width of the column prismatic strut (which was bound by the exterior edge of the column). In this respect, arbitrarily moving the node to the limit of the column was not possible, as it resulted in failure of the vertical prismatic node. Senturk also increased the capacity of the base specimen by changing the location of the upper node for the lumped stirrup tie. By decreasing the inclusive angle between the two struts at this node, the capacity increased. Thus, by adjusting the two nodes, Senturk was able to obtain the highest capacity for the given failure mode. Failure of the base STM model is shown in Fig. 5.29.

Modeling of the two bent caps in the current study followed a similar trial and error method in order to reach the highest base specimen capacity, with a few exceptions. First, the strength increase for the post tensioned specimen followed after moving the vertical column strut toward the shear span. Moving the second node upward also increased capacity, but it was limited to a height of 100 mm (4 in.) measured from the horizontal compression zone. Further vertical movement of the node would result in two parallel struts connected by a horizontal compression zone. The visualization of forces for such a model is unrealistic. For the CFRP repair specimen, the low concrete strength resulted in

the vertical strut placed at its vertical centroid as opposed to as close to the beam-column interface. The second node was moved vertically upward in order to increase the capacity. The failure load and distribution of forces for the CFRP and Post Tensioned specimens are shown in Fig. 5.30 and 5.31 respectively.

Another issue to note is that the CAST program assigns strength reduction factors and over strength parameters for each strut, tie, and node. The nominal capacity of any structure can be found, but all the default reduction and over strength factors must be changed to 1.0. The program provides the option to use the over strength or reduction factors. However, if neither option is checked, the program internally does use the over strength factors if they are greater than 1. Several international codes utilize a combination of an efficiency factored used in conjunction with a strength reduction factor. In order to compare the codes on a common threshold, the final factors for shear resistance (including efficiency and strength reduction factors where appropriate) are shown in Table 5.13. The weighted averages for each code reduction factor are show in Fig. 5.32.

Table 5.13 STM strength reduction factors for various elements

Element Strength Reduction Factors							
	Code:	ACI	AASHTO	Canadian	Eurocode2	CEB-FIP1990	CEB-FIP1999
Element:	Prismatic Strut	0.638	0.595	0.6375	0.667	0.521	0.515
	Other Shape	0.478	0.595	0.6375	0.368	0.368	0.412
	Tension Tie	0.75	0.9	0.9	0.87	0.87	0.87
Node:	No Tension Ties	0.638	0.595	0.595	0.613	0.560	0.680
	1 Tension Tie	0.510	0.525	0.525	0.521	0.395	-[2]
	2 Tension Ties	0.383	0.455	0.455	0.460	0.395	-[2]

[1]Largest value shown. Can vary to as low as 0.23184

[2]For nodes with tensile forces, the code requires a check of the anchorage length or bearing capacity. Compression ties are given a value of 0.80

Table 5.14 STM capacity based on code predictions

STM Models	D.T.C.PT			D.T.C.CF		
	V_P kN [kips]	V_{EXP} kN [kips]	Bias V_{EXP} / V_P	V_P kN [kips]	V_{EXP} kN [kips]	Bias V_{EXP} / V_P
ACI 318-05	1031 [231]	1398 [314]	1.36	1244 [280]	1527 [343]	1.23
AASHTO LRFD 2005	1031 [231]	1398 [314]	1.36	1244 [280]	1527 [343]	1.23
Canadian Bridge Code	1031 [231]	1398 [314]	1.36	1244 [280]	1527 [343]	1.23
Eurocode 2	1031 [231]	1398 [314]	1.36	1244 [280]	1527 [343]	1.23
CEB-FIB 1990	1031 [231]	1398 [314]	1.36	1244 [280]	1527 [343]	1.23
CEB-FIB 1999	1031 [231]	1398 [314]	1.36	1244 [280]	1527 [343]	1.23

Prior to discussion of results, the modeling of the repair types within the CAST program are subsequently described. For the post tensioned specimen, the yield strength of the steel was increased to reflect the additional flexural capacity provided by post-tensioning. However, the internal stirrup area was also subsequently reduced to offset the increased yield strength of the longitudinal steel (only one yield strength parameter for steel is available). As such, the strength increase estimate was marginal at best.

The carbon fiber repaired specimen was modeled by increasing the area of steel to coincide with the ACI 440 contribution for shear. With a large increase in capacity for the vertical tie, the failure was still dominated by the flexural bars at the beam-column interface which resulted in little to no increase in strength. In reality, the repair did provide additional strength. In order to check if the flexural bars within the column failed before or after the FRP failed in bond, the strain data was examined. Recall, the two anchorage bars embedded into each column were instrumented at three locations each along the embedment length. The strain data indicates only two of the strain gages (the east and west inner bars at the north end) reached yield prior to debonding of the FRP. The remaining active gages did not reach yield until after failure. This is evidence that the FRP was the critical link. Thus, increasing the capacity of the flexural bars was warranted CAST. The modeling of the bars into the column do not take into account the detailing (hook, mechanical anchorage, etc). Therefore, the capacity of the bars was increased due to the clamping force provided by the applied load within the column. Koester and Higgins provided an increase in the allowable bond stress for a bar in such a configuration as shown below [Koester and Higgins 2008].

$$\mu_{\text{mod}} = \left(0.8 + \frac{P}{800}\right) \cdot \mu_{ave} \qquad [5.9]$$

Where P is the active confining stress in the column. For the current investigation, the failure shear was divided by the column area to obtain the active confining pressure. The resulting increase in area for the bars permitted an increase in the shear strength due to the CFRP and provided failure in the vertical tie/flexural bars.

5.5.4 STM Code Comparisons

Table 5.14 provides a comparison of the repaired bent ca shear capacities predicted by the international codes and the experimental results. The governing elements in each model were the reinforcing tie at the beam/column interface and/or the vertical tie representing the lumped stirrups. As such, there is no difference in the capacity estimates for the various codes; however, for the strength condition, the strength reduction factors outlinedin Table 5.12 would be used. In both cases, the STM method conservatively estimates the specimen capacity by 23% and 36% for the CFRP and post-tensioned specimens respectively.

5.5.5 Bent Cap Modeling: Zararis Method

Previous work at OSU by Senturk included the prediction of shear capacity based on the Zararis Method [Zararis 2003]. Recall from Chapter 2, this method uses a reduced compression block based on the moment equilibrium calculated on two wedge shapes (above and below the critical shear crack). Using the reduced compression block, the capacity of the section is determined by moment equilibrium of the upper wedge (that includes the concrete compression block). However, the original method over estimated the capacity of the laboratory specimens, specifically for the horizontal compressive forces. Horizontal equilibrium was not satisfied, due to the limited longitudinal reinforcement embedded in the columns. Also, the method disregards the horizontal shear force contribution of the vertical web steel, which may be necessary to ensure horizontal force equilibrium.

The Zararis Method was modified by limiting the concrete compressive strength and by taking into account the horizontal shear contribution of the stirrups. The compressive strength was limited to 0.85*fc', as a result of compression softening due to indirect loading and lack of confinement of the compression zone. The horizontal shear force contribution of the web reinforcement was taken as shown in Equation [5.10] below.

$$V_{sd} = 0.4 \cdot V_s \cdot \tan\varphi \qquad [5.10]$$

For the modified analysis, the initial values of c, c_s, and P_u are computed using the original Zararis Method, but utilizing a reduced concrete strength as previously noted. Horizontal

equilibrium is checked against the compression force. The first analysis case assumes the tension capacity of the available longitudinal reinforcement denoted in Equation [5.11] below is greater than or equal to the compressive force.

$$T_{\max} = A_s f_y \geq C = 0.85 \cdot f_c^{'} \cdot b \cdot c_s \quad [5.11]$$

In this case, the strength is governed by the concrete and the original equation for shear capacity is used. If Equation [5.11] is not satisfied, applicability of a second case is checked, where the tension capacity of the longitudinal steel plus the horizontal shear force contribution from the web reinforcement is greater than the compressive force, as shown in Equation [5.12].

$$T_{\max} + V_{sd} \geq C = 0.85 \cdot f_c^{'} \cdot b \cdot c_s \quad [5.12]$$

In this case, the capacity is calculated as shown in Equation [5.13], where the horizontal shear component of the stirrups is limited to Equation [5.14].

$$V_{sd,limited} = C - T_{\max} \text{ if } T_{\max} + V_{sd} > C \quad [5.13]$$

$$V_p = \frac{T_{\max}\left(1 - 0.5 \cdot \frac{c_{s,initial}}{d}\right) + 0.5 \cdot V_s\left(\frac{a}{d}\right) + 0.5 \cdot V_{sd,limited}}{(a/d)} \quad [5.14]$$

A third case exists if the tensile stress plus horizontal shear component of the stirrups is less than the compressive force of the concrete. In this case, the strength is governed by the availability of the steel reinforcement and the compression block is further reduced, as denoted in Equation [5.15].

$$c_{s,limited} = \frac{T_{\max} + V_{sd}}{0.85 \cdot f_c^{'} b} \quad [5.15]$$

The resulting shear strength is shown in Equation [5.16].

$$V_p = \frac{T_{\max}\left(1 - 0.5 \cdot \frac{c_{s,limited}}{d}\right) + 0.5 \cdot V_s \cdot \left(\frac{a}{d}\right) + 0.5 \cdot V_{sd}}{(a/d)} \qquad [5.16]$$

Modifications for the post tensioned specimen include a second horizontal tensile force equal to the post-tensioned force and a second lever arm. The resulting modification to Equation [5.17] is shown below for the case of post-tensioning applied coincident with the longitudinal steel:

$$V_p = \frac{(T_{\max} + F_{PT}) \cdot \left(1 - 0.5 \cdot \frac{c_{s,limited}}{d}\right) + 0.5 \cdot V_s \cdot \left(\frac{a}{d}\right) + 0.5 \cdot V_{sd}}{(a/d)} \qquad [5.17]$$

For the carbon fiber repair, the base specimen capacity was determined by the Zararis method, with the repair contribution taken from ACI 440, which was governed by bond strength of the epoxy.

5.5.6 Bent Cap Modeling: VecTor2

Each of the repaired bent cap specimens were modeled in VecTor2. The post tensioned bent cap specimen's meshing scheme is show in Fig. 5.33. For this specimen, the post tensioning force was applied along five nodes that represent the limits of the height of the reaction section on each column section. An initial 22.5 kN (5 kip) was applied to each node and the force was applied in several incremental steps. The post tension force was

used in a seed file for the final loading cycle. The results of the capacity estimate are shown in Table 5.13. The VecTor2 model conservatively predicted the shear force within 4% of the failure load. The load versus midspan displacement is shown in Fig. 5.34. The specimen provides close correlation with the experimental data, noting that the VecTor2 model was loaded prior to cracking moment which would result in a more accurate slope along the initial portion of the curve.

The CFRP repaired bent cap was also modeled in VecTor2, utilizing the bond-slip relationships previously identified for the beam specimen. The meshing scheme for the repair is shown in Fig. 5.35. The strength estimate is shown in Table 5.13, which indicates no additional capacity was gained for the repair. To better understand the behavior of the model, the midspan load-deflection curve is shown in Fig. 5.36. The graph indicates a stiffness change for the cracked section with a gradual change in stiffness until failure. The constitutive models used in the literature were applied to beam specimens that have a larger a/d ratio than the existing deep beams. Therefore, the relationships may need to be modified accordingly. Also, the premature failure may be a question of scale, as many CFRP shear beam tests are performed at quarter or half scale. With the large width of cracks for the bent cap specimens in the current study, the bond slip relationship may have been violated prematurely.

5.5.7 Bent Cap Design Recommendations

Testing large scale specimens eliminates any question of size effect within the testing process. However, limited resources prevent production of many such specimens. Thus, the results of the current investigation provide an indication of two test specimens, and may not provide a clear indication of governing behavior for all deep beams. Design recommendations for base specimen capacity are as follows.

- STM consistently provided a lower bound for the capacity of the bent cap specimens.
- If more refined estimates for the base specimen capacity are required, the Zararis and Modified Zararis Method (proposed by Senturk) provide shear capacity estimates similar to previous bent cap specimens tested at OSU.
- ACI 440 was used to estimate the strength gain for the CFRP bent cap and conservatively predicted the design strength quite accurately. However, ACI 440 used in combination with R2K (thus providing a closer base specimen capacity estimate) over predicted the capacity of the beam specimens used in the current study.
- The post tensioned bent cap capacity was estimated by the Modified Zararis Method with a slightly over conservative estimate of the strength.
- The added strength gain by epoxy injection prior to post tensioning has been suggested in the available literature; however, the VecTor2 model for post

tensioning was completed such that post tensioning was applied prior to application of vertical load. As the results are comparable to the experimental capacity of the section (not off by a factor of 2, as indicated by Aravinthan and Suntharavadivel), the validity of such and increase by epoxy injection alone prior to post tensioning is drawn into question.

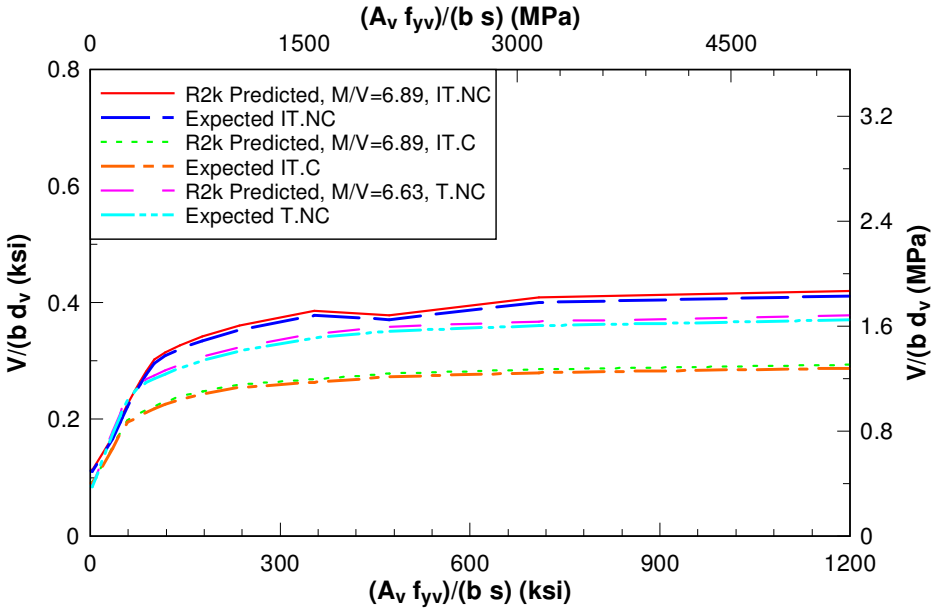

Fig. 5.1 – R2K behavior of beam specimens

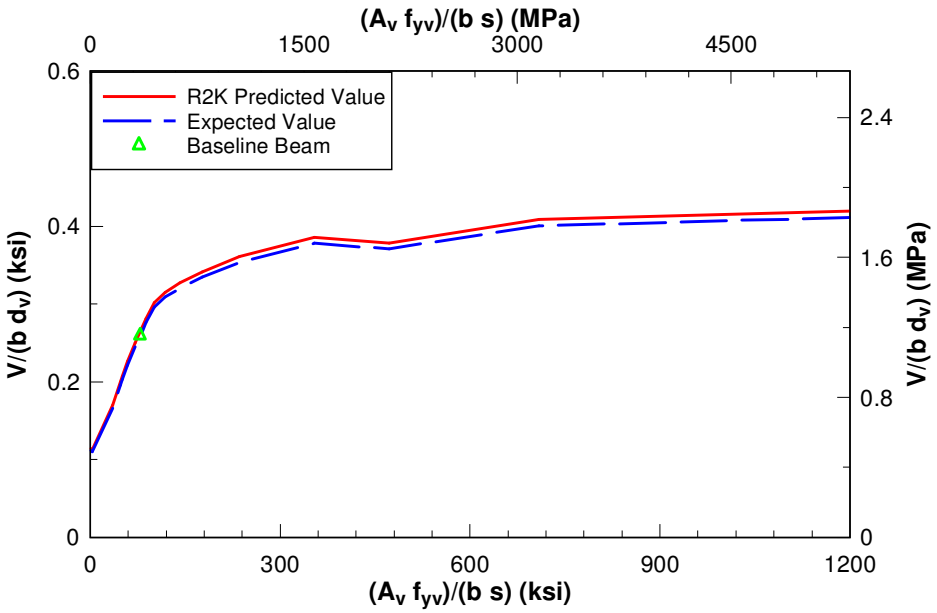

Fig. 5.2 – IT Beams without cutoffs baseline curve prediction

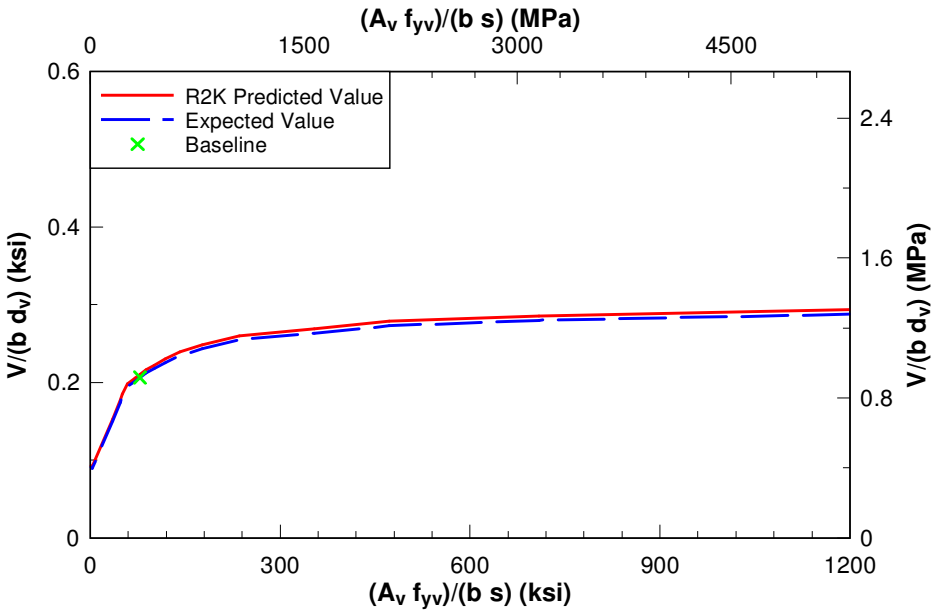

Fig. 5.3 – IT Beams with cutoffs baseline curve prediction

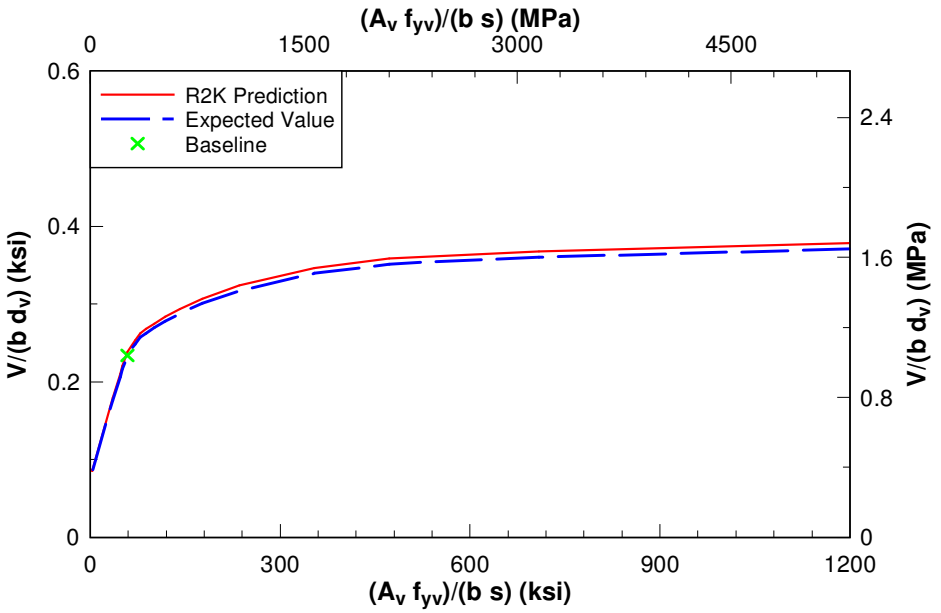

Fig. 5.4 – T Beams without cutoffs baseline curve prediction

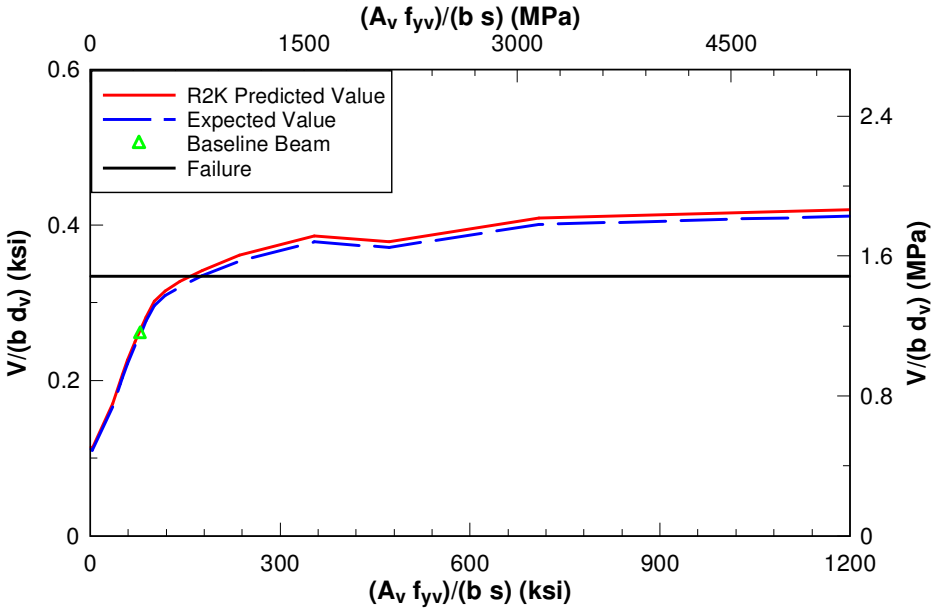

Fig. 5.5 – B.IT.NC.ES Comparison

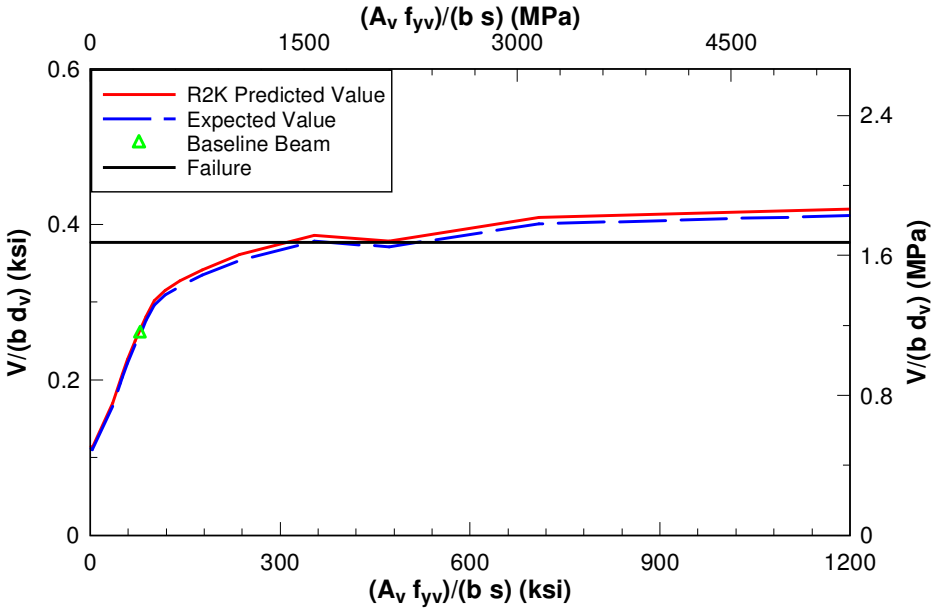

Fig. 5.6 – B.IT.NC.IS Comparison

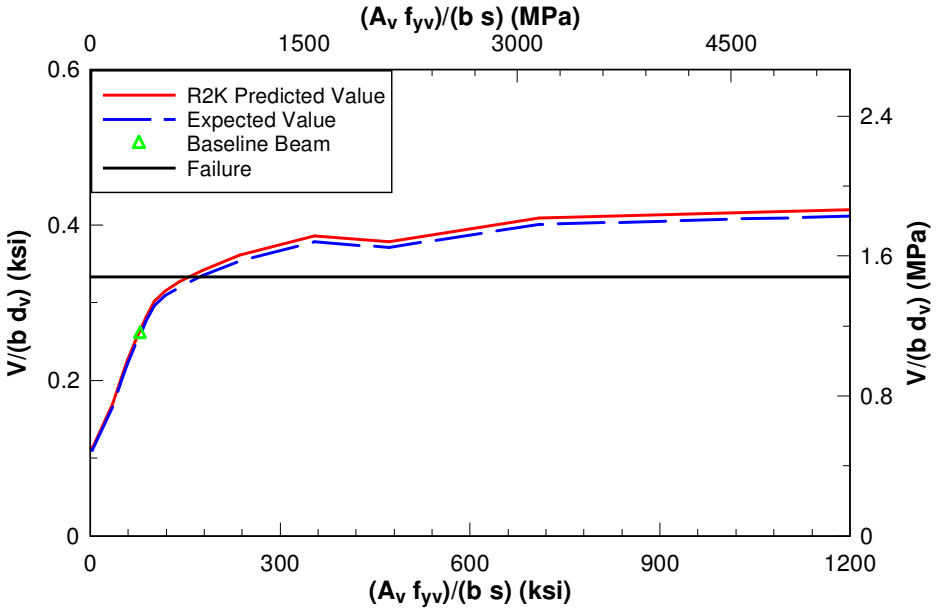

Fig. 5.7 – B.IT.NC.CF Comparison

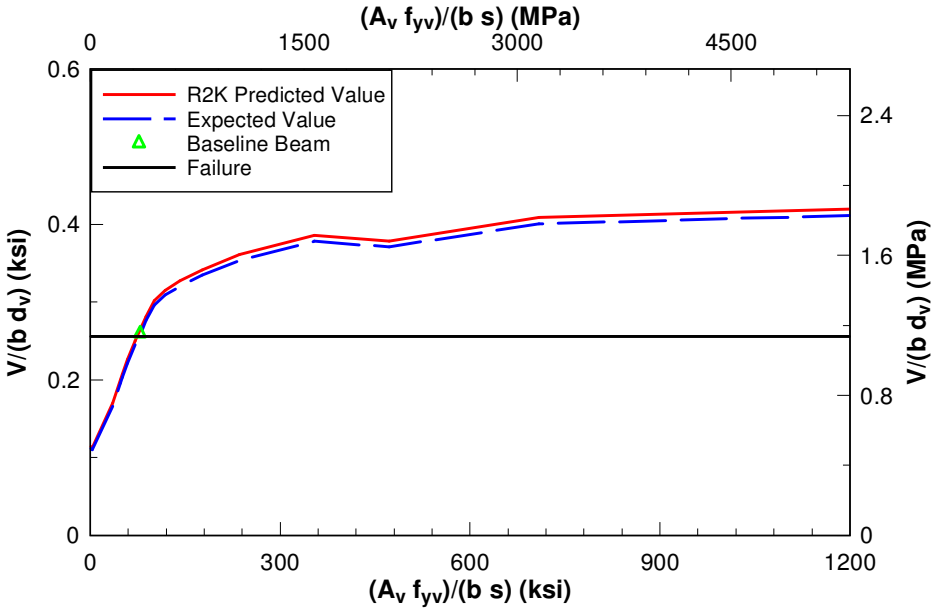

Fig. 5.8 – B.IT.NC.NS Comparison

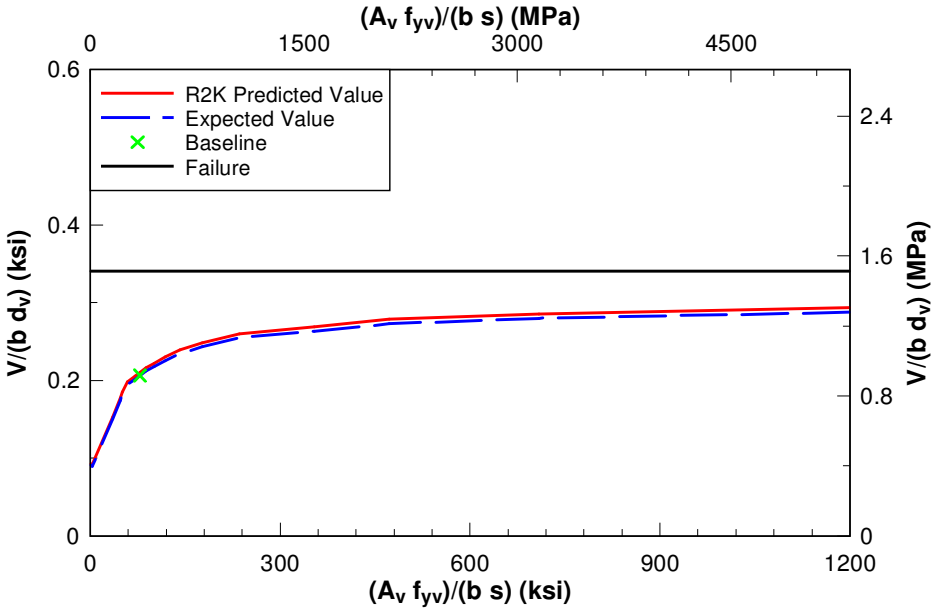

Fig. 5.9 – B.IT.C.ES Comparison

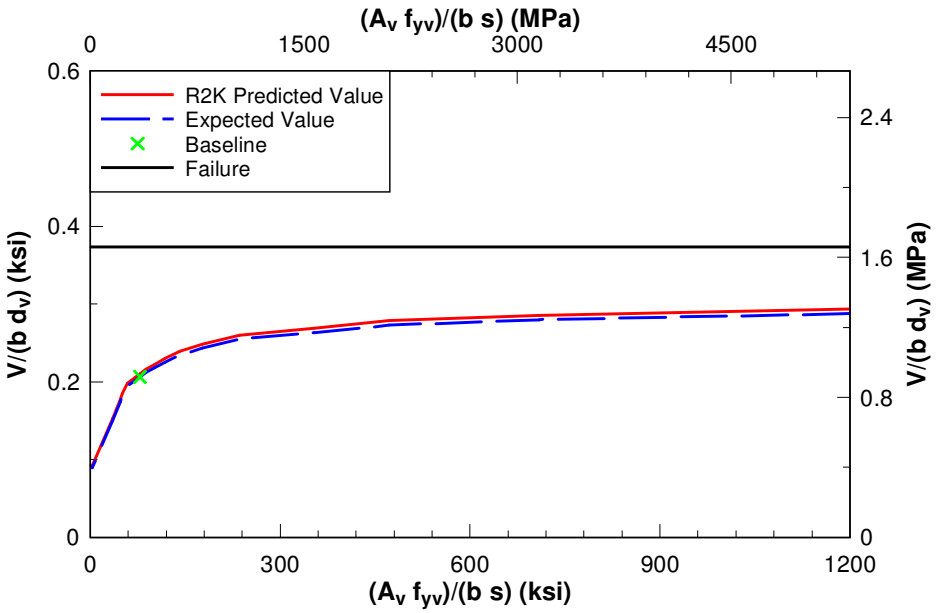

Fig. 5.10 –B.IT.C.IS Comparison

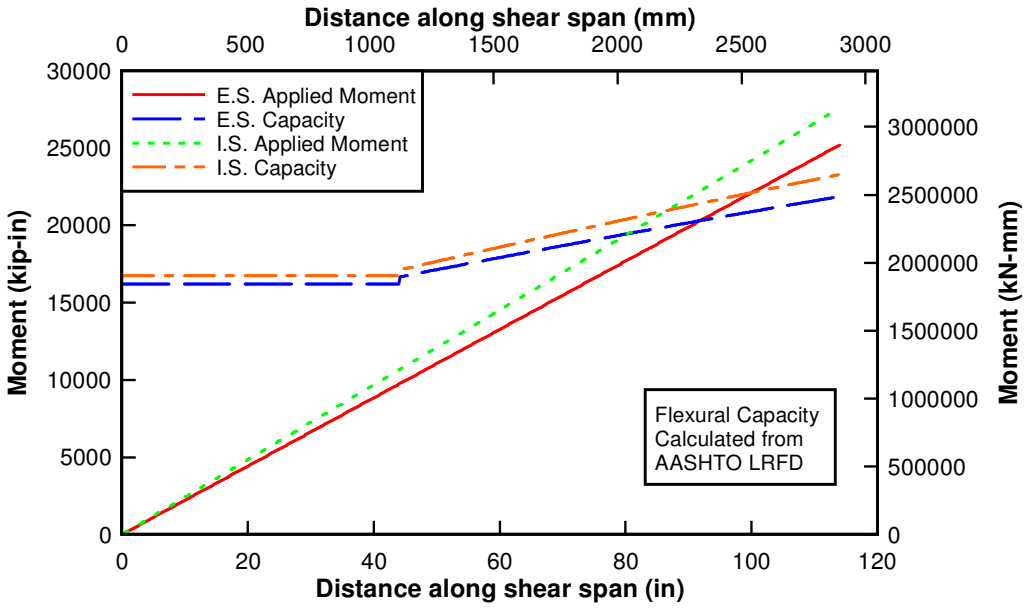

Fig. 5.11 – Cutoff specimens flexural demand and capacity

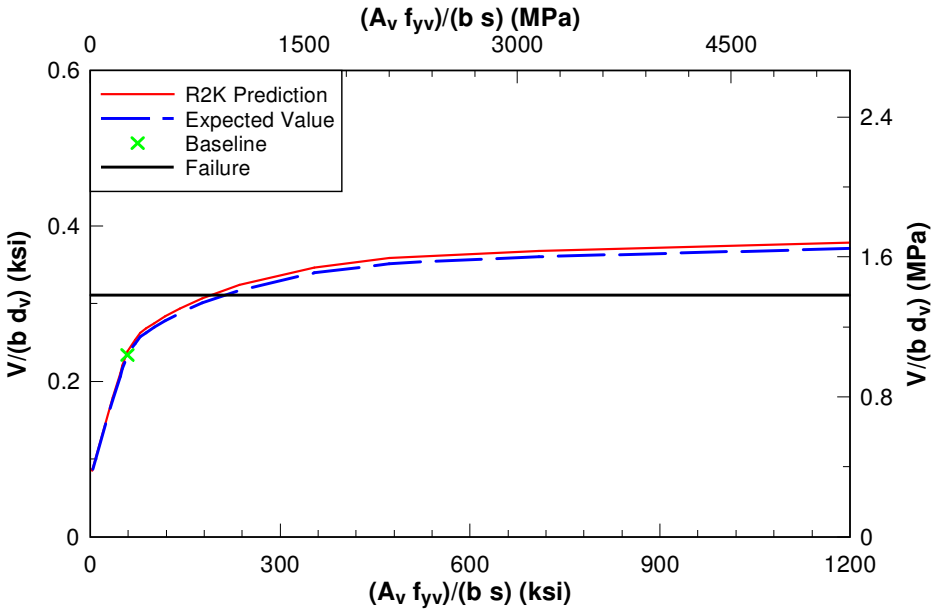

Fig. 5.12 – B.T.NC.ES Comparison

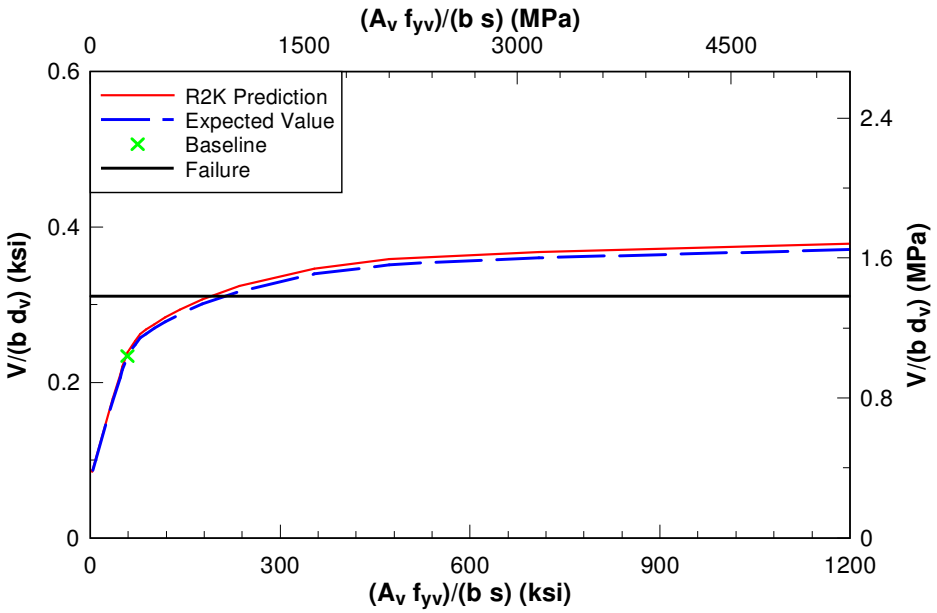

Fig. 5.13 – B.T.NC.IS Comparison

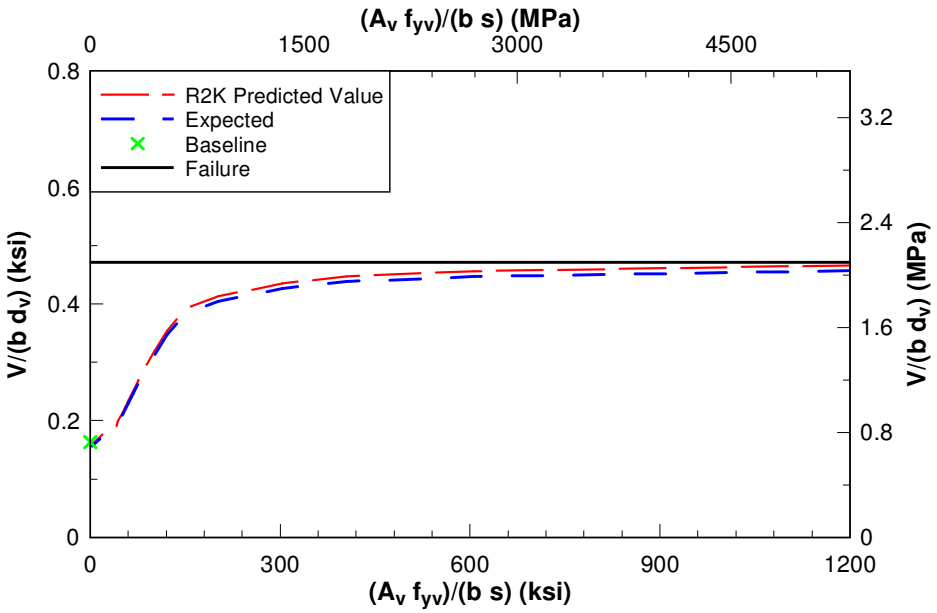

Fig. 5.14 – Minh et al. shear interaction diagram

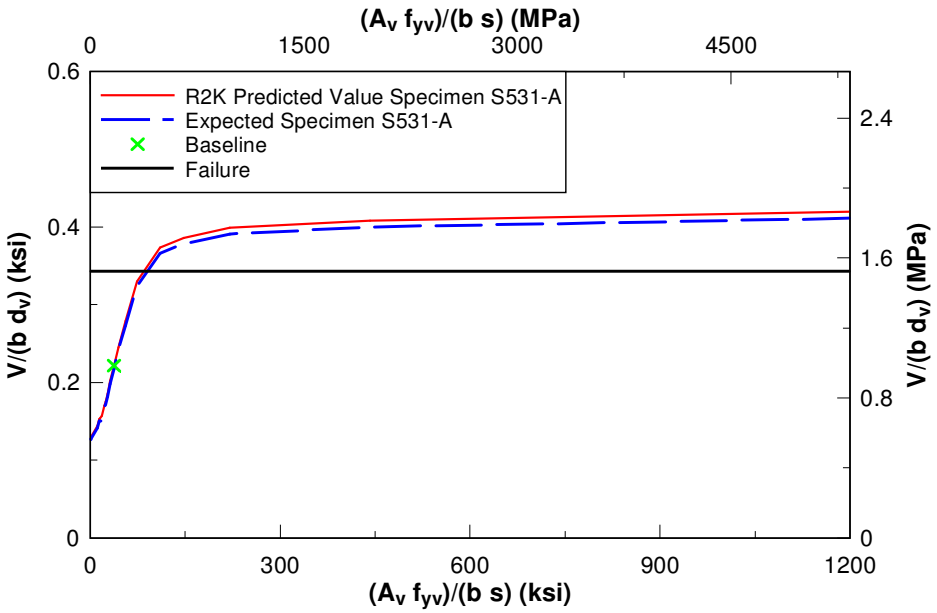

Fig. 5.15 – Altin et al. shear interaction diagram

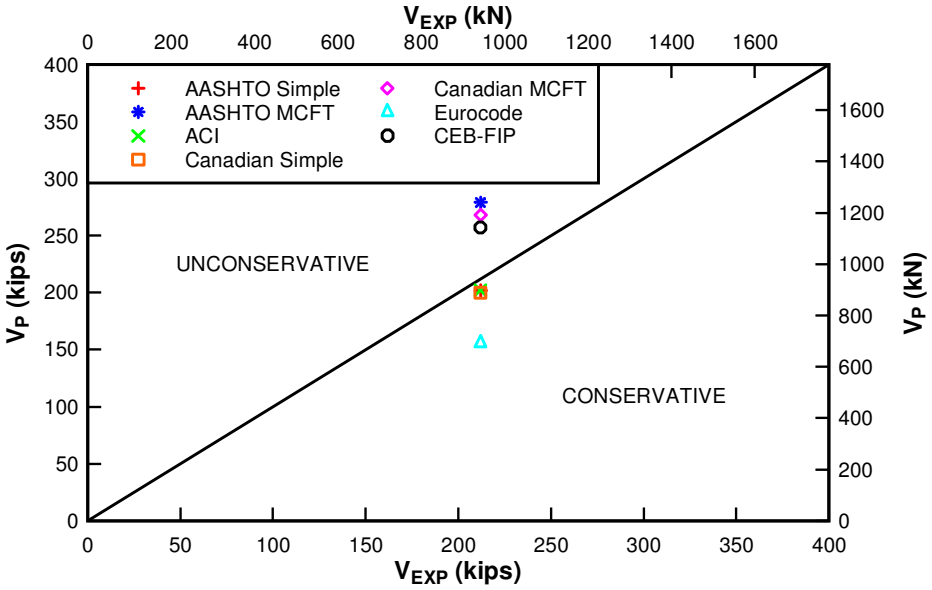
V_EXP (kN)
0 200 400 600 800 1000 1200 1400 1600
AASHTO Simple
AASHTO MCFT
ACI
Canadian Simple
Canadian MCFT
Eurocode
CEB-FIP
UNCONSERVATIVE
CONSERVATIVE
V_P (kips)
V_P (kN)
0 50 100 150 200 250 300 350 400
V_EXP (kips)

A)

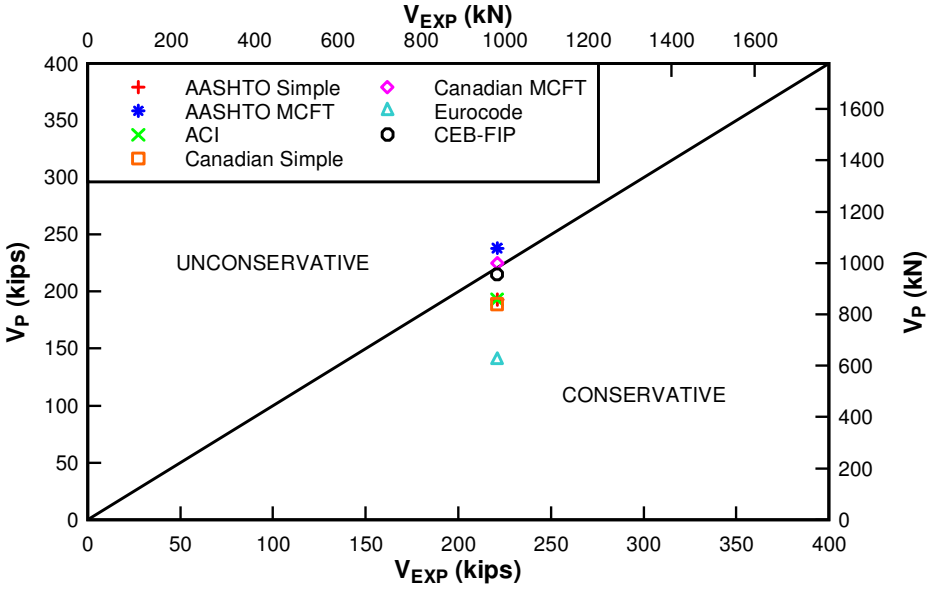
V_EXP (kN)
0 200 400 600 800 1000 1200 1400 1600
AASHTO Simple
AASHTO MCFT
ACI
Canadian Simple
Canadian MCFT
Eurocode
CEB-FIP
UNCONSERVATIVE
CONSERVATIVE
V_P (kips)
V_P (kN)
0 50 100 150 200 250 300 350 400
V_EXP (kips)

B)

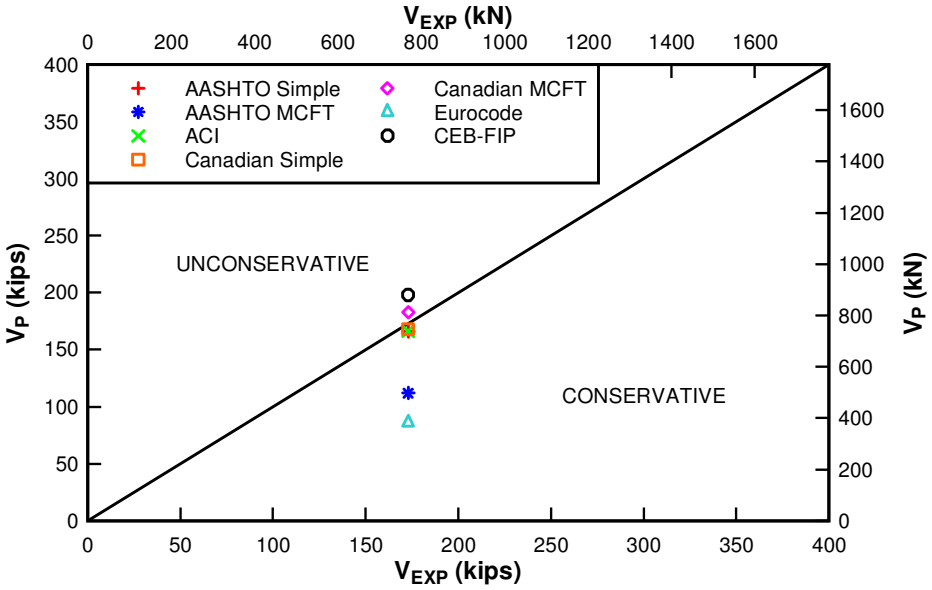

C)

Fig. 5.16 – Code Comparison for A) B.IT.NC.ES, B) B.IT.C.ES, & C) B.T.NC.ES

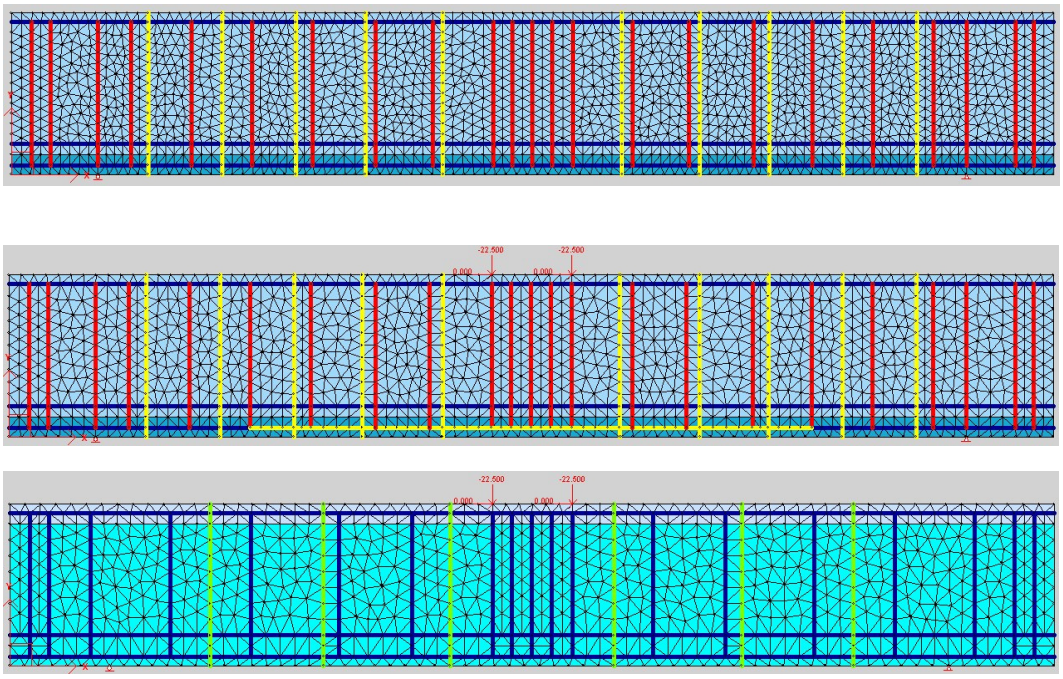

Fig. 5.17 – VecTor2 meshing schemes for A) B.IT.NC.ES, B) B.IT.C.ES, & C) B.T.NC.ES

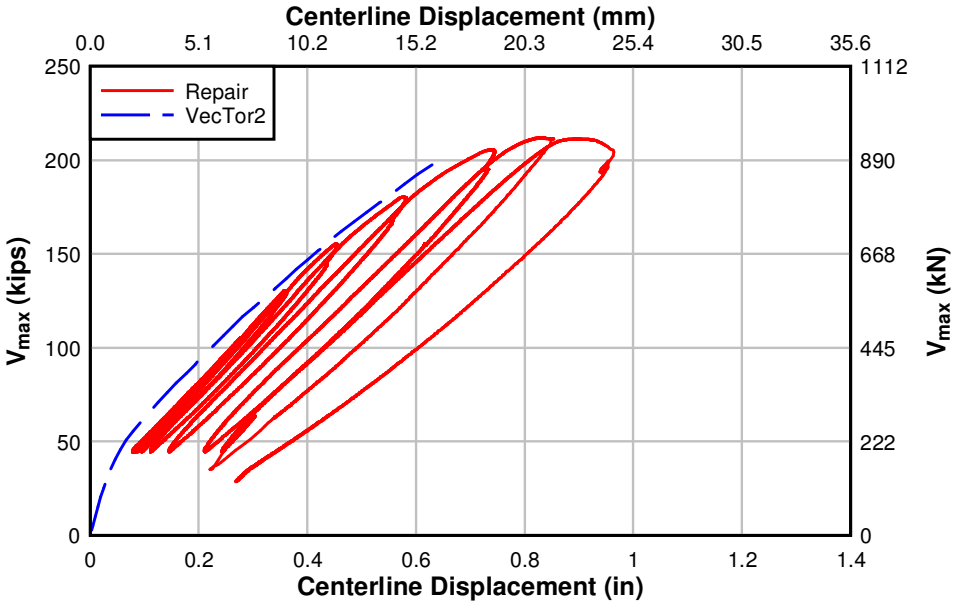

A)

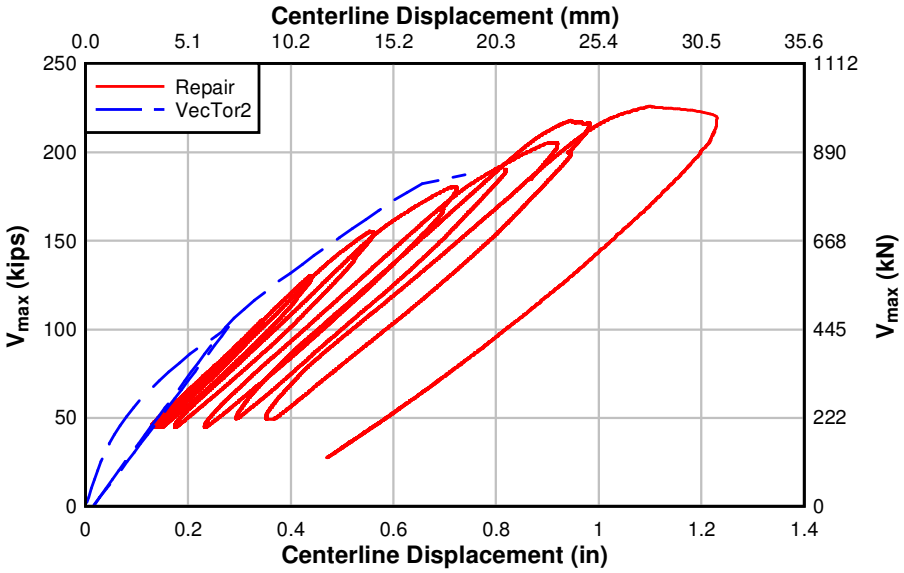

B)

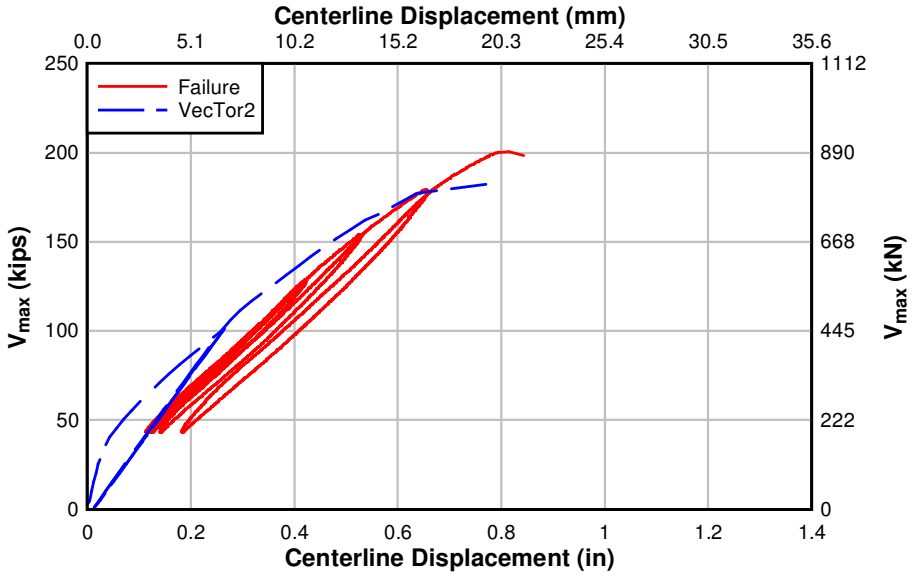

C)

Fig. 5.18 – VecTor2 external stirrup load deflection estimate for A) B.IT.NC.ES, B) B.IT.C.ES, C) B.T.NC.ES

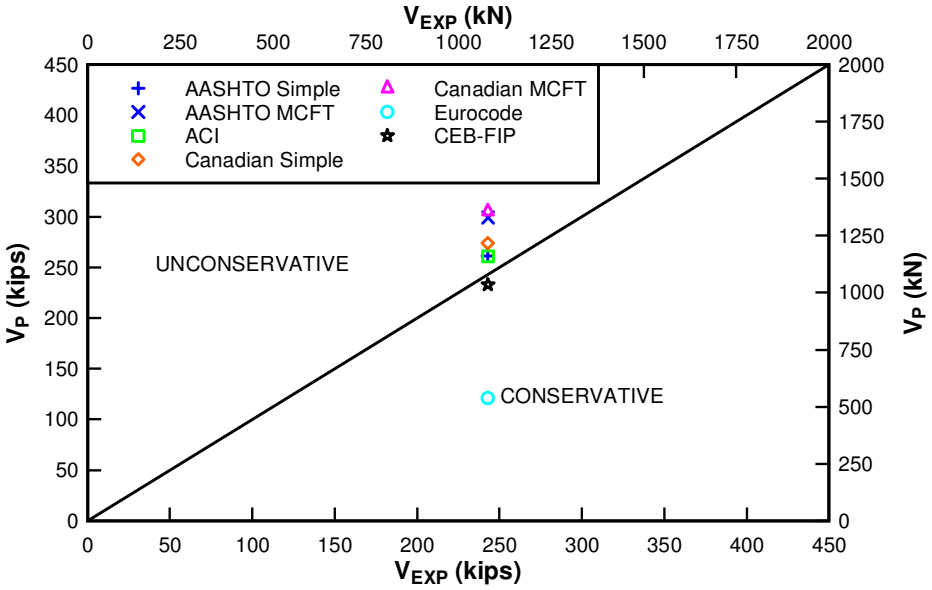
V_EXP (kN)
0 250 500 750 1000 1250 1500 1750 2000
AASHTO Simple
AASHTO MCFT
ACI
Canadian Simple
Canadian MCFT
Eurocode
CEB-FIP
UNCONSERVATIVE
CONSERVATIVE
V_P (kips)
V_P (kN)
V_EXP (kips)
0 50 100 150 200 250 300 350 400 450

A)

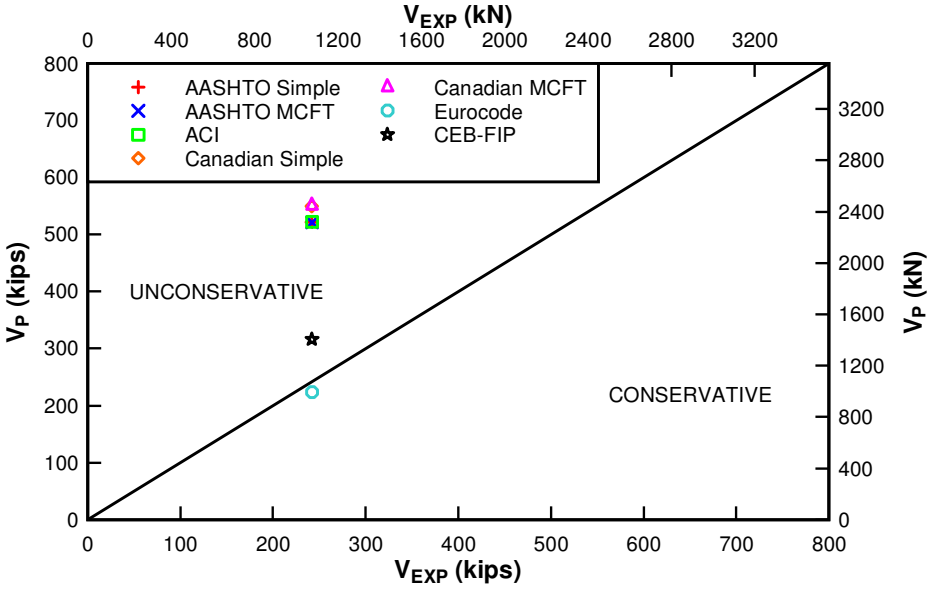
V_EXP (kN)
0 400 800 1200 1600 2000 2400 2800 3200
AASHTO Simple
AASHTO MCFT
ACI
Canadian Simple
Canadian MCFT
Eurocode
CEB-FIP
UNCONSERVATIVE
CONSERVATIVE
V_P (kips)
V_P (kN)
V_EXP (kips)
0 100 200 300 400 500 600 700 800

B)

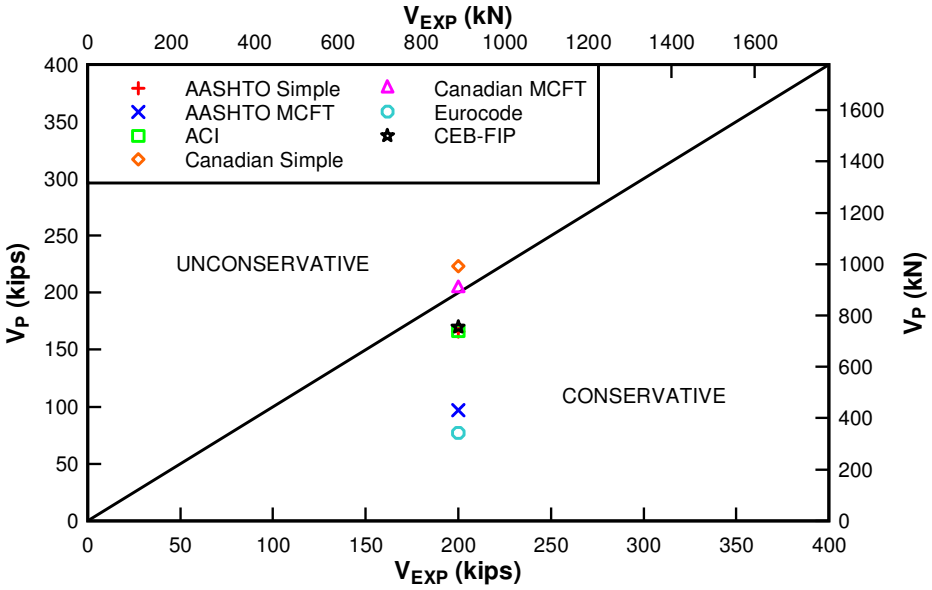

C)

Fig. 5.19 – Code Comparison for A) B.IT.NC.IS, B) B.IT.C.IS, & C) B.T.NC.IS

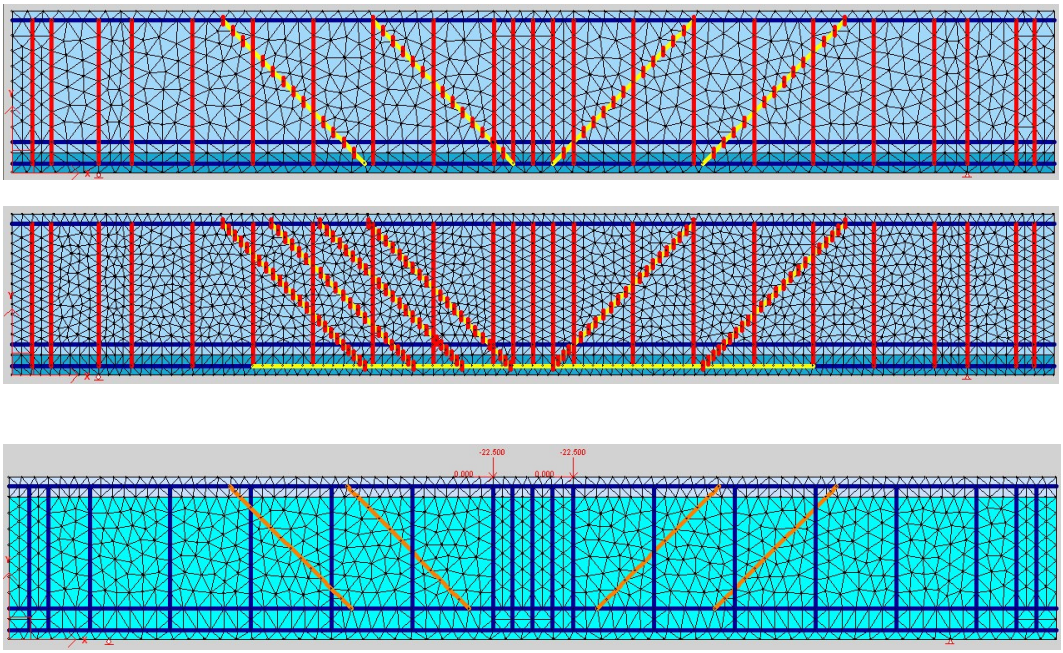

Fig. 5.20 – VecTor2 meshing schemes for A) B.IT.NC.IS, B) B.IT.C.IS, & C)B.T.NC.IS

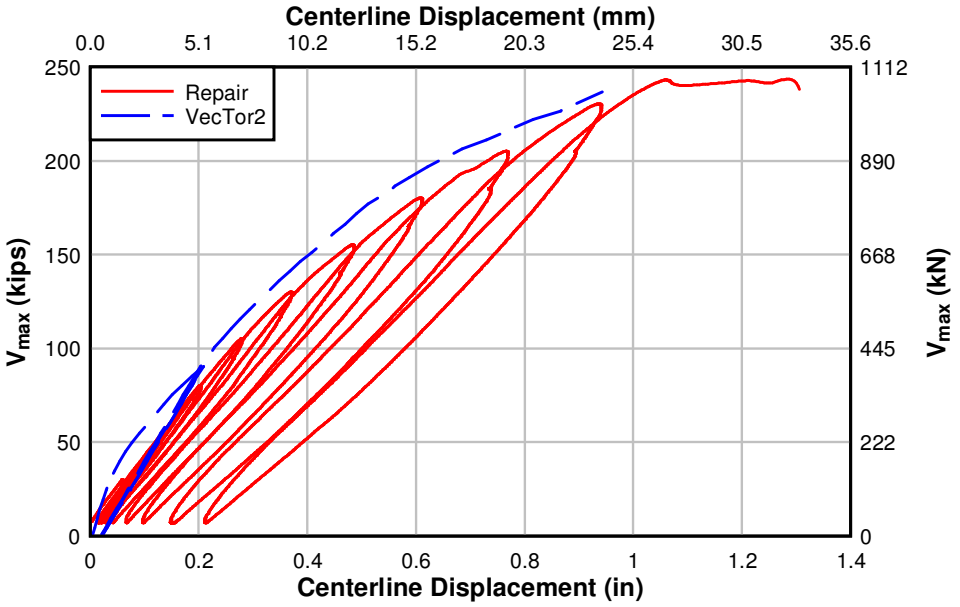
Centerline Displacement (mm)
0.0
5.1
10.2
15.2
20.3
25.4
30.5
35.6
Repair
VecTor2
250
200
150
100
50
0
1112
890
668
445
222
0
Vmax (kips)
Vmax (kN)
0
0.2
0.4
0.6
0.8
1
1.2
1.4
Centerline Displacement (in)

A)

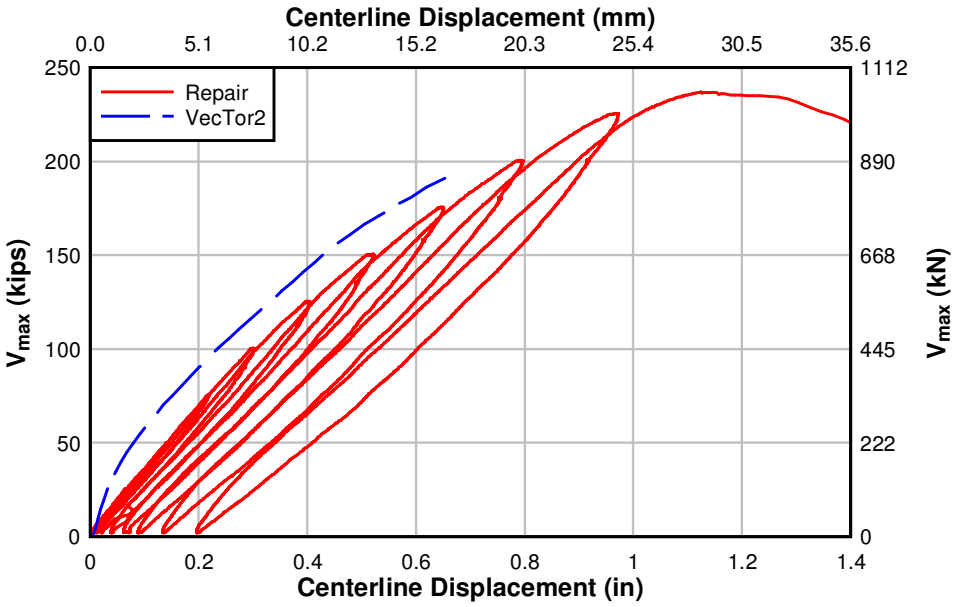
Centerline Displacement (mm)
0.0
5.1
10.2
15.2
20.3
25.4
30.5
35.6
Repair
VecTor2
250
200
150
100
50
0
1112
890
668
445
222
0
Vmax (kips)
Vmax (kN)
0
0.2
0.4
0.6
0.8
1
1.2
1.4
Centerline Displacement (in)

B)

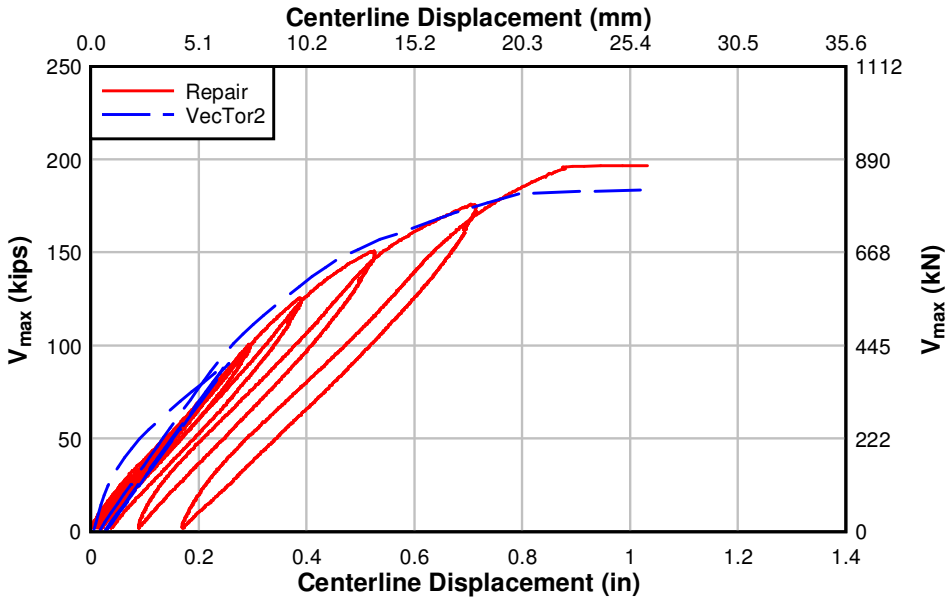

C)

Fig. 5.21 – VecTor2 internal stirrup load deflection estimate for A) B.IT.NC.IS, B) B.IT.C.IS, C) B.T.NC.IS

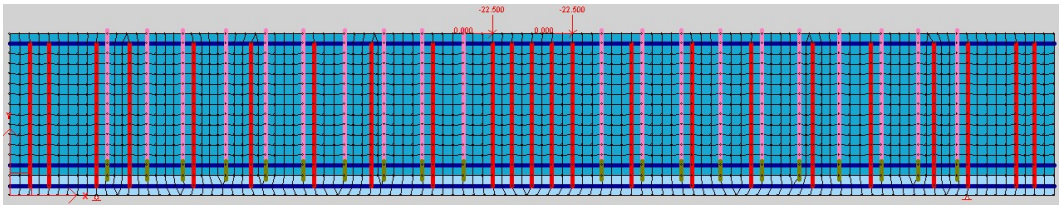

Fig. 5.22 – VecTor2 meshing scheme for B.IT.NC.CF

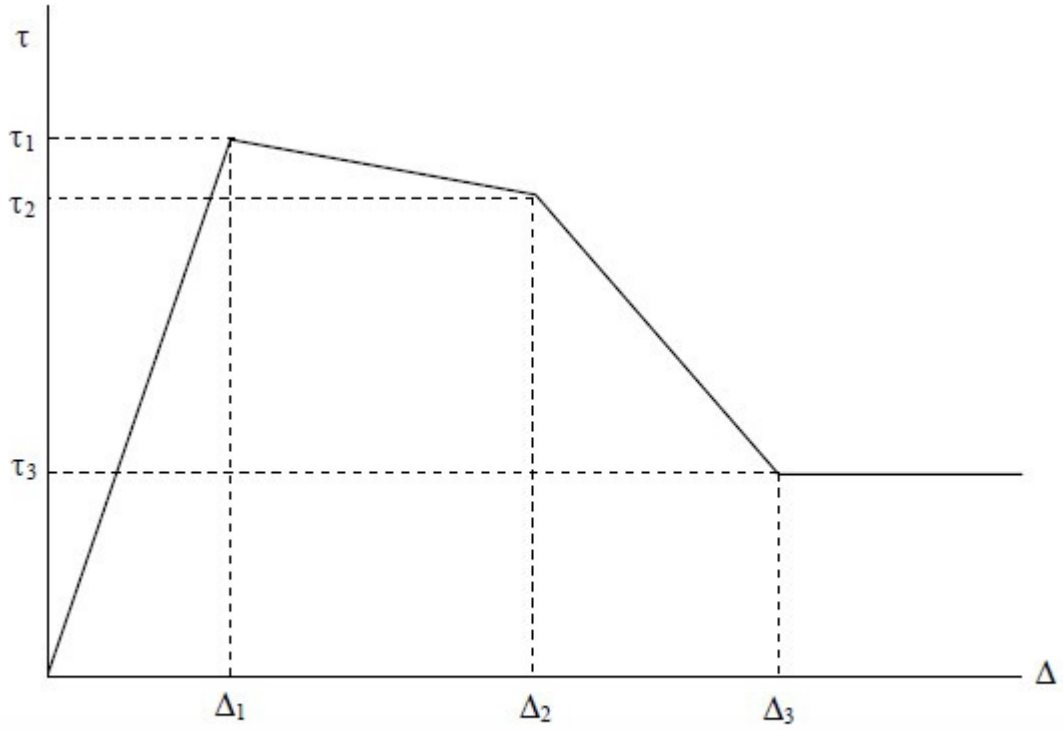

Figure 45: Bond stress-slip response for externally bonded plates or sheets

Fig. 5.23 – Bond slip relationship for VecTor2 modeling of CFRP sheets

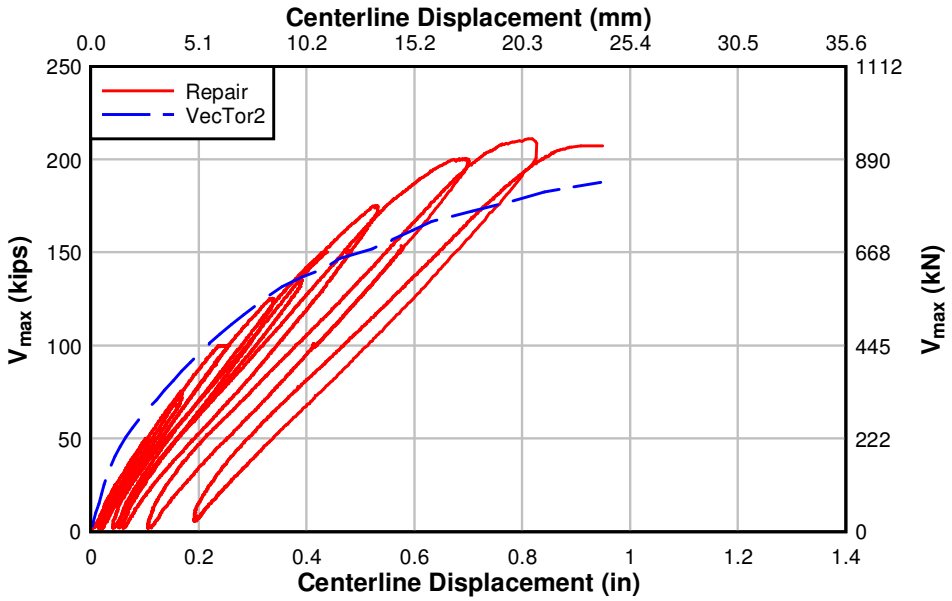

Fig. 5.24 – VecTor2 load-deflection response for B.IT.NC.CF

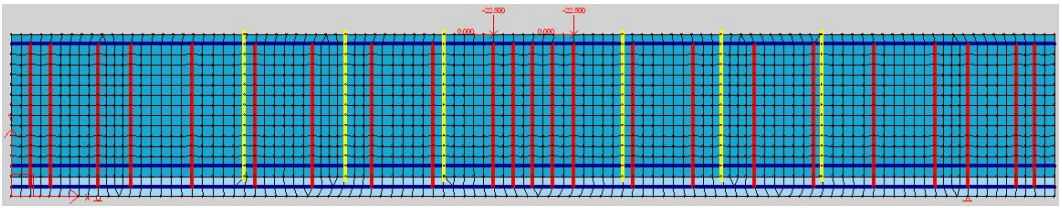

Fig. 5.25 – VecTor2 meshing scheme for B.IT.NC.NS

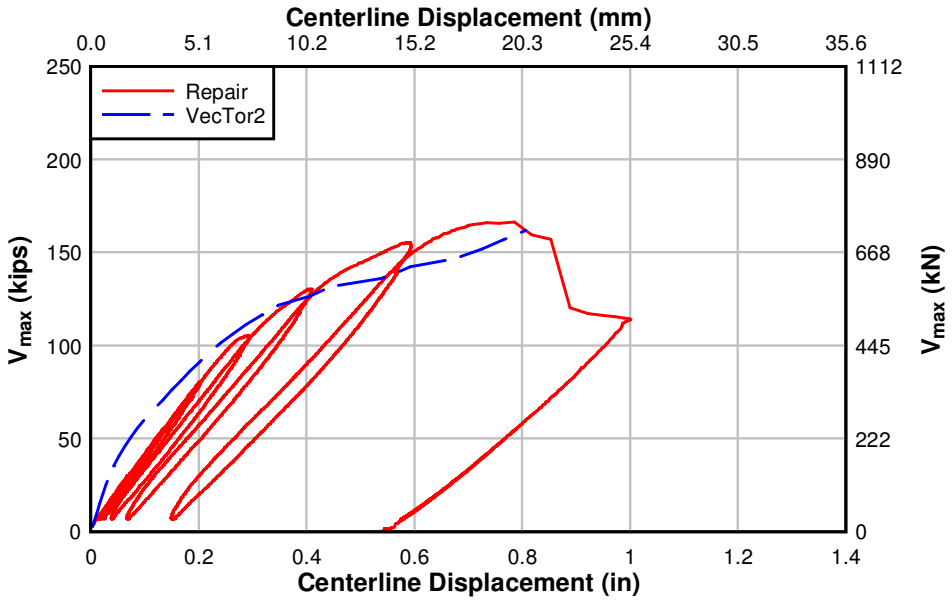

Fig. 5.26 – VecTor2 load-deformation response for B.IT.NC.NS

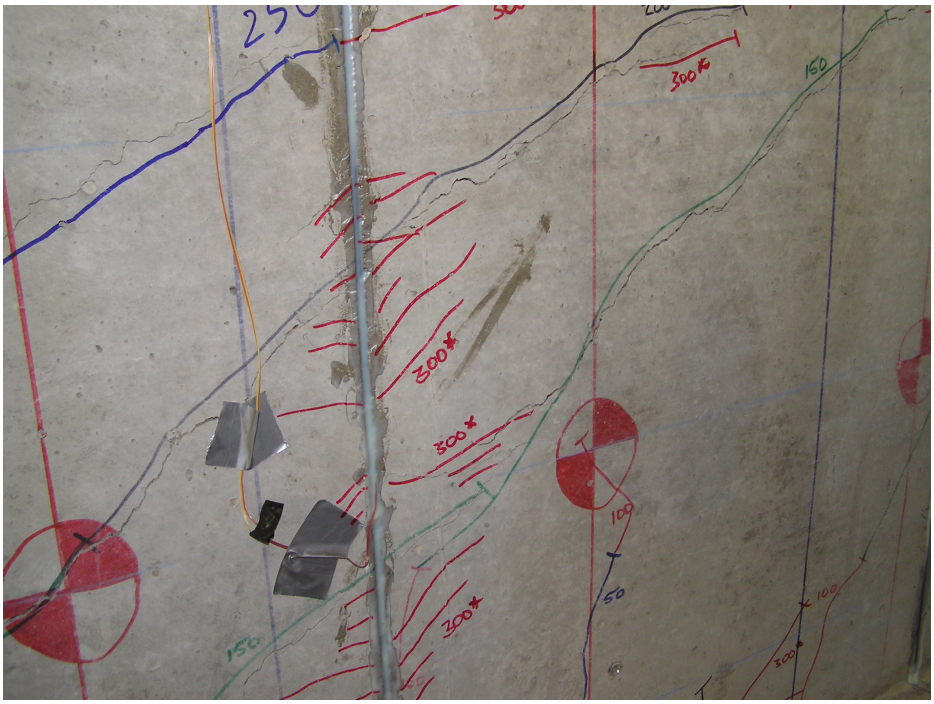

Fig. 5.27 – B.IT.NC.NS restraint of cracks under load

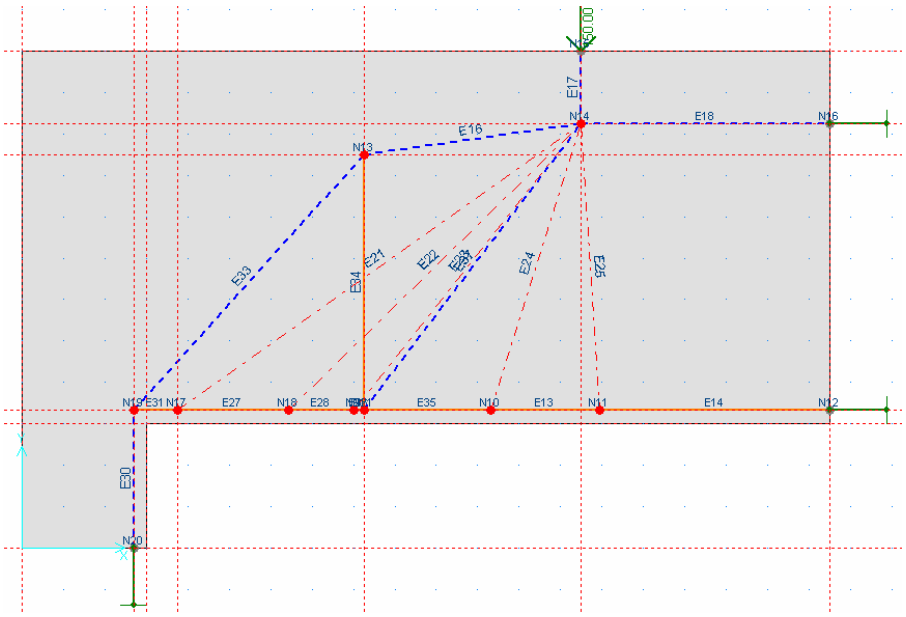

Fig. 5.28 – CAST STM Model Base Specimen: Member and Node Assignments

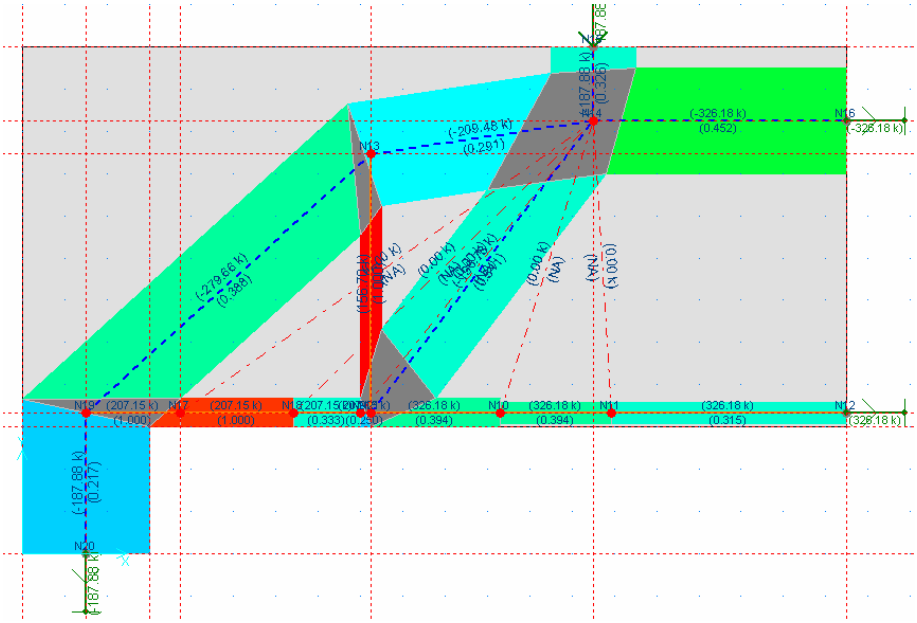

Fig. 5.29 – CAST STM Model Base Specimen Governing Member/Load

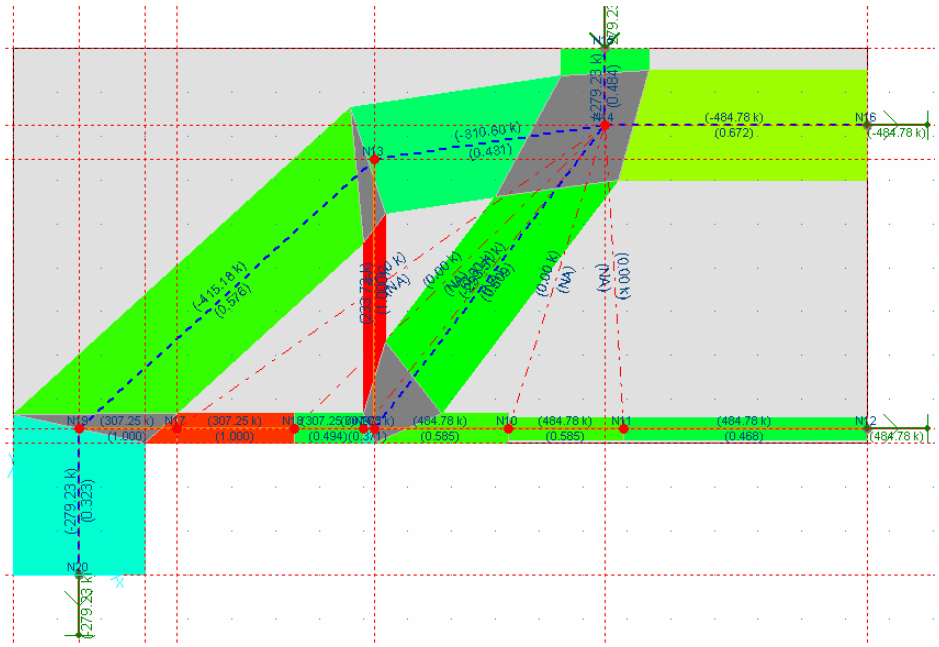

Fig. 5.30 – D.T.C.CF Failure Load-CAST STM Model

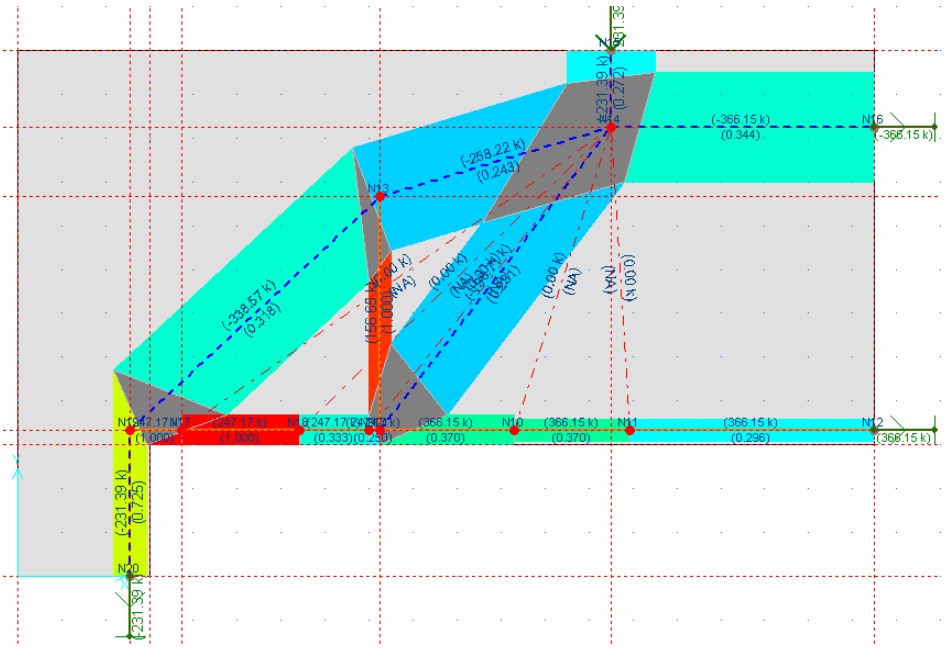

Fig. 5.31 – D.T.C.PT Failure Load-CAST STM Model

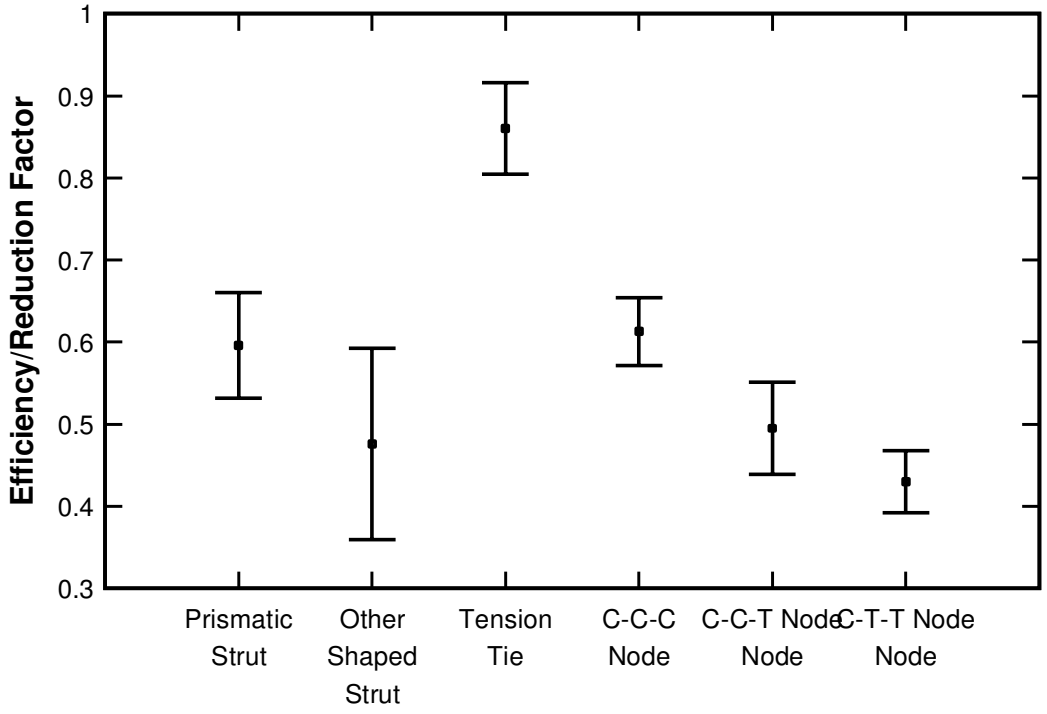

Fig. 5.32 – STM efficiency factors from international codes

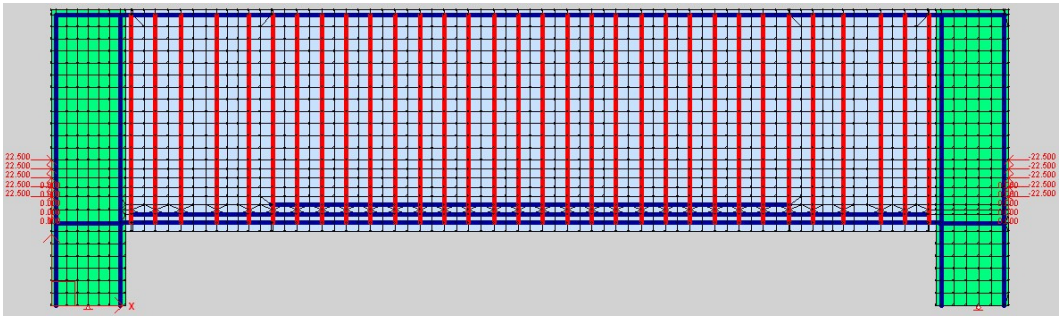

Fig. 5.33 – VecTor2 meshing scheme for D.T.C.PT

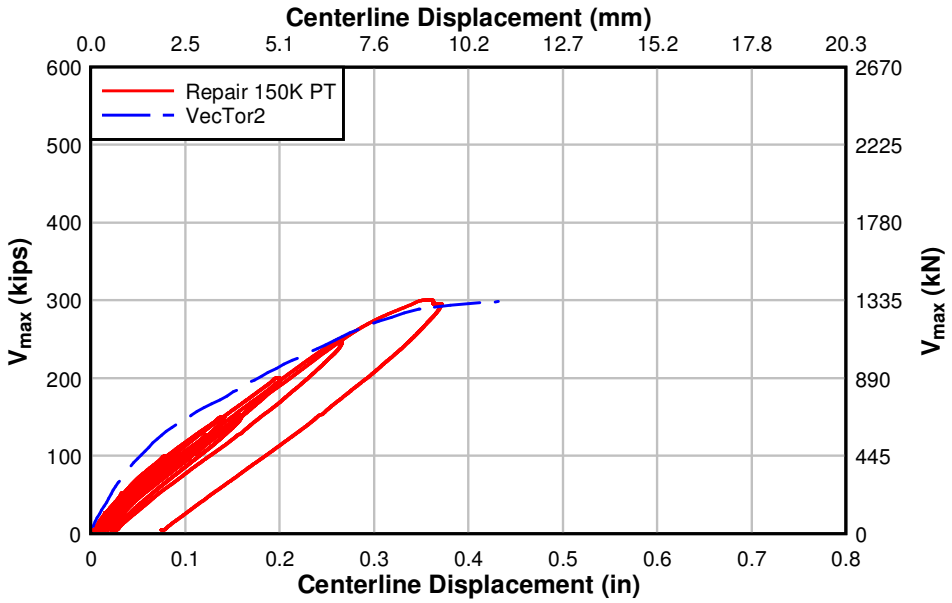

Fig. 5.34 – VecTor2 load-deformation response for D.T.C.PT

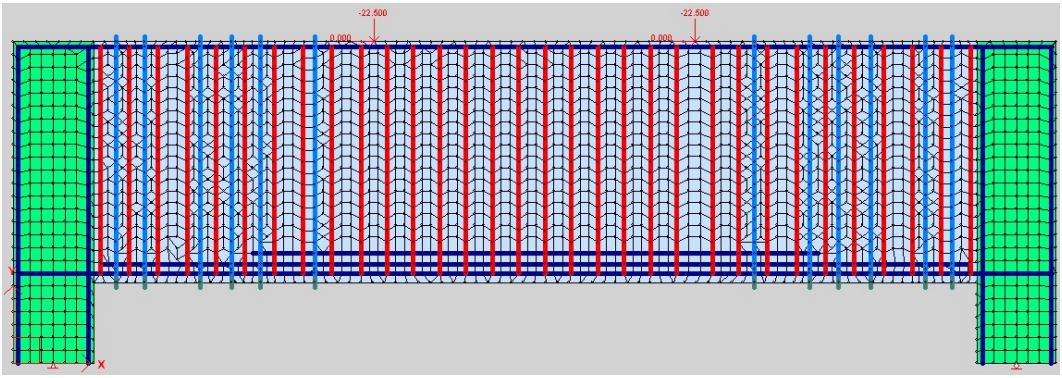

Fig. 5.35 – VecTor2 D.T.C.CF meshing scheme for D.T.C.CF

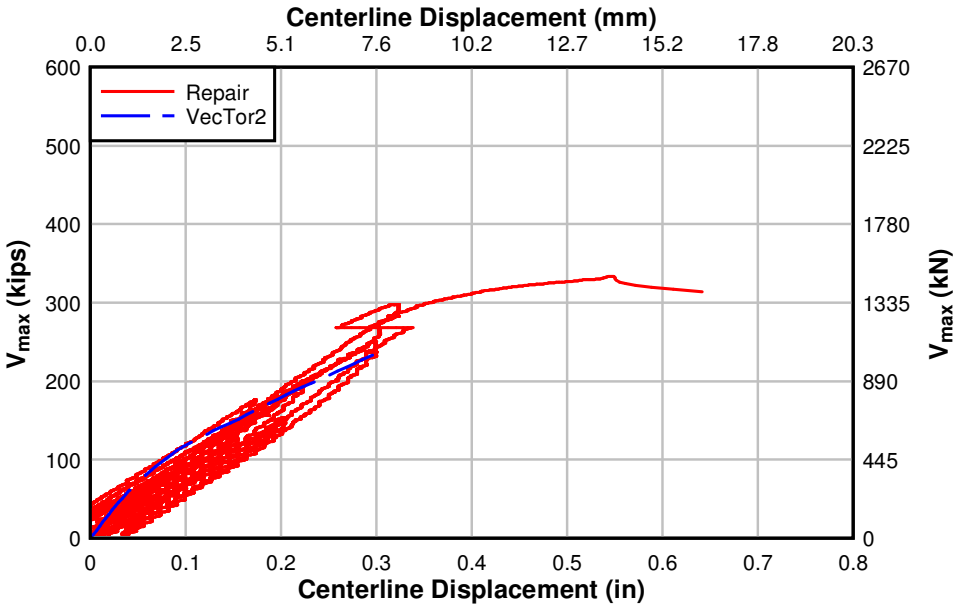

Fig. 5.36 – VecTor2 load-deformation response for D.T.C.CF

6. CONCLUSIONS

In this section, conclusions from the various repair methods are presented.

6.1 Summary and Conclusion

A research program was completed to investigate the behavior of lightly traditionally reinforced concrete girders and deep beams. The program included specimens tested at full scale, with vintage 1950's details including flexural cutoffs and widely spaced integrally cast stirrups within the shear span. Transverse steel and concrete mix design mimicked that of the original 1950's beams. For the beam repairs, sixteen specimens were utilized, with the initial eight specimens used as part of a separate research project to investigate epoxy injection repair; two bent cap specimens were included in the current research program. The results of the initial eight repair beams for epoxy injection, as documented by Smith, indicate epoxy injection provides a means of bonding concrete across cracks and reducing steel stirrup strains, assuming the subsequent applied load is less than the maximum value previously felt by the girder. However, even strict enforcement of truck weights results in occasional overloads, which could re-crack the girder and render the repair as ineffective. Further, it does not increase the strength of the girders.

The remaining eight repair beams encompassed the latest emerging technologies in structural engineering for strengthening existing reinforced concrete members. External stirrups, repaired for one IT beam with fully developed flexural steel, one IT beam with flexural cutoff details within the shear span, and one T beam with fully developed flexural steel, were included in the test matrix. The same three base specimens were constructed a second time, utilizing the supplemental internal stirrup repair. The remaining two beams were repaired with surface mounted CFRP strips in a 'U' shaped repair scheme, and rectangular FRP tape used in a NSM application.

All but two of the beams failed in shear after strengthening; both cutoff specimens failed due to anchorage. The bent cap specimens also failed in shear. For the beam specimens, the following general conclusions can be drawn:

- R2K can be used to develop design curves which take into account shear-moment interaction at a specific point of interest along a span.
- Using the shear 'pressure' term on the horizontal axis, and the required increase shear strength on the vertical axis, the required additional shear pressure for repair is readily apparent and the efficiency of the supplemental materials can be assessed relative to the base condition.

Results of the experimental work for the external stirrup repair indicate:

- The optimal repair utilizes the stiffest reaction section about the base of the stem combined with positioning the stirrup as close to the stem as possible to limit the affect of bending in the reaction section.

- Strain compatibility was obtained for the realistic case of a girder subjected to superimposed dead load consisting of safety barrier, additional wearing surface, diaphragms, and other miscellaneous hardware for the stiffest reaction section—a W beam in weak axis bending with a 25 mm (1 in.) thick steel plates mounted above the section.

- Under superimposed dead load, post tensioning of stirrups reduced the crack width and integrally cast stirrup strain; however, reductions were less pronounced compared to post tensioning under the beam's self weight.

- Post tensioning the external stirrups resulted in higher strain compatibility over the service range.

- The upper limit on post tensioning should take into account the remaining strain in the integrally cast stirrups and the nominal yield strength of the external stirrups. The external stirrups should be post tensioned such that they yield coincidentally with the internal stirrups.

- The ductile nature of the external stirrup repair results in larger crack widths throughout the service loading and beyond. Inspection of such structures should

take this into account, as it may be incorrectly be a cause for concern compared to the crack widths of the other methods.

- From the available literature, the reduction factor for weak axis bending typically results in a factor of 0.95, assuming the stirrups are mounted relatively close to the stem.

- Results from the available international codes varied, based on the assumption of a 45 degree truss analogy, or based on other mechanisms (MCFT) which dictate a different crack angle to be used.

- Comparison of the external stirrup repair with the R2K design curves previously mentioned indicated an efficiency rating of 0.84 for the fully developed IT beam while the fully developed T beam exhibited a higher efficiency rating.

- Modeling with the NLFEM program VecTor2 resulted in conservative strength estimates between 7%-18% less than the experimental data, with no consideration for weak axis bending of the reaction section.

- Utilizing all of the available comparison tools, a reduction factor of 0.80 is suggested for the external stirrup repair method.

Results from the supplemental internal stirrup repair indicate:

- Quality control of installation of this repair method is paramount to its success
- Knowledge of existing flexural steel and stirrups is required for coring purposes in order to avoid severing critical steel components
- The exterior faces of the web should be patched at the location of diagonal cracks, as seepage of the epoxy will eventually penetrate from the cored hole location to the exterior face of the beam
- Installation from the deck side of the bridge does not require any special equipment. On the other hand, installation from the bottom up may require a center hole reinforcing bar such that epoxy can be pumped through it in order to maintain even bond lines with no interference from air pockets.
- Spacers located around the reinforcing bar are required to position the bar such that it is sufficiently encapsulated by the epoxy, not skewed to one side of the hole.
- Selection of epoxy and size/grade of steel is important in the repair. The question of using a larger higher strength bar with fewer holes or more common mild steel with more holes is open to debate. Both methods were used in the current study with no noted disadvantage from a strength point of view. The additional cost of high strength rod, particularly for hollow rod, may provide an indication of the optimal repair combination.

- Post failure investigation of the internal stirrup specimens indicate a horizontal offset of the previous vertical grid lines on the specimen by dowel action.
- Crack widths at ultimate were smaller than those of the external stirrup repair.
- Providing supplemental stirrups close to the principle strain axis of the member provides the best use of materials.
- Comparison with international codes indicates an overestimation of strength for the IT beam by as much as 20%. For the T beam, the majority underestimated the strength, with one code overestimate of approximately 10%. Conservatively, a reduction factor of 0.80 is recommended for this repair.

Results from the surface bonded CFRP beam repair indicate:

- Failure of CFRP strips is non-ductile, with abrupt debonding of the strips at the free edge or from a diagonal crack toward the free edge.
- Design strengthening for CFRP should use ACI 318 for the base specimen capacity and ACI 440 for the CFRP contribution. This resulted in a conservative design which is sufficient for rehabilitation.
- Design strengthening utilizing R2K or another comparable MCFT based code in conjunction with ACI 440 is not recommended, as this results in an unconservative strength estimate that does not represent experimental data.

- Beam repair efficiencies from R2K design curves indicate the CFRP repair was 85% efficient, which coincidentally corresponds to the reduction factor that is specific to the CFRP component for shear as outlined in ACI440.

- The strength and load-deflection behavior of the repair, as modeled utilizing the approach outlined by Wong and Vecchio with VecTor2 underestimated the specimen behavior and capacity by 15%. This consequence may be more of an issue with the constitutive modeling of the bond-slip relationship.

- No additional design parameters are suggested for the ACI method for beams, as the conservative nature of the ACI 318 and ACI 440 combination is sufficient.

Results from the FRP NSM beam repair indicate:

- Installation of NSM is straightforward and required little surface preparation compared to surface bonded CFRP.

- The widely spaced strips resulted in only one location where the FRP was positioned equidistant from the eventual failure crack.

- Previous pioneering work on NSM dealt with round bars placed in square or rectangular grooves. In order the reduce the uncertainty associated with the width of epoxy bond lines, rectangular tape provides a better quality control measure for installation within a rectangular cut groove.

- Post failure of the FRP indicated the 3M epoxy provided excellent bond with the concrete such that failure was contained entirely within the concrete substrate.
- Modeling of the bond-slip relationship for NSM varies within the available literature.
- Modeling NSM within VecTor2, using the same bond-slip mechanisms from the surface bonded CFRP resulted in a slight underestimation of the capacity.
- Due to the minor increase in shear strength at ultimate, no conclusive conclusions or design recommendations can be ascertained from this test.

Results from the bent cap repairs indicate:

- The international codes all utilize the STM method for design of deep deams.
- As a design tool, STM results in a conservative design.
- STM is not recommended for evaluation of existing bent caps, due to the wide scatter of capacity estimates at the strength limit state from the various international codes.
- The Modified Zararis Method proposed by Senturk provides a simple, straightforward method to evaluate the existing strength of a deep beam.
- Using the Modified Zararis Method with the post-tensioned repair specimen, the ultimate capacity as estimated relatively well (overestimated capacity by 8%).

- The CFRP repair specimen utilized the base capacity from Zararis combined with the ACI 440 CFRP contribution. This resulted in excellent agreement with the experimental shear strength (4% underestimate).
- The STM nominal capacity resulted in conservative strength estimates 23% and 36% less than the experimental data.
- Comparison of the post-tensioned bent cap with VecTor2 resulted in a conservative estimate of strength (4% underestimate)
- The CFRP specimen failed prematurely within VecTor2 resulting in a 48% underestimate of strength—which is less than the base specimen capacity.

6.2 Future Work Considerations

Additional work is needed for the NSM repair in order to more accurately model the bond-slip relationship analytically for different FRP shapes and correlation with epoxy manufacturers products. Repair of deep beams is not well known or covered in the available literature or international codes. The single paper regarding the post-tensioned repair of bent caps suggests epoxy injection substantially increases the capacity. However, results from VecTor2 contradict this assumption, as does the Zararis Method which assumed no shear interlock along the characteristic crack. Repair of deep beams with CFRP resulted in excellent agreement of the Zararis and ACI 440 strength estimate. More tests are needed to confirm the effectiveness of this repair.

REFERENCES

AASHO, "Standard Specifications for Highway Bridges, 6th Edition," *American Association of State Highway Officials*, 1953.

AASHTO, "AASHTO LRFD Bridge Design Specifications, 3rd Edition with 2005 Interims", *American Association of State Highway Officials*, 2004, 1331 p.

Abu-Tair, A. I., Rigden, S. R., and Burley, E., "The Effectiveness of the Resin Injection Repair Method for Cracked RC Beams," *The Structural Engineer*, V. 69, No. 19, Oct. 1991, pp. 335-341.

ACI 318-05, "Building Code Requirements for Structural Concrete and Commentary," *American Concrete Institute*, 2005, 430 p.

ACI 440.1R-06, "Guide for the Design and Construction of Structural Concrete Reinforced with FRP Bars." *American Concrete Institute*, 2006, 44 p.

ACI 440.2R-02, "Design and Construction of Externally Bonded FRP Systems for Strengthening Concrete Structures," *American Concrete Institute*, 2002, 45 p.

Altin, S., Tankut, T., Anil, O., and Demirel, Y., "Response of Reinforced Concrete Beams with Clamps Applied Externally: an Experimental Study," *Engineering Structures*, No. 25, 2003, pp. 1217-1229.

Aravinthan, T. and Suntharavadivel, T. G., "Effects of Existing Shear Damage on Externally Posttensioned Repair of Bent Caps," *Journal of Structural Engineering*, November, 2007, pp. 1662-1669.

ASTM 615/615M-05A, "Standard Specification for Deformed and Plain Carbon-Steel Bars for Concrete Reinforcement," *ASTM International*, 2005.

ASTM A370-97a, "Standard Test Methods and Definitions for Mechanical Testing of Steel Products," *ASTM International*, 1997.

ASTM C192/C192M-05, "Standard Practice for Making and Curing Concrete Test Specimens in the Laboratory," *ASTM International*, 2005.

ASTM C39/C39M-05, "Standard Test Method for Compressive Strength of Cylindrical Concrete Specimens," *ASTM International*, 2003.

ASTM C617-98, "Standard Practice for Capping Cylindrical Concrete Specimens," *ASTM International*, 2003.

ASTM C496/C496M-04el, "Standard Test Method for Splitting Tensile Strength of Cylindrical Concrete Specimens," *ASTM International*, 2004.

ASTM D3039/D3039M-00, "Standard Test Method for Tensile Properties of Polymer Matrix Composite Materials," *ASTM International*, 2001.

ASTM D4541-02, "Standard Test Method for Pull-off Strength of Coatings using Portable Adhesion Testers," *ASTM International*, 2002.

ASTM E8-00, "Standard Test Methods for Tension Testing of Metallic Materials," *ASTM International*, 2000.

Barros, J. A. O., and Dias, S. J. E., "Near Surface Mounted CFRP Laminates for Shear Strengthening of Concrete Beams," *Cement & Concrete Composites*, No. 28, 2006, pp. 276-292.

Basunbul, I. A., Gubati, A. A., Al-Sulaimani, G. J., and Baluch, M. H., "Repaired Reinforced Concrete Beams," *ACI Materials Journal*, V. 87, No. 4, July-Aug. 1990, pp. 348-354.

Bentz, E.C., "Sectional Analysis of Reinforced Concrete Members," PhD thesis, Department of Civil Engineering, University of Toronto, 2000, 198 p.

CEB-FIP, "Model Code: Design Code Comite Euro-International du Beton 1990," *American Society of Civil Engineers*, 1993, 437 p.

CEN, "Eurocode 2: Design of Concrete Structures –Part 1-1: General Rules and Rules for Buildings (BS EN 1992-1-1:2004)," Comite Europeen de Normalisation, 2004.

Chajes, M. J., Januszka, T. F., Mertz, D. R., Thomson, T. A., and Finch, W. W., "Shear Strengthening of Reinforced Concrete Beams Using Externally Applied Composite Fabrics," *ACI Structural Journal*, Vol. 92, No. 3, 1995, pp. 295-303.

Chajes, M. J., Finch, W. W., Januszka, T. F., and Thomson, T. A., "Bond and Force Transfer of Composite Material Plate Bonded to Concrete," *ACI Structural Journal*, Vol. 93, No. 2, 1996, pp. 208-217.

Chung, H. W., "Epoxy-Repaired Reinforced Concrete Beams," *Journal of the American Concrete Institute,* V. 72, No. 5, May 1975, pp. 233-234.

Chung, H. W., "Epoxy Repair of Bond in Reinforced Concrete Members," *Journal of The American Concrete Institute*, V. 78, No.1, Jan.-Feb. 1981, pp. 79-82.

Colak, A. "Parametric Study of Factors Affecting the Pull-out Strength of Steel Rods Bonded into Precast Concrete Panels," *International Journal of Adhesion and Adhesives*, V. 21, No. 6, 2001, pp. 487-493.

Consenza, E., Manfredi, G., and Realfonzo, R., "Behavior and Modeling of Bond of FRP Rebars to Concrete," *Journal of Composites for Construction*, May 1997, pp. 40-51.

Cook, R. A., Kunz, J., Fuchs, W. and Konz, R. C., "Behavior and Design of Single Adhesive Anchors Under Tensile Load in Uncracked Concrete," *ACI Structural Journal*, V. 95, No. 1, Jan.-Feb. 1998, pp. 9-26.

Cruz, J. M. and Barros, J. A. O., "Bond Between Near-Surface Mounted Carbon-Fiber-Reinforced Polymer Laminate Strips and Concrete," *Journal of Composites for Construction*, November/December 2004, pp. 519-527.

CSA International, "Canadian Highway Bridge Design Code (CAN/CSA-S6-00)," Canadian Standards Association, 2000.

Dawson, M. "Scale Effects on Reinforced Concrete Beams Strengthened for Shear with Discrete Externally Bonded Carbon Fiber-Reinforced Polymer U-Wraps," Masters Thesis, Oregon State University, 2008, 125 p.

De Lorenzis, L. and Nanni, A., "Shear Strengthening of Reinforced Concrete Beams with Near-Surface Mounted Fiber-Reinforced Polymer Rods," *ACI Structural Journal*, Vol. 98, No. 1, January, 2001a, pp. 60-68.

De Lorenzis, L. and Nanni, A., "Shear Strengthening of Reinforced Concrete Beams with FRP Rods," *ASCE Journal of Composites for Construction*, Vol. 5, No. 2, May 2001b, pp. 114-121.

De Lorenzis, L. and Nanni, A., "Bond Between Near-Surface Mounted Fiber-Reinforced Polymer Rods and Concrete in Structural Strengthening," *ACI Structural Journal*, Vol. 99, No. 2, March, 2002, pp. 123-132.

De Lorenzis, L. "Anchorage Length of Near-Surface Mounted Fiber-Reinforced Polymer Rods for Concrete Strengthening-Analytical Modeling," *ACI Structural Journal*, Vol. 101, No. 3, May, 2004, pp. 375-386.

Dias, S. J. E. and Barros, J. A. O., "Shear Strengthening of T Cross Section Reinforced Concrete Beams by Near-Surface Mounted Technique," *Journal of Composites for Construction*, May/June 2008, pp. 300-311.

FIP-Commission 3 "Practical Design," "FIP Recommendations: Practical Design of Structural Concrete," 1999, 95 p.

Hammad, B. S., Al Hammoud, R., Kunz, J. "Evaluation of Bond Strength of Bonded-in or Post-installed Reinforcement," *ACI Structural Journal*, V. 103, No. 2, March/April, 2006, pp. 207-218.

Higgins, C., Yim, S.C., Miller, T.H., Robelo, M.J. and Potisuk, T., "Remaining Life of Reinforced Concrete Beams with Diagonal-Tension Cracks," *Rep. No. FHWA-OR-RD-04-12*, Federal Highway Administration, 2004a.

Higgins, C., Miller, T.H., Rosowsky, D.V., Yim, S.C., Potisuk, T., Daniels, T.K., Nicholas, B.S., Robelo, M.J., Lee, A.-Y., and Forrest, R. W., "Assessment Methodology for Diagonally Cracked Reinforced Concrete Deck Girders," *Rep. No. FHWA-OR-RD-05-04*, Federal Highway Administration, 2004b.

Horiguchi, T. and Saeki, N., "Effect of Test Methods and Quality of Concrete on Bond Strength of CFRP Sheets," *Proceedings: 3rd Symposium on Non-Metallic (FRP) Reinforcement for Concrete Structures*, Vol. 1, 1997, P. 265-270.

Kachlakev, D., and McCurry, D. D., "Behavior of Full-Scale Reinforced Concrete Beams Retrofitted for Shear and Flexure with FRP Laminates," *Composites, Part B*, Vol. 31, Issue 6-7, October 2000, pp. 445-452.

Koester, C. C. and Higgins, C. "Testing and Evaluation of Flexural Straight-Bar Anchorages in Columns," submitted to *ACI Structural Journal*, 2008.

Khalifa, A., Gold, W. J., Nanni, A., and Abdel Aziz, M. I., "Contribution of Externally Bonded FRP to Shear Capacity of RC Flexural Members," *ASCE Journal of Composites for Construction*, Vol. 2, No. 4, 1998, pp. 195-202.

Kim, S. Y., Yang, K. H., Byun, H. Y., and Ashour, A. F., "Tests of Reinforced Concrete Beams Strengthened with Wire Rope Units," *Engineering Structures*, V. 29, No. 10, October, 2007, pp. 2711-2722.

Kim, S. Y., Vecchio, F. J. "Modeling of Shear-Critical Reinforced Concrete Structures Repaired with Fiber-Reinforced Polymer Composites," *Journal of Structural Engineering*, V. 134, No. 8, August, 2008, pp. 1288-1299.

Maeda, T., Asano, Y., Sato, Y., Ueda, T., and Kakuta, Y. "A Study on Bond Mechanism of Carbon Fiber Sheet,"*Proceedings: 3rd Symposium on Non-Metallic (FRP) Reinforcement for Concrete Structures*, Vol. 1, 1997, P. 265-270.

Minh, H. Musuyoshi, H., Adhikary, B. B., and Watanabe, K., "Experimental and FEM Study for Shear Strengthening of Reinforced Concrete Beams Using Different Techniques," *Transactions of the Japan Concrete Institute*, Vol. 23, 2001, pp. 365-370.

Norris, T., Saadatmanesh, H., and Ehsani, M. "Shear and Flexural Strengthening of R/C Beams with Carbon Fiber Sheets," *Journal of Structural Engineering*, July 1997, pp. 903-911.

Popov, E. P., and Bertero, V. V., "Repaired R/C Members Under Cyclic Loading," *Earthquake Engineering and Structural Dynamics,* V. 4, No. 2, Oct.-Dec. 1975, pp. 129-144.

Rooney, R. A., "Epoxy Resins as a Structural Repair Material," State of California Department of Public Works Division of Highways, http://www.dot.ca.gov/hq/research/researchreports/1961-1963/63-23.pdf, Jan. 1963, pp. 15.

Sato, Y., Tanaka, T., Ueda, T, and Ono, S., "Shear Behavior of RC Beams Reinforced with Carbon Fiber Sheet," *Transactions of the Japan Concrete Institute*, V. 18, 1996, pp. 137-142.

Senturk, A. E., "Experimental and Analytical Evaluation of Conventionally Reinforced Deck-Girder Bridge Bent Caps with Vintage Details," Doctoral Thesis, July 11, 2008, Oregon State University, 376 p.

Senturk, A. E. and Higgins, C., "Evaluation of RCDG Bridge Bent Caps with 1950's Vintage Details: Analytical Methods," *ACI Structural Journal*, Submitted October 2008, in peer review.

Shamsai, M., Sezen, H., and Khaloo, A., "Behavior of Reinforced Concrete Beams Post-Tensioned in the Critical Shear Region," *Engineering Structures*, V. 29, No. 7, July 2007, pp. 1465-1474.

Shield, C., French, C. and Milde, E., "The Effect of Adhesive Type on the Bond of NSM Tape to Concrete," *ACI SP230: 7th International Symposium on Fiber-Reinforced Polymer (FRP) Reinforcement for Concrete Structures*, November, 2005, pp. 355-372.

Smith, M., "Investigation of the Behavior of Diagonally Cracked Full Scale CRC Deck-Girders Injected with Epoxy Resin and Subjected to Axial Tension," Masters Thesis, Oregon State University, 2007, 93 p.

Stratton, F. W., Alexander, R., Nolting, W., "Cracked Structural Concrete Repair through Epoxy Injection and Rebar Insertion," *FHWA-KS-RD-76-2*, Kansas Department of Transportation, Bureau of Materials and Research, May 1977, 47 p.

Stratton, F. W., Alexander, R., Nolting, W., "Cracked Structural Concrete Repair Through Epoxy Injection and Rebar Insertion," *FHWA-KS-RD-78-3*, Kansas Department of Transportation, Bureau of Materials and Research, November, 1978, 56 p.

Stratton, F. W., Alexander, R., and Nolting, W., "Development and Implementation of Concrete Girder Repair by Post-Reinforcement," *FHWA-KS-82-1*, Kansas Department of Transportation, Bureau of Materials and Research, May 1982, 36 p.

Tremper, B., "Repair of Damaged Concrete with Epoxy Resins," *Journal of the American Concrete Institute,* V. 32, No. 2, Aug. 1960, pp. 173-182.

Triantafillou, T., "Shear Strengthening of Reinforced Concrete Beams Using Epoxy-Bonded FRP Composites," *ACI Structural Journal*, V. 95, No. 2, March-April 1998, pp. 107-115.

Triantafillou, T. and Antonopoulos, C. P., "Design of Concrete Flexural Members Strengthened in Shear with FRP," *Journal of Composites for Construction*, November, 2000, pp. 198-205.

Vecchio, F. J. and Collins, M. P., "The Modified Compression Field Theory for Reinforced Concrete Elements Subjected to Shear," *ACI Structural Journal*, V. 83, No. 2, March, 1986, pp. 219-231.

Vecchio, F. J., "Disturbed Stress Field Model for Reinforced Concrete: Formulation," *ASCE Journal of Structural Engineering*, Vol. 126, No. 9, pp. 1070-1077.

Vecchio, F. J. and Wong, P., "VecTor2 and Formworks Users' Manual," *Technical Report*, Department of Civil Engineering, University of Toronto, 2002, 232 p.

Watson Bowman Acme Corporation, "Specification: Wabo® MBrace Composite Strengthening System with Carbon Fiber Reinforcement," March 2002.

Watson Bowman Acme Corporation, "Wabo® MBrace CF130," February 2003.

Wong, R. S. Y., and Vecchio, F. J., "Towards modeling of reinforced concrete members with externally bonded fiber-reinforced polymer composites," *ACI Structures Journal*, Vol. 100, No. 1, pp. 47-55.

Zaintz, L. and Long, J., "Oregon's Bridges at Breaking Point," *The Oregonian*, Sunday, February 3, 2002.

Zararis, P. D., "Shear Compression Failure of Reinforced Concrete Deep Beams," *Journal of Structural Engineering*, V. 129, No. 4, April, 2003, pp. 544-553.